



Study of dipole-dipole interaction between Rydberg atoms : toward quantum simulation with Rydberg atoms

Thanh Long Nguyen

► To cite this version:

Thanh Long Nguyen. Study of dipole-dipole interaction between Rydberg atoms : toward quantum simulation with Rydberg atoms. Physics [physics]. Université Pierre et Marie Curie - Paris VI, 2016. English. <NNT : 2016PA066695>. <tel-01609840>

HAL Id: tel-01609840

<https://tel.archives-ouvertes.fr/tel-01609840>

Submitted on 4 Oct 2017

HAL is a multi-disciplinary open access archive for the deposit and dissemination of scientific research documents, whether they are published or not. The documents may come from teaching and research institutions in France or abroad, or from public or private research centers.

L'archive ouverte pluridisciplinaire **HAL**, est destinée au dépôt et à la diffusion de documents scientifiques de niveau recherche, publiés ou non, émanant des établissements d'enseignement et de recherche français ou étrangers, des laboratoires publics ou privés.

DÉPARTEMENT DE PHYSIQUE DE L'ÉCOLE NORMALE SUPÉRIEURE
LABORATOIRE KASTLER BROSSEL



COLLÈGE
DE FRANCE
1530



THÈSE DE DOCTORAT
DE L'UNIVERSITÉ PIERRE ET MARIE CURIE

Spécialité : **PHYSIQUE QUANTIQUE**

Study of dipole-dipole interaction between Rydberg atoms
Toward quantum simulation with
Rydberg atoms

présentée par

Thanh Long NGUYEN

pour obtenir le grade de

DOCTEUR DE L'UNIVERSITÉ PIERRE ET MARIE CURIE

Soutenue le 18/11/2016 devant le jury composé de :

Dr. Michel BRUNE	Directeur de thèse
Dr. Thierry LAHAYE	Rapporteur
Pr. Shannon WHITLOCK	Rapporteur
Dr. Bruno LABURTHE-TOLRA	Examinateur
Pr. Jonathan HOME	Examinateur
Pr. Agnès MAITRE	Examinateur

*To my parents and my brother
To my wife and my daughter*

Acknowledgement

*"Voici mon secret. Il est très simple : on ne voit bien qu'avec le cœur.
L'essentiel est invisible pour les yeux."*

— Antoine de Saint-Exupéry, *Le petit prince*

This thesis is the culmination of many years of work, carried out with the support of so many people that I know when writing down these lines, it is impossible to give a special thank to each and every one of them. I, thus, list here only those who directly influenced this thesis. If someone is not mentioned, it does not by any means imply that he or she has played a less important role in making this thesis possible.

First and foremost, I would like to thank the permanent members of the “Cavity Quantum Electrodynamics” group, who gave me the wonderful opportunity to participate in one of their frontier researches at Laboratoire Kastler Brossel, where I have been surrounded by exceptional scientists, brilliant ideas and outstanding research equipments.

I am forever indebted to my academic supervisors: Serge Haroche, who through his series of lectures in Collège de France and by his Nobel prize, has inspired us, young PhD students to follow fundamental research; Jean-Michel Raimond, who keeps surprising us with his enormous imagination and is always available to lend a listening ear despite his busy schedule; and Michel Brune who agreed to supervise this thesis, and relentlessly guided and supported me throughout the process. With Michel’s insights into the field, he is a “super” problem solver and a driving force in innovative research. I always enjoy learning from his years of expertise, experimental skills, and above all, his endless enthusiasms on the experiment.

I have the utmost privilege of working closely with the R14 team and would like to give extensive gratitude to my team members. To Sha Liu for showing me how to correctly design and realize an optical system at the time of my first arrival even though she could stay with us only for a few short months before leaving for another job; Raul Teixeira for those long but enjoyable discussions on physics, his very good understanding of physics and willingness to tackle new problems every single time; Carla Hermann for teaching me how to treat the experiment gently, make the Helium transfer less boring and how to keep oneself optimistic even in the most depressed situation; Clément Sayrin for returning to lead the experiment after three-year doing post-doc in Vienna, as working with him is quite pleasant and gainful; Tigrane Cantat-

Moltrecht for his initial C++ and Qutip programs that helped save me a lot of time in building the simulation and Rodrigo Cortiña for his endless fundamental questions on quantum mechanics which helped me to understand better the formalization of the quantum theory.

My sincere thank goes next to Sébastien Gleyzes, who leads the fountain experiment – a new version of the cavity CQED experiment, and sacrifices his time working as the “Helium manager” of the group. Without him, the experiment would have been performed at room temperature. He also helped us tremendously in equipping the experiment, from “big” machines like frequency generators to “small” stuffs like SMA connectors, and was there every time if we have any problem in R14, either experimentally or personally. I am also grateful to him for correcting my M2 internship report, scanning and sending it to me and yet, I have not had a chance to thank him personally.

A warm thank you to Igor Dotsenko for always finding time for us for whatever problem that we have, his willingness to dive into hundreds of pages of code just to troubleshoot the experiment controls, his endless and fascinating stories about Ukraine, and many useful advices from both him and his wife on how to raise a child.

Beside those mentioned above, I would like to extend great thanks to my wonderful group members, who have made my PhD life so enjoyable and successful: Bruno Peaudecerf, Théo Rybarczyk, Stefan Gerlich, Adrien Signoles, Adrine Facon, Mariane Penasa, Eva-Katharina Dietsche, Dorian Grosso, Frédéric Assemat, Valentin Métillon and Arthur Larrouy.

I am thankful and honored to have Pr. Agnès Maître, Pr. Jonathan Home, Dr. Bruno Laburthe-Tolra, Dr. Thierry Lahaye and Pr. Shannon Whitlock in my defense committee.

I would like to thank also the administrative service, the electronic service, the cryogenic service as well as the mechanical workshop as their work has helped the experiment go on smoothly.

I am deeply thankful to my parents for their love, sacrifices and constant supports throughout my life, and to my brother for taking over my responsibilities to my parents when I am away. And most importantly, a special recognition goes to my wife for her unwavering love, quiet patience, constant encouragement and relentless support during the entire process that are undeniably what made this thesis happens. And finally, I would love to dedicate this last acknowledgment to my little lovely girl who is the pride and joy of my life.

Contents

Introduction 1

I A short review on Rydberg atoms 9

1 Properties of individual Rydberg atoms 11

- 1.1 From the Hydrogen atom to the Rubidium Rydberg atom 11
- 1.2 Electric dipole 16
- 1.3 Radiative lifetime 20
 - 1.3.1 Spontaneous emission 20
 - 1.3.2 Blackbody-radiation-induced decay 22
- 1.4 Rydberg atoms in external fields 23
 - 1.4.1 Magnetic field 23
 - 1.4.2 Electric field 25

2 Interacting Rydberg atoms 31

- 2.1 Two antennas in communication 31
- 2.2 A pair of atoms in the same state 32
- 2.3 An atom pair involving two different states 34

II Towards quantum simulation with low-*l* Rydberg atoms 37

3 Superconducting atom chip experiment 39

- 3.1 Ultra-cold atom source 40
 - 3.1.1 Cryostat 40
 - 3.1.2 Atom chip 42
 - 3.1.3 Atom imaging 44
 - 3.1.4 Laser system 46
 - 3.1.5 Trapping and cooling of atoms 47
- 3.2 Rydberg excitation 51
 - 3.2.1 Two-photon excitation 51
 - 3.2.2 Rydberg detection 53

3.3	Coherent manipulation of Rydberg atoms	54
3.3.1	Taming the stray electric fields	54
3.3.2	Coherent manipulation of the Rydberg atoms	56
4	Microwave ruler for dipole-dipole interaction	59
4.1	Two regimes of Rydberg excitation	59
4.1.1	Dipole blockade	59
4.1.2	Facilitated excitation — Rydberg aggregate	61
4.1.3	Optical spectra	63
4.2	Microwave probe of van der Waals interaction energy	65
4.2.1	Choice of levels	65
4.2.2	Experimental work	68
4.3	Preliminary interpretation	71
4.3.1	Monte Carlo simulation	71
4.3.2	Numerical result	72
4.3.3	Limitation	74
4.4	Monte Carlo - rate equations simulation	75
4.4.1	Rate equations limit of the optical Bloch equations	75
4.4.2	Algorithm	77
4.5	Experimental data simulation	79
4.5.1	Optical profile	79
4.5.2	Microwave spectra	82
4.5.3	Spatial distribution of Rydberg atoms	83
4.5.4	Discussion on the validity of the Monte Carlo – rate equations model	83
III	Quantum simulation with circular Rydberg atoms – A proposal	89
	Objectives	91
5	Principles of the quantum simulator	95
5.1	The quest for long-lived circular atoms	95
5.1.1	Inhibition of spontaneous emission	95
5.1.2	Suppression of blackbody radiation absorption	96
5.1.3	Background gas collisions	97
5.2	Trapping of circular atoms	97
5.2.1	Ponderomotive potential	97
5.2.2	Photo-ionization by trapping lasers	99
5.3	Two interacting circular atoms in free space	100
5.3.1	Application of a magnetic field	102
5.3.2	Dipole-dipole interaction and its scaling laws	105
5.4	1D spin chain's Hamiltonian	110
5.4.1	1D spin chain Hamiltonians	112
5.4.2	Choice of levels and tunable XXZ spin chain	115

5.5	Deterministic chain preparation	116
5.5.1	Initial irregular chain preparation	117
5.5.2	Spin chain tailoring	120
5.6	Arbitrary chain initialization	127
5.7	Site-resolved state-selective detection	128
5.8	Effects of decoherence	128

Conclusion and perspectives 131**Appendices** 137**A Electric dipole matrix element estimation** 139

A.1	Radial matrix element	139
A.2	Angular matrix element	140

B Laser frequency stabilization and laser distribution 143**C Measurement of the trap dimension** 145

C.1	Temperature measurement	145
C.2	Trap frequencies	145

D Fourier limited line width 147**E Two atoms: motion and spin exchange** 149**Résumé en français** 153

Introduction

At the beginning of the last century, physicists have realized the “weirdness” of the quantum world. Since then, they have witnessed revolutionary evolutions in our understanding of the quantum theory, which can be summarized in two achievements: the description of wave-particle duality and the understanding of superposition and entanglement, in which no classical model can fit [1–3]. Together with these conceptual progresses, technologies and applications have also achieved important advancements. One can mention the laser and the optical revolution, the atomic clocks and the precise time measurements or the transistor and the computer revolution [3, 4].

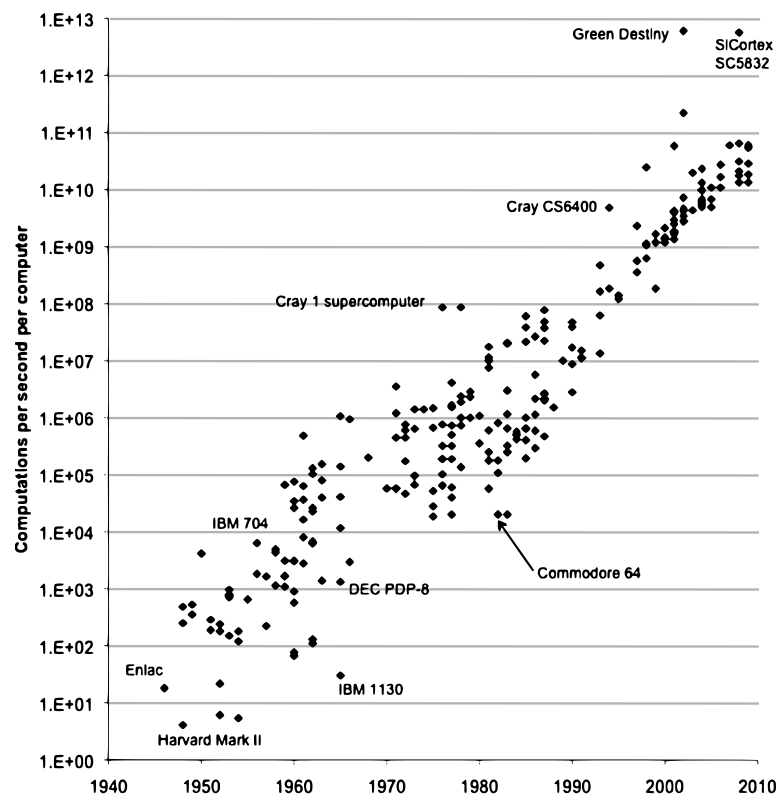


Figure 1 Improvement in computational power (in log scale) over the past century. Figure extracted from [5].

Let us focus on the latter. Born in the late 1940s, transistors followed by integrated circuits have dramatically changed the way we communicate, diagnose and compute.

Assemblies of cupboard-size boxes, packed with vacuum tubes and linked by kilometers of wires have been replaced by microchip processors of a stamp size, a thousand times smaller in weight and volume, but billion times more efficient in computational power (Figure 1) [5]. The data storage capacities have been improved in the same manner [6]. The reach of nowadays computers spreads from daily applications to heavy computational tasks like weather forecasting [7], probabilistic analysis [8] or deep learning and artificial intelligence [9, 10]. The range seems to continue increasing without any limitation.

Quantum simulations

The properties of electronic devices in modern computers are ruled by quantum laws at the microscopic scale: tunnel effects, exclusion principle,... However, the computational algorithms are still based on pre-quantum logics, i.e., classical bits, which take a value either 0 or 1. From the early 1980s, the limitations to which traditional computations have to face when dealing with quantum many body systems became clear [11]. Let us take as an example N interacting spin 1/2 particles. Due to the fact that a spin can be hung suspended between two states: up and down, the Hilbert space has a dimension 2^N . Calculating the time evolution of the system requires exponentiating matrices with $2^N \times 2^N$ elements. Classical stochastic methods, such as Monte Carlo algorithms have been developed to deal with this ‘exponential-explosion’ problem [12]. However for some quantum systems, especially fermionic and frustrated systems, they exhibit an exponential growth of statistical errors, which results in an exponential growth of calculation time with the number of particles [13]. A system of more than 40 spins is frequently cited in the literature [14–17] as the standard “threshold” above which classical computational methods fail.

When R. Feynman delivered his seminal lecture in 1982, he proposed a brilliant solution to this problem [11]

“Let the computer itself be built of quantum mechanical elements which obey quantum mechanical laws.”

That is to have “one controllable quantum system simulate another” [11]. This idea of quantum simulation [16, 18, 19] is very appealing in that one solves at the same time two problems: the problem of large amounts of information storage and the problem of large amount of information processing. In a general procedure, after preparing an initial state, one lets the simulator evolve into the final quantum state and measures some quantity of interest.

How does one quantum system simulate another? One way would be to approximate the time evolution of the simulated system by applying a sequence of elementary quantum gates on an ensemble of qubits that encodes the state of the quantum system. This follows the circuit model for quantum computation [20] and is referred to as *digital quantum simulation* – the yet-to-be-built quantum computers. Despite its universality [16], it comes at a high cost in gate number, and thus requires very high fidelity gates. Quantum error correction methods [21] have been developed to relax this requirement.

Another approach, *analog quantum simulation*, uses a quantum system to mimic (emulate) the evolution of another, i.e., “... be an exact simulation, that the computer will do exactly the same as nature” [11]. This approach has less stringent requirements on resources. Up to a certain tolerance level, the analog quantum simulator can give useful results even in the presence of errors. It is thus simpler to design an analog quantum simulator to handle a peculiar class of problems.

In recent years, quantum simulations has become one of the most promising sub-fields of the quantum information science. First, advanced technologies are mature enough to enable the control of quantum systems at a very high level. The 2012 Nobel prize in physics was awarded for “groundbreaking experimental methods that enable measuring and manipulation of individual quantum systems” [22]. The physical realization of quantum simulation is thus within reach. Second, quantum simulation, by overcoming the limitations encountered by classical computational methods, would be able to tackle difficult problems for quantum many-body systems. Let us take as an example spin networks. They present fascinating properties, such as quantum transport, exotic phase transition, localization, slow evolution. A complete understanding of these systems is of paramount importance for the advancement of fundamental science, related to physics, chemistry and even biology. It would also accelerate the development of radically new materials with fully engineered properties. Quantum simulations have thus the potential to shape future applications.

State of the art

Quantum simulations are attracting an increasing interest in many areas of physics ([Figure 2](#)). They have been intensively studied both theoretically and experimentally worldwide with cold atoms [23–26], trapped ions [27, 28], superconducting devices [29], polaritons in cavities [30], photons in networks [31, 32], polar molecules [33], quantum dots [34–36] and many others. Several proof-of-principle demonstrations have been performed [15, 37–40]; however, the majority have not yet outperformed the capacities of classical computers. Covering all these developments is out of the scope of this thesis. Instead, we briefly review here some of the most advanced systems, which rely on trapped ions, superconducting circuits or optical lattices.

Superconducting circuits

Superconducting circuits involve macroscopic qubits that display quantum behaviors like “artificial atoms” [41, 42]. They can be used to test quantum physics at macroscopic scale or to simulate atomic physics and quantum optics. These electric-circuit based qubits can be manipulated and measured with very high fidelity. In addition, the extremely strong coupling between them provides spin-spin interaction. This architecture is suitable for both digital [43, 44] and analog [45, 46] quantum simulations. Another advantage is that the artificial atoms are quite easy to design, fabricate and eventually wire together to realize various lattice geometries. The coherence times of the state-of-the-art superconducting qubits can exceed 100 µs. However, quantum simulation speed-up with a large number of qubits is still an open question [47–49].

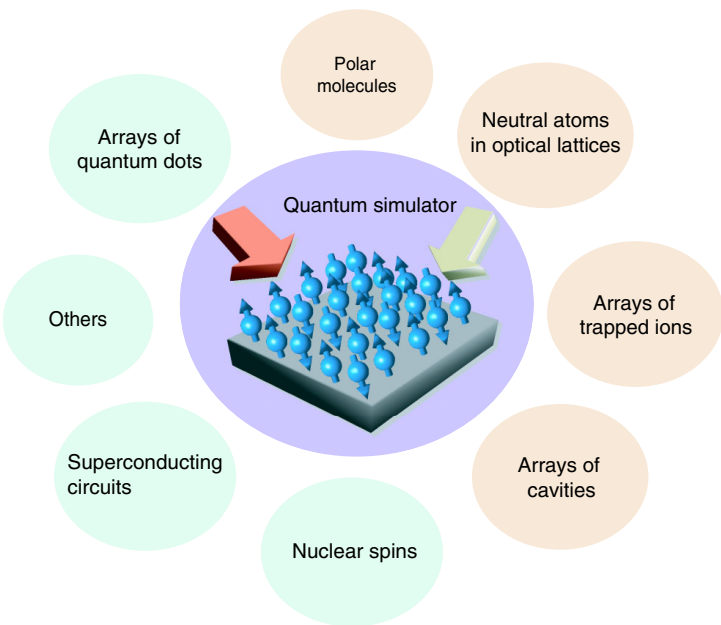


Figure 2 Quantum simulation has been raising interest from many areas of physics. Figure extracted from [19].

Trapped ions

Trapped ions [50, 51] have shown to be a very promising system for quantum information processing [52] and for quantum simulation [27, 53, 54]. Both the internal energy levels and the vibrational modes of the ions can be used to encode quantum information, which can be read out with almost unit efficiency. The coherence times of ion qubits when encoded on two hyperfine levels have reached in the order of seconds (even minutes) and application of sequences with hundreds of high-fidelity gates is feasible. Trapped ions have performed the most advanced implementation of digital quantum simulations [55, 56] to date, notably the simulation of a QED pair creation process [57]. When operating basing on the motional modes, the coherence time is much shorter.

Analog quantum simulation with trapped ions has also been demonstrated. Among these demonstrations are the realization of frustrated spin systems, of entanglement propagation [58, 59] and of many-body-localization [60]. The coupling between the internal states and the vibrational modes induced by laser driving leads to an effective spin-spin interaction, which can be tuned from long-range to medium-range behaviors [61, 62]. However, most of these experiments are performed with 1D chains of ions held in a linear Paul trap. Efforts to go to quantum simulations with 2D arrays have resulted in the realization of ferromagnetic and anti-ferromagnetic Hamiltonians with hundreds of ions in a Penning trap [63, 64]. The interactions, nevertheless, cannot be tuned in the nearest neighbor regime of great interest. There are other proposals using 2D Paul traps [65, 66] or arrays of microtraps [67, 68]; however coherence times in these systems have not yet been measured.

Cold atoms in optical lattices

Cold atoms in optical lattices are remarkable tools for analog quantum simulation [24–26]. The atoms, either bosons or fermions, are placed at the bottom of 1D, 2D or 3D optical potentials. Dynamics is then provided by the competition between adjacent site tunneling and on-site two-body interaction. The former is controlled by the lattice potential depth, while the latter is adjusted through the Feschbach resonance mechanism. Atoms are imaged individually with sophisticated optics [69, 70]. Their internal state is resolved by fluorescence. Cold atoms in optical lattices are flexible systems, not only because of their capability of realizing various geometries but also because of the tunability of the experimental parameters. Since the first observation of the phase transition from a superfluid to a Mott insulator [37], quantum simulation with cold atoms has become a very active field. It can address a wide range of problems such as the Bose-Hubbard Hamiltonian [24], the many-body localization [71, 72], or recently the artificial gauge fields [73, 74] and the fractional quantum Hall effect [75, 76].

In spite of these successes, quantum simulation with cold atoms in optical lattices has a drawback. The tunneling rate is relatively low (few hundred Hz) as compared to the lifetime of the trapped atomic cloud (seconds). The evolution is thus limited to a few hundred typical tunneling times. This is certainly a big disadvantage when slow dynamics is involved such as in many-body localization or spin glasses. As a solution, trapping with other type of lattices with smaller spacing has been proposed [77, 78]. Alternatively one can use polar molecules [79, 80] or atomic species with a large magnetic dipole moment [81, 82] to enhance the interaction strength. These systems are, however, rather challenging to realize.

Quantum simulation with Rydberg atoms

Rydberg states are highly excited atomic states with remarkable properties [3, 83], even quite exaggerated when compared to those of ordinary atomic states. Among their properties, one will note particularly their large electric dipole matrix elements and their long lifetimes, not to mention their simple internal structures and their easy experimental manipulation. Put into numbers, the dipole matrix elements are typically of a few hundred to thousand times larger than those of ground-state atoms. Rydberg states can last longer than hundreds of μs . In particular, *circular* Rydberg states — Rydberg states with maximum angular momentum and magnetic quantum numbers — have lifetimes in the order of tens of milliseconds. Their properties have been successfully exploited in the framework of *cavity quantum electrodynamics* (cavity QED) with a series of experiments developed at Laboratoire Kastler Brossel [84–95].

With large electric dipole matrix elements, these long-lived, highly excited atoms when placed close together interact strongly via the van der Waals dipole-dipole interaction, C_6/R^6 where R is the inter-atomic distance. With R of a few μm , the interaction energy can be in the MHz range, and even larger for the Förster-like resonant energy exchange interaction (scaling as $1/R^3$) [96]. Changing the principal quantum number, one can tune this interaction energy by orders of magnitude.

A protocol for digital quantum simulations with Rydberg atoms has been developed [97, 98]. It is based on the *dipole blockade* mechanism, which is a direct conse-

quence of the strong Rydberg-Rydberg interaction [99]. In a small sample of cold ground-state atoms, the van der Waals interaction is much higher than the typical laser excitation linewidth (~ 100 kHz). As soon as an atom is resonantly laser excited, all the others are tuned out of resonance, resulting in the excitation of one and only one Rydberg atom at a time [100, 101]. One can thus, realize a Controlled-NOT (CNOT) gate, in which depending on the state of the control qubit, the state of all other qubits is left unchanged or flipped [96, 99, 102–104].

The strong interaction between Rydberg atoms also makes them very promising tools for analog quantum simulation of spin networks. This has renewed the interest for these atoms, and led to many proposals for quantum simulations with Rydberg atoms [105–108]. Among many experimental demonstrations, the observation of coherent excitation transport over a chain of three Rydberg atoms is quite remarkable [109]. The Rydberg excitation dynamics of arrays with more than 20 atoms has been recently reported [110]. Efforts to mix ground-state atoms with Rydberg atoms, i.e., Rydberg dressing, in optical lattices have been proposed as a solution to the slow tunneling problem [111–115]. However, these experiments are at 300 K and thus suffer from the blackbody radiation, which modifies the Rydberg interaction in an uncontrolled way [116–118]. Going to cryogenic environment to suppress the number of thermal photons is a difficult solution.

However, Rydberg atoms used in the above systems have low angular momentum. Quantum simulation with low- l Rydberg atoms has intrinsic limitations. First of all, the Rydberg atoms experience mechanical forces either attractive or repulsive, due to their strong interactions. Without being trapped, any Rydberg crystal will “melt” down after a few tens μ s. Trapping Rydberg atoms in an optical lattice [119] has been studied. However, this trapping suffers from a strong reduction in the Rydberg lifetime due to photo-ionization by the trapping laser [120]. Second, the lifetimes of low- l Rydberg states are long compared to those of ordinary excited states, but still only of a few hundred μ s, corresponding to a few hundred of typical exchange periods. This prevents quantum simulation with low- l Rydberg atoms from studying slow dynamics of arrays with tens of spins.

In such a context, this thesis **studies the interaction between Rydberg atoms and explores new schemes for quantum simulations with Rydberg atoms**. Experimentally, we laser-excite Rydberg atoms, either resonantly or off-resonantly, from a cold and dense cloud of ground-state Rubidium atoms prepared using a superconducting atom chip. Since Rydberg atoms are quite sensitive to thermal radiation, the experiment is performed in a cryogenic environment, to which a superconducting chip is perfectly adapted. This work contributes to four main achievements, which can be summarized as follows.

Control of the electric field and coherent manipulation of Rydberg levels in the vicinity of the chip. The downside of having large dipole matrix elements is that Rydberg atoms are extremely sensitive to stray electric fields. The inevitable slow deposition of Rubidium atoms on the chip surface during the experiment creates patches of dipoles, resulting in a temporally unstable and spatially inhomogeneous electric field in the vicinity of the chip [121, 122]. The Stark effect thus enlarges the transition lines to an extent (~ 40 MHz) that completely destroys the dipole blockade mechanism. This has been a formidable experimental challenge for us and other teams. A solution

to this problem is finally rather simple. A thick layer (~ 100 nm) of Rubidium covering the chip in a large area saturates the effect of slow Rubidium deposition. The field inhomogeneity is thus strongly suppressed, providing a good environment to study the Rydberg-Rydberg interaction. This solution is detailed in Carla Hermann's thesis, and is the object of a highlight in Physical Review A [123].

Microwave probe of the van der Waals interaction energy in a cold Rydberg gas. Being laser excited from a dense cloud, Rydberg atoms strongly interact with each other. Microwave spectroscopy of the transition to a nearby Rydberg state allows us to precisely probe the interaction energy distribution. We have applied this technique to observe the mechanical expansion of an ensemble of Rydberg atoms under strong repulsive interaction. This observation sets up a time scale during which the frozen Rydberg gas approximation is still valid. A simple Monte Carlo model has also been developed to explain the microwave spectra. The method is the subject of Raul Teixeira's thesis and is summarized in a paper in Physical Review Letter [124].

Developing a more rigorous simulation of the Rydberg excitation process. Despite the fact that the simple Monte Carlo model succeeds in reconstructing the microwave spectra, it fails for the optical excitation lines and exhibits several limitations, preventing us from studying new excitation schemes. A new model has been developed during the reconstruction of the experiment after its re-localization in our new laboratory at Collège de France in 2014. This new model gives us a good insight into the excitation process.

Quantum simulation with laser-trapped circular atoms. Atoms in circular Rydberg states, despite their unique properties and successes with cavity QED experiment, have not yet been, to our knowledge, fully exploited for quantum simulation. After careful investigations on the interaction between them, we came up with a proposal for quantum simulation. The proposed scheme aims at overcoming the limitations of other systems, including those with low angular momentum Rydberg atoms. It is based on the groundbreaking concept of laser-trapped circular Rydberg atoms, protected from spontaneous decay and interacting strongly through a dipole-dipole coupling. More than that, it combines the flexibility found in atomic lattices, the strong interactions, typical of Rydberg atoms, and the exquisite control, typical of trapped ions. The realization of such a platform would allow quantum simulation to exceed the grasp of classical computational methods.

This manuscript is organized in three parts with five chapters. In the first part, we recall the important properties of Rydberg atoms. These properties make it clear why Rydberg atoms are very good tools for quantum simulation. The first part also includes elements necessary for the understanding of the two following parts. Chapter 1 concentrates on individual Rydberg atoms. It consists in the description of Rydberg states, Rydberg's lifetimes and their behaviors in an external electric and/or magnetic field. Low angular momentum Rydberg atoms and circular (high- l) Rydberg states are presented in parallel. Considering two Rydberg atoms close to each other, chapter 2 formalizes the interaction between Rydberg atoms in free space. We discuss in details the situation of the low l Rydberg atoms, but the concept can be easily extended to circular atoms as well.

In the second part of the manuscript, we present our studies on dipole interaction between low- l Rydberg atoms. Chapter 3 describes the current experimental setup, and the preparation of cold and dense ground-state atoms as well as the Rydberg excitation. We discuss briefly also how we managed to obtain an unprecedented long coherence time with Rydberg atoms near a metallic surface. Chapter 4 presents our new insight into the Rydberg excitation process. We recall the experimental results on the excitation of Rydberg atoms in the strong interaction regime as well as our preliminary interpretation. Then we develop a more rigorous model, the Monte Carlo – rate equations simulation, with which the Rydberg excitation process is better described. To end this chapter, we use the developed model to consider the preparation of a 1D Rydberg chain for quantum transport simulations.

In the third part, we describe our proposal of a new platform — laser-trapped circular atoms — for quantum simulation. After presenting the objective and principles of the proposal, we discuss in details the main ingredients for realizing the quantum simulator with circular atoms. We show that a tunable spin Hamiltonian for a 1D chain, based on the interaction between circular atoms is feasible with a proper choice of Rydberg states. We also present a complete experimental sequence to deterministically prepare a chain with more than 40 atoms. Many technical details will be considered, showing the realism of the proposal.

We conclude this manuscript by discussing a wide range of problems that trapped-circular-atoms could be able to address.

I.

A short review on Rydberg atoms

Properties of individual Rydberg atoms

1

In this chapter, we will discuss the main properties of Rydberg atoms, which make them very good tools for quantum simulation. They consist in their long lifetimes, their huge dipole matrix elements and, as a consequence, their strong mutual interaction. Not less important from the point of view of an experimentalist, are their easy manipulation using available microwave technology, their easy detection using field ionization and their simple internal structure. In each section, we will first discuss the general principles. Then, we will go into details for low- l states and for circular states. The differences between low- l states and circular states can be thus easily recognized. Examples given along this chapter are mainly for 60S state and for the circular 50C state. They are the levels chosen for our setup under technical constraints, which will be discussed in next parts.

1.1

From the Hydrogen atom to the Rubidium Rydberg atom

Hydrogen atom approximation

Rydberg atoms are highly excited atoms, very close to the ionization limit. Most of the time, the outer electron stays far away from the atomic core which is several orders of magnitude smaller than the orbit of the electron*. Rydberg atoms can therefore be very well approximated by a Hydrogen atom, where the outer electron held by the Coulomb force orbits around an elementary charge. If we consider that the core is infinitely massive the Hamiltonian reads

$$H_0 = -\frac{\hbar^2}{2m_e} \nabla^2 - \frac{e^2}{4\pi\epsilon_0 r}, \quad (1.1)$$

where m_e is the mass of the electron, e is the elementary charge, ϵ_0 is the vacuum electric permittivity, $\hbar = h/2\pi$ is the reduced Planck's constant and r is the distance of the electron from the core. In atomic units the Hamiltonian takes the form

$$H_0 = -\frac{\nabla^2}{2} - \frac{1}{r}. \quad (1.2)$$

*Here we consider only alkali atoms with a single valence electron

Its eigenfunctions are well known and are written as a product of radial and angular functions

$$\psi(r, \theta, \phi) = R_{nl}(r) Y_l^{m_l}(\theta, \phi), \quad (1.3)$$

where θ and ϕ are respectively the polar angle with respect to the quantization axis and the azimuthal angle [83, 125]. Here $Y_l^{m_l}(\theta, \phi)$ is a spherical harmonic function, which is proportional to an associated Legendre polynomial $P_l^{m_l}(\cos \theta)$

$$Y_l^{m_l}(\theta, \phi) = N e^{im_l\phi} P_l^{m_l}(\cos \theta), \quad (1.4)$$

where N is a normalization constant. The radial part $R_{nl}(r)$ can be expressed using a generalized Laguerre polynomial L_{n-l-1}^{2l+1} of degree $n - l - 1$

$$R_{nl}(r) = \sqrt{\left(\frac{2}{na_0}\right)^3 \frac{(n-l-1)!}{2n[(n+l)!]}} e^{-r/na_0} \left(\frac{2r}{na_0}\right)^l L_{n-l-1}^{2l+1}\left(\frac{2r}{na_0}\right), \quad (1.5)$$

where $a_0 \approx 5.29 \times 10^{-11}$ m = 0.529 Å is the Bohr's radius. The square root term is a normalization factor.

A state of the atom is therefore defined by three integers n, l and m whose values satisfy

$$\begin{aligned} n &= 1, 2, 3, \dots, \\ l &= 0, 1, 2, \dots, n-1, \\ m_l &= -l, -l+1, \dots, -1, 0, 1, \dots, l-1, l. \end{aligned} \quad (1.6)$$

They are called respectively the principal quantum number, the azimuthal quantum number and the magnetic quantum number. Using these three quantum numbers, we denote a state of the atom as $|nlm\rangle$. Rydberg atoms have very high principal quantum number $n \gg 1$. The binding energy is given by the Rydberg formula:

$$E_n = -\frac{1}{2n^2} = -\frac{1}{n^2} R_\infty, \quad (1.7)$$

where

$$R_\infty = \frac{m_e e^4}{8\epsilon_0^2 h^2} = 0.5 \text{ a.u} = 13.605693009(84) \text{ eV} \quad (1.8)$$

is the Rydberg constant [126]. To account for the finite mass M of the atomic core, one has to replace R_∞ by

$$R_M = \frac{R_\infty}{1 + \frac{m_e}{M}}. \quad (1.9)$$

Nevertheless the modification is small as $m_e \ll M$.

In addition, the state of the electron spin is represented by a fourth quantum number s (spin quantum number), which takes only two values, spin up $s = +1/2$, or spin down $s = -1/2$.

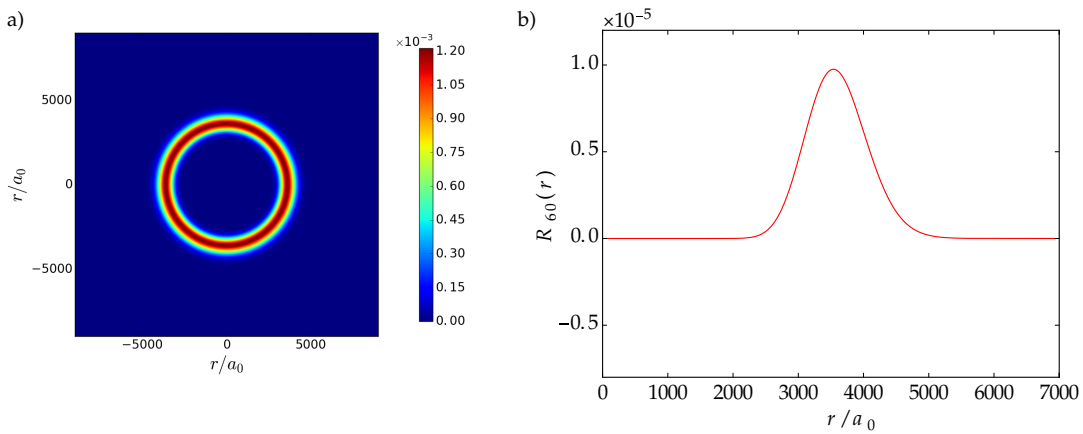


Figure 1.1 a) Radial probability of finding the outer electron $r^2 R_{60}(r)$ for ^{87}Rb 60C state. b) Radial part of wavefunction for the ^{87}Rb circular 60C state.

Circular Rydberg state

A remarkable case is when l and $|m_l|$ take their maximum values $l = |m_l| = n - 1$. From equations (1.3) and (1.5) the wavefunction has then a simple form

$$\psi(r, \theta, \phi) = \frac{1}{\sqrt{\pi a_0^3}} \frac{1}{nn!} \left(-\frac{r}{na_0} \sin \theta e^{i\phi} \right)^{n-1} e^{-r/na_0}. \quad (1.10)$$

The orbital is a torus of radius $n^2 a_0$ and thickness (dispersion) $\Delta r/r = \Delta\theta \approx 1/\sqrt{2n}$, lying perpendicular to the quantization axis Oz. A cut through the plane of the torus is depicted in Figure 1.1a. In the Bohr-Sommerfeld semi-classical model, the outer electron travels around the atomic core on eccentric elliptical trajectories depicted in Figure 1.2. The larger l , the less eccentric the orbit is. The torus somehow corresponds to the semi-classical image of a circular orbit with a maximum angular quantum number l , especially for very high n , where the confinement to the Bohr orbit is tighter. The state with $l = |m_l| = n - 1$ is thus given the name *circular* state, and denoted $|nC\rangle$. The other states are called *elliptical* to distinguish them from the circular one. There are two circular states in the same n manifold, corresponding to $m_l > 0$ and $m_l < 0$. In practice, a strong electric field is added to define the quantization axis. The behaviors of the two circular states in presence of an external electric field are the same (see subsection 1.4.2). If not specified otherwise, we implicitly consider the m_l positive case.

Fine structure

In a more complete picture, we have to take into account the interaction between the electron spin and its motion. The interaction Hamiltonian reads

$$H_{FS} = A \mathbf{L} \cdot \mathbf{S}, \quad (1.11)$$

where \mathbf{L} and \mathbf{S} are the total orbital momentum and the spin operators of the Rydberg electron. The strength of the interaction is represented by the constant A . We define

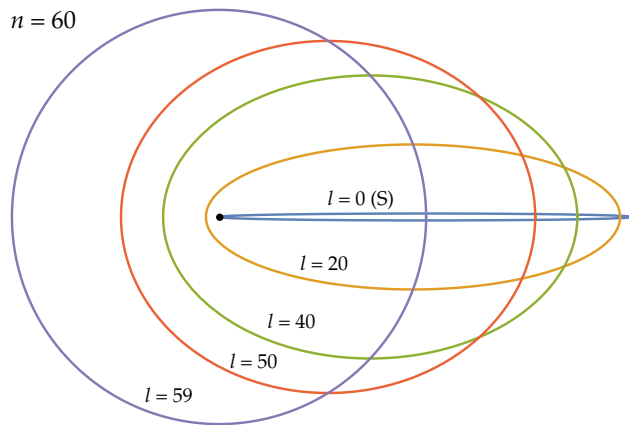


Figure 1.2 Trajectories of the outer electron as described by the Bohr-Sommefeld model, drawn for a $n = 60$ Hydrogen atom with $l = 0, 20, 40, 50$ and 59 . The black dot represents the position of the atomic core.

the total angular momentum operator

$$\mathbf{J} = \mathbf{S} + \mathbf{L} . \quad (1.12)$$

It can be shown that the five operator $H_0, \mathbf{J}^2, \mathbf{L}^2, \mathbf{S}^2$ and J_Z – the projection of \mathbf{J} on the quantization axis Oz all commute with each other and with H_{FS} . An eigenstate of the Hamiltonian is simultaneously an eigenstate of the five operators. In addition to n, l and s , we introduce two new quantum numbers to represent an eigenstate of the atom, the total angular momentum quantum number j and the total angular momentum projection quantum number m_j . Their possible values are

$$\begin{aligned} j &= l \pm \frac{1}{2} \\ m_j &= -j, -j+1, \dots, j-1, j . \end{aligned} \quad (1.13)$$

Since s takes only one value $s = 1/2$ for a single valence electron, the corresponding state of the atom can be denoted as $|n l s j m_j\rangle$. The fine structure takes into account both the spin-orbit interaction and the correction due to relativistic effects. The corrected binding energy is given by [127]

$$E_{nlj} = E_n + \frac{E_n \alpha_F^2}{n^2} \left(\frac{n}{j+1/2} - \frac{3}{4} \right) , \quad (1.14)$$

where $\alpha_F = e^2 / 4\pi\epsilon_0\hbar c \approx 1/137$ is the fine structure constant. For $l \approx n$, and thus $j \approx n$, the correction term is approximately $\alpha_F^2/4n^2$ times smaller than E_n . As an example, it is about 7.6 kHz for $n = 50$, much smaller than a typical interaction with an external electric or magnetic field (a few MHz). We thus ignore the fine structure for high- l Rydberg states, including the circular states.

One can go further with the hyperfine structure description in which the interaction couples the electron angular momentum with the nuclear spin. However for

Rydberg atoms, the coupling is typically much weaker than the interaction with external fields. For instance, the hyperfine shift of $60S_{1/2}$ state is of about 200 kHz [128]. We therefore neglect the hyperfine structure in the following.

Quantum defect

So far, we have treated the atomic core as a single point charge. This assumption holds as long as the outer electron is far away from the nucleus. As illustrated in [Figure 1.2](#), the eccentricity tells us how much the electron gets close to the core. All the description above in terms of the Hydrogen atom is valid for large l Rydberg states. Circular state is an extreme case where the hydrogenic approximation is nearly perfect.

However for low- l Rydberg states, one has to take into account the non-negligible penetration of the outer electron into the electronic cloud of the core. The electron sees the deviation of the ionic core potential from that of the Hydrogen atom. It feels a deeper Coulomb potential due to a smaller screening of the nucleus charge from the inner electronic cloud. In addition, the presence of the outer electron close to the core leads to a deformation of the inner electronic cloud. One needs to include higher order correction terms (dipole, quadrupole...) to account for the polarization of the atomic core. These effects lower the energy of the Rydberg state. It is interesting that the energy is still described by a modified Rydberg formula

$$E_{nl} = -\frac{1}{2(n - \delta_l)^2}, \quad (1.15)$$

where δ_l is called the quantum defect.

A more precise correction as suggested in [83] takes into account the spin orbit interaction and expresses the quantum defect as a power series of $1/(n - \delta_{lj,0})$:

$$\delta_{nlj} = \delta_{lj,0} + \frac{\delta_{lj,2}}{(n - \delta_{lj,0})^2} + \frac{\delta_{lj,4}}{(n - \delta_{lj,0})^4} + \frac{\delta_{lj,6}}{(n - \delta_{lj,0})^6} + \dots \quad (1.16)$$

The coefficients are determined experimentally using precise microwave spectroscopy for neighboring Rydberg transitions [129, 130] or by observing electromagnetically induced transparency with help of a calibrated frequency comb [131]. Only the first two terms (modified Rydberg - Ritz parameters) are sufficient to give a precision better than a hundred kHz. The measured quantum defects for ^{85}Rb and ^{87}Rb are summarized in [Table 1.1](#). Up to our knowledge, there are no precise measurements for ^{87}Rb so far other than for S and D levels. However, using the quantum defects of ^{85}Rb still yields good results as the electronic structure for the two Rubidium isotopes are quite similar. The only difference comes from the mass difference, which slightly modifies R_M . This approximation can be verified for S and D levels as depicted in [Table 1.1](#). No experimental measurements of the quantum defects have been reported for $l > 4$. As discussed by T. Gallagher in [83], the non-penetrating high-angular-momentum states have quantum defects scaling as l^{-5} . Knowing that $\delta_{G,0} = 0.004$, we can roughly estimate $\delta_{l \geq 4}$ as

$$\delta_{l \geq 4} = \delta_{G,0} \left(\frac{4}{l} \right)^5. \quad (1.17)$$

For very high- l Rydberg states, the quantum defects drop rapidly to zero as expected.

Letting n^* be the principal quantum number corrected by the quantum defect, the binding energy takes again the Rydberg formula form

$$E_{n^*} = -\frac{R_\infty}{1 + \frac{m_e}{M}} \frac{1}{(n - \delta_{nlj})^2} = -\frac{R_\infty}{1 + \frac{m_e}{M}} \frac{1}{n^{*2}} . \quad (1.18)$$

Table 1.1 Quantum defects for ^{85}Rb extracted from [129, 130] and for ^{87}Rb extracted from [131]

	^{85}Rb		^{87}Rb	
	$\delta_{lj,0}$	$\delta_{lj,2}$	$\delta_{lj,0}$	$\delta_{lj,2}$
$nS_{1/2}$	3.131 180 4(10)	0.1784(6)	3.131 180 7(8)	0.1787(2)
$nP_{1/2}$	2.654 884 9(10)	0.2900(6)		
$nP_{3/2}$	2.641 673 7(10)	0.2950(7)		
$nD_{3/2}$	1.348 091 71(40)	-0.602 86(26)	1.348 091 8(11)	-0.6054(4)
$nD_{5/2}$	1.346 465 72(30)	-0.596 00(18)	1.346 462 2(11)	-0.5940(4)
$nF_{5/2}$	0.016 519 2(9)	-0.085(9)		
$nF_{7/2}$	0.016 543 7(7)	-0.086(7)		
nG	0.004 00(9)			
$n, l > 4$	0.004(4/l) ⁵			

Figure 1.3 shows the energy level diagram for Rydberg levels with $n \approx 60$. The quantum defects break the degeneracy of S, P, D and F levels in the same n manifold. For $l > 3$, the states are almost degenerate and can be well approximated by a Hydrogen atom. Remarkably the transition between the Rydberg levels is in the microwave range. This allows us to use available microwave technologies in experiments with Rydberg atoms.

1.2

Electric dipole

In a simple picture, the electron is held loosely around the core by the Coulomb force. Any electric perturbation can lead to a deformation of the electron orbit, resulting in a large induced dipole moment. In the language of quantum mechanics, Rydberg atoms have huge matrix elements of the dipole operator, which correspond to a large coupling between Rydberg states induced by external (DC or AC) electric fields. The knowledge of the electric dipole helps to understand other properties of the Rydberg atoms such as radiative lifetime, Stark effect and the dipole-dipole interaction between them. The dipole matrix element between two levels $|nlm_l\rangle$ and $|n'l'm'_l\rangle$ is

$$\langle n'l'm'_l | \mathbf{d} | nlm_l \rangle = -e \langle n'l'm'_l | \mathbf{r} | nlm_l \rangle , \quad (1.19)$$

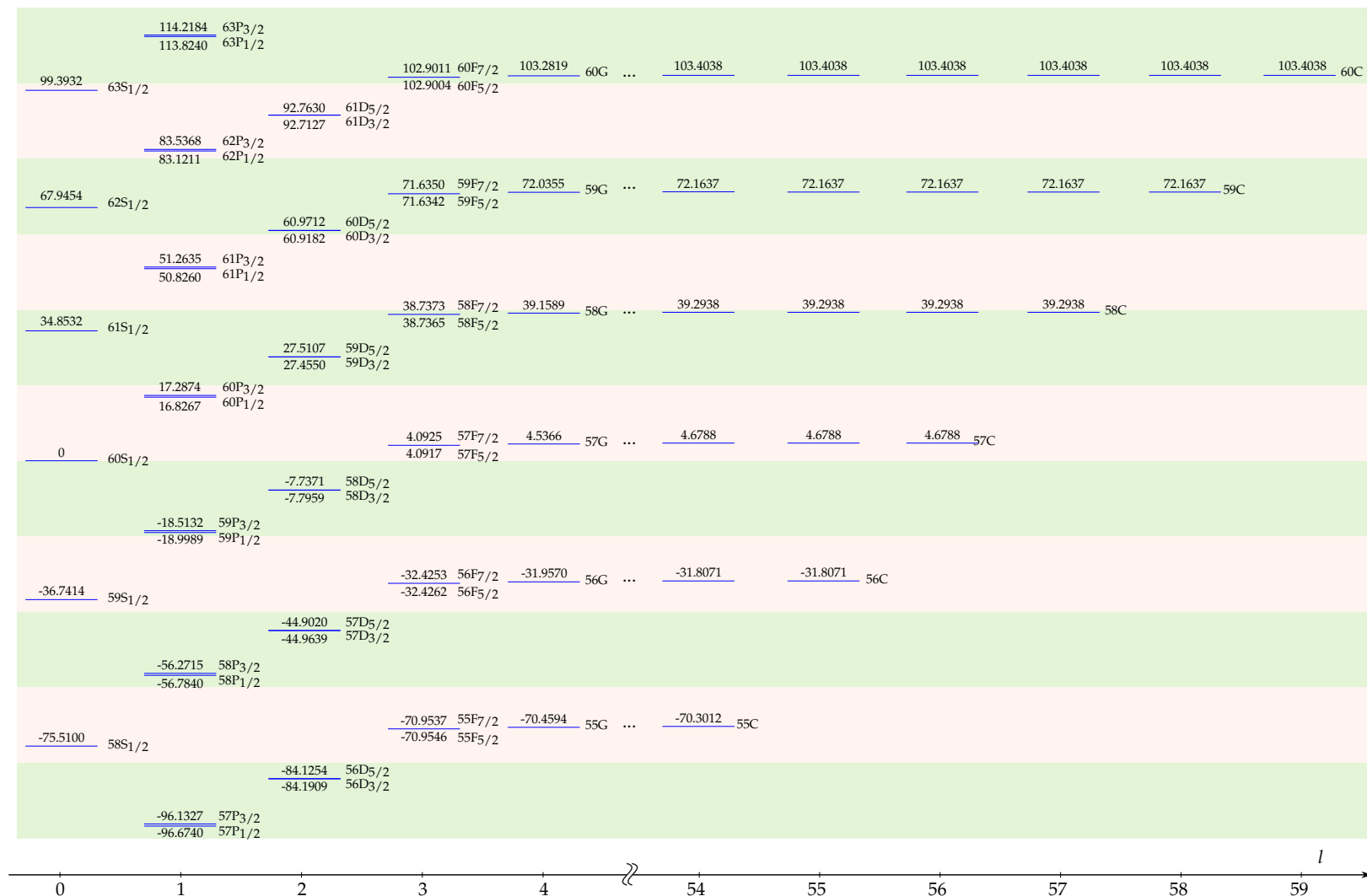


Figure 1.3 Energy diagram for Rydberg states around $n = 60$. The energy is given in GHz and is referenced to the $60S_{1/2}$ level.

where $\mathbf{d} = -e\mathbf{r}$ is the dipole operator. A convenient way to calculate this dipole coupling is to use the representation of the coordinates x, y and z in terms of the spherical harmonics

$$\begin{aligned} Y_1^{-1}(\theta, \phi) &= \frac{1}{2} \sqrt{\frac{3}{2\pi}} \sin \theta e^{-i\phi}, \\ Y_1^0(\theta, \phi) &= \frac{1}{2} \sqrt{\frac{3}{\pi}} \cos \theta, \\ Y_1^{+1}(\theta, \phi) &= -\frac{1}{2} \sqrt{\frac{3}{2\pi}} \sin \theta e^{i\phi}, \end{aligned} \quad (1.20)$$

i.e.,

$$\begin{aligned} x &= r \sqrt{\frac{4\pi}{3}} \frac{Y_1^{-1} - Y_1^{+1}}{\sqrt{2}}, \\ y &= r \sqrt{\frac{4\pi}{3}} \frac{Y_1^{-1} + Y_1^{+1}}{\sqrt{2}} i, \\ z &= r \sqrt{\frac{4\pi}{3}} Y_1^0. \end{aligned} \quad (1.21)$$

The calculation reduces to the evaluation of the following components

$$\langle n' l' m'_l | r Y_1^q | n l m_l \rangle = \langle n' l' | r | n l \rangle \langle l' m'_l | Y_1^q | l m_l \rangle, \quad (1.22)$$

where $q = 0$ or ± 1 . For low- l Rydberg atoms, equation (1.22) is written generalized to

$$\langle n' l' j' m'_j | r Y_1^q | n l j m_j \rangle = \langle n' l' j' m'_j | r | n l j \rangle \langle l' j' m'_j | Y_1^q | l j m_j \rangle \quad (1.23)$$

in order to take the fine structure into account. The integrations are therefore separated into a product of a radial part and an angular part.

Selection rules

The analytic forms of the angular parts in equation (1.22) and (1.23) can be derived as shown in [Appendix A](#). They are nonzero if l, l' and 1 satisfy a triangular relation. In addition $l + l'$ has to be an odd number. This restrains to

$$|l' - l| = 1. \quad (1.24)$$

Furthermore the momentum projection numbers have to fulfill

$$m_{l(j)} = m'_{l(j)} + q. \quad (1.25)$$

These conditions define selection rules for the dipole transitions. Those transitions correspond to the absorption or emission of a π polarized ($q = 0$) photon or of a σ^\pm polarized ($q = \pm 1$) photon. They are called dipole allowed transitions.

Table 1.2 Scaling laws for dipole coupling between two Rydberg levels $|nC\rangle = |nlm\rangle$ and $|n'l'm'\rangle$.

n'	l'	m'	Transition	Scaling law
n	$l - 1$	$m - 1$	σ^-	$n^{3/2}$
$n + 1$	$l + 1$	$m + 1$	σ^+	n^2
$n + 1$	$l + 1$	m	π	$n^{3/2}$
$n + 1$	$l + 1$	$m - 1$	σ^-	n
$n + 1$	$l - 1$	$m - 1$	σ^-	n^2

Numerov method

In order to estimate the radial part of the matrix element in (1.22), one needs to know the radial wavefunctions of each state. They are numerically obtained using the Numerov method. Here, we describe the main idea of the calculation.

The interaction of the outer electron with the ionic core only happens at short distances. Rydberg atom can be considered as an electron in a pure Coulomb potential with an energy given by the Rydberg formula modified by the quantum defects. The corresponding Schrödinger equation for the radial wavefunction R_{nl} reads

$$\frac{\partial^2 R_{nl}}{\partial r^2} + \frac{2}{r} \frac{\partial R_{nl}}{\partial r} + \left[2E_{n*} + \frac{2}{r} - \frac{l(l+1)}{r^2} \right] R_{nl} = 0, \quad (1.26)$$

where E_{n*} is given by (1.18). This equation can be solved numerically (see Appendix A for more details).

The integral starts far from the outer classical turning point of the electron orbit, at a typical distance $r = 2n(n + 15)a_0$ from the atomic core, where we know that the wavefunction exponentially decays to zero. A rough estimate of the initial values of the radial wavefunction thus quickly converges to the physical solution in the next steps of iteration. The integral is carried out inwards towards $r = 0$. Due to the nonzero quantum defect, the wavefunction diverges at small r . The integral has to be stopped as soon as it encounters the inner turning point and starts to diverge. The contribution at short distances to the dipole matrix element is nevertheless small. We still have a good estimation.

Figure 1.4a plots the radial part of the wavefunction for ^{87}Rb $60S_{1/2}$ state. The corresponding wavefunction of Hydrogen is also shown. A phase shift due to the interaction with the ^{87}Rb ionic core is clearly observed. Figure 1.4b illustrates the distribution of the outer electron which gives an intuitive image of the $60S_{1/2}$ orbital. The wavefunctions for high- l Rydberg states are approximately those of Hydrogen atom. Their analytical forms are given in (1.5). However, in all numerical simulations, we use the Numerov method to estimate the dipole matrix elements for all l .

Scaling laws

Understanding the scaling laws for the dipole matrix elements is very important. For low- l Rydberg states, the n dependence of the dipole matrix element is determined by

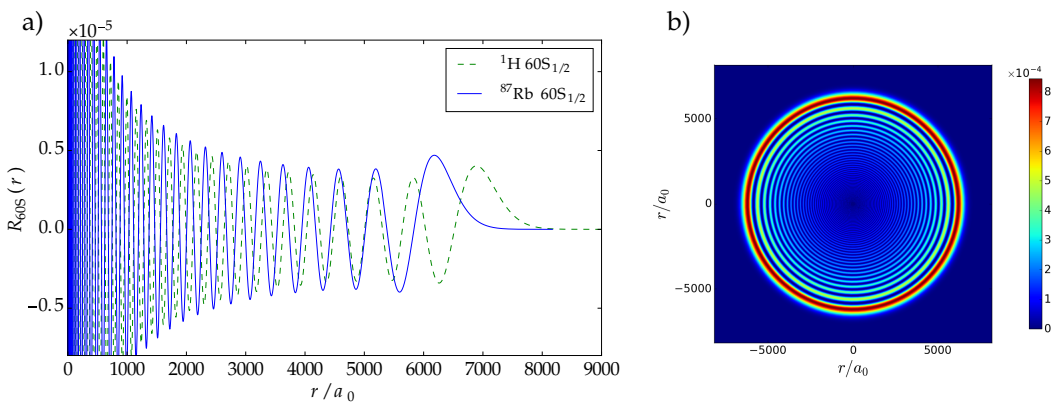


Figure 1.4 a) Radial wavefunctions $R_{60_{1/2}}(r)$ for $^{87}\text{Rb} 60\text{S}_{1/2}$ state (blue) and Hydrogen $60\text{S}_{1/2}$. b) Probability of finding the Rydberg electron $r^2 R_{60_{1/2}}(r)$.

the radial overlap of the two sub-levels. In the case of transitions between neighboring levels, it is proportional to size of the orbit radius. The dipole matrix element thus scales as n^2 . However, going to circular state, the dependency of the angular part on n has to be taken into account. One can prove that the dipole connecting a circular state with the nearest elliptical state in the same manifold scales as $n^{3/2}$ while that with the nearest manifold scales as n^2 , $n^{3/2}$ and n^2 for σ^+ , π and σ^- transition respectively. These scalings are summarized in Table 1.2

To give an order of magnitude, the dipole matrix element corresponding to the transition between $60\text{S}_{1/2}, m_j = 1/2$ and $60\text{P}_{3/2}, m_j = 3/2$ states is $2127 \text{ } ea_0$ and that of the 60C to 61C transition is $2556 \text{ } ea_0$. In comparison, the dipole matrix element for the $D2$ line transition $5\text{S}_{1/2} - 5\text{P}_{3/2}$ is of about $4.2 \text{ } ea_0$. Those of Rydberg atoms are obviously huge numbers. As a direct consequence, Rydberg atoms strongly couple to microwave radiation. In other words, using available microwave technology, one can easily manipulate transitions between Rydberg levels.

1.3

Radiative lifetime

1.3.1

Spontaneous emission

The long lifetime of Rydberg atoms can be classically interpreted as the result of the very low acceleration of the outer electron on its large orbit. The Larmor formula in the classical electrodynamics framework [132] predicts the radiated power of an electron orbiting around its nucleus on a circular orbit to be

$$P = \frac{2}{3} \frac{e^2 a^2}{4\pi\epsilon_0 c^3} \quad (1.27)$$

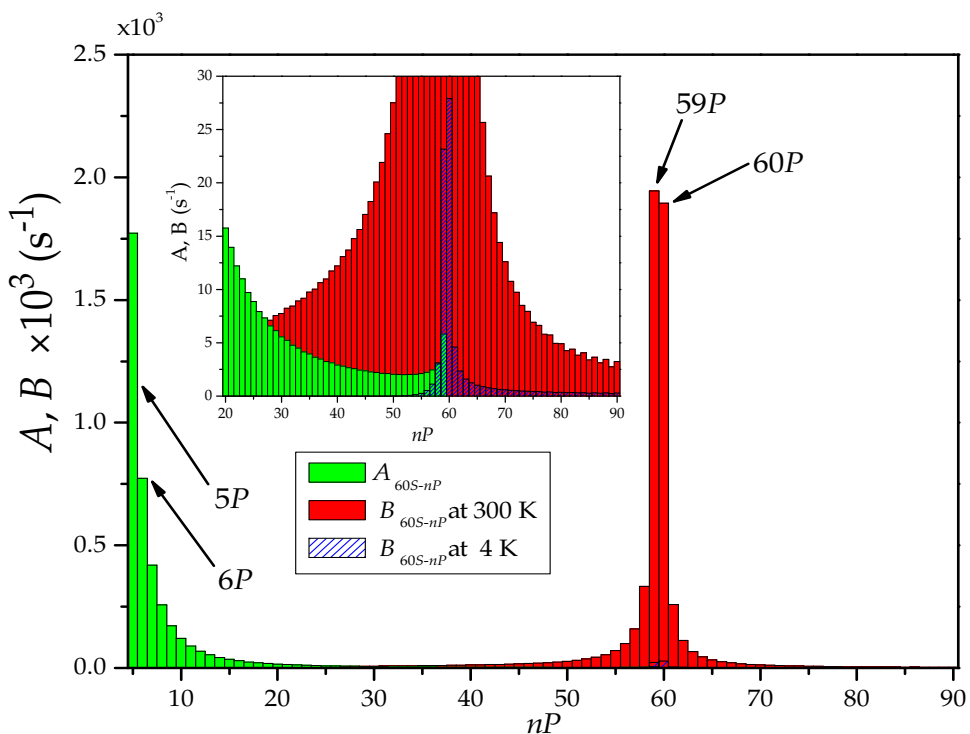


Figure 1.5 Contribution of individual transitions from 60S to other nP levels to the A and B Einstein coefficients for ^{87}Rb . B is calculated for $T = 300$ K and $T = 4.2$ K temperatures. Inset: a zoom showing the background radiation influence on the Rydberg lifetime.

where a is the acceleration given by the Coulomb force

$$a = \frac{1}{m_e} \frac{e^2}{4\pi\epsilon_0(n^2 a_0)^2}. \quad (1.28)$$

In a quantum mechanical description, the lifetime of the Rydberg state is due to the transition of the outer electron to inner states induced by modes of the electromagnetic field vacuum, i.e., spontaneous emission. The decay rate from a state i to a state f can be expressed by the Einstein A coefficient:

$$A_{if} = \frac{2\omega_{if}^3}{3\epsilon_0 c^3 h} |d_{if}|^2 = \frac{4\alpha_F \omega_{if}^3}{3c^2} |\langle i | r | f \rangle|^2 \quad (1.29)$$

where, d_{if} is the dipole coupling and $\omega_{if}/(2\pi)$ is the transition frequency. The spontaneous decay rate of the level i is calculated by summing over all possible decay channels.

Low l Rydberg atoms

For a $|nS\rangle$ state the only possible decay channels are to $|n'P\rangle$ states. Figure 1.5 shows the individual values of A_{ij} , numerically obtained from the evaluation of the dipole matrix elements for the 60S Rubidium state. The spontaneous emission is dominated by optical transitions to the lowest lying levels. The frequency of these short wave-

length transitions does not change that much with n . It turns out that the dependency of A_{if} on n is determined from the dipole coupling, which depends on the radial overlap of the Rydberg wavefunction with the ground state wavefunction. Its value differs significantly from zero only for short distances $r \ll na_0$. From equation (1.5) one finds that the radial overlap of the wavefunctions is proportional to $n^{-3/2}$. The spontaneous decay rate of nS Rydberg atom thus scales as n^3 . Summing up all the decay channels yield $A = 0.004\text{ }\mu\text{s}^{-1}$ corresponding to a lifetime of $244\text{ }\mu\text{s}$ for the $60S$ state.

Circular atoms

The situation is quite different for circular atoms. The only possible spontaneous decay channel is the transition to the next lower circular state by emission of a σ^+ photon. This explains why it takes a much longer time for a circular state to decay. For the $50C$ state, for instance, the strength of the dipole transition to the $49C$ state is $1706\text{ }ea_0$. Using equation (1.29), this corresponds to a lifetime of about 28.6 ms . A classical calculation with equation (1.27) also leads to the same result [3]. It is not a surprise because, as already discussed, the circular state is a perfect approximation of a classical Bohr atom. The coupling between two nearby circular states scales as n^2 while the transition frequency scales as n^{-3} . As a result, the lifetime of circular atoms scales as n^5 .

1.3.2

Blackbody-radiation-induced decay

In the presence of blackbody radiation, in addition to the spontaneous emission, the stimulated decay rate is enhanced by absorption or stimulated emission of a photon due to stimulation. The stimulated decay rate is larger than the spontaneous emission rate by a factor $\bar{n}(\omega)$. The enhanced Einstein's coefficients is

$$B_{if} = \bar{n}(\omega)A_{ij}, \quad (1.30)$$

where $\bar{n}(\omega)$ is the mean number of photon per mode in free space at thermodynamic equilibrium. It is given at a finite temperature T by

$$\bar{n}(\omega) = \frac{1}{e^{\hbar\omega/k_B T} - 1}, \quad (1.31)$$

where k_B is the Boltzmann constant. The total decay rate for a state $|i\rangle$ is then the sum of the spontaneous emission and the stimulated decay rates

$$\Gamma_i = \frac{1}{\tau_i} = \sum_{f < i} A_{if}[1 + \bar{n}(\omega)] + \sum_{f > i} A_{if}\bar{n}(\omega), \quad (1.32)$$

where τ_i is the radiative lifetime of the i state. The two summations run over all lower lying and higher lying levels $|f\rangle$ which satisfy the selection rules described in section 1.2.

The contributions from the stimulated transitions are also shown in Figure 1.5 at room temperature (300 K) and at liquid helium temperature (4.2 K) for the $60S_{1/2}$ state. The blackbody radiation slightly reduces the lifetime of the $60S$ Rubidium state, from $244\text{ }\mu\text{s}$ at 0 K to $240\text{ }\mu\text{s}$ at 4.2 K, and even further down to $99\text{ }\mu\text{s}$ at the room temperature.

In order to keep the Rydberg atoms long-lived, it is therefore necessary to put them in a cryogenic environment.

The circular states are not an exception to this rule. The blackbody radiation not only amplifies the decay rate to the lower circular state, it also opens new channels for the stimulated transitions to higher lying levels, leading to a reduction of the circular atom's lifetime. This again requires to cool down the system in order to fully exploit the long life of the circular states. We will further discuss on this in [section 5.1](#).

1.4

Rydberg atoms in external fields

On the one hand, Rydberg atoms are quite sensitive to stray electric fields due to their huge electric dipole matrix elements. On the other hand, in experiments where Rydberg atoms are excited from a magnetically trapped cold atomic cloud, they are immediately exposed to a strong magnetic field. It is therefore important to understand how Rydberg atoms behave under the presence of external fields. In the following, we treat the Stark and Zeeman effects separately for the sake of simplicity.

1.4.1

Magnetic field

The Zeeman Hamiltonian that describes the interaction of a Rydberg atom with an external magnetic field \mathbf{B} reads

$$H_Z = -\mu \cdot \mathbf{B} = \frac{\mu_B}{\hbar} (g_L \mathbf{L} + g_S \mathbf{S}) \cdot \mathbf{B}, \quad (1.33)$$

where μ_B is the Bohr magneton. The orbital g factor $g_L = 1$ and the spin g factor $g_S \approx 2$ (an about 0.1% correction comes from quantum electrodynamics). Let's choose the quantization axis Oz along \mathbf{B} .

Depending on the relative strength of the spin-orbit interaction with respect to the coupling with the magnetic field, we can distinguish three situations: the anomalous Zeeman effect for a weak magnetic field, the Paschen-Back effect for a strong magnetic field, and the intermediate case.

1.4.1.1 Paschen-Back effect

When the external magnetic field is strong enough, the angular momentum \mathbf{L} and the spin \mathbf{S} are decoupled. Each of them precesses independently around the magnetic field. The interaction energy is thus simply given by

$$E_Z = \mu_B (m_l + g_S m_s) B_z, \quad (1.34)$$

where B_z is the z component of \mathbf{B} . In a strong magnetic field, the fine structure is modified to

$$E_{FS} = A m_l m_s \quad (1.35)$$

since both \mathbf{L} and \mathbf{S} are polarized along Oz .

A dipole transition does not flip the electron spin. The spin part in the above equation does not change the transition spectrum. Therefore, we can neglect the spin part. Equation (1.34) simplifies to

$$E_Z = \mu_B m_l B_z . \quad (1.36)$$

1.4.1.2 Zeeman effect

In a weak magnetic field, we treat first the coupling of \mathbf{L} and \mathbf{S} into $\mathbf{J} = \mathbf{L} + \mathbf{S}$, then take the interaction with the magnetic field as a perturbation. The Zeeman Hamiltonian can be rewritten as

$$H_Z = \frac{\mu_B}{\hbar} \mathbf{J} \left(g_L \frac{\mathbf{L} \cdot \mathbf{J}}{\mathbf{J}^2} + g_S \frac{\mathbf{S} \cdot \mathbf{J}}{\mathbf{J}^2} \right) \cdot \mathbf{B} \quad (1.37)$$

A perturbative calculation yields the energy correction as

$$E_Z = \mu_B g_J m_j B_z = \mu_B \left[g_L + (g_S - g_L) \frac{j(j+1) - l(l+1) + s(s+1)}{2j(j+1)} \right] m_j B_z \quad (1.38)$$

where the term inside the square bracket is called the Landé- g factor g_J . For a single outer electron, s is equal to 1/2.

1.4.1.3 Breit-Rabi formula

In general, one can be in an intermediate case where the Zeeman shift is of the same order as the spin orbit splitting. One has to treat the two interactions at the same time. The Breit-Rabi formula describes the magnetic field dependence for $j = 1/2$ and includes the hyperfine structure. We can follow the same derivation for the spin-orbit coupling only and obtain [133, page 20].

$$E_Z(j, m_j) = -\frac{\Delta E_{so}}{2(2l+1)} + \mu_B m_j B_z \pm \frac{\Delta E_{so}}{2} \sqrt{1 + \frac{4m_j x}{2l+1} + x^2} \quad (1.39)$$

where ΔE_{so} is the fine structure splitting and $x = (g_S - 1)\mu_B B_z / \Delta E_{so}$ is called the field strength parameter. The \pm sign corresponds to sub-level with $j = l \pm 1/2$. This formula includes both the weak field Zeeman effect and Paschen-Back effect, and can be applied for all l and j .

Let us take $n = 60$ multiplicity in a magnetic field of 10 G as an example. The fine structure level splitting can be calculated from the quantum defects listed in Table 1.1. They are 460 MHz for the P level and 53 MHz for the D level, corresponding to $x = 0.03$ and $x = 0.26$ respectively. Therefore we can treat $l < 2$ states in the weak field regime but, for the D state, we enter the intermediate case. For $l \geq 3$, $x \geq 19$, the spin is decoupled from the angular momentum. Equation (1.36) then well describes the situation.

1.4.2

Electric field

In an external static electric field \mathbf{F} , the Rydberg levels are coupled by the electric field via dipole transitions, leading to energy shifts. This is known as the Stark effect. The interaction Hamiltonian reads

$$H_S = -\mathbf{F} \cdot \mathbf{d}. \quad (1.40)$$

Let us first consider a Hydrogen atom in an electric field. We also neglect for now the fine structure. The electric field breaks the spherical symmetry. l is no longer a good quantum number. However, the system is still cylindrically symmetric around the direction of the electric field that we choose as the quantization axis Oz . The angular projection quantum number m_l remains a good quantum number. The Stark Hamiltonian can be expressed as

$$H_S = -Fd_z = eFz = eFr\sqrt{\frac{4\pi}{3}}Y_1^0, \quad (1.41)$$

where $d_z = -ez$ is the z component of the dipole operator. Equation (1.21) has been used to obtain the last equality. The electric field thus couples only states with the same m_l .

Hydrogen atom – Circular state

For high- l Rydberg levels, and especially circular states, both the fine structure and the quantum defects are negligible to a very good approximation. The Stark effect lifts the degeneracy of the n manifold. Even a small electric field is enough to mix the levels. A straightforward way to deal with the problem is to change to the parabolic coordinates. The Schrödinger equation becomes separable and analytically solvable. In addition to n and m , parabolic quantum numbers n_1 and n_2 are introduced. They are non negative integers and related to n and m by

$$n = n_1 + n_2 + |m| + 1. \quad (1.42)$$

For convenience let's note

$$k = n_2 - n_1 = n - 2n_1 - |m| - 1. \quad (1.43)$$

For fixed n and m , there are $n - |m|$ possible values of k ranging from $-n - |m| + 1$ to $n - |m| - 1$. It is enough to specify n, k and m in order to define an eigenstate. Thus we use a ket $|n k m\rangle$ to represent the corresponding state. Its energy can be analytically expressed using the perturbation calculation [125]

$$E = E^{(0)} + E^{(1)} + E^{(2)} + \dots \quad (1.44)$$

with

$$\begin{aligned} E^{(0)} &= -\frac{1}{2n^2} \\ E^{(1)} &= \frac{3}{2}knF \\ E^{(2)} &= -\frac{1}{16} [17n^2 - 9m^2 + 19 - 3k^2] n^4 F^2, \end{aligned} \quad (1.45)$$

where $F = |\mathbf{F}|$. All quantities here are in atomic units.

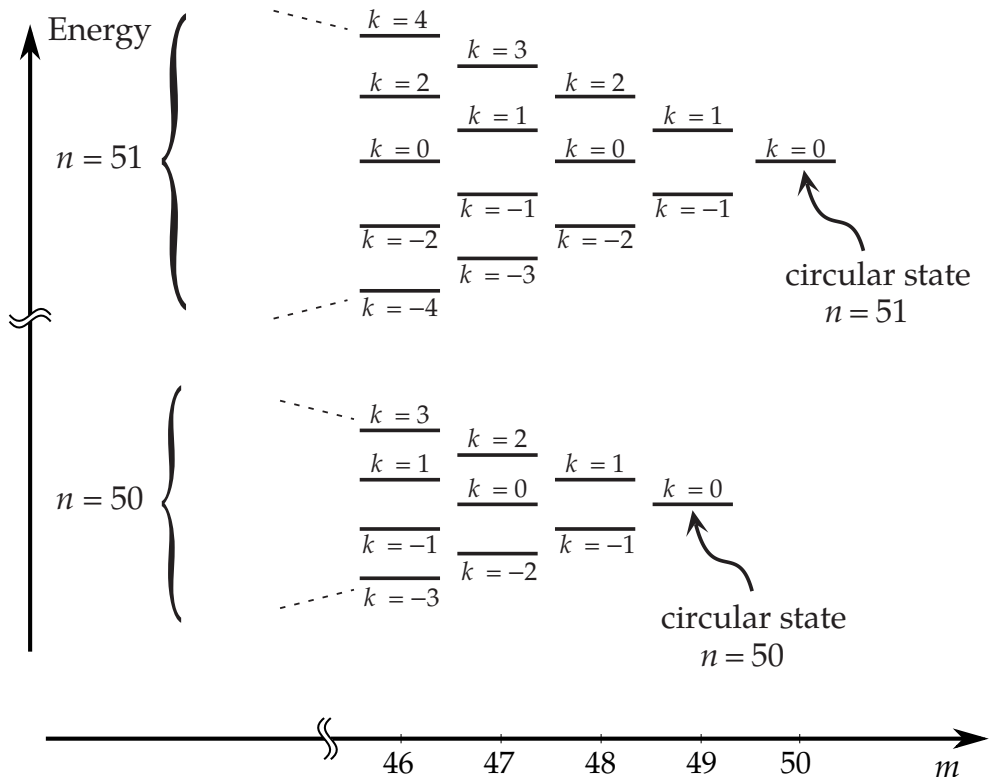


Figure 1.6 Energy levels for $n = 50$ and $n = 51$ states in an electric field. The diagram only shows states with $m \geq 46$.

Figure 1.6 illustrates the energy levels for high- l states with $n = 50$ and $n = 51$. From equation (1.45), one notes that the energy shift of a $m < 0$ state is the same as that of the corresponding $m > 0$ state. Thus we can consider only the case $m \geq 0$.

The circular state $|n, l = n - 1, m = n - 1\rangle$ in the spherical representation is unchanged to the first order in the presence of an electric field, and is the same as the *circular* state $|n, k = 0, m = n - 1\rangle$ in the parabolic representation. It does not have a linear Stark shift. Instead, the second-order Stark effect quadratically lowers down its energy level. For instance the $|50C\rangle$ state is shifted $-2.03 \text{ MHz}/(\text{V/cm})^2$.

States with $|m| \neq n - 1$ in the parabolic coordinates are linear combinations of states with the same m but different l . They are also called *elliptical* states to distinguish them with respect to the circular one. As an example, the two neighbors of the circular state, $|n, l = n - 1, m = n - 2\rangle$ and $|n, l = n - 2, m = n - 2\rangle$, combine either symmetri-

cally into $|n, k = +1, m = n - 2\rangle$ state or anti-symmetrically into $|n, k = -1, m = n - 2\rangle$ state. For convenience, we denote them $|nE^+\rangle$ and $|nE^-\rangle$ respectively. They are explicitly given by

$$\begin{aligned} |nE^+\rangle &= |n, k = +1, m = n - 2\rangle \\ &= \frac{1}{\sqrt{2}} (|n, l = n - 2, m = n - 2\rangle + |n, l = n - 1, m = n - 2\rangle) , \end{aligned} \quad (1.46)$$

and

$$\begin{aligned} |nE^-\rangle &= |n, k = -1, m = n - 2\rangle \\ &= \frac{1}{\sqrt{2}} (|n, l = n - 2, m = n - 2\rangle - |n, l = n - 1, m = n - 2\rangle) . \end{aligned} \quad (1.47)$$

According to (1.45), elliptical states are linearly shifted by the Stark effect.

Low l Rydberg atoms

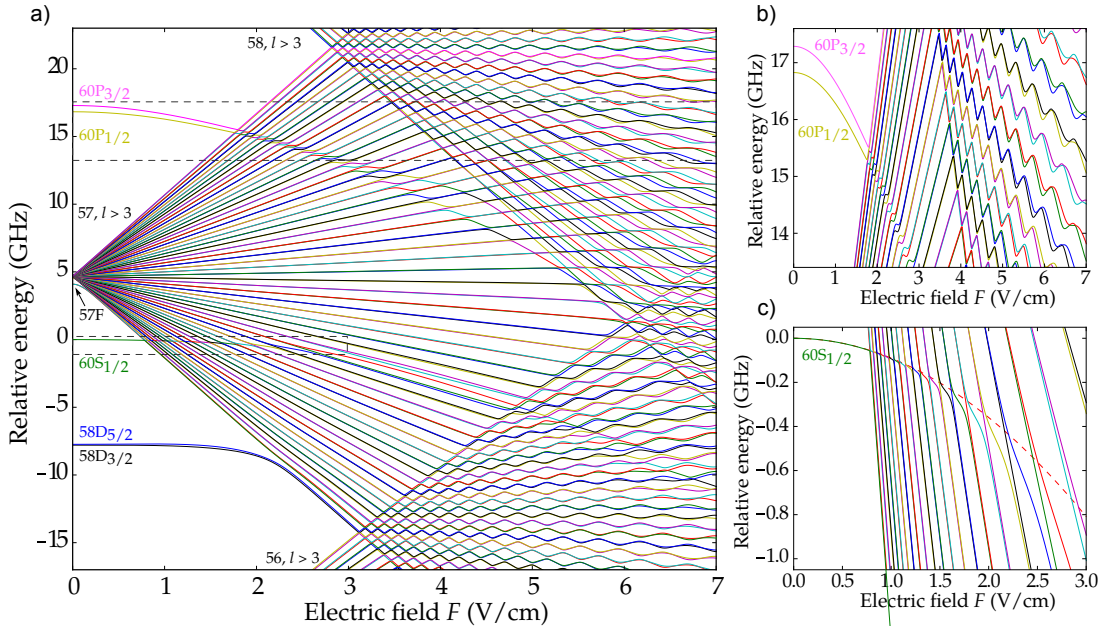


Figure 1.7 a) Stark map of ^{87}Rb for $m_j = +1/2$ states around 60S. The S, P, D and F levels are outside the manifold due to their quantum defects. Levels with $l > 3$ are quasi degenerate and are linearly shifted by the electric field. Zooms around b) 60P and c) 60S states are shown on the right. The corresponding regions are marked by dashed rectangles in a). Under strong electric field, complex level anti-crossings are observed. The dashed red line in c) is a parabolic fit for $0 \leq F < 0.5 \text{ V/cm}$.

For low- l Rydberg atoms, the quantum defects lift the degeneracy with the rest of the multiplicity. The parabolic coordinate transformation is no longer necessary. For a weak electric field, i.e., when the Stark shift is much smaller than the level separation, one can treat the problem directly using the perturbation theory. Noting that the dipole operator does not couple a state to itself, the Stark effect acts as a second-order

Table 1.3 Properties of Rydberg atoms and their n dependence.

Property	low- l state	circular state
Binding energy	n^{-2}	n^{-2}
Fine structure interval	n^{-3}	0
Orbital radius	n^2	n^2
Dipole moment $\langle nl er nl \pm 1\rangle$	n^2	$n^{3/2}$
Radiative lifetime	n^3	n^5
Electric polarizability	n^7	n^6
van der Waals coefficient*	n^{11}	n^6

* see chapter 2 and section 5.3.

perturbation. One thus expects a quadratic shift of the energy levels

$$\Delta E_S = \alpha F^2 \quad (1.48)$$

where α is the electric polarizability and given by

$$\alpha = \sum_{|n' l' j'\rangle \neq |nlj\rangle} \frac{|\langle nlj m_j | ez | n' l' j' m'_j \rangle|^2}{E_{nlj} - E_{n' l' j'}} \quad (1.49)$$

The summation is extended to all levels satisfying the selection rules. However, the main contribution comes from levels closest in energy, which have a larger radial overlap. The lowest l , i.e., $|nS\rangle$ state for example, couples mainly to $|nP\rangle$ and $|n-1P\rangle$ levels. Due to the effect of quantum defects, $E_{nS} - E_{n-1P} > E_{nP} - E_{nS} > 0$ (cf. Figure 1.3). As a result, $\alpha < 0$. The Stark effect lowers the energy. The numerator scales as n^4 (square of the dipole matrix element), while the energy differences in the denominator scale as n^{-3} for adjacent Rydberg levels. As a result, the Stark shift scales as n^7 .

The Stark diagram for levels around $60S$ with $m_j = +1/2$ is shown in Figure 1.7. It is obtained by numerical diagonalization of the full Stark Hamiltonian. The electric polarizability for the $60S$ level is found to be -89.9 MHz/(V/cm) 2 . Electric fields larger than 1 V/cm are enough to cause complex state mixing. Stronger quadratic shifts for $60P$ and $58D$ states are also observed. The $57F$ state is slightly shifted out of the manifold of $l \geq 4$. Inside, the levels are quasi degenerate and thus are linearly shifted by the electric field.

Summary

In this chapter, we briefly reviewed the major properties of individual Rydberg atoms both for low- l and high- l states. High- l states are approximated by a Hydrogen atom, especially for the case of circular states. For low- l Rydberg states, the quantum defect theory describes the energy correction due to the interaction with the alkali ionic core. The quantum defects remove the degeneracy of the S, P, D and F states from the rest of the manifold.

We studied the radiative lifetime of Rydberg atoms as well as their behaviors in an

external electric or magnetic field. Throughout this chapter, numerical calculations with the 60S state and the circular 50C state were used as examples. These two states lie at the focus of this thesis. The scaling laws for the properties of Rydberg atoms were discussed and are summarized in [Table 1.3](#).

Interacting Rydberg atoms

2

2.1

Two antennas in communication

Having huge dipole matrix elements, Rydberg atoms strongly interact with each other. This dipole-dipole interaction has been intensively studied and applied in the field of quantum information processing. It leads to non-trivial phenomena and is at the heart of this thesis. The dipole interaction operator is the combination of dipole operators acting on each atom

$$\begin{aligned} V_{dd}(R) &= \frac{1}{4\pi\epsilon_0 R^3} \left[\mathbf{d}_1 \cdot \mathbf{d}_2 - 3(\mathbf{d}_1 \cdot \frac{\mathbf{R}}{R})(\mathbf{d}_2 \cdot \frac{\mathbf{R}}{R}) \right] \\ &= \frac{e^2}{4\pi\epsilon_0 R^3} \left[\mathbf{r}_1 \cdot \mathbf{r}_2 - 3(\mathbf{r}_1 \cdot \frac{\mathbf{R}}{R})(\mathbf{r}_2 \cdot \frac{\mathbf{R}}{R}) \right], \end{aligned} \quad (2.1)$$

where $R = |\mathbf{R}|$ is the distance between the two atoms. The indices indicate which atom the operator acts on. Here, the distance between the two atoms is treated classically assuming that the spatial spread of the atomic wave-packet for each atom is much smaller than the distance between them.

The interaction can be seen as resulting from the simultaneous exchange of virtual photons between the two atoms. Strictly speaking one has to take into account in principle the retardation effect accounting for the propagation of the photons. However, the typical spacing between the Rydberg atoms in these experiments ranges from a few to several hundreds micrometers. It is much smaller than the photon wavelength, in the mm range. The retardation effect can be neglected and thus equation (2.1) is valid.

For simplicity, we choose the axis connecting the two atoms as the quantization axis and express the position operators \mathbf{r}_1 and \mathbf{r}_2 in terms of spherical harmonics (*cf. section 1.2*). The dipole interaction operator can then be rewritten as

$$V_{dd}(R) = -\frac{e^2}{3\epsilon_0 R^3} r_1 r_2 (Y_1^{-1} Y_1^{+1} + Y_1^{+1} Y_1^{-1} + 2Y_1^0 Y_1^0) \quad (2.2)$$

From this expression, it is clear that the interaction operator preserves the total magnetic quantum number $M = m_1 + m_2$.

In practice, we use a numerical approach to calculate the interaction between two Rydberg atoms. The Hilbert space is truncated to important terms due to limited memory and computation power. The interaction Hamiltonian is then constructed and directly diagonalized to find the interaction energy for each inter-atomic distance R . In order to discuss the physics of the interaction, we will make use of perturbation theory. In the following let's limit the discussions on the case $l = 0$. In section 5.3, we will discuss in details the dipole interaction between two circular atoms, which leads to interesting effects.

2.2

A pair of atoms in the same state

For a pair of two atoms in the same state a denoted $|aa\rangle$, the dipole interaction operator in general acts as an second-order perturbation, coupling to intermediate pair states $|cd\rangle$. The resulting interaction energy has the form

$$C_{aa} = \sum_{|cd\rangle} \frac{\langle aa | V_{dd} | cd \rangle \langle cd | V_{dd} | aa \rangle}{2E_a - E_c - E_d} = \frac{C_{6,a-a}}{R^6}, \quad (2.3)$$

corresponding to a van der Waals interaction with $C_{6,a-a}$ is the van der Waals coefficient. In the above equation, E_i is the energy of the single Rydberg atom i .

The situation is bit different when one of the coupled state $|cd\rangle$ is nearly degenerate, i.e., $\langle aa | V_{dd} | cd \rangle / R^3 \gg |2E_a - E_c - E_d|$. If $|c\rangle = |d\rangle$, the relevant subspace consists of two states $|aa\rangle$ and $|cc\rangle$. The corresponding Hamiltonian reads

$$H_{aa-cc} = \begin{pmatrix} |aa\rangle & |cc\rangle \\ |aa\rangle & \frac{\langle aa | V_{dd} | cc \rangle}{R^3} \end{pmatrix}. \quad (2.4)$$

Its eigenstates are a symmetric combination $(|aa\rangle + |cc\rangle)/\sqrt{2}$ and an anti-symmetric combination $(|aa\rangle - |cc\rangle)/\sqrt{2}$ of the two levels. The corresponding energy shifts are given by

$$\Delta E_{dd} = \pm \frac{\langle aa | V_{dd} | cc \rangle}{R^3} = \pm \frac{C_{3,a-a}}{R^3}, \quad (2.5)$$

where $C_{3,a-a} = \langle aa | V_{dd} | cc \rangle$ and the plus sign corresponds to the antisymmetric combination of $|aa\rangle$ and $|cc\rangle$.

If $|c\rangle \neq |d\rangle$, there are three nearly degenerate states $|aa\rangle$, $|cd\rangle$ and $|dc\rangle$. The symmetric and anti-symmetric combinations of $|cd\rangle$ and $|dc\rangle$ are $|C\rangle = (|cd\rangle + |dc\rangle)/\sqrt{2}$ and $|NC\rangle = (|cd\rangle - |dc\rangle)/\sqrt{2}$. One notes that $|aa\rangle$ does not couple to $|NC\rangle$ by V_{dd} . The relevant subspace thus consists of two states $|aa\rangle$ and $|C\rangle$. Similarly to the case of $|c\rangle = |d\rangle$, one gets two eigenstates $(|aa\rangle \mp |C\rangle)/\sqrt{2}$ whose energy shifts are

$$\Delta E_{dd} = \pm \frac{\langle aa | V_{dd} | C \rangle}{R^3} = \pm \frac{C_{3,a-a}}{R^3}, \quad (2.6)$$

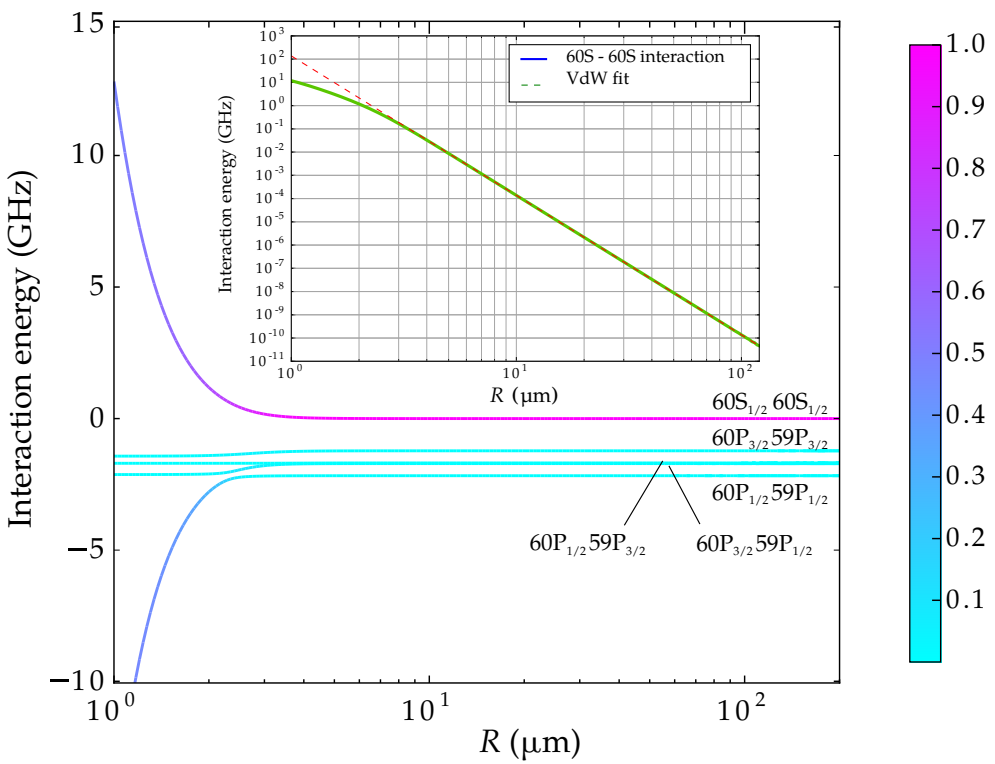


Figure 2.1 The energy shift of $|60S; 60S\rangle$ pair state due to their van der Waals interaction. Also shown are the nearby pair states. The color code represent the square of the projection on the unperturbed $|60S; 60S\rangle$ state. Inset plots the energy shift in log-log scale. At short distance, $|60S; 60S\rangle$ strongly couples to $|60P; 59P\rangle$ states, the interaction gradually changes to a resonant dipole interaction.

where $C_{3,a-a} = \sqrt{2} \langle aa | V_{dd} | cd \rangle$. These special situations are known as Rydberg Förster resonance [104].

$nS - nS$ interaction

In the case of the $|nS; nS\rangle$ state, the dominant term in (2.3) is the coupling with the $|nP; n-1P\rangle$ pair state. Since $E_{nS} - E_{n-1P} > E_{nP} - E_{nS}$ (cf. Figure 1.3), the denominator in (2.3) is positive. The $nS - nS$ interaction is thus always repulsive. Numerical calculation for the $60S - 60S$ pair gives $C_{6,60S-60S} = 137.6(1)$ GHz. μm^6 . Figure 2.1 depicts the numerically computed energy shift for the $|60S; 60S\rangle$ pair state. At distances larger than 3 μm , the interaction is well fitted by a van der Waals potential. At shorter distances, the dipole coupling is as strong as the energy difference of the two pair states $|nS; nS\rangle$ and $|nP; n-1P\rangle$ (~ 2 GHz). The interaction gradually changes to $1/R^3$ behavior. From equation (2.3), one can show that the van der Waals interaction scales as n^{11} .

2.3

An atom pair involving two different states

For an atom pair in two different states a and b , there are two degenerate pair states $|ab\rangle$ and $|ba\rangle$. According to the selection rules, $\langle ab|V_{\text{eff}}|ab\rangle = \langle ba|V_{\text{eff}}|ba\rangle = 0$. Formally, one writes an *effective* Hamiltonian V_{eff} [134] for a two level approximation including second-order coupling to other states. Its matrix elements are

$$C_{ab} = \langle ab|V_{\text{eff}}|ab\rangle = \langle ba|V_{\text{eff}}|ba\rangle , \quad (2.7)$$

and

$$A_{ab} = \langle ab|V_{\text{eff}}|ba\rangle = \langle ba|V_{\text{eff}}|ab\rangle . \quad (2.8)$$

The interaction Hamiltonian is expressed as

$$V_{\text{eff}} = \begin{pmatrix} |ab\rangle & |ba\rangle \\ |ab\rangle & |ba\rangle \end{pmatrix} \begin{pmatrix} C_{ab} & A_{ab} \\ A_{ab} & C_{ab} \end{pmatrix} . \quad (2.9)$$

The diagonal terms are the direct interaction of a pair state to itself, which is a second-order perturbation through the coupling to intermediate pair states $|cd\rangle$. They thus correspond to van der Waals interactions

$$C_{ab} = \sum_{|cd\rangle} \frac{\langle ab|V_{dd}|cd\rangle \langle cd|V_{dd}|ab\rangle}{E_a + E_b - E_c - E_d} = \frac{C_{6,a-b}}{R^6} , \quad (2.10)$$

where $C_{6,a-b}$ is the corresponding van der Waals coefficient.

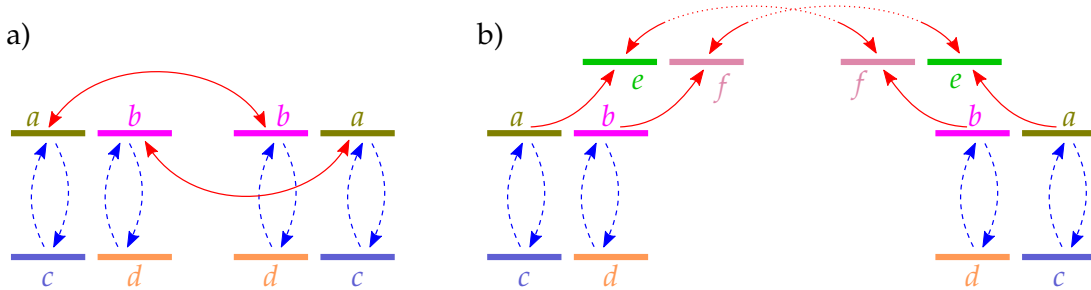


Figure 2.2 Scheme for calculating the dipole interaction between a and b states. The direct (diagonal) terms are represented by the dashed blue arrows and the exchange (off diagonal) terms by the solid red arrows. The direct interaction is the second-order perturbation coupling to intermediate pair states of c and d . The exchange interaction can be either a) first-order or b) higher order perturbation. In b) the pair state $|ef\rangle$ is an intermediate state for the coupling between $|ab\rangle$ and $|ba\rangle$.

The off-diagonal term A_{ab} corresponds to an interaction where the two atoms exchange their excitations. When the $a - b$ transition is dipole allowed, e.g., a $nS - n'P$ transition, the exchange interaction is a direct coupling of $|ab\rangle$ and $|ba\rangle$ (Figure 2.2a). It varies as a $1/R^3$ dipole potential. Otherwise, depending on the dipole coupling

between $|a\rangle$ and $|b\rangle$, the exchange interaction can be an indirect coupling of second (scaling as $1/R^6$) or higher order as demonstrated in Figure 2.2 b.

In general the direct interaction shifts the energy of the two levels in the same way while the exchange interaction breaks the degeneracy, splitting them into symmetric and antisymmetric combinations of the two levels. Their total energy shifts are

$$\Delta E_{dd} = C_{ab} \pm A_{ab}, \quad (2.11)$$

where the minus sign corresponds to the symmetric combination.

$nS - n'P$ interaction

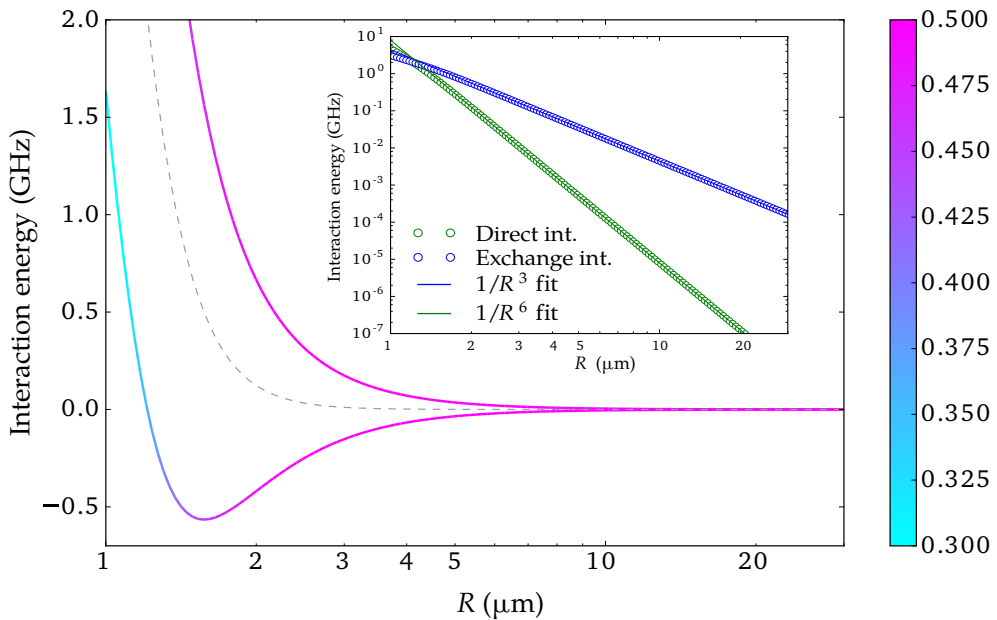


Figure 2.3 Interaction energy for $60S - 60P_{3/2}$ pair of atoms. The lower branch corresponds to the symmetric level while the upper one corresponds to the anti-symmetric level. The color code shows the projection on the initial pair state $|nS; n'P\rangle$ squared. The dashed line represents the direct energy shift. The inset shows in log-log scale the direct and the exchange interaction.

This is a rather simple case. The exchange interaction directly couples $|nS; n'P\rangle$ and $|n'P; nS\rangle$ state by a resonant (first-order) dipole interaction

$$A_{nS-n'P} = \langle nS; n'P | V_{dd} | n'P; nS \rangle = \frac{A_{3,nS-n'P}}{R^3}, \quad (2.12)$$

where $A_{3,nS-n'P}$ is a proportionality coefficient. Its n dependency originates from the dipole matrix elements, which scale as n^2 each, leading to a scaling as n^4 .

The direct interaction comes from the coupling to the intermediate levels $|n''P; n'''S\rangle$: $|nS; n'P\rangle \leftrightarrow |n''P; n'''S\rangle \leftrightarrow |nS; n'P\rangle$. From (2.10) one can easily find that it scales as n^{11} . Equation (2.11) takes the form

$$\Delta E_{dd,nS-n'P} = \frac{C_{6,nS-n'P}}{R^6} \pm \frac{A_{3,nS-n'P}}{R^3}. \quad (2.13)$$

Figure 2.3 depicts the numerical result for $60S - 60P_{3/2}$ pair. It is calculated from a subspace of about 500 pair states. The color code represents the probability of being in $|60S; 60P_{3/2}\rangle$ pair state. At long distances it corresponds to 0.5 for each branch as expected. Getting closer, the color is degraded, indicating the contamination by other levels. Fitting the energy shift for each branch with the potential described in (2.13) yields $C_{6,60S-60P_{3/2}} = 7.976(1)$ GHz. μm^6 and $A_{3,60S-60P_{3/2}} = 4.411(0)$ GHz. μm^3 . The van der Waals terms is shown by the dashed curve on the graph. Inset plots in log-log scale the mean energy and half the energy difference of the two branches, corresponding to the direct and exchange interactions respectively. A $1/R^6$ and a $1/R^3$ behaviors are clearly observed even down to distances smaller than $2 \mu\text{m}$. At distance larger than $4 \mu\text{m}$, the van der Waals shift is more than two orders of magnitude smaller than the dipole shift, and thus can be ignored.

Summary

In this chapter, we established the dipole-dipole interaction between a pair of Rydberg atoms under different situations. We particularly focused on the case where one of the atoms is in an nS state. However, the concepts discussed here can be extended to the general case.

For an atom pair in different states, the exchange interaction combines symmetrically or anti-symmetrically the two pair states $|nS; n'S(P)\rangle$ and $|n'S(P); nS\rangle$, lifting their degeneracy. The level splitting is proportional to either $1/R^3$ ($n'P$ state) or $1/R^6$ ($n'S$ state) depending on whether the transition between the two states is dipole allowed or not. Two S Rydberg atoms at distance R larger than $3 \mu\text{m}$ interact with each other by a van der Waals potential. We also performed numerical calculations for the interaction of a $60S$ Rydberg atom with another one in the $60S$ nearby state.

II.

Towards quantum simulation with low-*l* Rydberg atoms

Superconducting atom chip experiment

3

The prerequisite in most of quantum simulation experiments is to preserve the coherence of the system for a long time. Building a quantum simulator with Rydberg atoms on a superconducting atom chip imposes two main requirements: a high-level control of the stray electric fields and the use of cold/ultra cold atoms. The former comes from the high sensitivity of Rydberg atoms to electric field. The latter is meant to minimize the atomic motion, which might eventually map into time-dependent Stark and/or Zeeman shifts. In addition, a cold and dense atomic cloud helps to enter the strong Rydberg-Rydberg interaction regime.

Our experiment is dedicated to study the excitation of strongly interacting Rydberg atoms out of a cold Rubidium cloud near a superconducting atom chip. This is a rather complex experiment, in which we implement a superconducting atom chip with laser cooling and magnetic trapping techniques for ^{87}Rb inside a cryostat. The Rydberg excitation and detection are also performed in the cryogenic environment. The experiment is designed carefully in such a way that every component we put inside the cryostat has to consume a minimum amount of liquid Helium. The list includes the atom chip, the superconducting coils creating necessary bias magnetic fields for atom trapping and cooling, the electrodes for field-ionization system and the ion-counter channeltron. We recall here the main features of the experimental setup, which is divided into two parts: the preparation of ultra-cold atoms and the Rydberg excitation/detection. More details on the chip fabrication and characterization can be found in Raul Celistrino's thesis [135].

At the end of this chapter, we briefly represent our first investigations to demonstrate that Rydberg atoms are fully compatible with the atom chip, i.e., coherent manipulation of Rydberg atoms is feasible in the vicinity of the chip with a good control of stray electric fields. The experiment is performed with a low Rydberg density such that Rydberg-Rydberg interaction is negligible. This is the topic of Carla Hermann's thesis, where one can find a full description of the experiment [136].

3.1

Ultra-cold atom source

3.1.1

Cryostat

As discussed in [section 1.3](#), the Rydberg atom's lifetime strongly depends on the environment temperature. Of course, short lifetimes might be not a problem for certain experiments where all interesting dynamics happen on a short time scale. However, in order to fully exploit the long lifetime property of the Rydberg atoms, putting them in a cryogenic environment is necessary. In addition, the operation of the chip under non-superconducting state would turn the chip itself into a hot body right at the position of the Rydberg atoms due to the Joule heating effect. A superconducting atom chip suppresses this effect.

Our experiment uses a cryostat, which is schematically depicted in [Figure 3.1](#). The heart of the experiment, where all the science happens is kept at 4.2 K temperature by a ${}^4\text{He}$ shield, which is a copper shell in direct contact with a liquid ${}^4\text{He}$ reservoir. It is in turn thermally shielded from 300 K blackbody radiation by an intermediate stage at liquid nitrogen temperature, 77 K. The cryogenic stages are firmly mounted inside an external cylindrical shell, which provides a good vacuum. A layer of lead, which becomes superconducting at a temperature lower than 7 K, is installed around the inner wall of the He shield. It screens any external magnetic field fluctuation. Moreover, fast variations of the bias magnetic fields during the experiment are necessary. Without the superconducting lead shield, eddy currents would be induced on the outer copper thermal shields, preventing fast variations of the bias magnetic fields.

The He shield, with a few liters volume is sufficiently large to accommodate the chip mount, the magnetic bias coils as well as the Rydberg detection system, which are shown in [Figure 3.1](#). The chip wires and the bias coils are all superconducting to prevent heating and power dissipation. Several windows are opened on the walls of the cryostat (and the thermal shields) for optical access. Both laser and imaging systems are outside the cryostat. The size of the windows limits the numerical aperture for the collection lenses, but large windows expose the Rydberg atoms directly to the 300 K blackbody radiation. Therefore the windows are chosen to be 6 cm in diameter as a compromise.

On the one hand, the use of the cryostat sets up some constraints on optical access as well as on the complexity of experimental operation. On the other hand, it helps to have a high vacuum without much effort. Residual gases are strongly adsorbed on cold surfaces. A pressure smaller than 10^{-10} mbar^{*} can be obtained without time consuming baking of the system. Under such a pressure, the losses due to background gas collisions are strongly reduced and the trapping lifetime is thus improved, of the order of minutes [[138](#), [139](#)].

^{*}Expected to be lower than 10^{-13} mbar [[137](#)] but no direct measurement is available with our current setup.

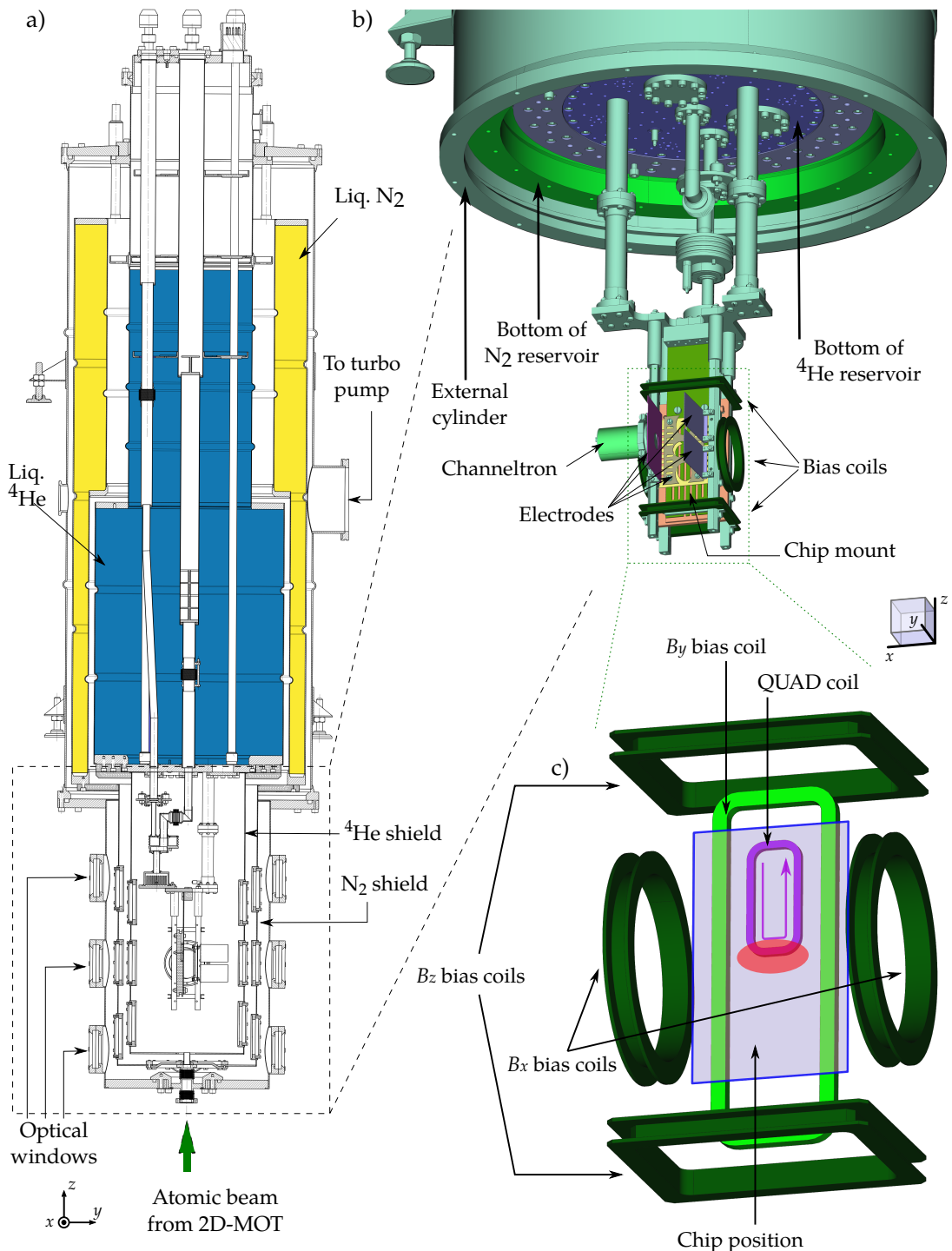


Figure 3.1 Sketch of the cryogenic setup. a) A vertical cut shows the construction of the cryostat. The liquid ${}^4\text{He}$ and liquid Nitrogen reservoirs are indicated by fake colors. A slow atomic beam from a 2D-MOT is injected inside the cryostat from the bottom. b) Schematic view of the heart of the experiment. The chip faces the y direction. The bias coils (dark green) and detection electrodes (blue) are also represented. The Helium and Nitrogen shields as well as the exterior shell are not shown. c) A closer view shows only the bias coils (green) and the “QUAD” coil (purple), which generate the quadrupole magnetic field for an on-chip MOT. The chip position is marked by the blue rectangle covering the B_y bias coil and the QUAD coil. The red zone indicates the place where the Rubidium atoms are trapped. The current flow in the QUAD coil is marked by the arrow.

3.1.2

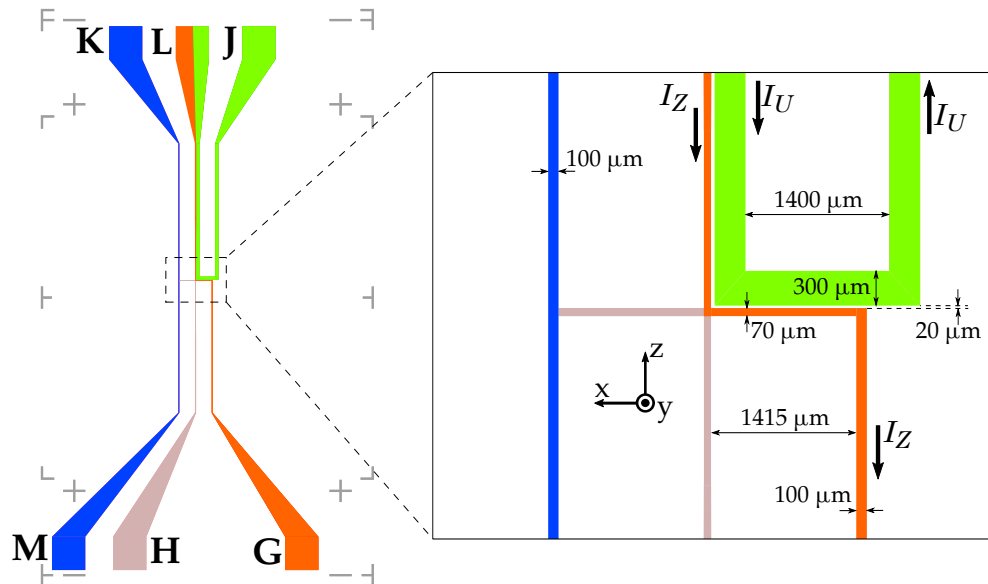
Atom chip

Figure 3.2 Scheme of the superconducting atom chip. The letters label the current input/output pads on the chip. The fake colors are to distinguish between the chip wires: green for the U-shaped wire, orange for the Z-shaped wire and blue for the RF wire. Directions of the currents are also indicated.

The atom chip used in our current experiment is rather simple and is depicted in Figure 3.2. The chip operation is based on three wires: a U-shaped wire (LJ), a Z-shaped wire (LG) and a straight wire (KM) as depicted in Figure 3.2.

The U-shaped or Z-shaped wire is a simplified version of a H-shaped wire, made up of a straight current crossing two parallel currents (Figure 3.3a). By passing a current I through the Z-shaped wire, the magnetic field created by the segment along the x direction, in combination with a bias field along the z direction B_z forms a quadrupole field in the yz plane (Figure 3.3b). The currents in the two parallel arms flow in the same direction. They create a magnetic field in the x direction, which exhibits a nonzero minimum near the center of the quadrupole field (marked by the yellow dots, Figure 3.3c). The total magnetic field forms an Ioffe-Pritchard magnetic trap.

Similarly, the U-shaped wire also has a quadrupole field in the yz plane. The currents in the two parallel arms flow in counter directions. As a result, the total magnetic field has a zero minimum near the center of the quadrupole field (Figure 3.3d). Such a magnetic field is suitable for a 3D magneto-optical trap (mirror MOT).

Numerical calculations of the fields created by our particular chip can be found in Raul Celistrino's thesis [135]. For either the U-shaped or the Z-shaped wire, the distance to the chip of the trap center is approximately given by

$$r_0 = \frac{\mu_0}{2\pi} \frac{I}{B_z}. \quad (3.1)$$

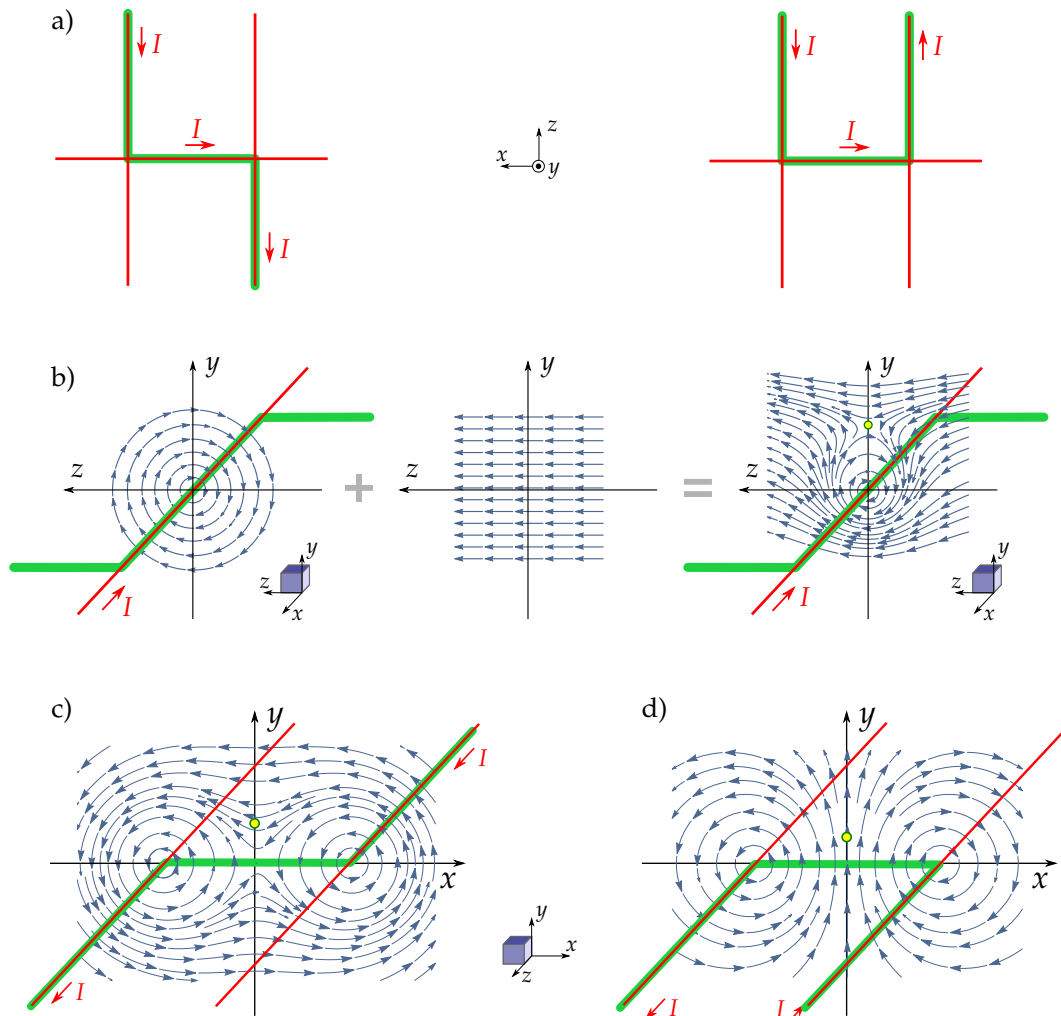


Figure 3.3 Magnetic field created by the chip wires. a) The $U(Z)$ -shaped wire is a simplified version of a H-shaped wire consisting of a straight current along the x direction and a pair of parallel currents along the z direction. b) A quadrupole field is formed by the straight current in superposition with a bias field. The pair of currents can be either c) in the same direction or d) in opposite directions. In modulus, the total field can accordingly have a zero or non zero minimum at the positions marked by yellow dots. The wires under consideration are shown in red while the corresponding $U(Z)$ -shaped wire is shown in green. In b) we plot only the Z-shaped wire but the situation is the same for the U-shaped wire.

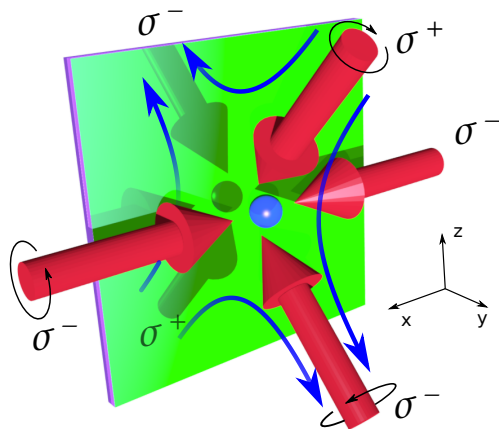


Figure 3.4 Mirror MOT. Two counter-propagating beams are sent parallel to the chip while the other two hit the chip at 45 degrees. The reflection of the latter adds up two beams with inverted helicities, thus correctly restoring the six-beam configuration.

while the gradient of the quadrupole field at the trap center is

$$|B'(r_0)| = \frac{2\pi}{\mu_0} \frac{B_z^2}{I} = \frac{\mu_0}{2\pi} \frac{I}{r_0^2}. \quad (3.2)$$

This is an important feature of the trap geometry. The closer it is to the chip, the tighter the confinement in the yz plane. Therefore at short distances from the chip, the trap is elongated along the x direction, taking a cigar shape.

The KM wire is used for generating the radio frequency during the RF-induced evaporative cooling of the atoms in the magnetic trap.

All the chip wires are 2 μm thick, made of Niobium (Nb) deposited on a silicon substrate. Nb wires at 4.2 K are superconducting. The critical current is measured to be 3.6 A for the thin Z-shaped wire, while it is up to 7.5 A for the thick U-shaped wire. The fabrication of the chip has been developed and realized in our group. A detailed discussion can be found in [135]. During the cooling of the chip from room temperature, the earth and stray magnetic fields are compensated to prevent the chip from trapping residual fields. Otherwise, magnetic vortices can be formed, leading to a deformation of the magnetic trap, and even to the formation of uncontrolled on-chip local magnetic traps.

The chip is covered with a 200 nm thick layer of gold. A special configuration of four cooling laser beams making use of the high reflectivity of the chip gold surface allows us to restore the standard six-beam configuration of a 3D-MOT (Figure 3.4). Such a MOT is called a mirror-MOT.

3.1.3

Atom imaging

The cryostat reduces our freedom in configuring the imaging system. Here we record the image of the atomic cloud both from the front and the size directions as schemat-

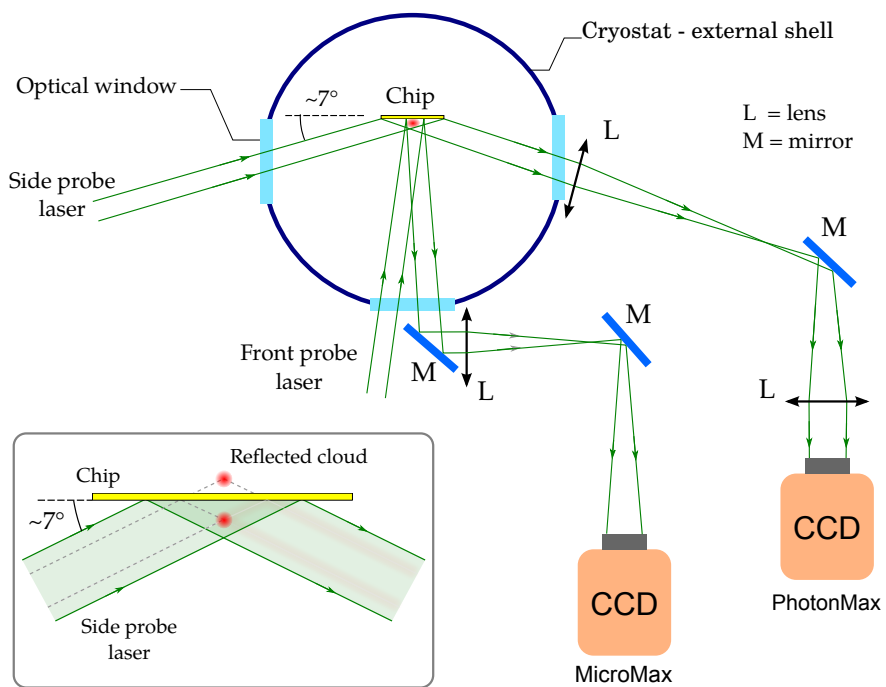


Figure 3.5 Scheme of the imaging system. The probe beam can be sent either nearly perpendicular (front probe) or parallel (side probe) to the chip surface. The reflected beams from the chip surface are collected on CCD cameras. The objective lenses are placed as close to the chip as possible. The atomic cloud casts a shadow on the reflected beam. For the side probe, the reflection of the chip surface adds another image of the cloud as illustrated in the inset.

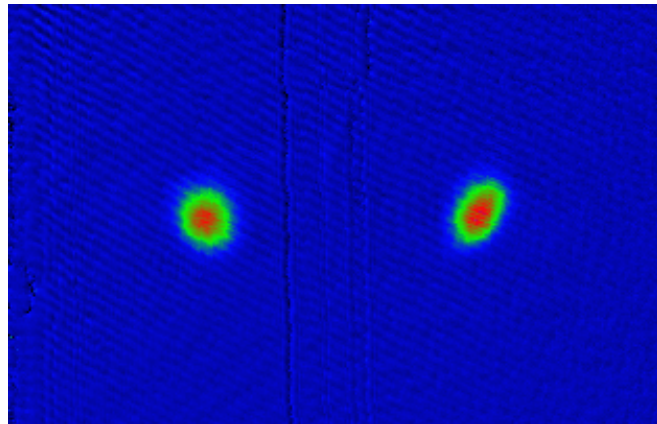


Figure 3.6 A cold cloud of Rubidium atom after 16.5 ms time of flight imaged by the side probe beam. We get two images: one is the direct image (right) and the other originates from the reflection on the chip.

ically depicted in [Figure 3.5](#). The probe beams are sent either (nearly) perpendicular to the chip surface (front imaging), or at an angle of about 7° from the chip surface (side imaging). The objective lenses are installed right at the external cylinder of the cryostat in a way such that they do not disturb other laser beams but still allow us to collect as much as possible the light scattered from the atomic cloud .

The atomic cloud can be imaged either by collecting its fluorescent light or by measuring the change of the probe beam intensity due to the absorption of the cloud. However, the latter method gives a more precise estimation of the number of atoms. Well below the saturation of the atomic transition, the optical density OD of the cloud at a point (x_p, y_p) is found by taking the natural logarithm of the transmission

$$OD(x_p, y_p) = -\ln \frac{I_f(x_p, y_p)}{I_i(x_p, y_p)}, \quad (3.3)$$

where $I_f(x_p, y_p)$ and $I_i(x_p, y_p)$ are the light intensities of the probe beam at point (x_p, y_p) with and without the absorption due to atoms. These intensities are measured directly with a CCD camera. Here we define the coordinates (x_p, y_p, z_p) such that Oz_p is the propagation direction of the probe beam. The Beer-Lambert's law relates the OD with the *column density* $\bar{n}(x_p, y_p) = \int n(x_p, y_p, z_p) dz_p$, where $n(x_p, y_p, z_p)$ is the atomic density

$$OD(x_p, y_p) = \sigma_0 \bar{n}(x_p, y_p). \quad (3.4)$$

Thus

$$\bar{n}(x_p, y_p) = \int n(x_p, y_p, z_p) dz_p = -\frac{1}{\sigma_0} \ln \frac{I_f(x_p, y_p)}{I_i(x_p, y_p)}. \quad (3.5)$$

In the above equation, σ_0 is the resonant scattering cross-section. Cold atoms in the magnetic trap are prepared in the $5S_{1/2}, F = 2, m_F = +2$ state. The probe beam is adjusted to drive the σ^+ cycling transition, i.e., between the $5S_{1/2}, F = 2, m_F = +2$ and the $5P_{3/2}, F' = 3, m_F = +3$ states. The corresponding cross-section is given by

$$\sigma_0 = \frac{3\lambda^2}{2\pi}, \quad (3.6)$$

where $\lambda = 780$ nm is the transition wavelength.

In practice, the probe polarization is not perfectly circular. In addition, the interference between the probe beam and its reflection from the chip surface modulates the light intensity. Due to these effects, the apparent cross-section σ_0 is reduced by a factor α_{abs} , which is experimentally calibrated [135, 140].

For the side imaging, α_{abs} is measured to be about 2.06 ± 0.1 . As shown in [Figure 3.6](#), we get in general two images of the cloud: one from the direct image of the cloud and the other corresponding to the reflection on the chip surface. Half of the distance between the two images is equal to the distance of the atomic cloud from the chip surface.

3.1.4

Laser system

A laser system is mandatory for trapping and cooling the atoms. In our experiment, we implement standard techniques for trapping and cooling ^{87}Rb atoms. A good control of the power, frequency and polarization of the lasers determines the success of the

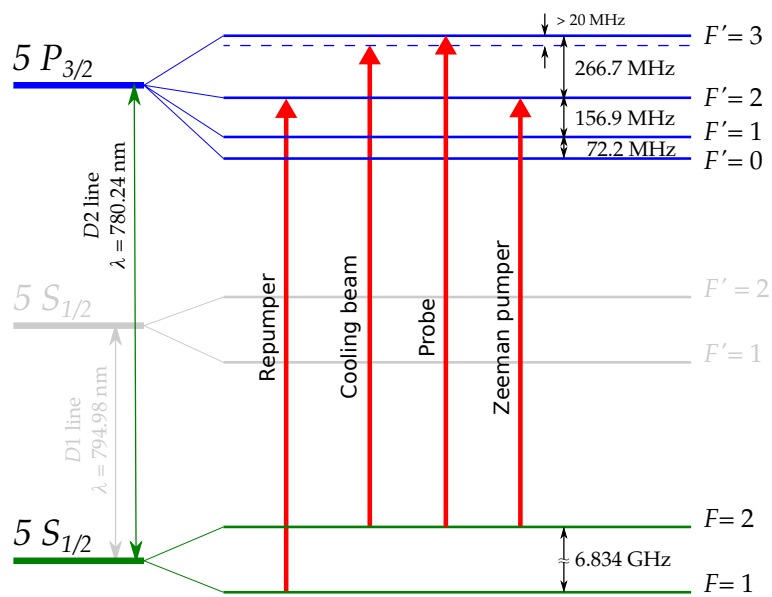


Figure 3.7 Hyperfine structure of ^{87}Rb . The cycling transitions are shown for the cooling laser, the repumper, the optical Zeeman pumper as well as for the probe beams.

experiment. The cooling laser comes from a commercial TOPTICA Master Oscillator Power Amplifier (MOPA-TA 110) laser. It is frequency-offset locked to the excitation red laser, which in turn is frequency-stabilized to a Fabry-Perot cavity. The cavity is locked to a transition line of ^{87}Rb (see [Appendix B](#) for optical scheme). The spectrum linewidth of the laser is of a few tens of kHz. The cooling cycle makes use of the D2 line $F = 2 - F' = 3$ transition. A repumper is required to bring back the atoms scattered out of the cooling cycle. Part of the cooling laser is extracted and frequency offset to serve as probe beams or to perform Zeeman optical pumping. The corresponding transitions are shown in [Figure 3.7](#). All the laser beams are guided to the cryostat by coupling to polarization maintaining fibers. [Appendix B](#) gives more details on the laser frequency stabilization scheme and laser distribution.

3.1.5

Trapping and cooling of atoms

[Figure 3.8](#) demonstrates the timing of a typical cooling and magnetic trapping sequence where each parameter is well controlled and optimized. It consists in two main stages: trapping and cooling the atoms in on-chip mirror MOTs followed by trapping in a magnetic trap, where RF evaporative cooling allows us to reach a sub- μK temperature.

On-chip mirror MOTs

1. *Loading a QUAD-MOT.* In a typical sequence of the experiment, Rubidium atoms are first cooled down in a 2D-MOT. They form a slow beam of atoms propagating up to a few mm in front of the chip. The atoms are then captured in an on-chip mirror

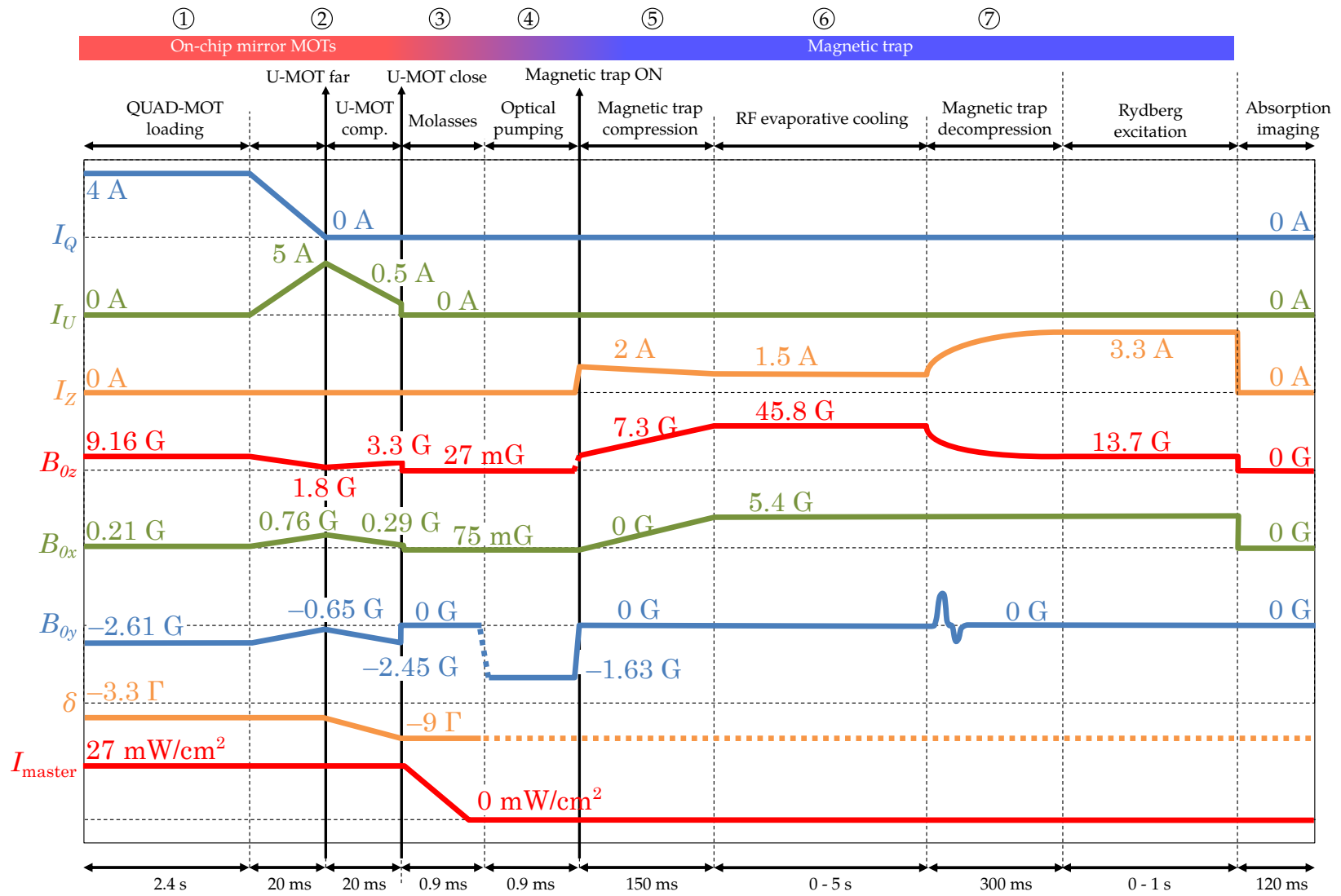


Figure 3.8 A typical experimental sequence. The timing and values of each parameters are carefully optimized as shown. Each step is numbered and discussed in the main text.

MOT.

A large magnetic field gradient is necessary to efficiently capture the atoms [141]. According to equation (3.2), one would increase the current I . This is obtained by using the lower part of a rectangular superconducting coil – the QUAD coil – to serve as a big U-shaped wire (Figure 3.1 c). The current is thus multiplied by the number of turns in the coil. About 10^8 atoms at about $400 \mu\text{K}$ are trapped in the QUAD-MOT.

2. *U-MOT*. The trap is then transferred to another MOT created by the U-shaped wire (U-MOT far). A higher magnetic field gradient, and thus a larger restoring light force, allows us to efficiently cool down the atoms. We therefore reduce the current in the U-shaped wire to increase the field gradient. In doing so, we also compress the size of the atomic cloud and approaching the chip (U-MOT close). A temperature of about $40 \mu\text{K}$ is obtained.

3. *Optical molasses*. At this stage, the currents in the bias coils are adjusted to precisely cancel the residual magnetic field. In the meantime, the cooling laser power is gradually reduced and the cooling laser detuning is increased to far off resonance. This 3D optical molasses technique allows us to form a viscous confinement of the atoms and further cool them down to about $13 \mu\text{K}$. The atoms are about $700 \mu\text{m}$ away from the chip.

Ioffe Pritchard magnetic trap

The cooling with a MOT is intrinsically based on the optical transition cycles of the atoms, and is thus limited by the recoil temperature. To further cool the atoms, we implement the magnetic field trapping in complement with the RF evaporative cooling.

4. *Optical Zeeman pumping*. The magnetic trap is a weak-field seeker trap. The trapping potential is given by

$$E_Z = g_F m_F \mu_B |B(x, y, z)| , \quad (3.7)$$

where g_F is the hyperfine-structure Landé g factor. Thus $5S_{1/2}, F = 2, m_F = +1$ and $m_F = +2$ are the two trapped states. We aim to trap the latter. An intermediate stage optical pumping is introduced to bring the atoms into the Zeeman sub-level $5S_{1/2}, F = 2, m_F = +2$. It increases the number of atoms transferred into the magnetic trap by a factor ~ 3 .

5. *Magnetic trap*. Note that the magnetic field configuration of the U-MOT cannot be used for magnetic trapping due to the presence of a zero field at the center of the trap, leading to spin-flip Majorana losses [142, 143]. The use of the Z-shaped wire ensures that the field at the trap center points along the x direction, removing the zero field at trap center. Furthermore, the bottom of the trap is risen up by a bias field to prevent atomic transitions to un-trapped states induced by low-frequency noises near the chip [138, 144].

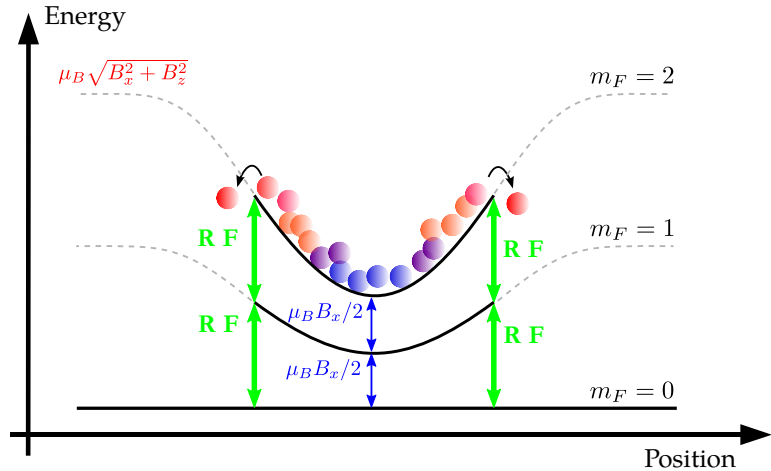


Figure 3.9 RF-induced evaporative cooling. The RF knife induces the transition to un-trapped states, through the $m_F = +1$ state. Gradually lowering the RF knife kicks out the hottest atoms, truncating the hot tail of the Boltzmann distribution. As a result, the temperature decreases after thermalization.

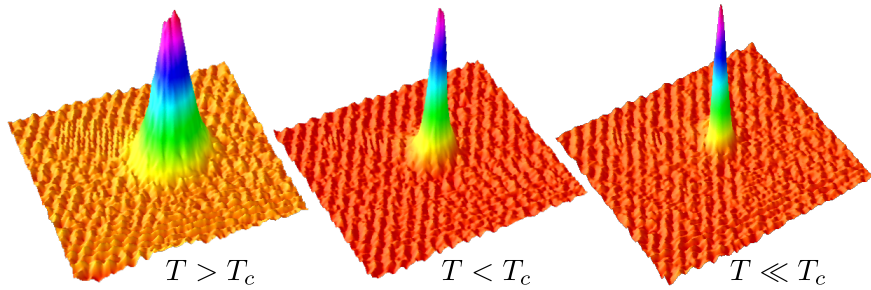


Figure 3.10 Rubidium cloud after 16.5 ms time-of-flight for different temperatures. The temperature is controlled by the final value of the evaporative cooling RF. The images reveal directly the momentum distribution. The three images correspond to a thermal cloud, a BEC, and a quasi pure BEC respectively

6. *Evaporative cooling.* For evaporating cooling, a RF knife is used as demonstrated in [Figure 3.9b](#) to remove the hottest atoms out of the trap, carrying with them a significant amount of kinetic energy, that helps to increase the phase space density. An important point is that the re-thermalization of the trapped cloud should be faster than the trap truncation [145]. Otherwise one removes also the “useful” cold atoms. In order to enter this runaway regime, we adiabatically compress the trap after the transfer in order to increase the collision rate. The evaporative cooling occurs at about $100\text{ }\mu\text{m}$ away from the chip. At the end of the evaporation, we can manage to bring the atomic cloud down to its quantum degeneracy (Bose-Einstein condensate BEC) [146, 147].

7. *Decompressed magnetic trap.* By changing the currents in the Z-shaped wire as well as in the bias coils, we can decompress and move the trap to the position of interest for the Rydberg excitation. A typical trap used throughout this thesis is about $210\text{ }\mu\text{m}$

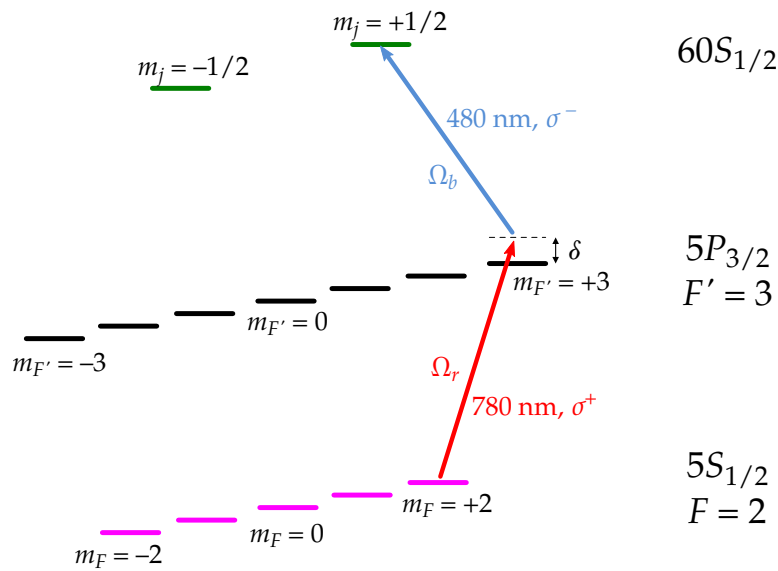


Figure 3.11 Rydberg excitation scheme. Trapped atoms in the $5S_{1/2}, m_F = +2$ are brought to the Rydberg state $60S_{1/2}, m_J = +1/2$ by two-photon transition, detuned by δ from the intermediate level $5P_{3/2}, m_F = +3$. The red laser is σ^+ polarized while the blue laser is σ^- polarized.

away from the chip surface. The trap frequencies are measured to be 47 Hz, 244 Hz and 262 Hz along the x , y and z directions respectively (see Appendix C).

Finally the atomic cloud is imaged by absorption imaging. Figure 3.10 shows images of three clouds taken for different final heights of the RF knife, with a 16.5 ms time-of-flight. They correspond to a thermal cloud, a BEC and a quasi-pure BEC respectively. The cloud in the last image contains about 30 000 atoms at 450 μm from the chip.

3.2

Rydberg excitation

3.2.1

Two-photon excitation

From a cold atomic cloud trapped on the atom chip, Rubidium atoms are brought to their Rydberg states by laser excitation. In the presence of the magnetic field, the dipole-dipole interaction between the Rydberg atoms generally strongly depends on the orientation of the atoms with respect to the magnetic field. However, this angular dependence for the $60S - 60S$ interaction is almost negligible thanks to the isotropy of the $60S$ orbital. To keep things simple, we concentrate on the $60S_{1/2}, m_J = +1/2$ level.

The transition from the trapped state $5S_{1/2}, F = 2, m_F = +2$ to $60S_{1/2}, m_J = +1/2$ is accomplished by absorbing two photons: one red photon at a 780 nm wavelength, and one blue photon at a 480 nm wavelength, going through the level $5P_{3/2}, F' = 3, m_F = +3$ with a detuning of δ . The two lasers are sent parallel to the chip surface, focused on the atomic cloud with 150 μm and 22 μm waists for the red and blue lasers,

respectively, as illustrated in [Figure 3.12](#). Here, the quantization axis is defined by the magnetic field at the bottom of the magnetic trap, oriented along the x axis. The red laser is σ^+ polarized while the blue laser is σ^- polarized. Under this configuration, the $60S_{1/2}, m_j = -1/2$ state is not excited. The excitation path is schematically shown in [Figure 3.11](#).

It is crucial to avoid sending the blue laser on the chip's Nb wires. This strongly focused and powerful blue laser makes the Nb wires locally transit to the normal state, forming local heating spots. The transition then quickly spreads out. Eventually, the chip is no longer superconducting and the experiment is interrupted. Another consequence is the photo-voltaic effect, by which the blue photons rip out electrons from the chip surface. Some of these electrons will end up on nearby dielectric surfaces, building up stray electric fields. These are unwanted effects.

The red laser is detuned $\delta = +2\pi \times 540$ MHz from the intermediate level $5P_{3/2}, F' = 3, m_F = +3$. Its power is typically $P_r = 50$ μ W. One finds the corresponding Rabi frequency $\Omega_r = 2\pi \times 40$ MHz. The spontaneous scattering rate of the red photons via transitions to the intermediate state, whose lifetime is about 26 ns [[148](#)], is given by

$$\Gamma_s = \frac{1}{2} \frac{\Omega_r^2 \Gamma}{\delta^2 + \Gamma^2 + \Omega_r^2} \approx \frac{1}{2} \frac{\Omega_r^2 \Gamma}{\delta^2}, \quad (3.8)$$

where $\Gamma = 2\pi \times 6.065$ MHz is the natural linewidth of the $5P_{3/2}$ state. The scattering rate is thus, estimated to be 0.1 photon per microsecond. The spontaneous scattering of a photon on average gives the cloud a kick in the direction of the red laser, pushing the cloud out of trap center. As a result, the cloud starts to oscillate and heats up. This is an important factor that limits the power of the red laser, the duration of excitation as well as the total number of Rydberg excitation laser pulses that can be sent on a single cloud.

Due to the relatively weak dipole transition between the $5P$ state and a Rydberg state, the blue laser must be much more powerful. We measured about 8 mW at the entrance of the cryostat. Taking into account the transmission of about 80% for a window[†], the power is 4 mW at the position of the cloud, after crossing three windows ([Figure 3.1](#)). The corresponding Rabi frequency is calculated to be $\Omega_b = 2\pi \times 7.9$ MHz.

From the fact that $\Omega_r, \Omega_b \ll \delta$, one can adiabatically eliminate the intermediate level and end up with an effective two-level system. The two-photon coupling strength of the ground state to the Rydberg state, i.e., the corresponding effective two-photon Rabi frequency can be expressed as

$$\Omega = \frac{\Omega_r \Omega_b}{2\delta}. \quad (3.9)$$

With the given parameters, one finds $\Omega = 2\pi \times 280$ kHz.

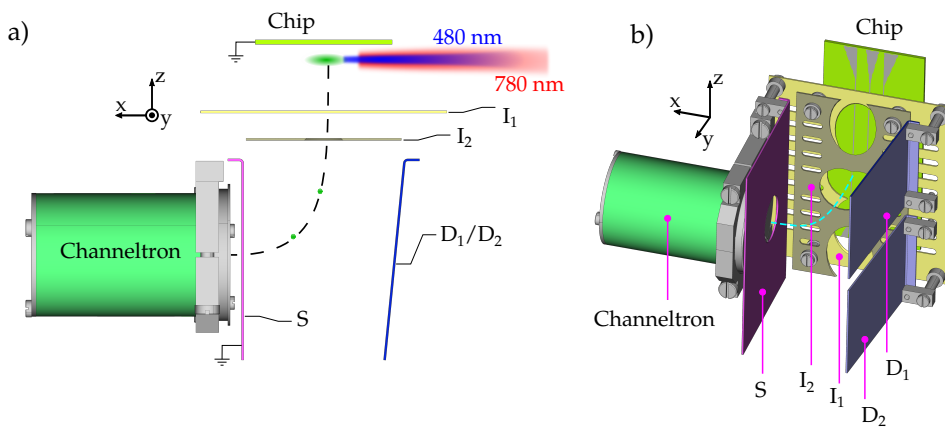


Figure 3.12 Scheme of the Rydberg detection setup for a) top view and b) axonometric view. I_1 (dark green) and I_2 (light green) are ionization electrodes, D_1 (blue) and D_2 (blue) are ion deflectors and S (purple) is the electric shield. The channeltron is mounted inside the channeltron house. The trajectory of the ions is represented by the dashed lines. Excitation lasers are also shown in a).

3.2.2

Rydberg detection

Rydberg atoms are very close to the ionization threshold and are very sensitive to electric fields. They are thus quite easy to detect using field-ionization technique. The scheme of the detection is depicted in Figure 3.12. A voltage V_{ion} is applied onto the electrodes I_1 and I_2 while the chip is kept grounded to ionize the Rydberg atoms. The obtained ions are then accelerated and guided with help of two deflector electrodes D_1 and D_2 to a channeltron. As soon as an ion hits the channeltron, it creates a signal sent to a discriminator, where we can count ions one by one. The channeltron operates under a high voltage of -3000 V. An additional electrode S screens the stray field from the channeltron. To improve the performance of the channeltron, it is kept "warm" at about 42 K.

Each Rydberg state is ionized at a different voltage. If one ramps down V_{ion} in time from ~ 0 V to a negative value, depending on the state of the initial Rydberg atom, the corresponding ion arrives at the channeltron at different times. Thus we can distinguish the Rydberg states as depicted in 3.13. The voltage ramp is designed so that it gives the best discrimination between the states of interest. Defining appropriate temporal windows as shown by the red and blue dashed lines in Figure 3.13, we can state-selectively detect the Rydberg atoms. The detection efficiency is measured to be up to $90\% \pm 10\%$.

Another advantage of the configuration shown in Figure 3.12 is that, during the Rydberg excitation, one can apply an appropriate voltage on the two electrodes I_1 and I_2 to compensate for the stray fields perpendicular to the chip surface at the atom position. The required voltage for the field compensation is typically less than 1 V.

[†]The windows are not yet coated for the blue laser.

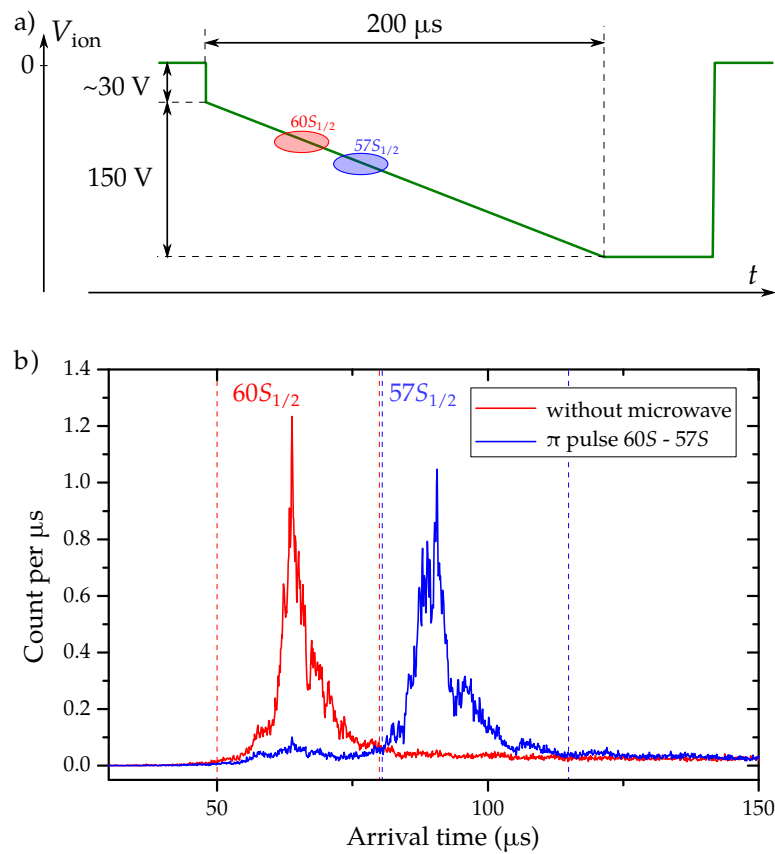


Figure 3.13 State-selective detection of Rydberg atoms. a) A typical ionization voltage ramp in our experiment. Rydberg atoms in $60S_{1/2}$ and $57S_{1/2}$ are ionized at different times marked by red and blue ovals respectively. b) The arrival time of the corresponding ions fall in defined temporal windows, allowing us to state-selectively detect the Rydberg atoms. The atoms are prepared in the $60S_{1/2}$ state. The $57S_{1/2}$ is experimentally populated by transferring atoms from the $60S_{1/2}$ state with a π microwave pulse. The detections with and without the microwave pulse correspond to the detections of $60S_{1/2}$ and $57S_{1/2}$ atoms respectively.

3.3 Coherent manipulation of Rydberg atoms

Thanks to their huge electric dipole matrix elements, Rydberg atoms are very easy to manipulate by making use of the Stark effect and microwave transition. However at the same time, Rydberg atoms are also extremely sensitive to stray electric fields, which will potentially wash out any coherences between the Rydberg atoms. To build a quantum system from Rydberg atoms, the very first requirement is thus to reduce the influence of the stray fields.

3.3.1

Taming the stray electric fields

During the experiment, some Rubidium atoms inevitably stick to the chip front gold surface. The direct deposition of Rubidium atoms on the gold layer forms huge elec-

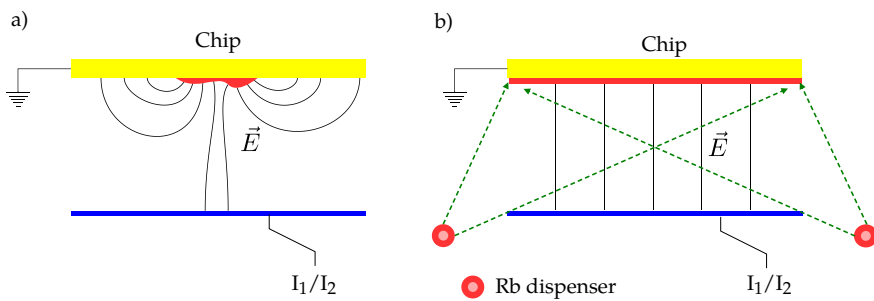


Figure 3.14 The electric field close to the chip a) before and b) after the Rubidium coating of the chip. The electrodes I_1 and I_2 are schematically shown. Rubidium is represented in red color, either as a patch or as a homogeneous layer.

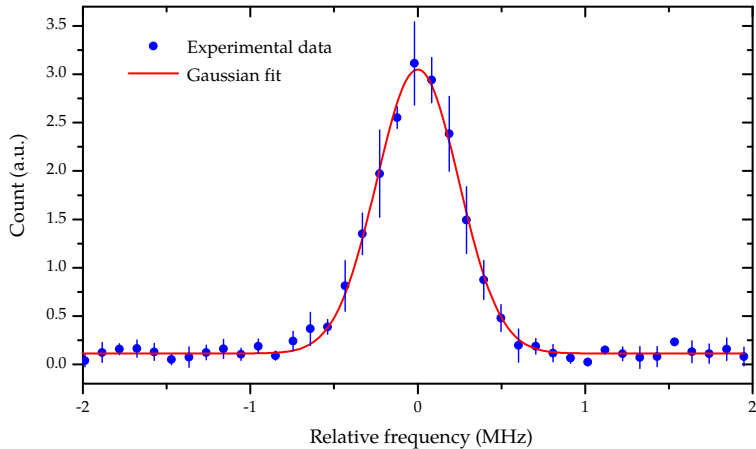


Figure 3.15 Optical transition with a dilute cloud in a magnetic trap (blue dots). Rydberg-Rydberg interaction is expected to be negligible. The excitation duration is 10 μ s. A fit with a Gaussian profile (red solid line) gives the FWHM of 579 kHz. The error bars are 1 standard deviation of the statistical error.

tric dipoles due to the big mismatch in the work functions of Rubidium and gold[†]. These Rubidium patches on the chip surface keep building up, leading to very inhomogeneous and unstable stray electric fields right at the position of the atoms.

As a solution, two Rubidium dispensers were installed inside the cryostat to cover the chip surface with a thick enough layer of Rubidium (~ 80 nm). The idea is to perform a fast and controlled Rubidium deposition on a large area so that the later adsorbed cold atoms do not affect the electric field. The Rubidium coating also helps to cover some small dust dielectric particles that could have stuck to the chip surface, and reduce their contribution to the stray fields. The coating of the chip was performed under cryogenic temperature conditions. Figure 3.14 illustrates qualitatively the structure of the electric field before and after the Rubidium coating.

As a result, we obtain a narrow and stable optical transition. Figure 3.15 shows an optical spectrum recorded with a dilute cloud after the Rubidium coating. It is well fitted by a Gaussian profile; the FWHM is 579 kHz, which is mainly due to the spectral

[†]Work function of Rubidium is 2.26 eV [149] and that of gold is 5.30 – 5.45 eV [150].

width of our laser. More details on the field characterization can be found in [136].

3.3.2

Coherent manipulation of the Rydberg atoms

In order to access the coherence time, we first perform a spectroscopy measurement using the $60S_{1/2}, m_j = +1/2 - 61S_{1/2}, m_j = +1/2$ two-photon transition. This transition is relatively insensitive to the differential Stark effect ($-10.9 \text{ MHz}/(\text{V/cm})^2$), and has no differential linear Zeeman shift. About 0.3 Rydberg atoms are excited out of a dilute ground-state cloud. The driven microwave pulse lasts $300 \mu\text{s}$. Figure 3.16 represents the measured spectrum. It exhibits a quite narrow Lorentzian profile with a 6.6 kHz full width half maximum (FWHM).

The transverse coherence time T_2 is measured using the Hahn spin-echo technique. Its principle is depicted in Figure 3.17a illustrating the evolution of the spins on a Bloch sphere during this sequence. We apply a π microwave pulse (duration $0.6 \mu\text{s}$) in between two Ramsey $\pi/2$ microwave pulses ($0.3 \mu\text{s}$). The first $\pi/2$ pulse prepares the atoms in a superposition of the $60S_{1/2}$ and $61S_{1/2}$ states. They evolve freely during $T/2$. At this time, the π pulse mirrors the spins through the yz plane. The free evolution in the second half time compensates for the dephasing accumulated during the first half. The coherence of the superposition is best recovered at the *refocusing time* T . It is then projected on the $60S_{1/2}$ state by the second $\pi/2$ pulse. We detune the microwave pulses 70 kHz from the atomic transition and scan the (time) position of the second $\pi/2$ pulse around T to observe the revival of the Ramsey fringes. Figure 3.17 plots the contrast of the fringes probed for different total durations T . It is well fitted by a Gaussian, allowing us to deduce a coherence lifetime (at $1/e$ contrast) of $T_2 = 631 \mu\text{s}$. Knowing that the lifetime of the corresponding Rydberg levels is measured to be about $T_1 = 210 \mu\text{s}$, the coherence time is sufficiently long for many applications of our system.

Summary

Throughout this chapter, the experimental setup has been briefly presented. This cryogenic setup allows us to prepare a cold atomic cloud at a sub- μK temperature. Techniques for Rydberg excitation and detection have been also discussed.

Covering the chip with a Rubidium layer provides a very good homogeneous and stable electric field in the vicinity of the chip surface. As a result we obtain a rather narrow optical line as well as the longest coherence time measured so far ($630 \mu\text{s}$) with Rydberg atoms near a chip. This sets a very good playground to study the Rydberg interactions.

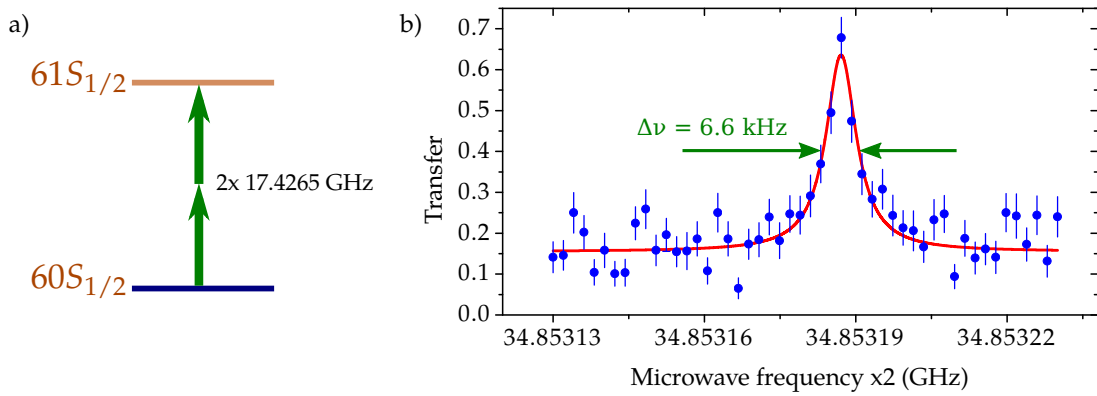


Figure 3.16 Microwave spectroscopy on the Rydberg transition $60S_{1/2} - 61S_{1/2}$. a) Energy diagram of the two-photon process b) Microwave spectrum taken with a $300 \mu\text{s}$ long microwave pulse. The dots are experimental data with statistical error bars (1 s.d.). They are fitted by a Lorentzian shape (solid red line) with a 6.6 kHz width.

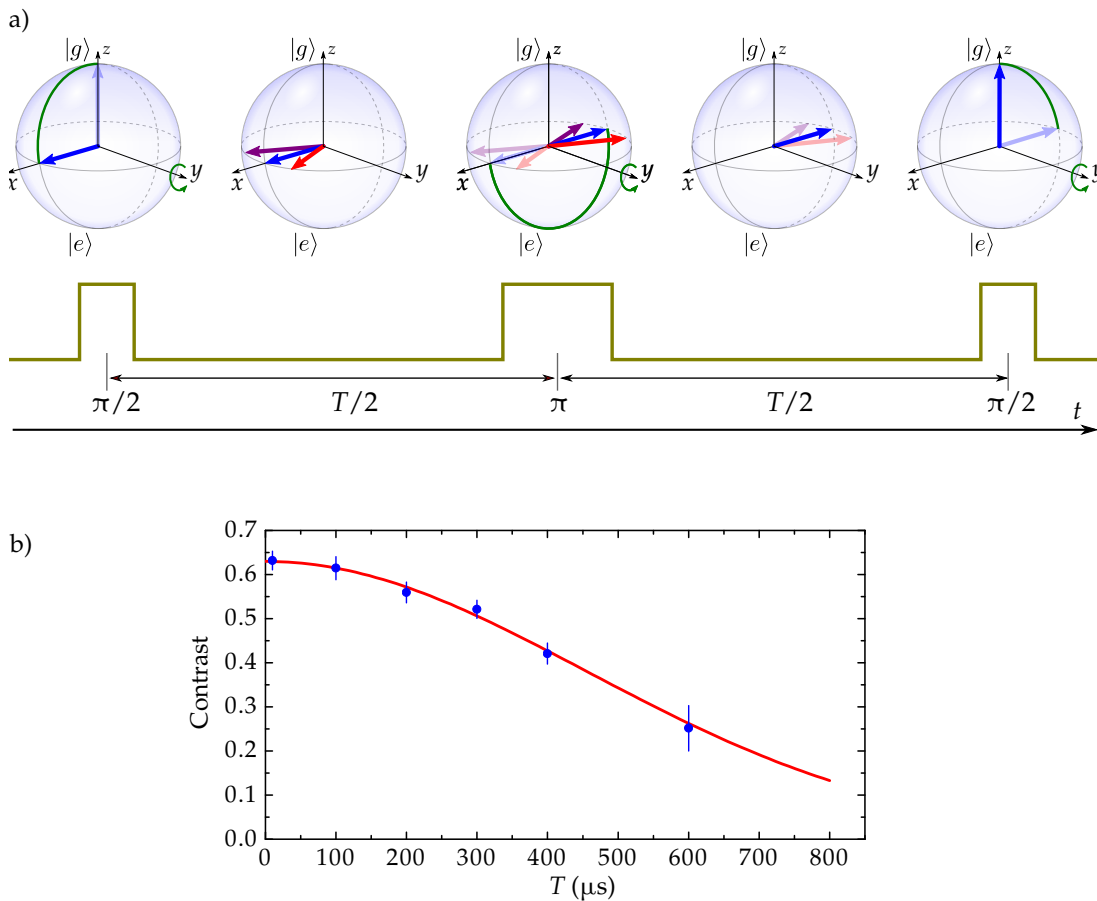


Figure 3.17 Coherent manipulation of the Rydberg transition $60S_{1/2} - 61S_{1/2}$. a) Principle of the spin-echo represented on Bloch sphere. $|g\rangle$ and $|e\rangle$ denote the states $60S_{1/2}$ and $61S_{1/2}$ respectively. b) Contrast of the spin-echo sequence as a function of its total duration T . The dots are experimental with statistical error bars (1 s.d.) and the solid red line is a Gaussian fit.

Microwave ruler for dipole-dipole interaction

4

This experiment is devoted to the study of the Rydberg excitation of a cold atomic cloud with strong dipole interaction. It is explained in details in Raul Teixeira's thesis [135], in which a simple quantitative analysis was presented. Here, we develop a new, more quantitative model, based on a rigorous simulation of rate equations. In the first section, we describe the optical transition from the ground state to the Rydberg $60S_{1/2}$ state for different laser detunings. One can distinguish two regimes: the dipole blockade regime, where the Rydberg excitation is suppressed at short inter-atomic distances, and the anti-blockade regime, where the Rydberg excitation is favored for specific inter-atomic distances. In the second section, we use microwave spectroscopy to directly measure the interaction energy of the created Rydberg cloud. In the third section, we recall our preliminary interpretation of the experimental results. In the two last sections, we concentrate on a refined numerical model which allows us to efficiently reproduce the experimental results.

4.1

Two regimes of Rydberg excitation

Benefiting from advanced improvement of laser trapping and cooling techniques, we record the spectral line for the Rydberg excitation in a regime of strong Rydberg-Rydberg interaction. Let us first discuss two regimes of excitation.

4.1.1

Dipole blockade

The mechanism of "dipole blockade" is based on the dipole-dipole interaction between Rydberg atoms. [Figure 4.1a](#) illustrates the idea by considering a pair of atoms under optical excitation. The laser is tuned on resonance to excite a single Rydberg atom $|r,g\rangle$ or $|g,r\rangle$ out of two ground-state atoms $|g,g\rangle$. The corresponding frequency hardly depends on the atom separation because of the weak interaction between a Rydberg atom and a ground-state atom. However, the Rydberg-Rydberg interaction strongly shifts the Rydberg pair level $|r,r\rangle$ at short distances, which makes the excitation with the same laser from the singly excited state to the doubly excited state out of

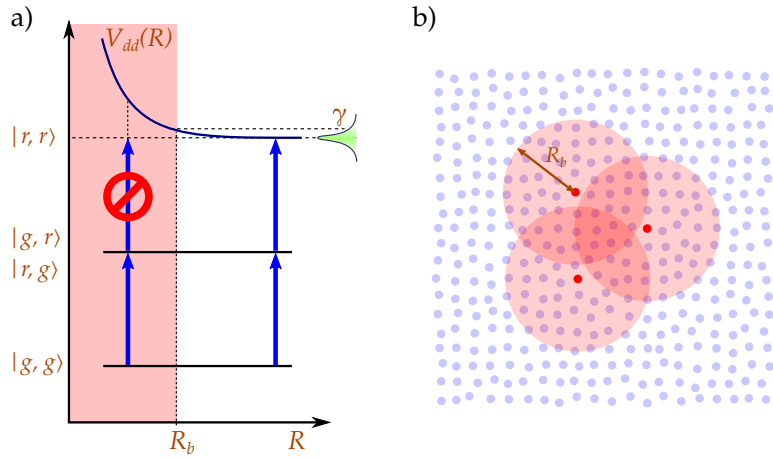


Figure 4.1 Dipole blockade mechanism. a) At short distance, the van der Waals interaction pushes the excitation of the second Rydberg atom out of resonance. The red shaded circles in b) represent the blockade volumes, where no more than one Rydberg atom can be excited.

resonance. The detuning is exactly equal to the van der Waals interaction energy V_{dd}^* . Let us define the blockade radius as the distance at which the van der Waals shift is equal to the excitation linewidth $\gamma/2$

$$\frac{C_6}{R^6} = \gamma/2 \quad (4.1)$$

thus,

$$R_b = \left(\frac{C_6}{\gamma/2} \right)^{1/6}, \quad (4.2)$$

where C_6 is the interaction strength. At distances smaller than R_b , the probability of having two excited atoms is strongly reduced. The excitation of the second Rydberg atom is blocked. There are two degenerate states of one-Rydberg-excitation $|g, r\rangle$ and $|r, g\rangle$. The symmetric combination of the two states $|D\rangle = (|g, r\rangle + |r, g\rangle)/\sqrt{2}$ is called the collective Dicke state of two atoms. The laser couples equally $|g, g\rangle$ to either $|g, r\rangle$ or $|r, g\rangle$ with the effective two-photon Rabi frequency Ω . Thus the strength of the coupling between the ground state and the collective Dicke state $|D\rangle$ is $\Omega\sqrt{2}$, enhanced by a factor $\sqrt{2}$. This enhancement factor was experimentally observed using two atoms in optical tweezers [151]. The authors recorded the Rabi oscillation of the probability to have one Rydberg excitation when one atom is trapped and when both atoms are illuminated with the same excitation laser. In the latter case, the frequency of the Rabi oscillation is about $\sqrt{2}$ times faster than that in the former case as represented in Figure 4.2.

The concept is extended to more than two atoms and depicted in Figure 4.1b. Due to the blockade effect, one cannot find more than one Rydberg atom inside a sphere of blockade radius R_b . The sphere is called the blockade volume. The stronger the van

*We explicitly consider the van der Waals interaction, but the mechanism can be applied for the resonant dipole interaction as well.

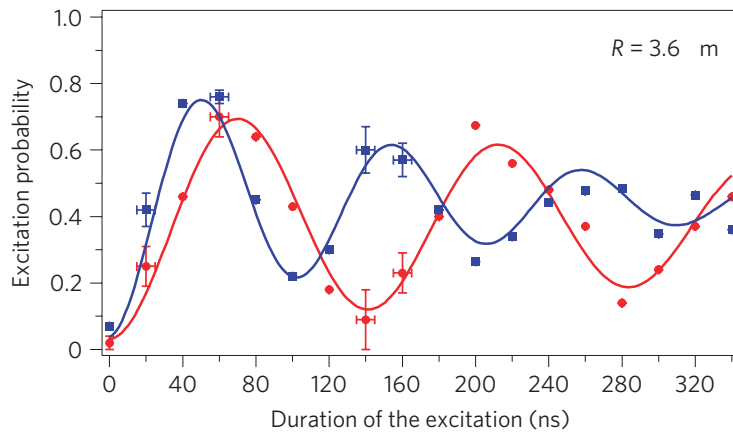


Figure 4.2 Experimental demonstration of the collective excitation with two atoms. Each atom is trapped in an optical tweezers. They are separated by $3.6 \mu\text{m}$. The red circles represent the probability to excite the first atom when the second one is absent. The blue squares represent the probability to excite only one atom when the two atoms are trapped and are exposed to the same excitation pulse. The solid lines are fits to the data, yielding Rabi frequencies of 7.0 ± 0.2 MHz and 9.7 ± 0.2 MHz respectively. Their ratio is 1.38 ± 0.03 , close to the value $\sqrt{2}$. Figure from [151].

der Waals interaction over the excitation linewidth, the more pronounced the blockade effect. Let N_b be the number of atoms inside a blockade volume. Due to the blockade effect these atoms get correlated. Similarly to the case of two atoms, the coupling between the ground state and the singly excited state, i.e., the collective Dicke state, is $\Omega\sqrt{N_b}$. A very simple model consists in describing the blockaded mesoscopic ensemble of N_b atoms as a single “super-atom” with a $\sqrt{N_b}$ times larger electric dipole moment. This super-atom model has been recently used to successfully explain experimental results in [117] and [152].

4.1.2

Facilitated excitation — Rydberg aggregate

In the Rydberg blockade regime, the interaction pushes the excitation out of resonance at short distances. Note that the van der Waals interaction between two Rydberg atoms in the same state is repulsive. If one blue detunes the excitation ($\Delta > 0$), the interaction energy now compensates the excitation mismatch. One can thus recover the resonant excitation regime.

The transition of the pair of atoms can be accomplished in two successive steps: an off resonant excitation of a first atom followed by a resonant excitation of the second one. The second step requires that the atom separation R_f satisfies

$$\Delta = V_{dd}(R_f) = \frac{C_6}{R_f^6} \quad (4.3)$$

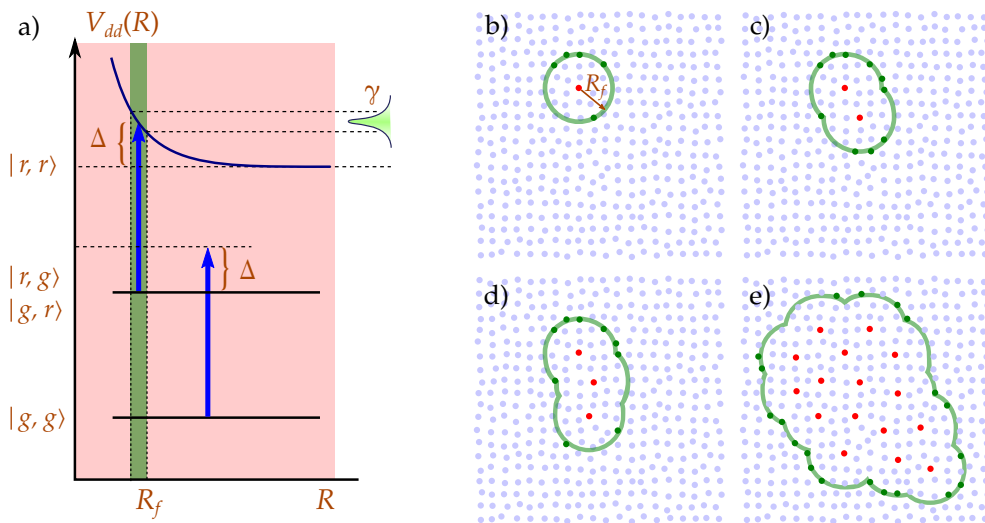


Figure 4.3 Facilitated excitation of Rydberg aggregate via a sequential excitation process. a) The energy diagram for a pair of atoms as a function of the distance shows that the facilitated effect happens only for distance R_f defined by the laser detuning Δ . b–e) Temporal evolution of a Rydberg aggregate out of a ground atom ensemble. The blue points represent the ground atoms and the red points the Rydberg atoms. The green bands represent the facilitated region where atoms (shown by dark green points) can be resonantly excited.

or

$$R_f = \left(\frac{C_6}{\Delta} \right)^{1/6}. \quad (4.4)$$

The excitation of the second Rydberg atom is thus facilitated by the presence of the first one. Moreover the position of the second atom is controlled by the laser detuning Δ ((4.4)). Due to the finite linewidth of the excitation, this requirement is a little bit relaxed into $R_f \pm \delta R_f$, where $\delta R_f = 6R_f\gamma/\Delta$. It is represented by a green strip in Figure 4.3a.

For an ensemble of atoms, any of them has more or less the same chance of being the first atom to be excited to the Rydberg state. However as soon as we get the first Rydberg atom, the excitation becomes more favorable for atoms that satisfy (4.3), i.e., at distance R_f to the already excited atom. These atoms are represented by the green points lying on the light green spherical shell of radius R_f — the facilitated volume—in Figure 4.3b.

The resonant facilitated excitation continues adding up Rydberg atoms as long as there is an atom i satisfying

$$\Delta = \sum_{\text{Ryd } j \neq i} \frac{C_6}{R_{ij}}, \quad (4.5)$$

where the summation runs over all already excited Rydberg atom j . Here, R_{ij} denotes the distance from the atom j to the atom i . Writing down this equation, we assumed that the van der Waals interaction energy can be added up to a good approximation

from all individual Rydberg pairs [153]. As a result, the dipole blockade is broken; a strongly correlated Rydberg aggregate quickly grows around the first Rydberg atom “seed”. The process is demonstrated in [Figure 4.3b–e](#). The relative distance between the atoms is controlled by equation (4.5), or in another word, the laser detuning Δ .

4.1.3

Optical spectra

Choice of the atomic density

In order to experimentally observe the facilitated excitation, we record the optical spectra of the Rydberg excitation with a cold cloud. A crucial technical point is that for a given detuning, the avalanche excitation process requires a dense cloud to maintain the conditions described in (4.3) and (4.5).

On the other hand, the nearly free Rydberg electron is scattered by the ground-state atoms. In a first approximation, the interaction energy V_e between the Rydberg electron and the ground-state atoms is proportional to the atomic density $\bar{\rho}$ [154]

$$V_e = \frac{2\pi\hbar^2 a_s}{m_e} \bar{\rho}, \quad (4.6)$$

where the interaction strength is characterized by the scattering length a_s , which is independent of the principal quantum number n and equal to $-16.1 a_0$ for ^{87}Rb [154]. The minus sign represents an attractive interaction $V_e < 0$. The interaction energy is about -0.1 MHz per 10^{12} cm^{-3} . For a BEC with a typical density of 10^{13} cm^{-3} , the interaction energy V_e is 1 MHz . As a result, there are two competing interactions of the same order of strength, the repulsive van der Waals interaction, which shifts up the energy levels and the electron–ground-state atom interaction, which lowers down the energy levels. One finds that the blockade radius is effectively reduced. This is not a favorable situation to study the Rydberg interaction.

As a compromise on the two conflicting requirements on the atomic density, we choose a thermal cloud in a magnetic trap rather than a BEC. The cloud has about 10 000 atoms, held $210 \mu\text{m}$ away from the chip. The atoms are cooled to around 500 nK , just above quantum degeneracy. The cloud takes a quasi 1D cigar-shape elongated along the x direction. The extensions in each direction follow a Gaussian profile with the width (at $e^{-1/2}$) given by $\sigma_x = 23.2 \mu\text{m}$, $\sigma_y = 4.5 \mu\text{m}$ and $\sigma_z = 4.2 \mu\text{m}$ (see [Appendix C](#)). The peak density is about $1.4 \times 10^{12} \text{ cm}^{-3}$, corresponding to a maximum red-shift of 150 kHz . We can thus neglect V_e in the next of discussion.

Result

The optical excitation line is displayed in [Figure 4.4](#) for different laser durations. A broadening to the blue side, i.e., high frequency, is observed, which is a strong signature of the Rydberg–Rydberg interactions (compared to that of a dilute cloud in [Figure 3.15](#)). Using $\gamma = 579 \text{ kHz}$ found from [Figure 3.15](#), one estimates a blockade radius of about $8.8 \mu\text{m}$. Comparing this value to the inter-atomic distance of $0.9 \mu\text{m}$ at the center of the trap, we are definitely in the strong blockade regime.

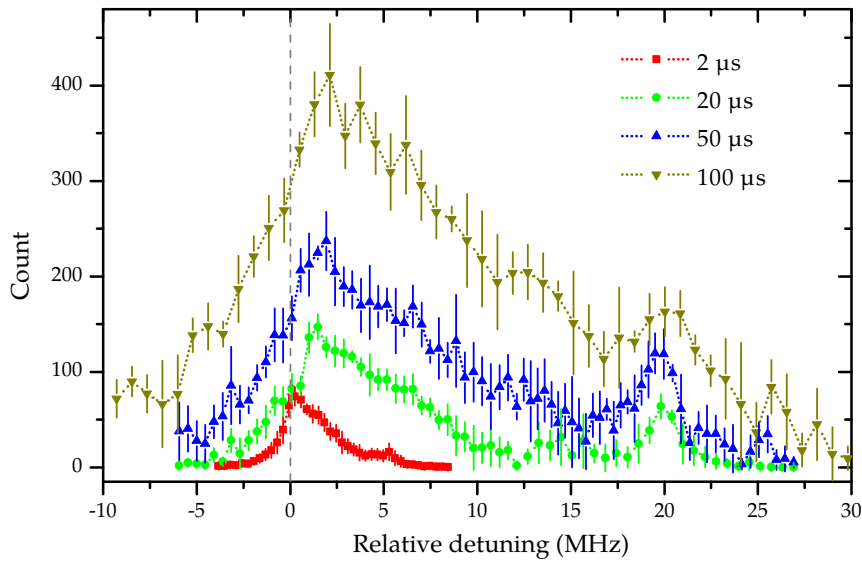


Figure 4.4 Optical spectra for excitation durations of $2\text{ }\mu\text{s}$, $20\text{ }\mu\text{s}$, $50\text{ }\mu\text{s}$ and $100\text{ }\mu\text{s}$. The peaks at 20 MHz are due to a residual sideband modulation of the blue laser, which is required for the Pound-Drever-Hall locking scheme [155]. The error bars denote one standard deviation of the statistical error.

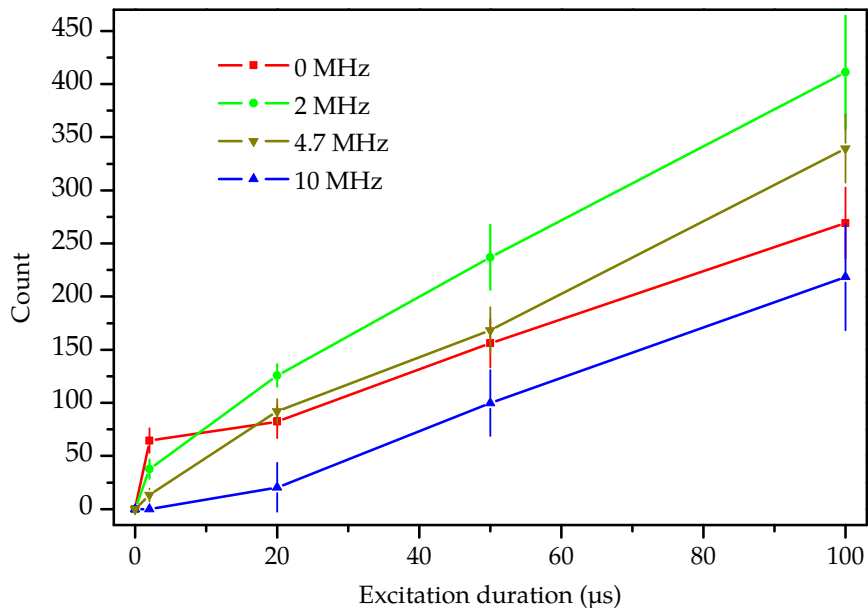


Figure 4.5 Number of Rydberg atoms as a function of the excitation duration. Data extracted from [Figure 4.4](#).

Figure 4.5 plots the number of Rydberg atoms, extracted from **Figure 4.4**, as a function of the excitation duration for $\Delta = 0, 2$ and 10 MHz. One finds that the excitation starts slowly for large detunings, and then speeds up at later times. This can be interpreted as the time needed to off-resonantly create the initial “seed” necessary for the facilitated growth of the Rydberg aggregate. One also notes a change in the number of Rydberg atoms in the first few microseconds at zero-detuning. This corresponds to the saturation of the Rydberg excitation when the cloud is filled with super-atoms. Further excitation of Rydberg atoms is possible at the border of the cloud but with slower dynamics. The decay of a Rydberg atom due to its finite lifetime, or the motion of the Rydberg atoms due to, for instance, the repulsive van der Waals force between them can open a gap between the super-atoms, where a new Rydberg atom can be excited. This explains why the number of Rydberg atoms continues to increase instead of staying constant in the context of the frozen Rydberg gas approximation commonly used.

The formation of Rydberg aggregates was also observed with cesium atoms in a vapor cell [156], with Rubidium atoms in a MOT [157] or in a dipole trap [158]. Notably, in the latter reference, the authors observe also a strong broadening to the blue side when they systematically increase the density of the cloud.

4.2

Microwave probe of van der Waals interaction energy

Microwave spectroscopy can be used as a probe of the energy distribution in a Rydberg ensemble. This will be a useful tool to measure the regularity of a Rydberg chain used for quantum simulation. In the following, we describe the principle of the method as well as experimental results.

The idea is quite simple. Different Rydberg levels are shifted differently by the van der Waals interaction. The transition frequencies between two Rydberg levels are thus changed correspondingly. Probing these shifts by microwave spectroscopy will directly give us the van der Waals interaction energy. However, one has to carefully design the measurement to extract useful information.

4.2.1

Choice of levels

The laser excitation prepares an ensemble of the $60S_{1/2}$ Rydberg atoms. The question to ask now is “which Rydberg transition should we use?”.

The strong attractive branch of the resonant $60S - n'P$ dipole interaction would trigger a fast Penning ionization process, in which the surrounding $60S$ atoms collapse on the $n'P$ atoms and get ionized. The spectrum will not be useful. Thus this pair of levels is not relevant for our purpose. A $60S - n'S$ two-photon excitation with a narrow spectral line is a good option[†]. Let us first consider the $60S - n'S$ dipole-dipole interaction.

[†]The momentum quantum number $j = s = 1/2$ and its projection m_j is conserved (no spin flip). We thus omitted them for convenience.

Table 4.1 van der Waals coefficients for different pairs of $60S - n'S$ atoms.

	$C_{6,60S-n'S}$ (GHz. μm^6)	$A_{6,60S-n'S}$ (GHz. μm^6)
$60S - 63S$	-89.26	0.61
$60S - 62S$	-411.36	14.96
$60S - 61S$	292.25	248.60
$60S - 60S$	137.62	-
$60S - 59S$	245.13	209.55
$60S - 58S$	-209.26	7.77
$60S - 57S$	-43.67	0.30

 $60S - n'S$ interaction

The dipole operator does not directly couple $|60S\rangle$ to $|n'S\rangle$ due to the selection rules. The exchange interaction, as well as the direct interaction, results from a second-order perturbation. It takes the form of a van der Waals potential. The effective interaction Hamiltonian in (2.9) is rewritten as

$$V_{\text{eff}} = \begin{pmatrix} |60S; n'S\rangle & |n'S; 60S\rangle \\ |60S; n'S\rangle & C_{6,60S-n'S} & A_{6,60S-n'S} \\ |n'S; 60S\rangle & A_{6,60S-n'S} & C_{6,60S-n'S} \end{pmatrix} \frac{1}{R^6}, \quad (4.7)$$

where $C_{6,60S-n'S}$ and $A_{6,60S-n'S}$ are respectively the van der Waals coefficients of the direct and the exchange interactions. As a result, the degenerate pair states $|60S; nS\rangle$ and $|nS; 60S\rangle$ are split into a symmetric and an anti-symmetric combination of the two bare states. Each of them is shifted $(C_{6,60S-nS} \pm A_{6,60S-nS})/R^6$.

Table 4.1 lists the van der Waals coefficients for the interaction of a $60S$ atom with another atom in nearby $n'S$ level. The exchange interaction drops much faster than the direct interaction when the difference between n and n' increases. For $|n - n'| \geq 3$, the exchange interaction is two orders of magnitude smaller than the direct interaction. It can thus be neglected. Interestingly, the direct interaction changes from repulsive to attractive when $|n - n'| \geq 2$.

 $nS - n'S$ transition

Let us now consider a pair of two $60S$ atoms at a distance R undergoing such a transition. There are four pair states involved: $|60S; 60S\rangle$, $|60S; nS\rangle$, $|nS; 60S\rangle$ and $|nS; nS\rangle$. However, weak microwave pulses couple $|60S; 60S\rangle$ to $|nS; nS\rangle$ only to the second order. We thus neglect the doubly excited state $|nS; nS\rangle$.

Due to the level splitting, we get in general two excitation lines, separated by $2A_{6,60S-nS}/R^6$. If one adds another Rydberg atom, we would have three interacting pairs, resulting in an even more complex spectrum. One thus has difficulty to relate each line to its corresponding transition, which is necessary to deduce the interaction energy. The situation is even worse when more Rydberg atoms are involved.

If $A_{6,60S-nS} \ll C_{6,60S-nS}$, the situation is much simpler as the two lines merge into

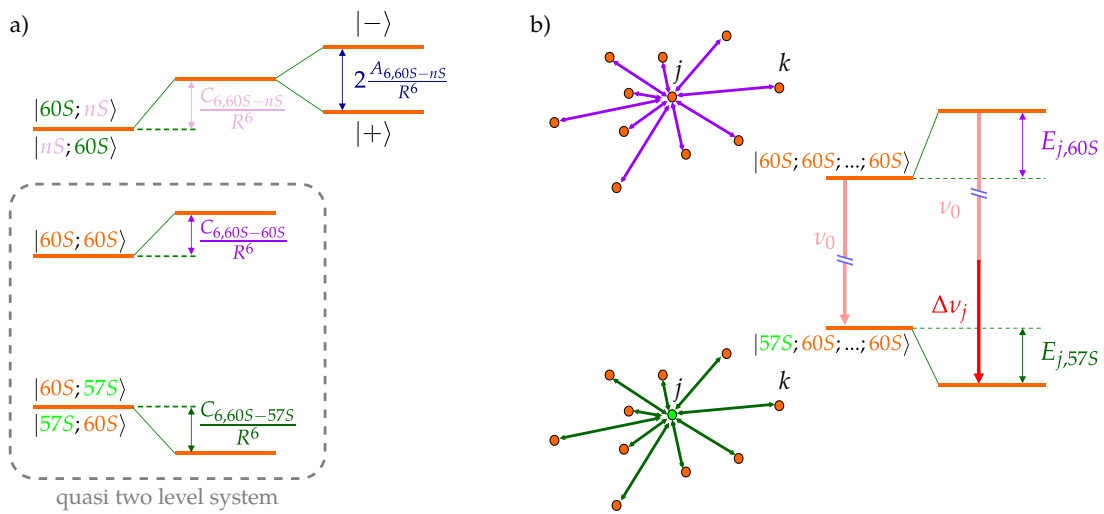


Figure 4.6 a) The van der Waals interactions lead to an energy shift for a Rydberg pair state as well as to a level splitting. The \$60S - 57S\$ pair is however quasi degenerate, leading to a quasi two-level system for the corresponding transition. b) The shift of microwave photon energy bringing an atom \$j\$ from the \$60S\$ to the \$57S\$ state is proportional to the initial interaction energy of the atom \$j\$. The doubly excited state \$|nS; nS\rangle\$ is not shown as it is rarely populated under weak excitation.

one. According to table 4.1, this should happen for either the \$60S - 57S\$ or \$60S - 63S\$ transition, where the exchange interaction is two orders of magnitude smaller than the direct interaction. In the following, we focus on the \$60S - 57S\$ transition but similar results could be obtained with the \$60S - 63S\$ transition. Figure 4.6a summarizes the idea.

For two noninteracting atoms, we obtain a single two-photon transition line centered at the frequency \$\nu_0/2 = 58.229\$ GHz, where \$\hbar\nu_0\$ is the energy separation of the \$60S - 57S\$ levels. In the presence of interactions, the excitation line is shifted to \$[\nu_0 + \Delta\nu(R)]/2\$, with \$\Delta\nu(R)\$ given by

$$\Delta\nu(R) = \frac{C_{6,60S-60S} - C_{6,60S-57S}}{R^6} = \eta \frac{C_{6,60S-60S}}{R^6}, \quad (4.8)$$

where \$\eta \approx 1.317\$.

The above result can be generalized for an ensemble of \$N_{\text{Ryd}}\$ interacting Rydberg atoms. Initially all of them are in the \$60S\$ state. We assume that the microwave pulse can excite at most one atom (\$j\$) at a time to the \$57S\$ state. The total interaction energy of the atom before and after the excitation respectively read

$$E_{j,60S} = C_{6,60S-60S} \sum_{k \neq j}^{N_{\text{Ryd}}} \frac{1}{R_{jk}^6}, \quad (4.9)$$

and

$$E_{j,57S} = C_{6,60S-57S} \sum_{k \neq j}^{N_{\text{Ryd}}} \frac{1}{R_{jk}^6}, \quad (4.10)$$

where we merely add up the interaction energies of the atom j with every individual atom k , at a distance R_{jk} away. The shift of the microwave frequency $\Delta\nu_j$ from the non-interacting case is given by

$$\Delta\nu_j = \frac{E_{j,60S} - E_{j,57S}}{h} = \eta \frac{E_{j,60S}}{h}. \quad (4.11)$$

The probability $n(\Delta\nu_j)$ of having an atom whose frequency shift is $\Delta\nu_j$ is directly the van der Waals energy distribution $P(E_{j,60S})$

$$n(\Delta\nu_j) = n\left(\eta \frac{E_{j,60S}}{h}\right) = P(E_{j,60S}). \quad (4.12)$$

The microwave spectrum, which probes $n(\Delta\nu_j)$, takes the shape of the Rydberg ensemble's interaction energy histogram within a known scaling factor .

4.2.2

Experimental work

4.2.2.1 Microwave spectra

A microwave probe is used to extract information on the interaction energy distribution of Rydberg aggregates created by a 2 μs -long laser field. The corresponding optical excitation spectrum in Figure 4.4 is shown again in Figure 4.7. We use three laser detunings $\Delta = 0, 1$ and 2 MHz. A microwave pulse is applied just after the laser excitation so that the energy distribution is not yet modified due to the atomic motion[†]. For the same reason, the microwave pulse duration is set to 1 μs . The microwave power is adjusted on a dilute Rydberg cloud to a π pulse. The timing of the experiment is schematically depicted in Figure 4.7a. The experiment sequence is repeated 10 times on the same atomic cloud, with a 3 ms time interval, without noticeable heating effect.

The fraction of atoms transferred into the $57S$ state is plotted as a function of the scaled microwave frequency shift $\Delta\nu/\eta$ in Figure 4.7c. Less than 3 atoms are excited in $57S$, and thus the interaction between them can be neglected. Strictly speaking, some of the $57S$ atoms undergo Penning ionization with surrounding $60S$ atoms due to their attractive interaction. However, this is a weak attraction. Most atoms are not yet ionized until their detection. The microwave spectrum is therefore not altered by the Penning ionization process.

In Figure 4.7c, the horizontal axis gives directly the interaction energy E of the atoms. According to (4.9), the nearest neighbor of an atom whose interaction energy is E , can not be closer than $R_E = (C_{6,60S-60S}/E)^{1/6}$. At $\Delta = 0$, the microwave spectrum is slightly shifted by about the laser linewidth γ . Noting that $E = 2 \text{ MHz}$ corresponding

[†]A short delay of 0.5 μs is introduced to avoid any overlap of the laser and the microwave pulses.

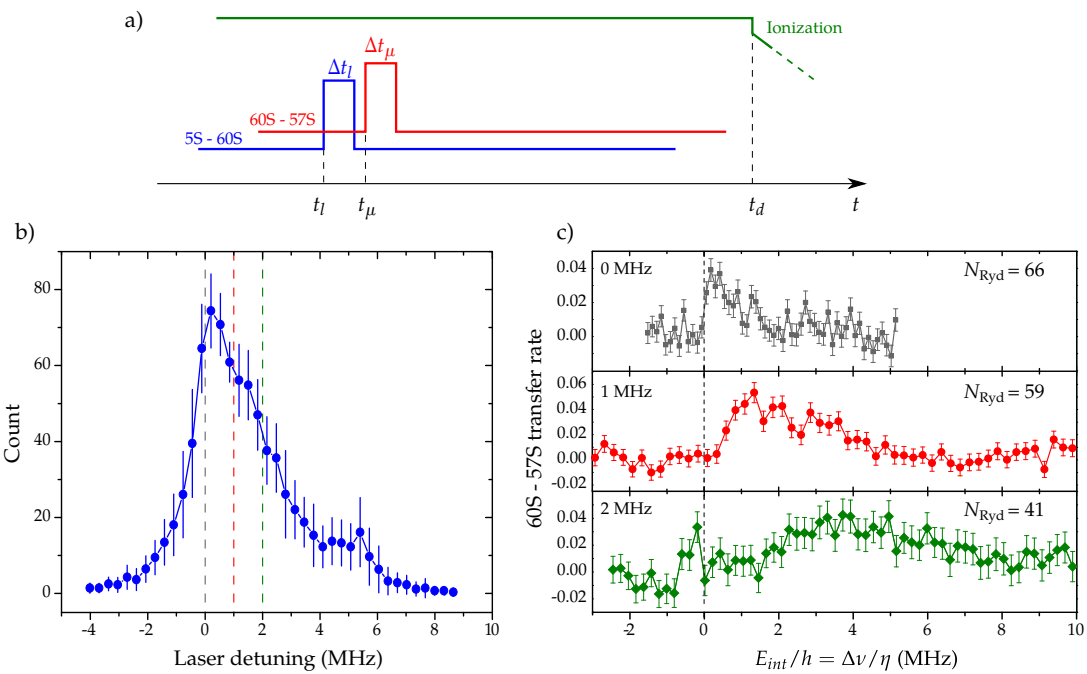


Figure 4.7 Microwave probe of van der Waals energy. a) Experimental sequence showing the timing (not to scale) of the Rydberg ensemble preparation laser pulse, the microwave probe and the detection. b) Optical excitation spectrum. The dashed lines marks the detunings of 0, 1 and 2 MHz. The error bars are one standard deviation of the statistical error. c) Microwave spectra at 0, 1 and 2 MHz detunings. The small peak at 5.8 MHz in b) is due to a small fraction of atoms trapped in $5S, F = 2, m_F = +1$ state which is populated during the RF evaporation stage. The error bars denote one standard error of the mean.

to $R_E = 6.4 \mu\text{m}$ (*cf.* Table 4.1), the microwave spectrum shows no Rydberg pair closer than this distance due to the blockade effect. When we detune the laser to the blue, $\Delta > 0$, the facilitated excitation correspondingly shifts the spectrum. A larger detuning gives a higher interaction energy to the Rydberg cloud. The distance between the atoms is expected to be smaller. We thus somehow compact the Rydberg ensemble.

The long tails to the blue side observed in Figure 4.7c is due to the interaction energy accumulated by the already excited Rydberg atoms during the aggregate formation as illustrated in Figure 4.8. The development of a Rydberg cluster around a Rydberg atom gradually gives to this atom an interaction energy larger than Δ . It also has more neighbors and eventually becomes an atom in the cloud bulk.

4.2.2.2 Time evolution of the Rydberg cloud

Under the repulsive interaction energy given by $\Delta > 0$, the $60S$ Rydberg atoms repel each other, making the whole cloud expand. The initial interaction energy is converted into kinetic energy. Probing the van der Waals interaction energy of the $60S$ cloud at different time delays Δt after the laser excitation allows us to observe this expansion. The timing and results are represented in Figure 4.9 for $\Delta = 1 \text{ MHz}$ and $\Delta = 2 \text{ MHz}$.

As time goes, the spectrum gets narrower and approaches that of a dilute cloud where the van der Waals interaction is negligible. The atoms are cooled to 500 nK

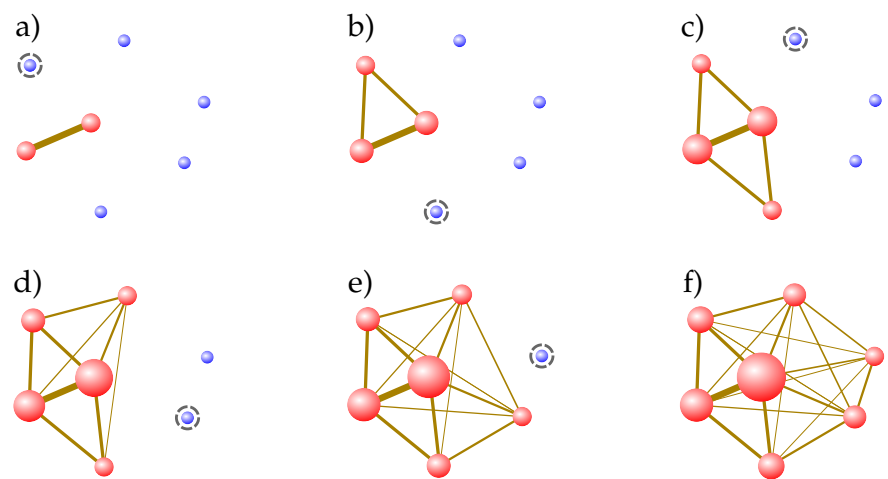


Figure 4.8 Illustration of the interaction energy accumulation during the growth of a Rydberg aggregate from a) to e). The blue spheres are ground state atoms and the red spheres are the Rydberg atoms. The thickness of the solid lines connecting Rydberg atoms show the strength of the corresponding interaction. The size of the red sphere represents the total interaction energy of the corresponding atom. The dashed circle around a ground-state atom indicates which atom will be excited in the next step.

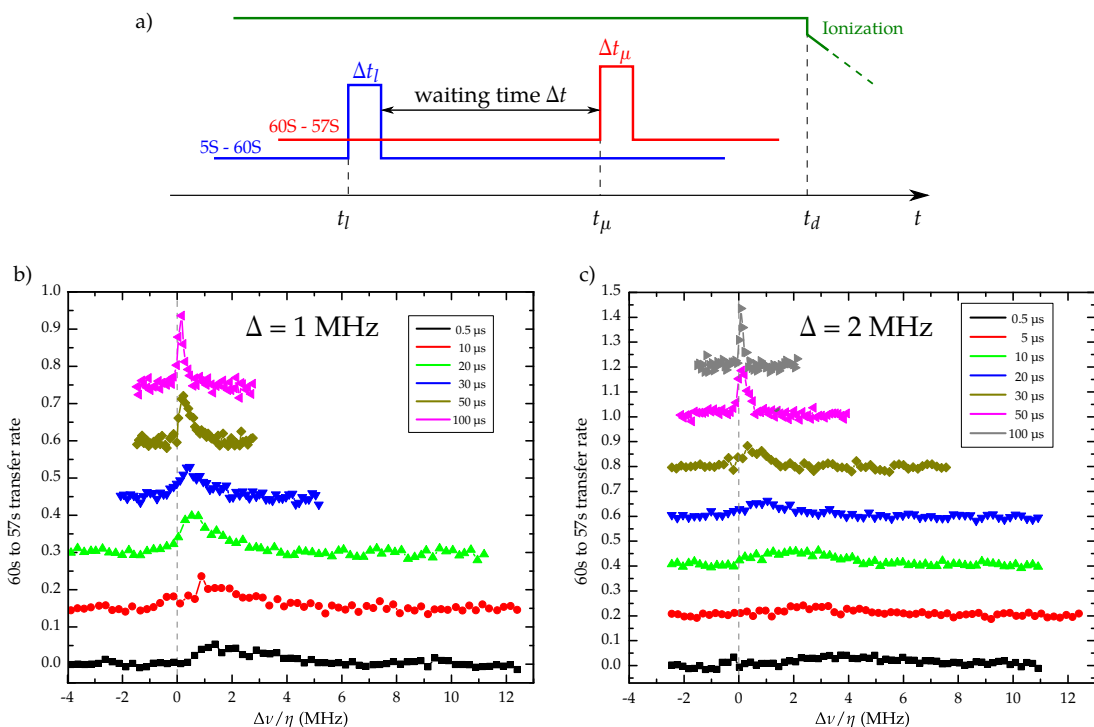


Figure 4.9 Expansion of a repulsive Rydberg ensemble probed by microwave spectroscopy. a) Timing of the experimental sequence and the results for b) 1MHz and c) 2MHz. The spectra are vertically shifted for a better visibility.

corresponding to about 10 kHz kinetic energy, a hundred times smaller than the interaction energy; therefore thermal motion plays no significant role in the observed spectra. The recoil velocity[§] due to the absorption of a 480 nm and a 780 nm photon during the excitation only makes the Rydberg cloud globally drift, and thus gives no change in the relative distance between the Rydberg atoms. The evolution of the microwave spectrum therefore results from the expansion of the Rydberg cloud in the strong interaction regime.

The motion of the Rydberg atoms is not negligible after $\sim 5 \mu\text{s}$ for $\Delta = 2 \text{ MHz}$. The commonly used frozen Rydberg gas approximation is no longer valid. This thus sets a time limit over which one can perform quantum simulations with a Rydberg crystal, i.e., a regularly prepared array of Rydberg atoms.

4.3

Preliminary interpretation

The time-dependent Schrödinger equation for 10 000 strongly correlated atoms cannot be exactly integrated. Instead, quantum Monte Carlo simulation is more relevant and is widely used for such a problem. In the thesis of Raul Teixeira, we used a preliminary simulation to explain the experimental results. Here, we recall this simple excitation model as well as its outcome. We discuss also the limitations of this model.

4.3.1

Monte Carlo simulation

A C++ simulation program was built based on a simple algorithm. It is a model of incoherent excitation. To run the simulation, we need to provide the following parameters:

- The number of ground-state atoms N and the spatial distribution of the cloud, i.e., a Gaussian profile ([Appendix C](#)).
- The intensity distribution of the excitation lasers (red and blue lasers).
- The laser excitation spectrum. We approximate it by a normalized Voigt profile $P^{\text{Voigt}}(\Delta)$ of 0.9 MHz FWHM, which is a convolution of a 720 kHz FWHM Gaussian profile and a 360 kHz FWHM Lorentzian profile.
- The laser detuning Δ .
- The total number of Rydberg atoms at the end of the excitation N_{Ryd} , which is an integer close to the experimental results obtained for Δ . Specifically, it is 66 atoms for zero-detuning, 59 for $\Delta = 1 \text{ MHz}$ and 41 for $\Delta = 2 \text{ MHz}$ ([Figure 4.7](#)).

The simulation can be summarized as follows

[§]The recoil velocity is of about $15 \mu\text{m}/\text{ms}$, corresponding to a recoil energy of 26 kHz.

Algorithm

(a) *Initialization.* We begin the simulation by drawing the positions of N ground-state atoms according to the spatial distribution of the atomic cloud.

(b) *Calculation of excitation probability.* We choose randomly a ground-state atom i and calculate its excitation detuning taking into account the interaction with the already excited Rydberg atom(s) j

$$\Delta_i = \Delta - \sum_{\text{Ryd } j \neq i} \frac{C_6}{R_{ij}^6}. \quad (4.13)$$

If there is no other Rydberg atom, then $\Delta_i = \Delta$. Based on the linewidth of the excitation, we determine the excitation probability P_i^{Voigt} of the atom i . This probability is then weighted by the intensity distribution of excitation lasers (relative to that at the beam center) to take into account the laser profiles. This gives the final probability P_i for the atom i to be excited.

(c) *State update.* Next, we decide whether the atom i gets excited or not according to P_i calculated in step (b). For this, a random real number r between 0 and 1 is drawn. The atom i is excited if $P_i > r$.

(d) *Loop of the Monte Carlo sequence.* The steps (b) and (c) are now repeated until the total number of Rydberg atoms reaches N_{Ryd} .

The state flipping of an atom is considered as incoherent in this model. The atomic cloud is assumed to be frozen during the excitation. The simulation explicitly describes only a sequential incoherent one-photon excitation process[¶].

Another important remark is that the model has no timescale. Thus it cannot predict the final number of Rydberg atoms. Instead, an empirical number N_{Ryd} , obtained from the experiment is required to stop the simulation.

4.3.2

Numerical result

The mechanical expansion of a Rydberg gas due to the repulsive van der Waals interaction after the excitation can be easily calculated by integrating Newton's second law of motion. The finite lifetime of the 60S state can also be included in the calculation. Together with the Monte Carlo simulation, this allows us to generate microwave spectra at different delays Δt , represented by the solid lines in [Figure 4.11](#). Although the model is quite simple, the resulting microwave spectra agree fairly with the experiment.

We aim at reproducing the microwave spectra in [subsection 4.2.2](#). For a fixed detuning Δ , from the numerically generated Rydberg ensemble with the above program, we calculate the van der Waals interaction energy for each Rydberg atom. After 50 to 200 Monte Carlo realizations, we can construct a histogram of the interaction energy.

[¶]By one-photon excitation, we mean an effective two-photon process, simultaneously absorbing a red and a blue photons.

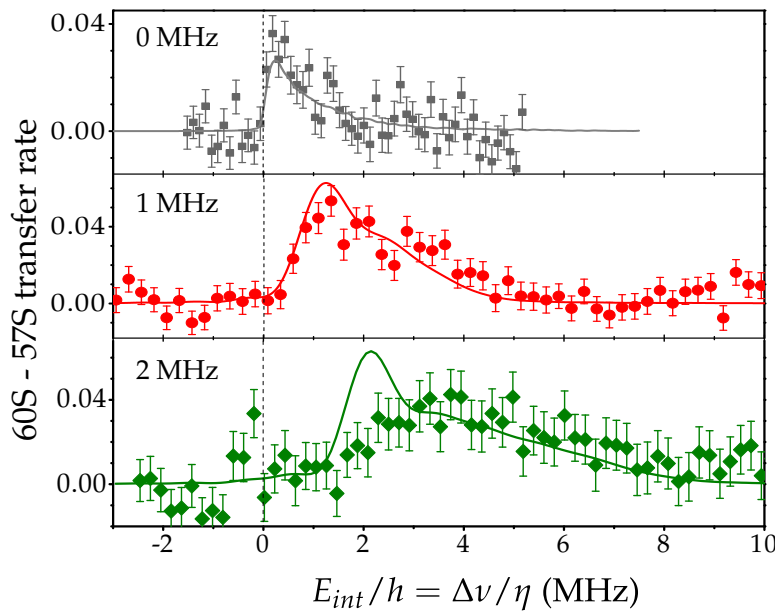


Figure 4.10 Monte Carlo simulation results (solid lines) superposed with the experimental data (points) for the van der Waals energy measurement of a Rydberg ensemble. The laser detuning is set to 0 MHz (squares), 1 MHz (circles) and 2 MHz (diamonds). The error bars indicate one standard error of the mean.

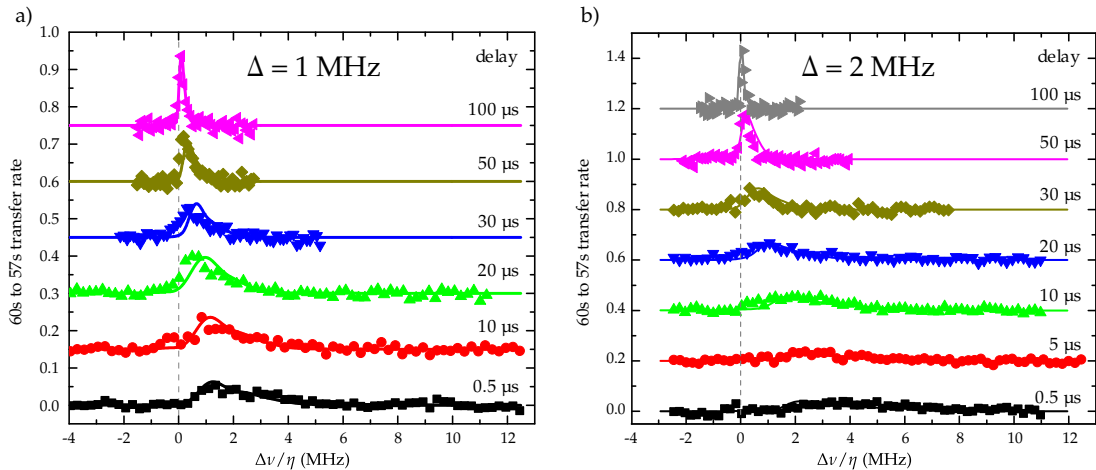


Figure 4.11 Monte Carlo simulation results (solid lines) superposed with the experimental data (points) for the expansion of a repulsive Rydberg ensemble. The laser detuning is set to a) 1 MHz and b) 2 MHz.

The final microwave spectrum is a convolution of this histogram with the microwave pulse Fourier transform limited linewidth (see [Appendix D](#)). The obtained results are plotted as the solid lines in [Figure 4.10](#). They are vertically scaled to best fit the experimental data.

4.3.3

Limitation

Although the simple Monte Carlo model can reproduce rather well the microwave spectra, it fails in explaining the optical spectra. This comes from the fact that the model lacks an excitation dynamics, i.e., a real physical time scale. As a workaround, one can relate the number of iterations to the excitation duration. A reasonable assumption is a linear correlation between them. We thus keep the number of iterations the same for all laser detunings and for each excitation duration. The number of iterations is chosen so that the simulation best fits the high frequency tail of the optical spectrum. The assumption of a linear correlation between the number of iterations and the excitation duration allows us to include the mechanical motion of the Rydberg atoms due to the repulsive van der Waals force between them. The simulation provides us the solid lines in [Figure 4.12](#). There are two problems. First the used number of iterations and the excitation durations exhibit no clear linear dependency. Second the resulting curves does not fit the optical spectra at low frequencies.

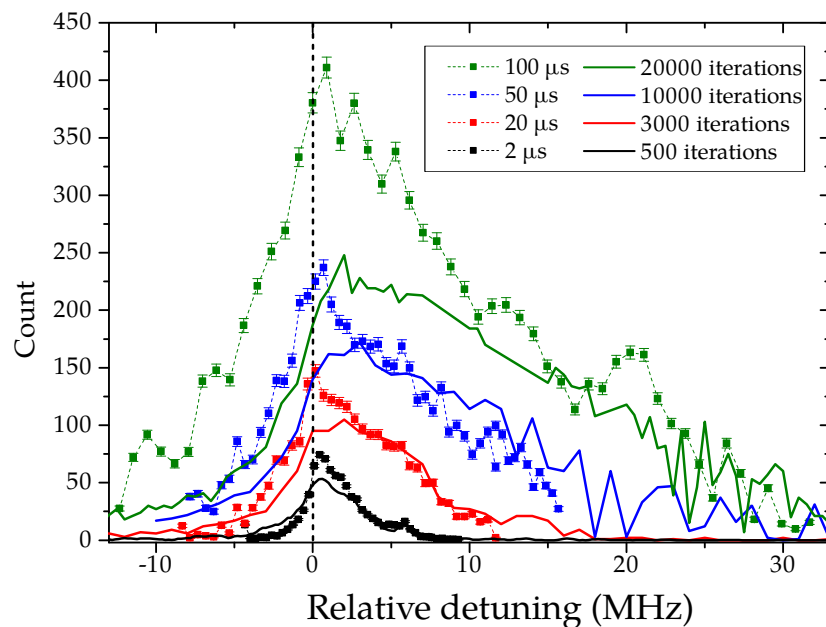


Figure 4.12 Reproduction of optical spectra with Monte Carlo simulation. For each excitation duration, the number of iterations is the same for all laser detunings so that the simulation best reproduces the high frequency tail of the spectrum. The calculation includes the mechanical expansion of the repulsive Rydberg ensemble during the excitation.

The lack of a physical time scale coaxes us to provide the final Rydberg atom number, N_{Ryd} , a parameter coming from the experimental results. Feeding the experimental outcome at the input of the simulation, this phenomenological approach makes the model unable to predict results for different sets of excitation parameters. We thus cannot use the model to test new excitation schemes.

Another limitation is the exclusion of the de-excitation of Rydberg atoms. If the number of ground state atoms in resonance with the excitation is large, the de-excitation of a Rydberg atom is immediately compensated by the excitation of another Rydberg

atom. This is no longer true in the case of large detunings. The facilitated excitation searches for atoms at very short distances to an already excited Rydberg atom, a condition hardly fulfilled with a cloud that is not dense enough. Even for a dense cloud, a similar situation happens at later times when big Rydberg aggregates already fill the cloud. One has to look for atoms at the border of the cloud, where the density is much lower.

4.4

Monte Carlo - rate equations simulation

Another model is needed to overcome the limitations of the previous one. M. Weidmüller and coworkers obtain similar optical spectra [158]. They explain the results by integrating the rate equations. However, they do not include the atomic motion, resulting from the strong interaction between the Rydberg atoms, which is a must-to-have in a model to simulate the dynamics of long excitations at high detunings.

In this section, we present our approach, solving the rigorous rate equations by a Monte Carlo simulation — the Monte Carlo - rate equations simulation. Before entering into details, we first revisit the optical Bloch equations in the strong dephasing regime.

4.4.1

Rate equations limit of the optical Bloch equations

Let us consider a two-level atom in a laser field. The density matrix of the system is

$$\rho = \rho_{rr} |r\rangle\langle r| + \rho_{gg} |g\rangle\langle g| + \rho_{rg} |r\rangle\langle g| + \rho_{gr} |g\rangle\langle r| , \quad (4.14)$$

where ρ_{rr} and ρ_{gg} are the populations of the excited state and the ground state respectively. The coherence between the two states is $\rho_{gr} = \rho_{rg}^*$. Under the transformation to the rotating frame defined by the unitary operator $U = \exp(i\omega t |r\rangle\langle r|)$, where ω is the laser frequency, the populations are unchanged while the coherences take the form

$$\tilde{\rho}_{gr} = \tilde{\rho}_{rg}^* = \rho_{gr} e^{-i\omega t} . \quad (4.15)$$

The time evolution of the density matrix elements in the rotating frame after discarding fast oscillating terms, i.e., using the rotating wave approximation, are described by the optical Bloch equations

$$\partial_t \rho_{rr} = i \frac{\Omega}{2} (\tilde{\rho}_{rg} - \tilde{\rho}_{gr}) - \frac{1}{\tau} \rho_{rr} \quad (4.16a)$$

$$\partial_t \tilde{\rho}_{rg} = -\left(\frac{\gamma}{2} - i\Delta\right) \tilde{\rho}_{rg} + i \frac{\Omega}{2} (\rho_{rr} - \rho_{gg}) , \quad (4.16b)$$

where Ω is the Rabi frequency, τ is the lifetime of the corresponding Rydberg state and γ is the dephasing rate.

In the limit of strong dephasing, $\gamma \gg \Omega \gg \tau^{-1}$ and $t \gtrsim \gamma^{-1}$, the coherences quickly

reach their steady state values, i.e., $\partial_t \tilde{\rho}_{rg} \rightarrow 0$. Extracting $\tilde{\rho}_{rg}$ (and $\tilde{\rho}_{gr}$) from (4.16b) under this assumption and substituting into (4.16a), we obtain

$$\partial_t \rho_{rr} = -\frac{(\Omega/2)^2 \gamma}{(\gamma/2)^2 + \Delta^2} (\rho_{rr} - \rho_{gg}) - \frac{1}{\tau} \rho_{rr}. \quad (4.17)$$

This equation describes the time evolution of the excited state depending on the relative population between the excited and the ground states. One can immediately identify it as the rate equations limit of the optical Bloch equations, i.e., the Einstein's coefficients model. The problem of atomic excitation is reduced to a classical stochastic process in which the atom gets excited with a rate

$$\Gamma = \frac{(\Omega/2)^2 \gamma}{(\gamma/2)^2 + \Delta^2}, \quad (4.18)$$

and de-excited with rate

$$\Gamma_d = \Gamma + \tau^{-1}. \quad (4.19)$$

Extending the model to an ensemble of N atoms, the detuning of the i -th atom is modified due to the van der Waals interaction with surrounding Rydberg atoms as given by (4.13). The corresponding rates of excitation and de-excitation become

$$\Gamma_i = \frac{(\Omega/2)^2 \gamma}{(\gamma/2)^2 + \left(\Delta - \sum_{\text{Ryd } j \neq i} \frac{C_6}{R_{ij}^6} \right)^2} \quad (4.20)$$

and

$$\Gamma_{d,i} = \Gamma_i + \tau^{-1} \quad (4.21)$$

respectively.

A question arises: how can the dephasing rate γ be estimated? Equation (4.17) is valid for a dilute Rydberg cloud where the van der Waals interactions are negligible. For long-lived Rydberg state, $\tau^{-1} \ll \Gamma$, one can neglect the decay of the Rydberg state. The solution when all the atoms are initially in the ground state is found to be

$$\rho_{rr} = \frac{1}{2} (1 - e^{-2\Gamma t}). \quad (4.22)$$

It is approximately given by

$$\rho_{rr} = \Gamma t = \frac{(\Omega/2)^2 \gamma}{(\gamma/2)^2 + \Delta^2} t \quad (4.23)$$

at short time scale, $\Gamma t \ll 1$. The excitation spectrum is thus a Lorentzian profile with a FWHM given by γ . Figure 3.15 gives $\gamma = 579$ kHz in our case.

4.4.2

Algorithm

We have all the ingredients to build a Monte Carlo simulation. For each time interval dt , it calculates the excitation rate for each atom and decides whether the atom get excited or not. The simulation iterates over the excitation duration. The parameters required by the simulation consist of

- The number of ground-state atoms N and the spatial distribution of the cloud, i.e., a Gaussian profile ([Appendix C](#)).
- The peak two-photon Rabi frequency Ω_0 at the center of excitation lasers.
- The intensity distribution of the excitation lasers.
- The laser excitation linewidth γ .
- The laser detuning Δ .
- The iteration time step dt and the total excitation duration Δt .

In the following we describe the algorithm of the simulation.

Algorithm

(a) *Initialization.* The simulation starts by drawing the positions of N ground-state atoms according to the spatial distribution of the atomic cloud. The time t is set to zero.

(b) *Calculation of transition probability for each atom.* We calculate the transition probability P_i of atom i during time interval dt , taking into account the interaction with surrounding already excited Rydberg atoms. This probability is calculated by multiplying the excitation rate Γ_i for a ground-state atom, or the de-excitation rate $\Gamma_{d,i}$ for a Rydberg atom with the time step dt . These rates are given by (4.20) and (4.21) respectively. The transition is driven with a Rabi frequency Ω_i , estimated using the peak Rabi frequency Ω_0 and the laser profiles. Similarly, we carry out the calculation for all N atoms in the cloud.

(c) *State update.* Next, we determine whether the state of the atom i is flipped or not according to P_i calculated in step (b). We draw a random real number r between 0 and 1. The atom i get excited or de-excited if $P_i > r$. This step is performed for all N atoms.

(d) *Mechanical motion.* We calculate the displacements of the Rydberg atoms during dt due to the van der Waals forces between them.

(e) *Loop of the Monte Carlo sequence.* The time t is incremented by dt . The steps (b) and (c) are repeated until t reaches the total excitation duration.

Running the simulation, it can arrive a situation in which two or more atoms have the more or less the same chance of being excited in an iteration. If these atoms are close to each other, the excitation of an atom will modify the flipping rate of the others. One

thus has to choose the time step dt small enough such that only one atom is flipped in an iteration $\sum_i \Gamma_i \times dt < 1$. Take the case of a resonant excitation of N atoms initially in the ground state as an example. The excitation rate for each of them is approximately given by $\Gamma_{\text{res}} = \Omega_0^2/\gamma$. The excitation of one atom will suppress the excitation of all other $N_b - 1$ atoms in a blockade sphere. Thus dt should be chosen at least smaller than $1/(N_b \Gamma_{\text{res}})$. As a consequence, the simulation take quite a long time to finish.

We replace the step (c) by another step (c*) described below to speed up the simulation. The idea is to create a list of candidates that can be excited. The excitation of each candidate is decided considering the states of the other candidates.

(c*) *State update.* We compare the transition probability P_i of the atom i with a real number r randomly generated between 0 and 1. If $P_i > r$ and the atom i is in the Rydberg state, it is then de-excited. If $P_i > r$ and the atom i is currently in the ground state, it is then added to a list of candidates \mathcal{L} . The criterion is applied for all N atoms. We now have a full list of candidates \mathcal{L} but not yet new Rydberg atoms. Each of candidate in the list \mathcal{L} has more or less the same chance of being excited. We successively consider each candidate ν in the list in a random order. The chance for it to be excited is given by a Lorentzian

$$w_\nu = \frac{(\gamma/2)^2}{(\gamma/2)^2 + \left(\sum_{\mu \neq \nu}^{\mathcal{L}} \frac{C_6}{R_{\nu\mu}} \delta_\mu \right)^2}, \quad (4.24)$$

where the summation runs over the list \mathcal{L} . The “Rydberg kronecker” δ_μ takes a value 0 or 1 depending on whether the candidate μ is in the ground state or Rydberg state respectively. By comparing w_ν to a random real number r_ν drawn between 0 and 1, we decide whether the candidate ν gets excited ($w_\nu > r_\nu$) or not. After updating the state of the candidate ν , we move on with the next candidate.

Equation (4.24) prevents one from exciting two candidates in the same time step at a distance shorter than a blockade radius. If the candidate ν is far from the other candidates, $w_\nu \approx 1$. It gets excited no matter what the states of the other candidates are.

The same argument applies for the de-excitation of already excited Rydberg atoms. However, the number of atoms in the Rydberg state in a blockade volume is much smaller than that of atoms in the ground state. One can choose a time step dt such that it is small enough for the probability of having two Rydberg atoms decay in an iteration to be negligible, but still large enough to speed up the program. Thus in the step (c*), it is not necessary to create a list of de-excitation candidates and follow a procedure similar to that of the excitation process.

Choice of time step

Decreasing the time step dt will yield a better precision. However, the simulation becomes time-consuming. We want to choose dt such that the simulation has a reasonable precision with an acceptable computation time. Especially, we want to test whether the step (c*) speeds up the simulation without loss of precision. We perform for each $dt = 1$ ns and $dt = 50$ ns a hundred realizations. The atomic cloud profile

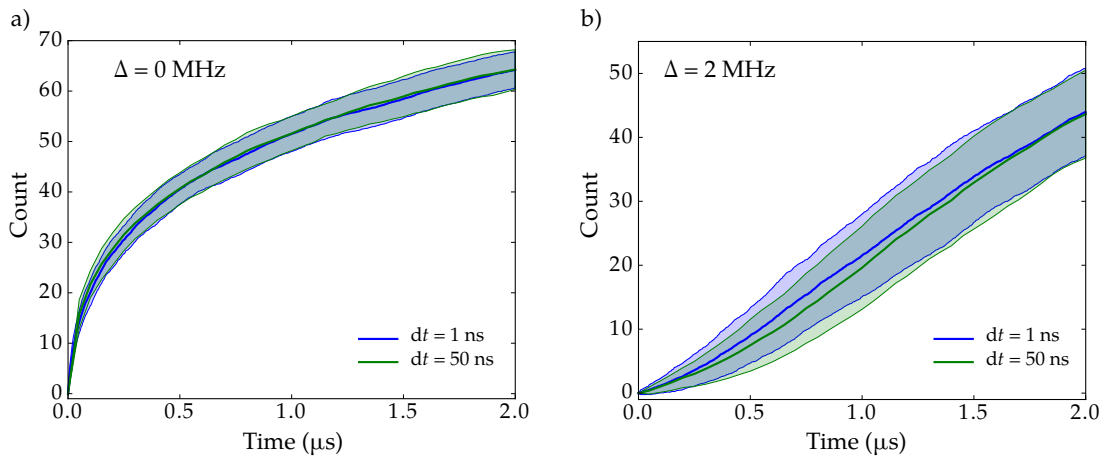


Figure 4.13 The time evolution of the Rydberg excitations averaged over 100 realizations of the Monte Carlo -rate equations model with $dt = 1$ ns (blue) and $dt = 50$ ns (green) . The shaded areas correspond to one standard deviation.

and the excitation parameters are those that allow us to reproduce the experimental data as will be discussed in the next section. [Figure 4.13](#) shows the numerical results for $\Delta = 0$ MHz and $\Delta = 2$ MHz. The discrepancy in the number of Rydberg atoms obtained with $dt = 1$ ns and $dt = 50$ ns is much smaller than the standard deviations. With $dt = 1$ ns, we observed almost no iteration with more than one candidate in a blockade sphere (< 1%). This gives us confidence to use the procedure (c*) in the model. From now on, we fix $dt = 50$ ns, and thus save a factor of about 50 on the calculation time.

4.5 Experimental data simulation

4.5.1

Optical profile

In addition to the ground-state atoms distribution and the excitation laser beam profiles, the new algorithm requires two more parameters: the Rabi frequency Ω and the dephasing rate γ . In our attempt to reproduce the experimental optical spectra, we vary Ω , starting from its measured value. However, in order to best fit the experimental data, we have to increase the temperature of the cloud with the excitation duration. This reflects a non-negligible heating effect in our measurements. Nevertheless, the heating mechanism is not clear. We thus approximate the heating effect by raising the average temperature. [Figure 4.14](#) represents the numerical results (solid lines), superposed with the experimental data (points). [Table 4.2](#) summarizes the parameters used in the simulation. We show as well the parameter used in our preliminary simulation.

Compared to [Figure 4.12](#), we now obtain a much better fit. We do not just capture the shapes of the optical spectra but more than that, within the error bar the experimental data is reproduced. This is what the simple Monte Carlo model is incapable

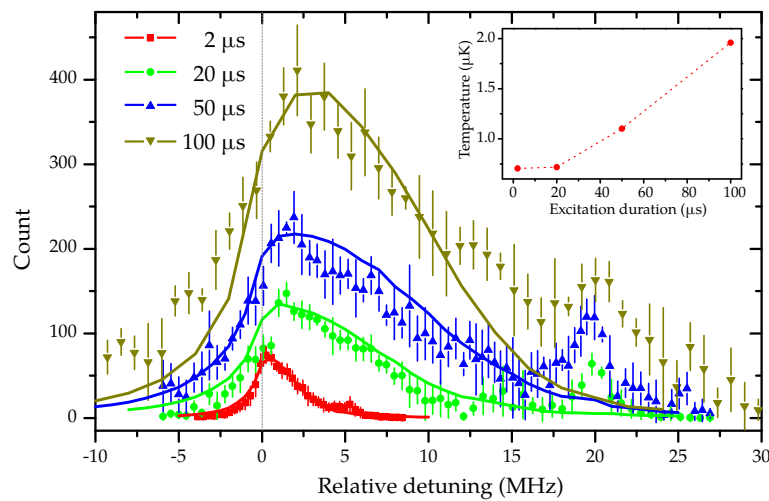


Figure 4.14 Optical spectra for different excitation durations. The dots are experimental data while the solid lines are obtained from the Monte Carlo - rate equations simulation. The error bars denote one standard deviation of the statistical error. For each excitation duration, the cloud temperature is adjusted for the best result: 0.7 μK , 0.7 μK , 1.1 μK and 1.9 μK for 2 μs , 20 μs , 50 μs and 100 μs respectively as shown in the inset.

Table 4.2 Parameters used to reproduce the experimental optical spectra.

Parameter	Exp. value	MC sim.	MC - rate equ. sim.
Trap frequency f_x (Hz)	47	47	47
Trap frequency f_y (Hz)	244	244	47
Trap frequency f_z (Hz)	262	262	262
Temperature (μK)	0.5 ± 0.15	0.5	0.7*
Number of atoms	$12\,000 \pm 2000$	10 000	12 000
Blue laser waist (μm)	22	22	22
Red laser waist (μm)	150	∞	∞
Dephasing - linewidth(kHz)	579	900	500
Peak Rabi frequency (kHz)	170	—	76*
Number of Rydberg atoms [†]	41	41	—

* Fit parameters.

† Values for $\Delta = 2$ MHz.

of. A time scale is also naturally included in the new model, instead of a “fake” time scale based on the iteration number - duration relation.

The difference between the simulation and the experimental values in the Rabi frequency can be attributed to the low transmission of the optical windows, resulting from the fog-like deposition of residual gases or grease on the cold optical surfaces. The transmission of the optical windows were measured at room temperature at which this deposition disappears. The same fogging phenomenon was observed on other cryogenic experiments [159].

The simulation also figures out a non-negligible heating effect in the experiment

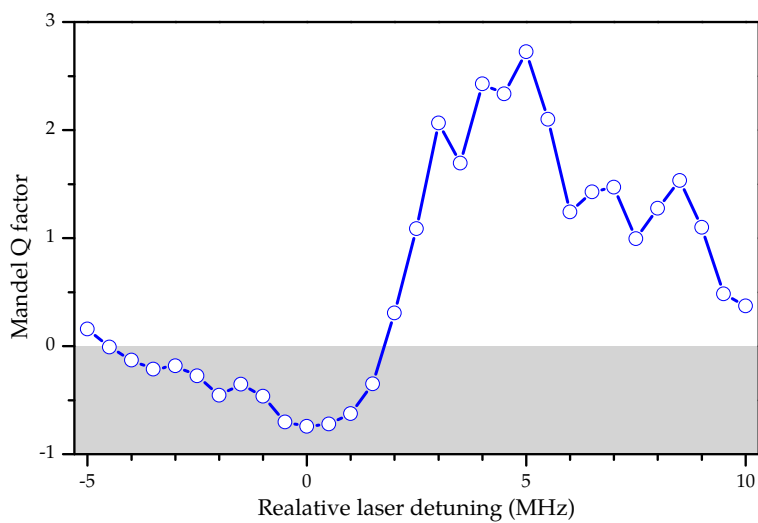


Figure 4.15 Mandel Q -factor as a function of the excitation detuning. The results are obtained using the Monte Carlo - rate equations simulation. The laser pulse is fixed to $2\ \mu\text{s}$. The gray shaded region corresponds to a sub-Poissonian statistics.

Figure 4.14. This heating may originate from technical noises such as the fluctuations of currents that lead to fluctuations of the trap center and the trap frequency. A quantitative investigation is thus necessary.

Mandel Q -factor

Another useful information that one can extract from the simulation is the fluctuation of the number of Rydberg atoms excited out of the cold atomic cloud in a fixed excitation duration. Technically we use the Mandel Q -factor to characterize whether the fluctuation obeys a Poissonian distribution. It is defined as

$$Q = \frac{\langle N_{\text{Ryd}}^2 \rangle - \langle N_{\text{Ryd}} \rangle^2}{\langle N_{\text{Ryd}} \rangle} - 1. \quad (4.25)$$

A Poissonian distribution yields $Q = 0$ while a deterministic source of Rydberg atoms gives $Q = -1$, i.e., zero variance. In between, a negative value of Q indicates a sub-Poissonian statistics. A super-Poissonian distribution corresponds to a positive Q .

With a $2\ \mu\text{s}$ excitation, the calculated value of Q is plotted in Figure 4.15 for different laser detunings. As a result of the strong Rydberg blockade at zero detuning, we enter in a deep sub-Poissonian region. On the blue side, the Q -factor quickly grows up, becoming a super-Poissonian statistics. The statistics fluctuation of one atom excitation is amplified by the facilitated development of the Rydberg aggregates. This behavior of the Q -factor characterizes the strong Rydberg interaction regime and was experimentally observed in [158]. A comparison of Figure 4.15 with experimental data would strengthen the validity of the Monte Carlo - rate equations model. Nevertheless, the measurement has not yet been performed in our particular situation.

4.5.2

Microwave spectra

Running the simulation with the parameters given in the previous section to generate Rydberg clusters after 2 μ s of excitation, and then following the same procedure as in subsection 4.3.2, we obtain Figure 4.16 and 4.17 for the microwave spectra. A very good agreement between the simulation and the experimental data is observed.

Although our first preliminary numerical results with a very simple Monte Carlo

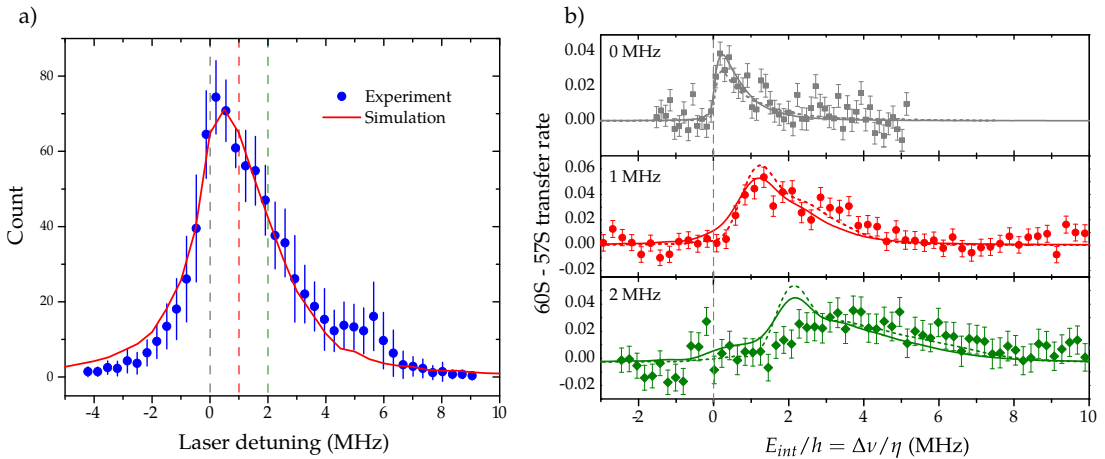


Figure 4.16 Monte Carlo - rate equations simulation results (solid lines) superposed with the experimental data (points). a) Optical profile of 2 μ s excitation duration and b) the microwave spectra probing the interaction energy. The dashed lines in a) indicate the corresponding laser detuning for the microwave spectra in b). The dashed line in b) represents the zero interaction point. The error bars indicate one standard deviation in a) and one standard error of the mean in b).

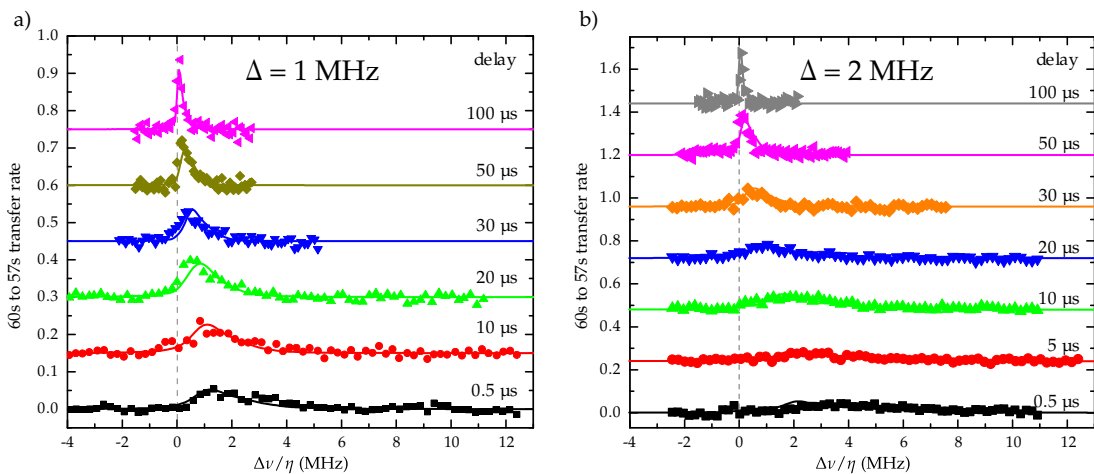


Figure 4.17 Monte Carlo - rate equations simulation results (solid lines) superposed with the experimental data (points) for the expansion of a repulsive Rydberg ensemble. The laser detuning is set to a) 1 MHz and b) 2 MHz.

model cannot explain the optical profile, it can reproduce quite well the microwave spectra. This confirms the fact that Rydberg clusters are developed from one or several initial “seeds” by sequential one-photon process.

The mismatch between the numerical result and the experimental data in [Figure 4.16](#) for $\Delta = 2$ MHz is interpreted as an incorrect positioning of the laser detuning Δ when taking the data for this curve. The same measurement performed on another cloud with a slightly different geometry yield a good agreement with the numerical calculation. Taking again the data at this detuning would confirm whether there was a mistake or another mechanism underlining.

4.5.3

Spatial distribution of Rydberg atoms

The simulation allow us to get informations that are difficult to access experimentally. Rydberg atoms are hard to image optically and the spatial distribution of the Rydberg cluster, for us at least, cannot be directly measured. Here, using the simulations, we extract the spatial distribution of the generated Rydberg cluster. The results are represented in [Figure 4.18](#) for zero detuning and in [Figure 4.19](#) for 2 MHz detuning. The Rydberg blockade effect forces to search for Rydberg atoms at the edge of the cloud, resulting in a larger Rydberg cluster as compared to the initial ground atomic cloud. Blue detuning the laser somehow compacts the Rydberg cluster. These results are consistent with those observed by microwave spectra.

More interestingly, [Figure 4.20](#) plots the temporal evolution of the transverse and the longitudinal sizes during the free expansion of a Rydberg cluster. Comparing to the “expansion” of a pair of atoms whose initial energy is Δ , the peak van der Waals interaction energy of the Rydberg cluster (the dashed line), one finds that the dynamics of the free expansion is slowed down. A bulk atom has to wait for the edge atoms to get away before it can move. Moreover, the expansion is found to be anisotropic. The microwave spectra reveal the hydrodynamics expansion of a Rydberg cluster in a regime of strong van der Waals interactions.

4.5.4

Discussion on the validity of the Monte Carlo – rate equations model

The Monte Carlo – rate equations simulation includes the spatial distribution of the cold atomic cloud, the laser intensity profiles, the finite lifetime of the Rydberg state, the mechanical repulsion between the Rydberg atoms and more importantly the dynamics of the excitation. However, there are several effects that this model does not take into account.

First, the model describes only a sequential one-photon excitation process. The resonant excitation of an atom pair can also be achieved by simultaneous absorption of two photons[¶]. [Figure 4.21](#) illustrates the two excitation processes. If $\Delta \gg \gamma$, one

[¶]For the $5S - 60S$ transition, this corresponds to the absorption of four photons: two red and two blue photons.

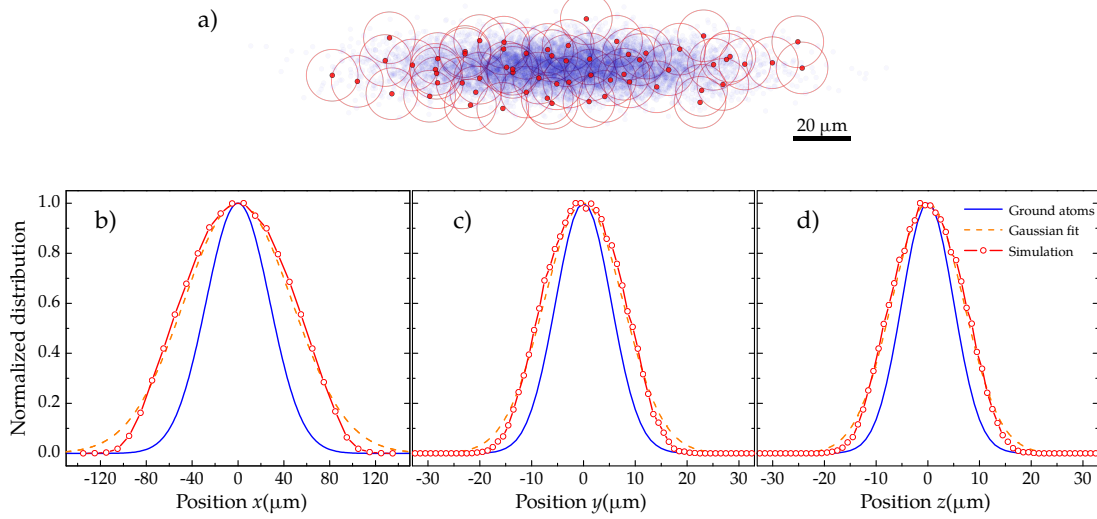


Figure 4.18 Spatial distribution of the Rydberg ensemble for 0 MHz laser detuning. a) A realization of the simulation. The blue dots are the ground state atoms and the red dots are the Rydberg atoms. The radius of the circles centered on each Rydberg atom is equal to the blockade radius R_b . b)-d) Statistical spatial distribution of the Rydberg ensemble along the x , y and z respectively. A discrepancy from a Gaussian fit (dashed lines) is observed at the lower edges and is attributed to the Rydberg interactions. The distributions of the ground state atoms are also shown in blue solid lines.

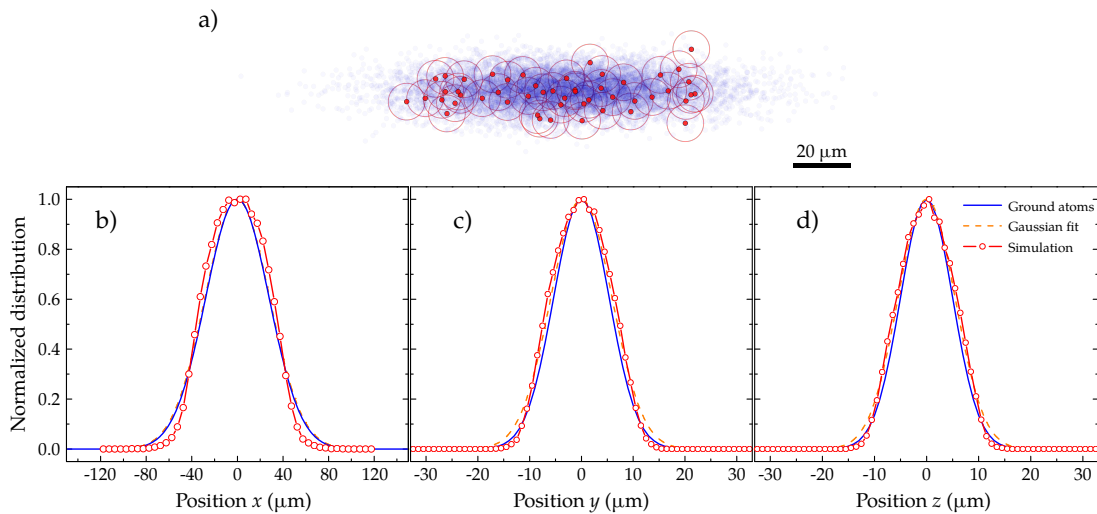


Figure 4.19 The same as Figure 4.18 for 2 MHz laser detuning.

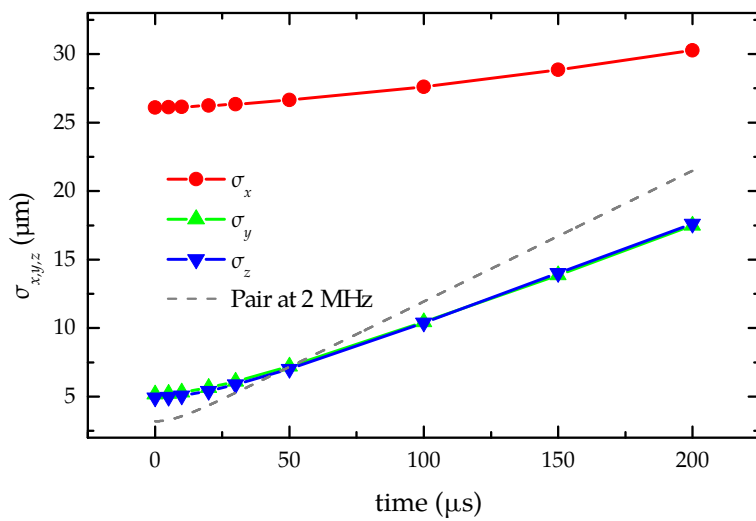


Figure 4.20 The statistical widths of the Rydberg ensemble as functions of the expansion time. Shown in dashed line is the distance of a pair of Rydberg atoms initially placed at $6.4 \mu\text{m}$, corresponding to an interaction energy of 2 MHz.

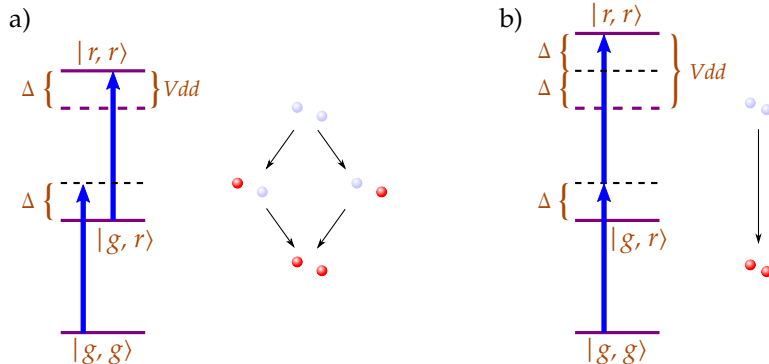


Figure 4.21 Illustration by energy diagrams of the facilitated excitation where the laser detuning compensates for the van der Waals shift. The excitation can be either a) a sequential single-photon process or b) a simultaneous multi-photon process. The blue spheres stand for ground state atoms and the red spheres for Rydberg atoms.

find the rate to simultaneously excite a pair of atoms

$$\Gamma^{(2)} = \frac{(\Omega^2/2\Delta)^2}{2\gamma} = \Gamma \frac{\Omega^2}{2\gamma^2} \left[1 + \left(\frac{\gamma}{2\Delta} \right)^2 \right] \quad (4.26)$$

by adiabatically eliminating the intermediate one-excitation state. The strong dephasing assumption $\gamma \gg \Omega$ leads to $\Gamma^{(2)} \ll \Gamma$. One can generalize for the simultaneous m -photon excitation $\Gamma^{(m)} \ll \dots \ll \Gamma^{(2)} \ll \Gamma$. Thus, the sequential one-photon excitation is the dominant process.

Second, this is a model of an incoherent excitation process. The solution of the rate equations is valid if $t \gg \gamma^{-1}$ and $\gamma \gg \Omega$. From Table 4.2, $\gamma \approx 6.5\Omega$. The latter condition is more or less satisfied. The former requires that $t \gg 2 \mu\text{s}$. The model can

not reproduce the coherent evolution of the excitation of an atom at a time shorter than this value. However, if there are many atoms inside a blockade volume, the collective state decays faster than γ^{-1} . This explains why we obtain a good fit to the optical spectrum with 2 μ s excitation duration.

Summary

Under the strong Rydberg blockade regime of a dense atomic cloud, the optical spectra are broadened to the blue as a result of the facilitated excitation, in which Rydberg atoms are resonantly excited at distances defined by the laser detuning. The repulsive interaction energy acquired during the excitation causes the Rydberg cloud to expand. The van der Waals interaction energy of the Rydberg ensemble is directly revealed via microwave spectra.

We have developed a simple Monte Carlo simulation that allows us to explain the measured microwave spectra. Better results were obtained with the Monte Carlo - rate equations simulation, where the dynamics of the excitation is included. Both optical and microwave spectra were reproduced with a reasonable agreement. This encourages us in using this model to explore new routes towards quantum simulation of many-body systems.

Perspective

We aimed at performing quantum transport simulations with a 1D chain of Rydberg atoms. The first requirement is to prepare a regular Rydberg chain. Our microwave tool probing the interaction energy can reveal information on the regularity of a Rydberg chain.

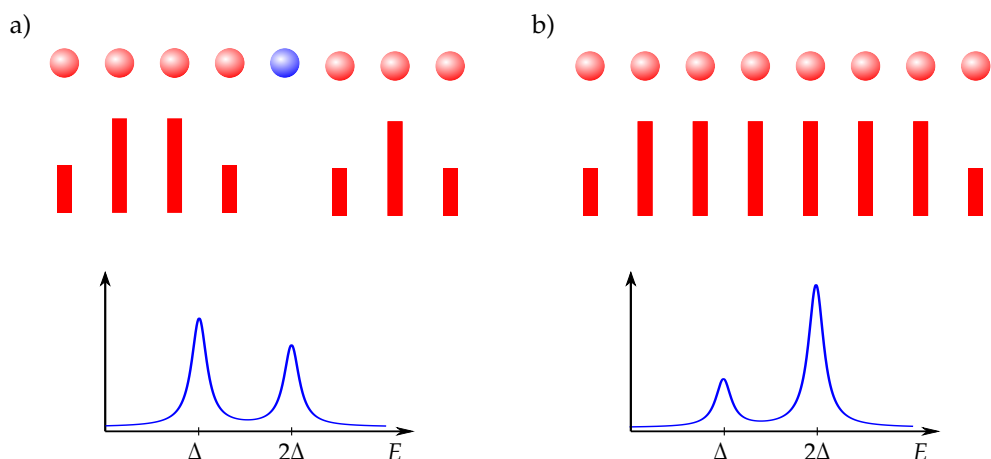


Figure 4.22 Chain regularity probed by microwave spectroscopy. Red spheres represent Rydberg atoms while the blue spheres represent a missing site (gap). The height of the red bar under a atom indicates the relative interaction energy of the atom. The graphs at the bottom show the expected microwave spectra.

The principle of the technique is depicted in [Figure 4.22](#). If the van der Waals interaction energy of two adjacent atoms is Δ , then each “bulk” atom has twice this

energy due to the contributions from its two neighbors. As a result, one expects two peaks in the microwave spectrum, one at Δ corresponding to atoms at the ends, and another at 2Δ for the “bulk” atoms. The ratio of the peak height (or area) is equal to the number of “bulk” atoms over the number of atoms at the ends. If some sites are empty forming N_s sub-chains, the ratio is found to be $(N_R - 2N_s)/(2N_s)$, where N_R is the total Rydberg atoms detected by the channeltron. One thus immediately identifies whether a gap exists or not from the microwave spectra. Moreover, the width of each microwave peak gives the interaction energy dispersion, which maps into the dispersion of the inter-atomic distance. In other words, it represents the disorder of the chain.

But, how to prepare a regular Rydberg chain?. An idea is to make use of the facilitated excitation. By blue detuning the excitation laser, one expects to control the distance between Rydberg atoms excited out of a 1D ground-state atomic cloud and resonantly develop a chain from an initial “seed”.

However, for the same atomic density, the number of atoms in a facilitated volume is much smaller for a 1D than a 3D cloud. Thus, the facilitated excitation hardly occurs. One would increase the number of atoms in the 1D cloud. Nevertheless, by doing so, one also increases the scattering of the Rydberg electron by the ground-state atoms as discussed in [subsection 4.1.3](#). As a result, the energy level is lowered, and thus, destroying the facilitated regime.

A more efficient method to prepare a regular Rydberg chain is turning to *laser-trapped-circular-atoms*, which will be the central part of our proposal for quantum simulation.

III.

Quantum simulation with circular Rydberg atoms – A proposal

Objectives

The phase transitions of quantum magnetic systems are of long-lasting interest, both from the experimental and theoretical points of view. Among many models used in the study of these problems is the anisotropic Heisenberg “XXZ” model. It describes at a microscopic level an anisotropic anti-ferromagnetic spin-1/2 chain in a magnetic field. The spin coupling along the longitudinal direction J_Z differs from that along the transverse direction $J_X = J_Y = J$. The Hamiltonian of the system is expressed in terms of Pauli matrices as

$$H_{XXZ} = J \left[\sum_j \left(\sigma_j^X \sigma_{j+1}^X + \sigma_j^Y \sigma_{j+1}^Y + \Delta \sigma_j^Z \sigma_{j+1}^Z \right) - h_Z \sum_j \sigma_j^Z - h_X \sum_j \sigma_j^X \right], \quad (\text{III})$$

where σ^i is the spin operator along the i direction. The dimensionless parameters h_Z and h_X represent the interaction with the longitudinal and transversal magnetic fields, respectively. The anisotropy parameter Δ is defined as J_Z/J .

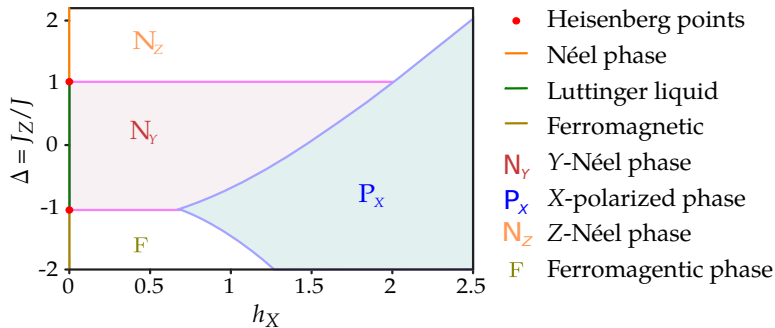


Figure III.1 Qualitative ground-state phase diagram of the model when $\Delta = 0$. Figure extracted from [160].

The magnetic properties of the system depend on the direction of the applied magnetic field. In the absence of a transverse field, the model can be exactly solved by the Bethe ansatz [161]. A transverse field, however, breaks the symmetry and makes the system behave differently. The dynamics of the system, for instance, quenches, are difficult to study numerically, since it involves a Hilbert space of very large dimension.

The ground state has been studied theoretically using various approximation methods [162–164]. Figure III.1 quantitatively sketches the phase diagram in the presence of

a transverse field only, in the thermodynamic limit [165–167]. The horizontal axis represents the dimensionless transverse field h_X . The system features at least two gapped Néel phases with a staggered order parameter (N_Y and N_Z), a ferromagnetic domain (F), a gapless Luttinger liquid phase for $|J_Z| < J$ and $h_X = 0$. One can explore the phase transition in this diagram by adiabatic variation of the anisotropy parameters and/or the transverse field, starting from an easily accessed ground state, for instance in the P_X region where all spins polarized along the X direction.

In order to simulate this “XXZ” Hamiltonian, a quantum simulator has to satisfy several requirements. First, the spins have to be long-lived, which allows for thousands of typical exchange times to happen. This is required for an adiabatic transition from one phase to another. Second, a defect-free, regular chain of spins is necessary. Third, one has to be able to apply a “magnetic field” on the spin chain and to tune the interaction between the spins. And last but not least, one needs a scheme to read-out the final state of the system.

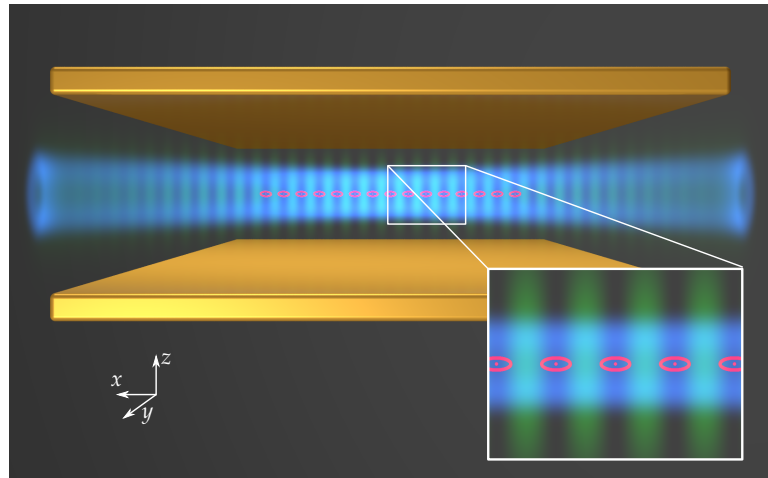


Figure III.2 Artist’s view of the laser-trapped circular Rydberg atom chain inside a spontaneous- emission-inhibiting capacitor. The circular atoms (red) are placed at the minimum intensity of a CO₂ laser optical lattice (green) superposed with a hollow Laguerre-Gaussian beam (blue).

We propose hereby a scheme to realize such a quantum simulator by turning to *laser-trapped circular atoms* as depicted in [Figure III.2](#). The key ingredient of the proposal is an ensemble of extremely long-lived circular Rydberg atoms laser-trapped inside a spontaneous-emission inhibiting capacitor. A chain of tens of atoms can be deterministically prepared. The interaction between the atoms allows us to realize the “XXZ” Hamiltonian. Moreover, this Hamiltonian is tunable over a wide range by microwave dressing and electric field adjustment. Finally, the atoms can be individually state-selectively detected. By overcoming the bottlenecks of other systems, including the quantum simulation with low- l Rydberg atoms, this new approach would allow us to address a wide range of spin networks problems: from the quantum transport over a 1D chain to the phase transitions of the “XXZ” spin model, and even problems beyond the grasp of classical computation methods.

In [section 5.1](#), we show that the spontaneous decay can be efficiently inhibited, by

placing the atoms between the two parallel plane plates of a capacitor, with a spacing below the cut-off for the radiated wavelength ([Figure III.2](#)). In a cryogenic environment below 1 K, circular states are preserved for durations in the minute range, leading to a trapping time of a few seconds without a single loss for a chain with tens of atoms.

In [section 5.2](#), we describe the trapping of circular atoms, using the ponderomotive force acting on the nearly free Rydberg electron. For low- l Rydberg states, photo-ionization in the laser field strongly reduces the lifetime. However, this effect drops exponentially with l , down to negligible values for circular states. A 1 μm -wavelength Laguerre-Gaussian beam in combination with a co-propagating 10 μm -wavelength (CO₂ laser) standing wave forms a 1D lattice, in which the circular atoms are trapped in intensity minima, regularly separated by 5 μm ([Figure III.2](#)). Trapping of circular atoms will be discussed in [section 5.2](#).

In [section 5.3](#), we study the interaction between two circular atoms, and then in [section 5.4](#), we derive the spin XXZ Hamiltonian. By encoding the spin state on the 48C and 50C circular levels, the van der Waals interaction between the atoms is in a good range to realize a spin XXZ Hamiltonian. The spin coupling is directly related to the direct and the exchange dipole-dipole interactions. Moreover, the direct interaction between the circular atoms depends strongly on the electric field while the exchange interaction does not. Their relative strength is thus tunable through the electric field. The “transverse magnetic field” is obtained via a resonant microwave dressing, which is under full experimental control. As a result, the spin Hamiltonian, can be tuned over the whole range of the phase diagram in [Figure III.1](#), by merely varying the dressing strength and the static electric field. This is a unique feature of quantum simulation with trapped circular atoms.

In [section 5.5](#), we propose an innovative approach to the deterministic preparation of a vacancy-free, regular chain with more than 40 atoms. It is a variant of evaporative cooling, successively removing atoms, one by one, out of a chain in a controlled way. The mechanism is based on the repulsive van der Waals interactions, that strongly push on the atoms at the two ends of a compressed chain.

In [section 5.6](#) and [section 5.7](#), we respectively represent methods to initialize a spin chain and to detect the spin states individually. Finally, we discuss some decoherence effects that present in our proposed system.

Principles of the quantum simulator

5

5.1

The quest for long-lived circular atoms

A circular atom, as discussed in [section 1.3](#), can decay only toward the next lower circular state, emitting a σ^+ -polarized photon. In the presence of blackbody radiation, the circular state can absorb a photon and get excited to a higher Rydberg state. The former process can be efficiently inhibited by means of a capacitor, while the latter can be suppressed by going to a cryogenic environment. Collisions with the residual background gas can also reduce the lifetime of a circular atom. We show here that we can manage to reach a 100 s lifetime.

5.1.1

Inhibition of spontaneous emission

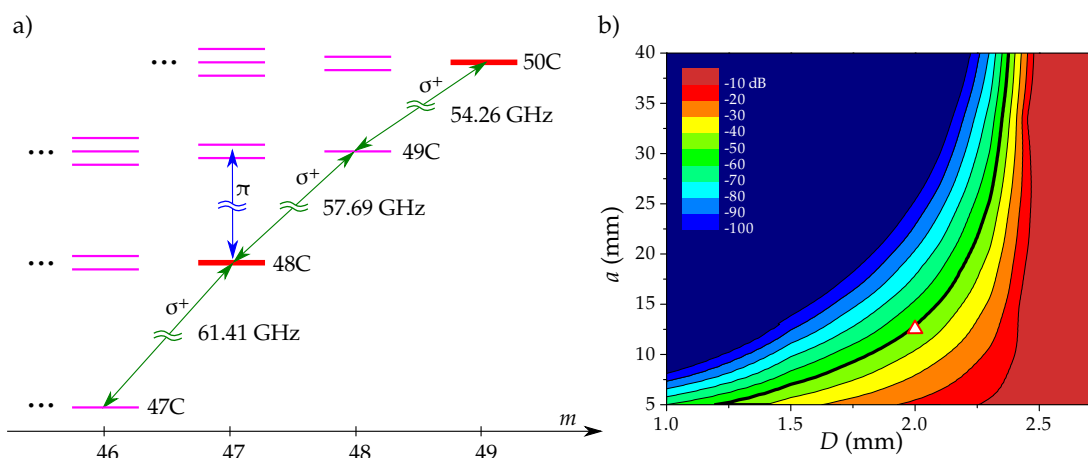


Figure 5.1 a) Level scheme. The horizontal axis corresponds to the magnetic quantum number m . b) Γ/Γ_{48} (log scale) as a function of the capacitor geometry: spacing D and size a . The thick solid black line indicates a 40 dB inhibition. The open red triangle shows the chosen operation point.

Despite the fact that circular atoms are long-lived, the intrinsic spontaneous emission lifetime (25 ms for the 48C circular state) limits the duration over which one can run quantum simulations with a large number of atoms. A chain of 40 circular atoms will decay in less than 650 μ s, corresponding to about 45 exchange times only. However, spontaneous emission can be inhibited using the following method.

We place the circular chain in between a plane-parallel capacitor as depicted in [Figure III.2](#). We also apply an electric field F between the two capacitor plates. This electric field defines the quantization axis Oz , stabilizing the circular orbit plane [168] parallel to the capacitor plates. A circular state nC decays by emitting a σ^+ polarized photon w.r.t to the quantization axis Oz ([Figure 5.1a](#)). The emitted electric field is thus parallel to the capacitor plates. As the electric field must cancel at the surface of each plate, in an ideal infinitely large capacitor, there should be no emission mode in which the circular state can decay, as long as the separation D of the two plates is smaller than half the corresponding wavelength: $D < \lambda/2 = 2.5$ mm for the 48C. The spontaneous emission rate thus drops to zero [169]. Using the same principle, Klepner *et. al.* experimentally observed that the natural lifetime of a circular state is enhanced by a factor of more than 20 compared to that in free space [170]. The experiment was performed in 1985.

In order to determine the capacitor geometry, we have performed a classical simulation with a square capacitor made of gold, cooled to 1 K. Each plate is a square with size a . We model a circular atom by an antenna (dipole) placed inside the capacitor, and calculate the radiated powers with and without the presence of the capacitor. The ratio of the two powers directly provides us the spontaneous-emission inhibition factor, i.e., the ratio of the residual spontaneous emission rate Γ over the natural spontaneous emission rate Γ_{nC} . The calculation is carried out using the CST-Studio suite. The result for 48C state is represented in [Figure 5.1b](#).

We choose to use a capacitor made with two square 13 mm-wide plates separated by 2 mm (open red triangle in [Figure 5.1b](#)). A suppression better than 50 dB is achieved. It corresponds to a single atom lifetime of 2500 s. Note that the inhibition is even stronger for the 50C state since the emission wavelength is larger (5.5 mm). This geometry, as will be clear later, allows a large enough optical access for the trapping laser beams.

5.1.2

Suppression of blackbody radiation absorption

While a σ -polarized field is efficiently inhibited by the capacitor, a π -polarized field is not inhibited due to different boundary conditions. On the contrary, the capacitor structure leads to a higher mode density, resulting in a slight enhancement in the stimulated absorption rate[169]. At a finite temperature, blackbody radiation induces upwards transition from a nC circular state into the elliptical states of the $n + p$ manifolds ([Figure 5.1a](#)). The dipole matrix element on these transitions drops rapidly with p , as the radial overlap of the wavefunctions decreases. We thus consider only the $p = 1$ case. In free space, the stimulated absorption rate is given by (1.30). At a temperature $T = 0.4$ K (the base temperature of a standard ${}^3\text{He}$ cryostat), this corresponds to a lifetime of 1260 s for the 48C and ~ 720 s for the 50C state. Taking into account the

decay rate enhancement due to the capacitor structure, we estimate an enhancement factor of less than 2 in the absorption rate[169]. We thus still reach lifetimes longer than 350 s at 0.4 K.

5.1.3

Background gas collisions

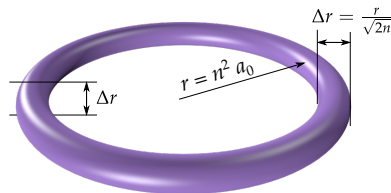


Figure 5.2 Toroidal orbital of a circular atom.

Another effect that may conspire to reduce the circular state lifetime is that of the collisions with the background gas. The main residual gas in a cryogenic setup is Helium. De Prunelle calculated the state-transfer cross-section $\sigma_{c,20}$ to be about 3200 atomic unit for the $n = 20$ circular state [171]. The collision mainly results from the interaction between the Helium atoms and the nearly free Rydberg electron. Assuming that $\sigma_{c,n}$ is proportional to the volume of the orbital — a torus of radius $r = n^2 a_0$, and thickness $\Delta r = n^2 a_0 / \sqrt{2n}$ (Figure 5.2) — the cross section scales as n^5 . We thus, estimate $\sigma_{c,50}$ for $n = 50$ to be $313\,000 a_0^2$. This value is a bit smaller for $n = 48$, and thus less dramatic. The circular atom is lost after a time $\tau_{c,50} = 1 / (\sigma_{c,50} n_{He} v_{He})$, where n_{He} and v_{He} are the density and velocity of Helium atoms at the cryogenic temperature 0.4 K. For a pressure smaller than 10^{-15} mbar, which is realistic at cryogenic temperatures at about 0.4 K [137, 172], $\tau_{c,50}$ exceeds 1200 s.

By means of spontaneous-emission inhibition and suppression of blackbody radiation absorption at a cryogenic temperature $T = 0.4$ K and ultra-high-vacuum $\sim 10^{-15}$ mbar, a circular atom can live more than 250 s. As a result, a chain with 40 atoms should last longer than 10 s without loss of a single atom. We could drive up to 1 000 000 typical exchange periods (~ 100 kHz) with just a single chain. The study of slow dynamics of a 1D spin chain would be made possible.

5.2

Trapping of circular atoms

5.2.1

Ponderomotive potential

A method for trapping circular atoms in an electric field gradient has been proposed in our group in 2004 [169, 173]. In this scheme, the transition line is broadened due to the Stark effect. In order to preserve the coherence between two circular states, one can

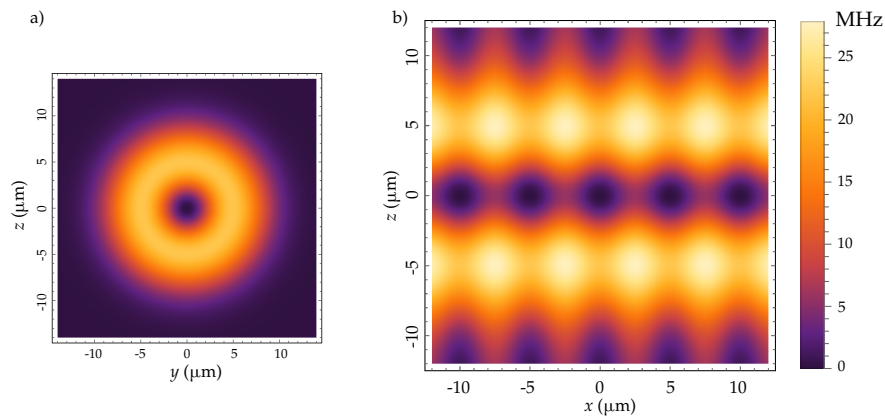


Figure 5.3 Laser trapping ponderomotive potential. a) Transverse profile of a Laguerre-Gaussian beam of $7 \mu\text{m}$ waist and 2 W in power. b) The total trapping potential is produced by superposing a Laguerre-Gauss beam with a standing wave CO₂ laser optical lattice.

microwave dress one of them on a transition to an auxiliary elliptical state such that the differential Stark shift of the two circular states is canceled. Extending this complex scheme to an array of circular atoms is not yet clear and requires a good control of the Stark effect.

We propose here, an alternative method to trap circular atoms, based on the ponderomotive force acting on the nearly free Rydberg electron. The interaction energy is given by

$$\mathcal{E} = \frac{e^2 E_L^2}{4m_e \omega_L^2}, \quad (5.1)$$

where ω_L is the laser angular frequency, and m_e is the electron mass. Note that the atomic core also experiences a similar force. Nevertheless, it is several thousand times heavier than the electron, and thus the corresponding force is negligible.

Knowing that the laser intensity is related to the electric field amplitude by

$$I = \frac{1}{2} \epsilon_0 c E_L^2, \quad (5.2)$$

the ponderomotive potential can be expressed in terms of the laser intensity as

$$\mathcal{E} = \frac{e^2 I}{2m_e \epsilon_0 c \omega_L^2}, \quad (5.3)$$

that is, proportional to the laser intensity. Acting on the Rydberg electron, this potential effectively acts on the atom as a whole. As a result, the atom seeks low intensity regions.

The transverse profile of a Laguerre-Gaussian laser beam is circularly symmetric. It is expressed in cylindrical coordinates (r, θ, z) , using a generalized Laguerre polynomial $L_p^l(2r^2/w(z)^2)$, where $w(z)$ is the beam radius at z . Accordingly, a Laguerre-Gaussian beam is called in the mode (l, p) . A Laguerre-Gaussian beam mode $(0, 0)$, for

instance, corresponds to the well known Gaussian beam. The next mode, a Laguerre-Gaussian beam mode $(0, 1)$ is a hollow beam. Its transverse profile takes a donut shape, exhibiting a zero of intensity at the beam center as depicted in [Figure 5.3a](#). Such a long tube of light provides a confinement of the atoms in a 1D geometry.

More specifically, we create a Laguerre-Gaussian beam mode $(0, 1)$ of $7\text{ }\mu\text{m}$ -waist using a $1\text{ }\mu\text{m}$ -wavelength laser*. This beam aligns the atoms along the Ox direction, between the two capacitor plates as shown in [Figure III.2](#). The transverse ponderomotive potential provided by the Laguerre-Gaussian beam with a 2 W-power is plotted in [Figure 5.3a](#). The transverse trapping frequencies are $\omega_y = \omega_z = 2\pi \times 24\text{ kHz}$. The beam diameter at the edges of the capacitor is about $630\text{ }\mu\text{m}$. The clipping due to the capacitor (2 mm spacing) is thus negligible ($\sim 10^{-8}\%$), avoiding power dissipation.

We also send two counter-propagating $10\text{ }\mu\text{m}$ -wavelength CO_2 laser beams to form an optical lattice, superposed with the Laguerre-Gaussian beam ([Figure III.2](#)). Atoms are trapped at the intensity minima of the standing wave. An inter-site spacing of $5\text{ }\mu\text{m}$ is achieved. The beam waist and the power are adjusted so that we obtain an isotropic trapping potential in three dimensions. A waist of $80\text{ }\mu\text{m}$ and a power of 70 mW provide the required trapping frequency $\omega_x = 2\pi \times 24\text{ kHz}$. The resulting trapping potential is represented in [Figure 5.3b](#). The beam diameter at the edges of the capacitor is $570\text{ }\mu\text{m}$. The beams are thus negligibly clipped by the capacitor plates.

5.2.2

Photo-ionization by trapping lasers

One might worry about the photo-ionization effect due to the trapping lasers which has been found to be prohibitive for low angular momentum Rydberg states [[120](#), [174](#)]. From [[175](#)], an analytical hydrogenic expression for the photo-ionization cross-section σ_{PI} of a $|nl\rangle$ Rydberg state is

$$\sigma_{PI} = \frac{4l^4}{9cn^3\omega_L} \left[K_{2/3}^2\left(\frac{\omega_L l^3}{3}\right) + K_{1/3}^2\left(\frac{\omega_L l^3}{3}\right) \right], \quad (5.4)$$

where $K_\nu(x)$ is the modified Bessel function of the second kind, which vanishes rapidly when increasing x . Here, ω_L is written in atomic units. For the case of circular atoms, the loss of atoms due to the photo-ionization is predicted to be negligible ($\sigma_{PI} \sim 10^{-137} a_0^2$ for 48C and $10^{-155} a_0^2$ for 50C) as compared to that due to the background gas collision discussed previously.

We can think of the problem in terms of the wavefunction overlap. A photon couples the Rydberg electron to the continuum. If the photon energy is much larger than the Rydberg binding energy, we can approximate the continuum wavefunction by a plane wave of wave vector \mathbf{k}_c . The photo-ionization cross-section can be expressed in terms of the transition matrix element as

$$\sigma_{PI} \propto \left| \langle \text{Ryd} | e^{-i\mathbf{k}_p \mathbf{r}} | e^{-i\mathbf{k}_c \mathbf{r}} \rangle \right|^2, \quad (5.5)$$

where $|\text{Ryd}\rangle$ is the Rydberg wavefunction and \mathbf{k}_p is the wave vector of the laser. The

* A Laguerre-Gaussian beam mode $(0,1)$ is obtained by sending a Gaussian beam through a vortex lens or a spatial light modulator (SLM), appropriately modifying the spatial phase of the Gaussian beam.

wavelength of the continuum state is about a few Bohr radii while that of the laser is about 1 μm. As a result, $e^{-i\mathbf{k}_p \cdot \mathbf{r}}$ is almost constant. With this dipole approximation, the above equation simplifies to

$$\sigma_{PI} \propto |\langle \text{Ryd} | e^{-i\mathbf{k}_c \cdot \mathbf{r}} \rangle|^2, \quad (5.6)$$

which is the wavefunction overlap between the Rydberg state and the continuum. The wavefunction of high- l Rydberg state varies slowly with r (c.f. Figure 1.1 for circular state) while that of the continuum quickly oscillates. The mismatch of the two wavefunctions thus, makes $\sigma_{PI} \approx 0$; the photo-ionization is negligibly small.

On the contrary, the wavefunction of low- l Rydberg state oscillates much faster when approaching the atomic core (c.f. Figure 1.4), becoming comparable to the wavefunction of the continuum. As a result, the photo-ionization cross-section for low- l Rydberg state is significantly larger. This argument agrees well with the observations in [174] and [120]. In the former, the authors calculated the photo-ionization cross-section and find it to exponentially drop with $1 \leq l \leq 7$, while in the latter, an enhancement of the photo-ionization rate is experimentally measured when shining more light close to the nucleus (for $l = 2$).

5.3

Two interacting circular atoms in free space

The simulation of the Hamiltonian in (III) is based on the dipole-dipole interaction between circular Rydberg atoms. The theoretical discussion for two interacting atoms in low angular momentum Rydberg states, given in chapter 2, can be generalized and extended to circular states. In this section, we will go into details for special cases that are relevant to our proposal. We will consider the scaling laws with n that will help us to pick up appropriate states to realize the quantum simulator.

As discussed previously, an electric field \mathbf{F} across the spontaneous-emission inhibition capacitor is necessary to maintain the circular orbit parallel to the capacitor plates. This thus sets up a configuration in which the inter-atomic axis Ox , i.e., the trapping laser axis, is perpendicular to the electric field \mathbf{F} (Figure III.2).

Before going into details, it is useful to remind here the energy of a circular state $|nC\rangle$ and of the two next elliptical states $|nE\rangle$ and $|nE^-\rangle$, taking into account the Stark shifts

$$\begin{aligned} E_{nC} &= -\frac{1}{2n^2} - \frac{1}{16}n^4(8n^2 + 18n + 10)F^2 \\ &= \frac{1}{2n^2} + \alpha_{nC}F^2, \end{aligned} \quad (5.7)$$

$$\begin{aligned} E_{nE^\pm} &= -\frac{1}{2n^2} \pm \frac{3n}{2}F - \frac{1}{16}n^4(8n^2 + 36n - 20)F^2 \\ &= -\frac{1}{2n^2} \pm \frac{3n}{2}F + \alpha_{nE}F^2. \end{aligned} \quad (5.8)$$

In the above equations, we have introduced the coefficients α_{nC} and α_{nE} for conve-

nience. We denote also the $m = n - 3$ elliptical states in the same manifold as that of a circular state $|nC\rangle$

$$\begin{aligned} |nEE^+\rangle &= |n, k = +2, m = n - 3\rangle \\ |nEE^0\rangle &= |n, k = 0, m = n - 3\rangle \\ |nEE^-\rangle &= |n, k = -2, m = n - 3\rangle . \end{aligned} \quad (5.9)$$

The level scheme is depicted in Figure 5.4a (c.f Figure 1.6). Table 5.1 summarizes the scaling laws of the dipole matrix element coupling $|nC\rangle$ and a nearby level.

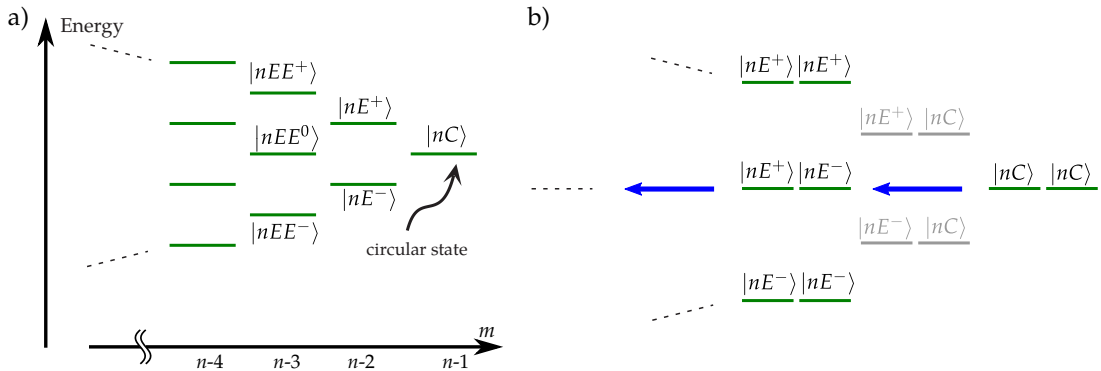


Figure 5.4 a) Level scheme for high- l states in an electric field. b) Level scheme for atomic pair states. The $|nC; nC\rangle$ and $|nE^+; nE^-\rangle$ are quasi-degenerate. The dipole-dipole interaction thus, mixes the circular state with non-circular states. Pair states shown in gray are not coupled to the $|nC; nC\rangle$ state.

Table 5.1 Scaling laws for dipole coupling between a circular state $|nC\rangle$ to a nearby state. The last column shows the corresponding dipole coupling d_{50} for $n = 50$.

$ nC\rangle \leftrightarrow$	Transition	Scaling law	d_{50} ($e.a_0$)
$ nE^+\rangle$	σ^-	$n^{3/2}$	372
$ nE^-\rangle$	σ^+	$n^{3/2}$	372
$ (n \pm 1)C\rangle$	σ^+	n^2	1776
$ (n+1)E^+\rangle$	π	$n^{3/2}$	177
$ (n+1)E^-\rangle$	π	$n^{3/2}$	177
$ (n+1)EE^+\rangle$	σ^-	n^2	7
$ (n+1)EE^0\rangle$	σ^-	n^2	26
$ (n+1)EE^-\rangle$	σ^-	n^2	7

The equation (2.2) gives the dipole-dipole interaction Hamiltonian when choosing a quantization axis along the inter-atomic axis. The interaction preserves the total magnetic quantum number. However, the presence of a transverse electric field breaks the cylindrical symmetry of the system. With a typical field of a few V/cm, the Stark effect is, in general, dominant. We thus choose the quantization axis along F , i.e., along

the Oz direction in [Figure III.2](#). The dipole-dipole interaction Hamiltonian reads

$$V_{dd} = \frac{e^2 r_1 r_2}{3\epsilon_0 R^3} \left[Y_1^0 Y_1^0 + \frac{1}{2}(Y_1^{+1} Y_1^{-1} + Y_1^{-1} Y_1^{+1}) - \frac{3}{2}(Y_1^{+1} Y_1^{+1} + Y_1^{-1} Y_1^{-1}) \right], \quad (5.10)$$

where the notations are the same as those in [\(2.2\)](#). The two last terms indicate that the total magnetic quantum number is no longer preserved. [Figure 5.4b](#) extends the level scheme of single atomic state to pair states. The circular pair state $|nC; nC\rangle$ is quasi-resonantly coupled by the dipole-dipole interaction to the elliptical pair state $|nE^+; nE^-\rangle$, which is in turn coupled to the pair state $|nEE^+; nEE^-\rangle$, and so on (blue arrows in [Figure 5.4b](#)). The circular state is thus, strongly mixed with non-circular states.

The structure of the capacitor can efficiently inhibit only the emission of a σ^\pm -polarized photon of wavelength larger than twice the capacitor spacing. It cannot suppress the decay of an elliptical state towards the next lower manifold by emitting a π -polarized photon, not to mention the transitions to low lying state with shorter wavelengths. The dipole-dipole coupling, by mixing with non-circular states, thus leads to a strong reduction in the lifetime of the circular state.

5.3.1

Application of a magnetic field

In order to prevent the detrimental level mixing with non-circular states, we have to apply a magnetic field \mathbf{B} to Zeeman shift the levels, remove any degeneracies of the circular pair state with the non-circular ones. The question now is: at which strength and in which direction do we apply the magnetic field? In the following, we assume that the Stark effect is dominant over the dipole-dipole coupling and the Zeeman effect. We thus keep the quantization axis along Oz . The Zeeman Hamiltonian for a circular state reads

$$\begin{aligned} H_Z &= \frac{\mu_B}{\hbar} g_L \mathbf{L} \cdot \mathbf{B} \\ &= \frac{\mu_B}{\hbar} g_L (L_x B_x + L_y B_y + L_z B_z), \end{aligned} \quad (5.11)$$

where the spin part is omitted since the spin is not flipped by the dipole-dipole interaction. The Zeeman Hamiltonian can be expressed as

$$H_Z = \frac{\mu_B}{\hbar} g_L \left(\frac{L_+ + L_-}{2} B_x + \frac{L_+ - L_-}{2i} B_y + L_z B_z \right), \quad (5.12)$$

by defining two ladder operators

$$\begin{aligned} L_+ &= L_x + iL_y \\ L_- &= L_x - iL_y, \end{aligned} \quad (5.13)$$

Accordingly, B_x and B_y , via the ladder operators L_\pm , couple a circular state $|nC\rangle$ to the two next elliptical states $|nE^\pm\rangle$. As a result, the pair state $|nC; nC\rangle$ is mixed with the non-circular $|nE^+; nE^-\rangle$ (resonant coupling). This, again, leads to a reduction in

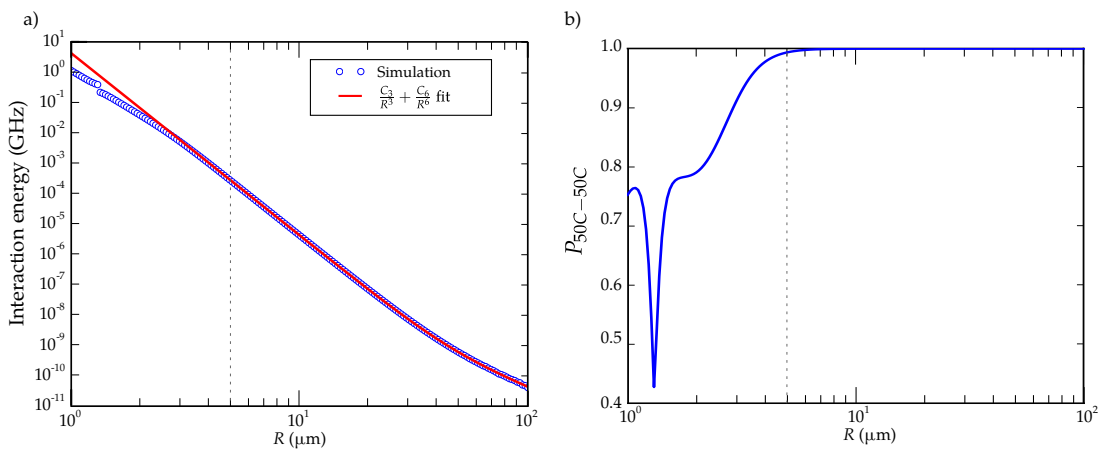


Figure 5.5 a) Interaction energy (log scale) for two atoms in 50C state as a function of the distance. The solid line is a fit with a summation of a van der Waals and a resonant dipole potentials $C_6/R^6 + C_3/R^3$ to $R \geq 4 \mu\text{m}$. b) Probability of the bare $|50C; 50C\rangle$ state in the final state. The dashed lines in a) and b) mark $R = 5 \mu\text{m}$ position.

the lifetime of the circular state. We thus keep only B_z , i.e., \mathbf{B} perpendicular to the capacitor plates.

We now have to find the magnitude of \mathbf{B} such that the mixing with the $|nE^+; nE^-\rangle$ is negligible. We have successfully used the full-Hamiltonian-diagonalization technique to numerically calculate the dipole-dipole interaction between low angular momentum Rydberg atoms. We extend this technique for two atoms in the $|nC\rangle$ circular state. We first create a Hilbert space of pair states with several cutoffs. The difference in the magnetic quantum number of an atom in a pair from that of the $|nC\rangle$ circular state is not larger than 2: $\Delta m < 2$. Another criteria is that an atom in a pair is less than 3 manifold away from the $|nC\rangle$ state ($\Delta n < 3$), since the transition dipole matrix element quickly decreases with Δn . The resulting Hilbert space consists of 361 pair states.

We then construct the full Hamiltonian, including the Stark effect, the Zeeman effect and the dipole-dipole interaction for $n = 50$ with $B = 1 \text{ mT}$ and $F = 2 \text{ V/cm}$. By diagonalizing this Hamiltonian, we deduce the interaction energy of the two circular atoms at distance R . We also carefully check that, relaxing the cutoffs, i.e., changing to $\Delta m < 3$ (1225 pair states), or $\Delta n < 4$ (961 pair states) does not yield a significantly different result (< 150 Hz at $R = 5 \mu\text{m}$)[†]. A 1 mT magnetic field along Oz , corresponding to a differential Zeeman shift of 14 MHz between two successive m states, is found to be enough to suppress the detrimental mixing effect. This value will be used throughout the rest of this thesis.

Figure 5.5a represents the interaction energy between two circular 50C atoms as a function of the inter-atomic distance R . It is well fitted with a summation of a van der Waals C_6/R^6 and a dipole C_3/R^3 potential with $C_6 = 4.23 \text{ GHz} \cdot \mu\text{m}^6$ and $C_3 = 3.95 \times 10^{-5} \text{ GHz} \cdot \mu\text{m}^3$ (red line).

The dipole interaction is interpreted as the interaction between two induced dipoles, which result from the displacement of the circular orbit with respect to the atomic core

[†] A further relax of the cutoffs would result in a Hilbert space of more than 2000 pair states, which is out of the performance of our desktop computer.

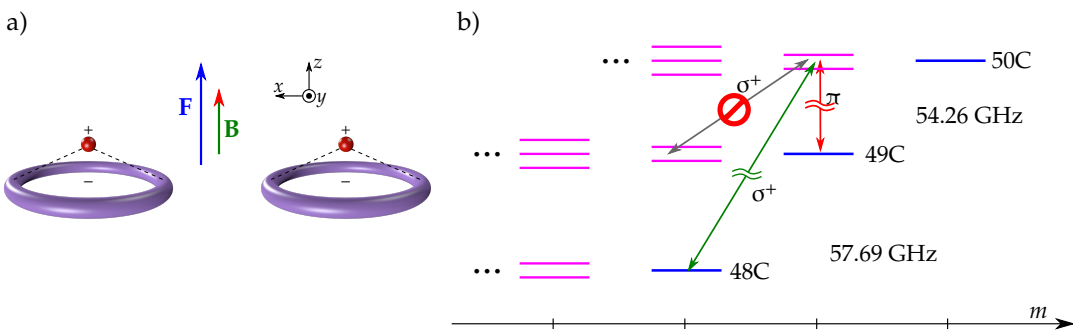


Figure 5.6 a) The deformations of the electronic orbitals induced by external electric field, leads to two dipoles aligned in the same direction.b) Level scheme for spontaneous emission of the $|50E^\pm\rangle$ states.

in the electric field (Figure 5.6a). From (1.45), one can deduce the induced dipole

$$d_i = \frac{1}{4} (4n^2 + 9n + 5) n^4 F, \quad (5.14)$$

and find the corresponding interaction coefficient

$$C_{i3,a-b} = \frac{d_i^2}{4\pi\epsilon_0}, \quad (5.15)$$

which is 3.95×10^{-5} GHz. μm^3 at $F = 2$ V/cm for $n = 50$, in good agreement with the numerical result. Since the two induced dipoles align to the electric field, they repel each other.

For a separation larger than $3\ \mu\text{m}$, the induced dipole interaction is smaller than 1.5 kHz and thus can be neglected. However for higher n and/or F , it grows quickly as $n^{12}F^2$, according to (5.14) and (5.15), and becomes more significant. Therefore one should be careful when neglecting this induced dipole interaction. At the distance of interest $R = 5\ \mu\text{m}$, the interaction of two circular atoms can be approximated by a van der Waals interaction. The dipole-dipole interaction acts as a second order perturbation by coupling to intermediate pair states.

Figure 5.5b plots the contribution from the bare state $|50C; 50C\rangle$ to the resulting level. The contamination from non-circular states at $5\ \mu\text{m}$ is about 0.65%, mainly from the elliptic $(|50E^+; 50E^- \rangle + |50E^-; 50E^+\rangle)/\sqrt{2}$ state. As depicted in Figure 5.6b, the spontaneous emission path to the $|49E^\pm\rangle$ by the emission of a σ^+ -polarized photon is inhibited since the radiated wavelength is below the cutoff of the capacitor. The two possible decay channels are transitions to the $|49C\rangle$ and $|48C\rangle$ states. The decay rates are about $1/1.4\ \text{s}^{-1}$ for the π transition and $1/0.3\ \text{s}^{-1}$ for the σ^+ transition. As a result, the lifetime of the circular state is reduced to about 70 s, which is still in the minute range.

5.3.2

Dipole-dipole interaction and its scaling laws

In this section, we will figure out the scaling laws of the interaction between two circular atoms of different n . On the one hand, this will help us in choosing a pair of levels, on which we will encode the spin state, but on the other hand, this is a cross check of the numerical simulation.

In the presence of the magnetic field along Oz , equations (5.7) and (5.8) are modified into

$$\begin{aligned} E_{nC} &= -\frac{1}{2n^2} + \alpha_{nC} F^2 + (n-1)\mu_B B_z, \\ E_{nE^\pm} &= -\frac{1}{2n^2} \pm \frac{3n}{2} F + \alpha_{nE} F^2 + (n-2)\mu_B B_z. \end{aligned} \quad (5.16)$$

5.3.2.1 $nC - nC$ interaction

The interaction acts as a second order perturbation by coupling to intermediate pair states $|c; d\rangle$, where $|c\rangle$ and $|d\rangle$ are single atom Rydberg states. The interaction is given by

$$\Delta E_{dd} = \sum_{|c;d\rangle} \frac{|\langle nC; nC | V_{dd} | c; d \rangle|^2}{\Delta_{cd}}, \quad (5.17)$$

where $\Delta_{cd} = E_c + E_d - 2E_{nC}$ is the corresponding detuning.

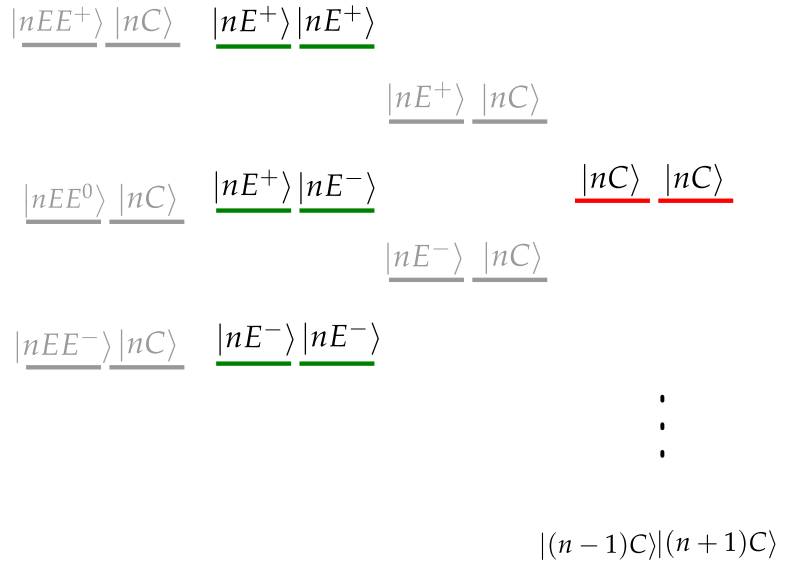


Figure 5.7 Level scheme for pair states around the $|nC; nC\rangle$ level. Pair states that do not couple to the $|nC; nC\rangle$ state by the dipole-dipole operator are shown in gray.

From (5.10), the total magnetic quantum number is either unchanged or changed by two units. The closest intermediate pair states in terms of energy that satisfy this condition are $|nE^+; nE^+\rangle$, $|nE^-; nE^-\rangle$ and $(|nE^+; nE^-\rangle + |nE^-; nE^+\rangle)/\sqrt{2}$ as shown in

Figure 5.7. Note that the anti-symmetric state $(|nE^+; nE^- \rangle - |nE^-; nE^+ \rangle)/\sqrt{2}$ does not couple to $|nC; nC\rangle$. According to table 5.1, the dipole coupling between a circular state $|nC\rangle$ and its next elliptical neighbors $|nE^\pm\rangle$ scales as $n^{3/2}$. As a result, all the numerators in (5.17) for the listed pair states scale as n^6 . Let us now consider the denominator for each term.

1. $|nE^\pm; nE^\pm\rangle$: the detuning reads

$$\Delta_\pm = \pm 3nF + 2(\alpha_{nE} - \alpha_{nC})F^2 - 2\mu_B B_z \approx \pm 3nF , \quad (5.18)$$

as the linear Stark shifts are dominant. The couplings of $|nE^+; nE^+\rangle$ and $|nE^-; nE^-\rangle$ to $|nC; nC\rangle$ are therefore of the same strength but of opposite signs. They cancel each other.

2. $|nE^+; nE^-\rangle + |nE^-; nE^+\rangle$: the detuning is given by

$$\Delta = 2(\alpha_{nE} - \alpha_{nC})F^2 - 2\mu_B B_z \approx -\frac{9}{4}n^5F^2 - 2\mu_B B_z + \mathcal{O}(n^7) . \quad (5.19)$$

Note that, the n^6 terms cancel when taking the difference $\alpha_{nE} - \alpha_{nC}$.

The van der Waals coefficient of two $|nC\rangle$ atoms can, therefore, be expressed as

$$C_{6,nC-nC} = \frac{An^6}{Bn^5F^2 + 1} , \quad (5.20)$$

where A and B are proportionality coefficients.

In addition, there is a small correction to the interaction energy, coming from the coupling with the $|(n-1)C; (n+1)C\rangle$ state. The quadratic Stark shifts and the Zeeman shifts are negligible compared to the energy separation between the two manifolds. The detuning is approximately

$$\Delta = \frac{1}{2(n-1)^2} + \frac{1}{2(n+1)^2} - \frac{2}{2n^2} = \frac{3n^2 - 1}{n^2(n^2 - 1)^2} , \quad (5.21)$$

which scales as $1/n^4$. Since the dipole coupling between two neighboring circular states scales as n^2 , the corresponding van der Waals interaction thus varies as Cn^{12} , where C is a proportionality coefficient. The van der Waals coefficient of the total interaction is modified into

$$C_{6,nC-nC} = \frac{An^6}{Bn^5F^2 + 1} + Cn^{12} . \quad (5.22)$$

Figure 5.8 plots the van der Waals coefficient $C_{6,nC-nC}$ determined numerically as a function of the principal quantum number $n = 45 - 61$ for different values of F . The solid lines are fit curves with equation (5.22) where A, B, C are global fit parameters, i.e., shared between curves. We can observe a very good agreement between the analytic expression and the simulation.

Now, for two atoms in two different circular states $|nC\rangle$ and $(n+p)C$, where $p \neq 0$,

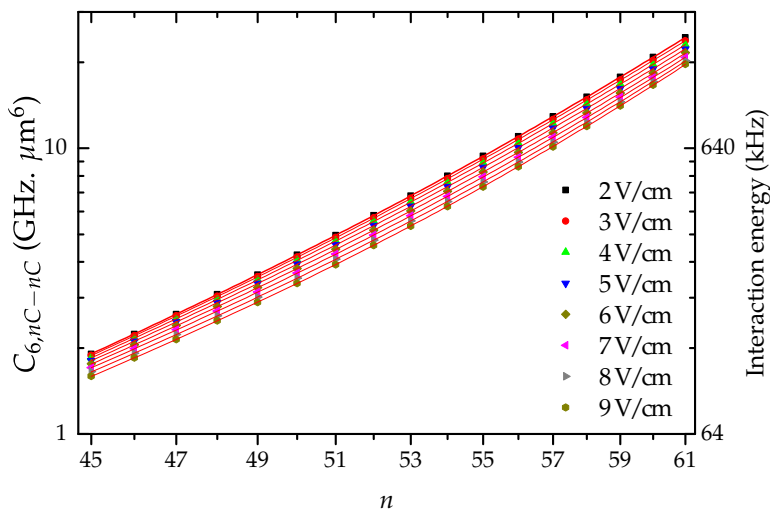


Figure 5.8 Van der Waals coefficients C_6 as function of n for a $|nC, nC\rangle$ pair. The corresponding interaction at $R = 5 \mu\text{m}$ is shown on the right axis. Solid lines are fitting curves using equation (5.22).

as discussed in [section 2.3](#), one can write the effective interaction Hamiltonian as

$$V_{\text{eff}} = \begin{pmatrix} C_{nC-(n+p)C} & A_{nC-(n+p)C} \\ A_{nC-(n+p)C} & C_{nC-(n+p)C} \end{pmatrix}, \quad (5.23)$$

where $C_{nC-(n+p)C}$ and $A_{nC-(n+p)C}$ are respectively the direct and the exchange interactions.

5.3.2.2 $nC - (n + 1)C$ interaction

Similarly to the case of the $nS - n'P$ interaction (see [section 2.3](#)), one finds that for a pair made up of an $|nC\rangle$ atom and an $|(n + 1)C\rangle$ atom, the exchange interaction varies as $1/R^3$ while the direct interaction takes the form of a van der Waals interaction. The n dependency of the exchange interaction comes only from the corresponding dipole matrix elements, thus it scales as n^4 . [Figure 5.9a](#) plots the van der Waals coefficient of the exchange interaction as a function of n for different values of F . The solid line is a fit with a n^4 function.

The scaling laws of the direct interaction can be derived with an argument similar to that used for the $nC - nC$ interaction case. The main contributions come from the coupling to the pair states $|nE^+; (n + 1)E^+\rangle$, $|nE^-; (n + 1)E^-\rangle$ and the symmetric combination $|nE^+; (n + 1)E^-\rangle + |nE^-; (n + 1)E^+\rangle$. Adding up a small correction from the $|(n - 1)C; (n + 2)C\rangle$ level, one can express the dependency of the direct interaction on n and F as

$$C_{6,nC-(n+1)C} = \frac{A'n^6}{B'n^5F^2 + D'F + 1} + C'n^{12}, \quad (5.24)$$

where A' , B' , C' and D' are proportionality coefficients. [Figure 5.9b](#) shows the numeri-

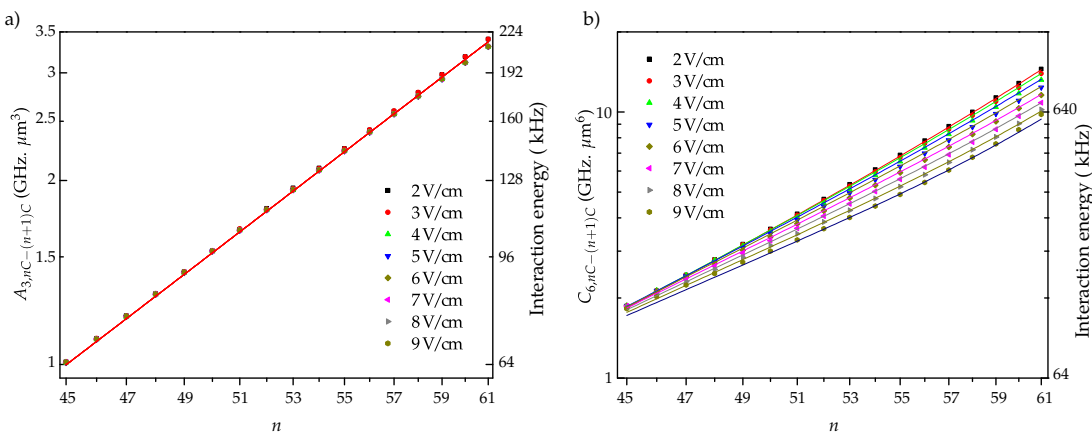


Figure 5.9 Interaction of a $nC - (n+1)C$ pair at different electric fields F . a) The exchange interaction exhibits a $1/R^3$ dependence. The dipole coefficient is independent of F and scales as n^4 . The solid line is a fit with a power law n^4 . b) The van der Waals coefficient calculated from simulations for the direct interaction. The solid lines are fits with equation (5.24).

cally calculated van der Waals coefficients for $n = 45$ to 61 at different values of F . The solid lines are fit curves by equation (5.24) with A' , B' , C' and D' as fit parameters. A good agreement is observed for $n \geq 48$. The small deviations at high F around $n = 45$ can be attributed to the weak coupling to $|(n+1)EE^{0,\pm}, nC\rangle$ levels.

5.3.2.3 $nC - (n+2)C$ interaction

Both the exchange interaction and the direct interaction are second order couplings through intermediate states $|c; d\rangle$. Respectively, they are given by

$$\Delta E_{dd}^{exc} = \sum_{|c;d\rangle} \frac{\langle nC; (n+2)C | V_{dd} | c; d \rangle \langle c; d | V_{dd} | (n+2)C; nC \rangle}{\Delta_{cd}} = h \frac{A_{6,nC-(n+2)C}}{R^6} \quad (5.25)$$

and

$$\Delta E_{dd}^{dir} = \sum_{|c;d\rangle} \frac{|\langle nC; (n+2)C | V_{dd} | c; d \rangle|^2}{\Delta_{cd}} = h \frac{C_{6,nC-(n+2)C}}{R^6}, \quad (5.26)$$

where $\Delta_{cd} = E_c + E_d - E_{nC} - E_{(n+2)C}$. The strengths of the interactions are given by the corresponding van der Waals coefficients $A_{6,nC-(n+2)C}$ and $C_{6,nC-(n+2)C}$.

Let us have a look first at the exchange interaction. Due to the selection rules, the only nonzero term stems from the coupling to $|(n+1)C; (n+1)C\rangle$ state. One can easily deduce that it scales as n^{12} and almost does not depend on F . Figure 5.10 shows the numerical results for the exchange coefficient $A_{6,nC-(n+2)C}$ for different $|nC; (n+2)C\rangle$ states and different electric fields.

On the contrary, there are several intermediate states contributing to the direct interaction. Table 5.2 lists some of the main contributions as well as their corresponding scaling laws. As can be seen from the fourth and the two last rows of table 5.2, for high F and/or n , the Stark shifts can compensate for the level spacing ($\Delta = 0$), recovering

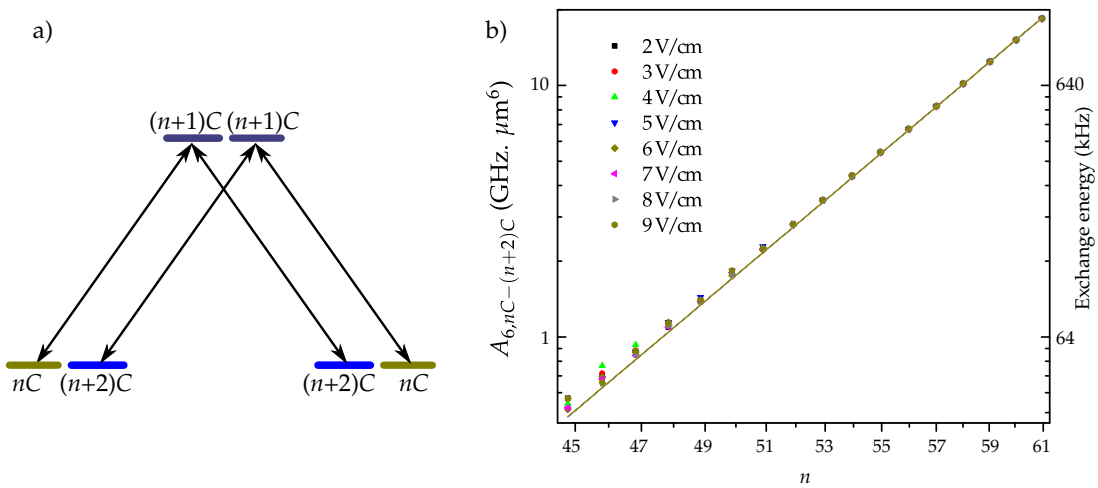


Figure 5.10 a) Level scheme for the exchange interaction between two atoms in the nC and $(n + 2)C$ states. b) Exchange van der Waals coefficient as a function of n for a $nC - (n + 2)C$ pair. The solid line is a fit with a n^{12} power law.

Table 5.2 Scaling laws for dipole coupling between a $|nC; (n + 2)C\rangle$ pair state and a nearby state.

$ nC; (n + 2)C\rangle$	Numerator	Detuning
$ nE^+; (n + 2)E^+\rangle$	n^6	nF
$ nE^-; (n + 2)E^-\rangle$	n^6	$-nF$
$ nE^+; (n + 2)E^-\rangle$	n^6	$-12F - 9n^5F^2 - 8\mu_B B$
$ nE^-; (n + 2)E^+\rangle$	n^6	$+12F - 9n^5F^2 - 8\mu_B B$
$ (n + 1)C; (n + 1)C\rangle$	n^8	n^{-4}
$ (n - 1)C; (n + 3)C\rangle$	n^8	n^{-4}
$ (n + 1)EE^-; (n + 1)C\rangle$	n^8	$1/n^4 - 3nF$
$ (n - 1)C; (n + 3)EE^+\rangle$	n^8	$-1/n^4 + 3nF$

the resonant dipole-dipole coupling which scales as $1/R^3$. The pair state $|nC; (n + 2)C\rangle$ is mixed with non-circular states, resulting in a reduction in the lifetime of the circular states. To observe the mixing effect, we consider the direct interaction for a pair at a $5 \mu\text{m}$ distance. Assuming a power law for the interaction $V_{dd} \propto 1/R^\alpha$, we numerically calculate the effective power α at $R_0 = 5 \mu\text{m}$. Figure 5.11 represents the results. With n smaller than 55 and in a moderate field up to 7 V/cm, the direct interaction is well approximated by a van der Waals interaction.

5.3.2.4 $nC - (n + p)C$ interaction with $p > 2$

To complete the discussion, let us discuss the $nC - (n + p)C$ interaction, with $p > 2$. The selection rules allow only the p order of perturbation to be non zero for the exchange interaction of a $nC - n'C$ pair where $p = n' - n$. Figure 5.12 illustrates the coupling path that leads to the exchange of excitations. As a result, the exchange interaction varies as $1/R^{3p}$ and quickly drops when increasing the difference of n and n' . One expects

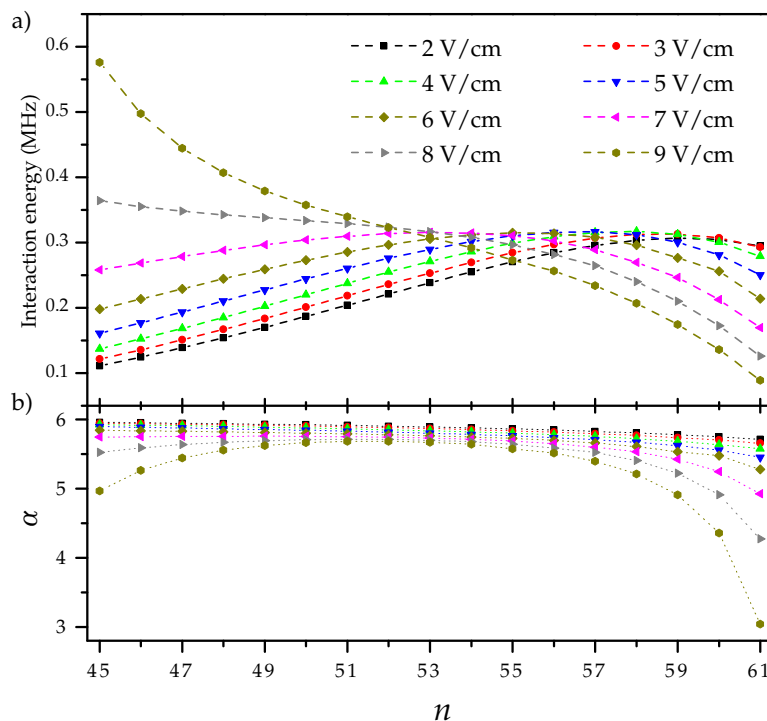


Figure 5.11 a) Direct interaction energy of a $nC - (n+2)C$ pair at $5 \mu\text{m}$. b) Effective power law α obtained from numerical derivation shows the deviation from a van der Waals interaction ($\alpha = 6$) to a resonant dipole interaction ($\alpha = 3$).

a $n^{4(2p-1)}$ dependency. [Figure 5.13a](#) and [Figure 5.14a](#) plot the exchange interaction coefficient for $p = 3$ and $p = 4$ as a function of n at different values of F . Power laws of n^{20} and n^{28} are found, respectively. The exchange interaction coefficient of the $47C - 50C$ pair is $42 \text{ MHz} \cdot \mu\text{m}^9$ while that of $46C - 50C$ is $1.2 \text{ MHz} \cdot \mu\text{m}^{12}$. At $5 \mu\text{m}$, these correspond to 21 Hz and 5 mHz respectively. They are thus negligible.

The diagonal terms have a quite complex behavior. The Stark effect changes the detuning in the denominators of the second order coupling to nearby pair states. Similarly to the $nC - (n+2)C$ case, with some values of F , the interaction can recover resonant dipole coupling, scaling as $1/R^3$. This leads to a strong reduction in the lifetime of the circular states of interest. [Figure 5.13](#) and [5.14](#) represent the numerical results for $nC - (n+3)C$ and $nC - (n+4)C$ pairs at a $5 \mu\text{m}$ distance, together with the corresponding effective power α .

5.4

1D spin chain's Hamiltonian

We now discuss how to construct the spin Hamiltonian in (III) with trapped circular atoms. We encode the spin states $|\uparrow\rangle$ and $|\downarrow\rangle$ onto two circular levels. A $nC - (n+1)C$ pair would lead to a very strong exchange interaction (few MHz for $n \sim 50$). On the one hand, it overwhelms the direct van der Waals interaction between two atoms in nC (few tens of kHz). This would limit the accessible range of Hamiltonians. On the

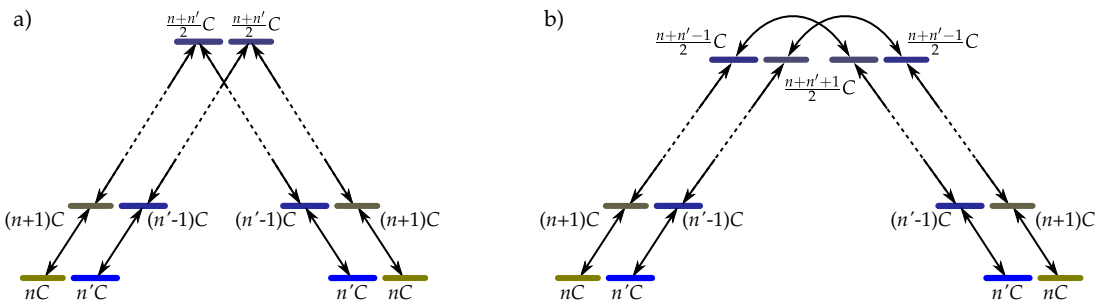


Figure 5.12 Exchange interaction as a multi-photon process shown for $n' - n$ is an a) even or b) an odd number.

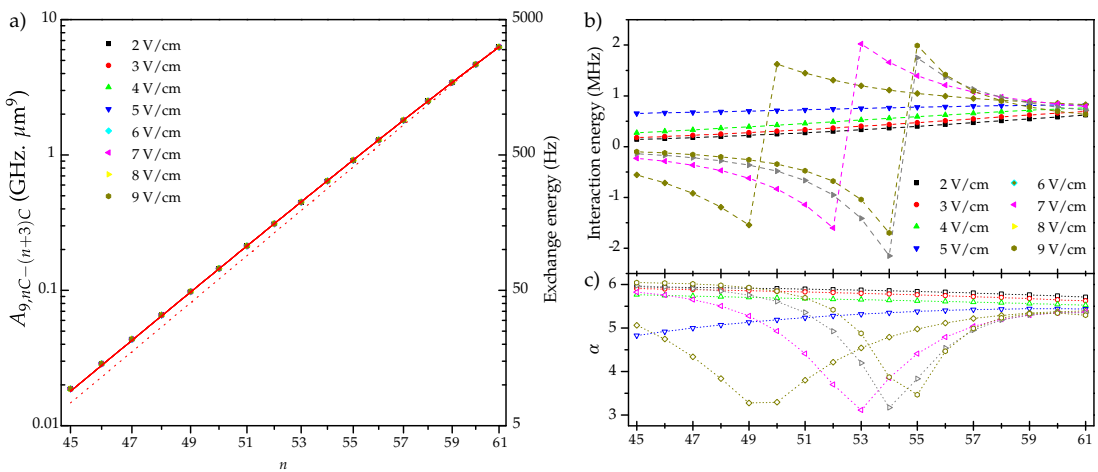


Figure 5.13 a) Coefficient A_9 of the exchange interaction between two atoms in the nC and $(n + 3)C$ states. The dotted line is a fit with a n^{20} power law and the solid line is that with the next order correction n^{28} . The corresponding energy at a $5 \mu\text{m}$ separation is shown on the right axis. b) Direct interaction energy of the same pair at a $5 \mu\text{m}$ separation. c) The corresponding effective power law α .

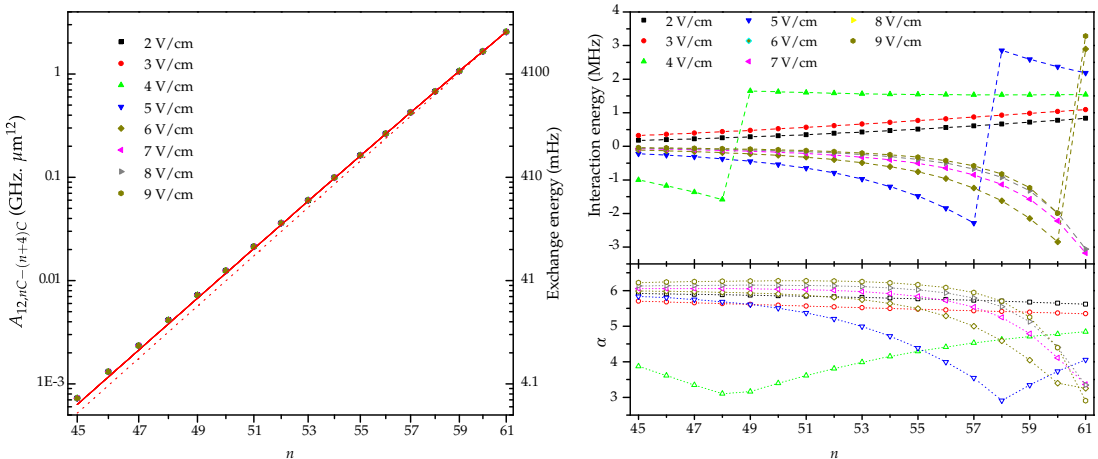


Figure 5.14 The same as [Figure 5.13](#) for two atoms in the nC and $(n + 4)C$ states. The exchange interaction scales as n^{28} . Dotted line is the corresponding fit. The solid line is obtained when adding a n^{32} correction term.

other hand, the strong exchange interaction, similarly to the $nS - nP$ interaction discussed in chapter 2, results in two branches: an attractive branch, corresponding to a symmetric combination of the two spins $|+\rangle = (|\uparrow\rangle + |\downarrow\rangle)/\sqrt{2}$, and a repulsive branch, corresponding to an anti-symmetric combination $|-\rangle = (|\uparrow\rangle - |\downarrow\rangle)/\sqrt{2}$. Since the interaction varies as $1/R^\alpha$ ($\alpha = 3$ or 6), if it is strong enough, it makes the two atoms move closer or away from each other, depending on whether the atoms are in the $|+\rangle$ or $|-\rangle$ state. Starting from the $|\uparrow\downarrow\rangle$ state, for instance, which is a superposition state of $|+\rangle$ and $|-\rangle$. The time evolution of the two spins gives rise to an entanglement of the spin with the atomic motion in the lattice, which alternatively washes out the coherence of the spins. One needs to weaken the exchange interaction or tighten the trap so that the induced atomic motion is much smaller than the extension of the atomic wavefunction. Appendix E discusses the problem in more details.

A $nC - n'C$ pair where $|n' - n| > 2$, on the contrary, would lead to a very weak exchange interaction. The system can be considered as a repulsive ensemble of particles without any excitation exchange: a classical Newton's cradle. A choice of nC and $(n+2)C$ is thus the most relevant. Both the exchange and the direct interactions vary as $1/R^6$ and are of comparable magnitudes.

5.4.1

1D spin chain Hamiltonians

5.4.1.1 Two-atom Hamiltonian

Let us first write down the Hamiltonian for an atom pair. They are separated by a distance $d = 5 \mu\text{m}$.

In the basis $\{|nC; nC\rangle, |nC; (n+2)C\rangle, |(n+2)C; nC\rangle, |(n+2)C; (n+2)C\rangle\}$ the effective interaction Hamiltonian reads

$$V_{\text{eff}} = \frac{\hbar}{d^6} \begin{pmatrix} C_{6,nC-nC} & 0 & 0 & 0 \\ 0 & C_{6,nC-(n+2)C} & A_{6,nC-(n+2)C} & 0 \\ 0 & A_{6,nC-(n+2)C} & C_{6,nC-(n+2)C} & 0 \\ 0 & 0 & 0 & C_{6,(n+2)C-(n+2)C} \end{pmatrix}. \quad (5.27)$$

Using the Pauli matrices σ^i , where $i = X, Y$ or Z , we define the spin operators for each atom acting on the tensor product space as follows

$$\begin{aligned} \sigma_1^i &= \sigma^i \otimes \mathbb{I} \\ \sigma_2^i &= \mathbb{I} \otimes \sigma^i, \end{aligned} \quad (5.28)$$

where the index indicates which spin is manipulated, and

$$\mathbb{I} = \begin{pmatrix} 1 & 0 \\ 0 & 1 \end{pmatrix} \quad (5.29)$$

is the identity matrix.

The effective interaction Hamiltonian can be decomposed into

$$\frac{V_{\text{eff}}}{h} = \delta E \mathbb{I}^{\otimes 2} + \frac{\delta\zeta}{2} (\sigma_1^Z + \sigma_2^Z) + J_Z \sigma_1^Z \sigma_2^Z + J (\sigma_1^X \sigma_2^X + \sigma_1^Y \sigma_2^Y), \quad (5.30)$$

where

$$\begin{aligned} \delta E &= \frac{C_{6,nC-nC} + 2C_{6,nC-(n+2)C} + C_{6,(n+2)C-(n+2)C}}{4d^6} \\ \delta\zeta &= \frac{C_{6,nC-nC} - C_{6,(n+2)C-(n+2)C}}{2d^6} \\ J_Z &= \frac{C_{6,nC-nC} - 2C_{6,nC-(n+2)C} + C_{6,(n+2)C-(n+2)C}}{4d^6} \\ J &= \frac{A_{6,nC-(n+2)C}}{2d^6}. \end{aligned} \quad (5.31)$$

The first term in (5.30) just redefines the energy origin and thus can be omitted. The interaction Hamiltonian is thus rewritten as

$$\frac{V_{\text{eff}}}{h} = \frac{\delta\zeta}{2} (\sigma_1^Z + \sigma_2^Z) + J_Z \sigma_1^Z \sigma_2^Z + J (\sigma_1^X \sigma_2^X + \sigma_1^Y \sigma_2^Y). \quad (5.32)$$

5.4.1.2 Chain Hamiltonian

We now extend the above Hamiltonian to a 1D chain of N atoms regularly separated by d . We keep only the nearest neighbor interaction terms since the contribution from the next nearest neighbor is already 64 times smaller than that from the nearest one. The interaction Hamiltonian for the spin chain is generalized from the above two-atom Hamiltonian

$$\begin{aligned} \frac{V_{\text{eff}}}{h} &= \frac{\delta\zeta}{2} (\sigma_1^Z + \sigma_N^Z) + \delta\zeta \sum_{j=2}^{N-1} \sigma_j^Z + \\ &\quad J_Z \sum_{j=1}^{N-1} \sigma_j^Z \sigma_{j+1}^Z + J \sum_{j=1}^{N-1} (\sigma_j^X \sigma_{j+1}^X + \sigma_j^Y \sigma_{j+1}^Y). \end{aligned} \quad (5.33)$$

Here we define the spin operators σ_j^i acting on the spin number j as

$$\sigma_j^i = \underbrace{\mathbb{I} \otimes \cdots \otimes}_{\substack{1 \\ \downarrow \\ j}} \sigma^i \otimes \cdots \otimes \underbrace{\mathbb{I}}_{N \downarrow}, \quad (5.34)$$

where $i = X, Y$ or Z . The first term in (5.33) comes from the “border” effect of the chain. It is clear that the interaction energy of an atom at an end of the chain, having only one neighbor, is half that of a “bulk” atom, which interacts with its two neighbors (*c.f.* chapter 4).

Let ν_0 be the transition frequency from nC to $(n+2)C$ levels without any interaction. The Hamiltonian for a non-interacting chain is given by

$$\frac{H_0}{h} = \frac{\nu_0}{2} \sum_{j=1}^N \sigma_j^Z. \quad (5.35)$$

The total Hamiltonian is thus written as a summation of (5.35) and (5.33)

$$\frac{H}{\hbar} = \frac{\nu_0}{2} \sum_{j=1}^N \sigma_j^Z + \frac{V_{\text{eff}}}{\hbar}. \quad (5.36)$$

Rearranging the above equation, we obtain

$$\begin{aligned} \frac{H}{\hbar} = & \frac{\nu_0 + \delta\zeta}{2} (\sigma_1^Z + \sigma_N^Z) + \left(\frac{\nu_0}{2} + \delta\zeta \right) \sum_{j=2}^{N-1} \sigma_j^Z + \\ & J_Z \sum_{j=1}^{N-1} \sigma_j^Z \sigma_{j+1}^Z + J \sum_{j=1}^{N-1} (\sigma_j^X \sigma_{j+1}^X + \sigma_j^Y \sigma_{j+1}^Y). \end{aligned} \quad (5.37)$$

At a distance $d = 5 \mu\text{m}$, J_Z and J typically range from several kHz up to a few MHz while ν_0 is more than 50 GHz. The atomic energy is thus by far dominant, making the ground state trivial: all the atoms are in the lower nC state. However, when introducing one or more excitations, the system is out of equilibrium. The excitations propagate over the chain. The study of quantum transport is thus feasible.

5.4.1.3 Adding some “spices” — Rydberg microwave dressing

The situation is much more appealing when adding a classical field at a frequency $\nu \approx \nu_0/2$ to dress the two states, via a two-photon transition. The coupling strength is represented by the effective two-photon Rabi frequency Ω . The Hamiltonian is modified to

$$\begin{aligned} \frac{H}{\hbar} = & \frac{\nu_0 + \delta\zeta}{2} (\sigma_1^Z + \sigma_N^Z) + \left(\frac{\nu_0}{2} + \delta\zeta \right) \sum_{j=2}^{N-1} \sigma_j^Z + J_Z \sum_{j=1}^{N-1} \sigma_j^Z \sigma_{j+1}^Z + \\ & J \sum_{j=1}^{N-1} (\sigma_j^X \sigma_{j+1}^X + \sigma_j^Y \sigma_{j+1}^Y) + \Omega \cos(4\pi\nu t) \sum_{i=1}^N \sigma_i^X, \end{aligned} \quad (5.38)$$

where the driving phase is set to zero explicitly without loss of generality.

We change to the rotating frame defined by the unitary transformation

$$U = \exp \left(i2\pi\nu t \sum_{j=1}^N \sigma_j^Z \right). \quad (5.39)$$

The new Hamiltonian is given by

$$\tilde{H} = U H U^\dagger + i\hbar(\partial_t U) U^\dagger. \quad (5.40)$$

Under this transformation, $\sigma_j^{X(Y)}$ is replaced by $\cos(4\pi\nu t)\sigma_j^{X(Y)} \mp \sin(4\pi\nu t)\sigma_j^{Y(X)}$

while σ_j^Z is unchanged. We have

$$\begin{aligned} \frac{\tilde{H}}{h} = & \frac{\Delta'}{2} (\sigma_1^Z + \sigma_N^Z) + \frac{\Delta}{2} \sum_{j=2}^{N-1} \sigma_j^Z + \\ & + J_Z \sum_{j=1}^{N-1} \sigma_j^Z \sigma_{j+1}^Z + J \sum_{j=1}^{N-1} (\sigma_j^X \sigma_{j+1}^X + \sigma_j^Y \sigma_{j+1}^Y) + \frac{\Omega}{2} \sum_{i=1}^N \sigma_j^X, \end{aligned} \quad (5.41)$$

with $\Delta = 2\nu - (\nu_0 + 2\delta\zeta)$ and $\Delta' = 2\nu - (\nu_0 + \delta\zeta)$. In the derivation of the last term, we have used the rotating wave approximation to drop out fast oscillating terms. Rearranging the above equation, we obtain

$$\begin{aligned} \frac{\tilde{H}}{h} = & J \left[\sum_{j=1}^{N-1} \left(\sigma_j^X \sigma_{j+1}^X + \sigma_j^Y \sigma_{j+1}^Y + \frac{J_Z}{J} \sigma_j^Z \sigma_{j+1}^Z \right) + \right. \\ & \left. \frac{\Delta}{2J} \sum_{j=1}^N \sigma_j^Z + \frac{\Omega}{2J} \sum_{i=1}^N \sigma_j^X \right] - \frac{\delta\zeta}{2} (\sigma_1^Z + \sigma_N^Z), \end{aligned} \quad (5.42)$$

where the last term accounts for the “border” effect. Compared to (III), the above equation represents the general form of a XXZ-spin Hamiltonian for a spin chain in an external magnetic field. Here, J and J_Z correspond to the transversal and longitudinal spin couplings respectively. The anisotropic parameter is given directly by J_Z/J . The longitudinal and the transverse “magnetic fields” are given by the microwave detuning $\Delta/(2J)$ and the dressing strength $\Omega/(2J)$ respectively.

5.4.2

Choice of levels and tunable XXZ spin chain

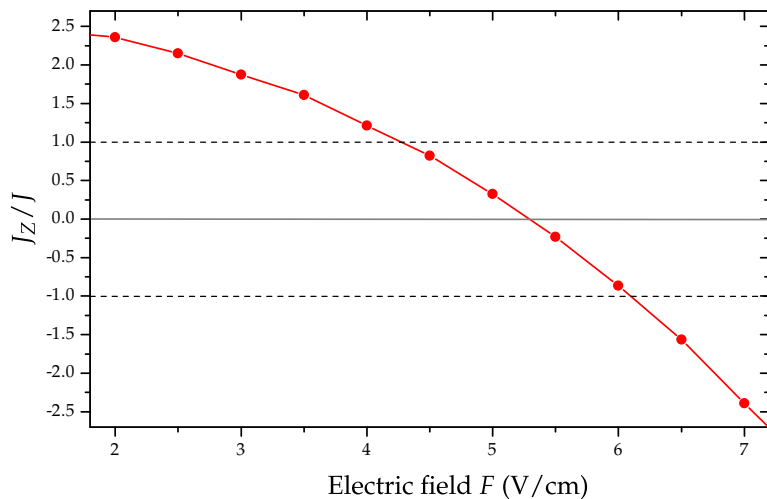


Figure 5.15 The ratio J_Z/J as a function of the electric field F for the 48C and 50C states. The dotted lines indicate the isotropic Heisenberg model. The central solid line corresponds to the pure XX model.

According to section 5.3, J_Z and J scale differently when changing the principal quantum number n . As a result, we can choose a range of n values in which J_Z is of the same order of magnitude as J ($n \sim 50$). Moreover, for a given n , the direct interaction terms do depend on the electric field F while the exchange interaction and thus J is nearly constant. This gives us the possibility of tuning the J_Z/J ratio. Figure 5.15 plots this ratio for a 48C – 50C pair as a function of F . For a variation of F between 2 and 7 V/cm, J_Z varies between $2.3J$ and $-2.3J$. We can thus tune our spin chain from a purely transverse XX Hamiltonian ($J_Z = 0$, only spin coupling in the transverse direction) to an isotropic Heisenberg XXZ model ($J_X = J_Y = J_Z = J$) by a mere voltage control. In addition, Ω and Δ (Δ') are fully controlled in the experiment and can be varied over a wide range (a few MHz) in a rather short time scale (less than a μ s). In other words, we have the possibility to explore the whole range of the phase diagram depicted in Figure III.1 (resonant dressing $\Delta = 0$) and beyond.

For such a flexibility, we will encode the spin states on the 48C and 50C levels. The difference between Δ and Δ' is about 33 kHz. On the one hand, this difference allows us to easily address the two atoms at the ends of the chain using a microwave pulse. On the other hand, with a chain with tens of atoms, what happens inside the chain would be less affected by the boundary condition effect. This “border” effect will be neglected in the next sections.

5.5

Deterministic chain preparation

The Hamiltonian described by (5.42) is valid provided that the spin chain is gap-less, i.e., has no empty site. In this section, we propose a protocol to deterministically load the optical lattice with unit filling. The principle is based on a variant of evaporative cooling as described below

We start with a dilute and large sample of circular atoms held in the Laguerre-Gaussian light-tube. With two “plug” focused laser beams crossing the hollow trap beam, we create two barriers, one higher than the other, confining the atoms longitudinally as demonstrated in Figure 5.16. We slowly reduce the distance L between the two “plug” beams. The atoms are thus squeezed, building up the repulsive van der Waals forces between them. As soon as the energy of the last atom at the weak barrier side exceeds the height of the barrier, it is expelled and escapes along the Laguerre-Gauss beam. By compressing further the chain, we remove more and more atoms. The number of atoms left in the trap is determined by the final barrier distance.

As soon as the number of atoms of interest is reached, we rise up the heights of the two barriers to prevent further losses of atoms. By adjusting the separation of the two barriers, we match the inter-atomic distance with the optical lattice spacing, and transfer all the trapped atoms into the lattice, thereby achieving a unit filling factor.

In the following, we discuss in details our proposal of a full experimental sequence. It consists in two main steps as illustrated in Figure 5.17:

1. Preparing a long irregular chain of circular atoms,
2. Ordering the chain by evaporative cooling and transferring it into the trapping standing-wave potential.

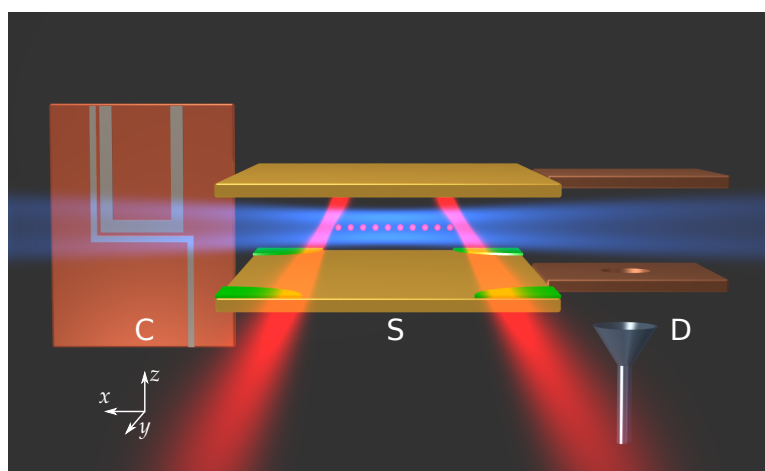


Figure 5.16 Sketch of the proposed experimental setup. Cold atoms are prepared with the atom chip C , and transferred into the science zone S where they are excited to the Rydberg state, circularized and trapped in the hollow Laguerre-Gaussian beam (blue). Two plug beams (red) compress the chain, removing atoms one by one until the final number of atoms of interest reached. At the end of the sequence, the state of the circular atoms is read out at the detection zone D .

5.5.1

Initial irregular chain preparation

In order to prepare a long and dilute chain of circular atoms, we first excite low angular momentum Rydberg atoms out of a long and cold ground-state cloud in the dipole blockade regime, and then transfer them into the circular state by a *circularization* process [94].

Laser excitation of a Rydberg atom chain

We start with a cigar shaped ground state rubidium cloud at a sub- μK temperature prepared with the atom chip setup. For instance, a BEC of about 30 000 atoms can be experimentally prepared (Figure 3.10). We adiabatically transfer and let the atoms expand into a red-detuned dipole trap made of a $1 \mu\text{m}$ -wavelength Gaussian beam. The use of the dipole trap enables an elongated cloud while maintaining tight transverse confinements. This dipole trap also serves as an optical tweezer to move the cloud from the atom chip C into the “science capacitor” S (Figure 5.16). Further cooling in the dipole trap can be an option. We assume that about 2000 atoms are held in the dipole trap, forming a cloud of $\sim 1 \text{ mm}$ long.

We now turn off the dipole trap and apply a $10 \mu\text{s}$ -long laser pulse to bring the atoms into the $50S$ Rydberg state in the dipole blockade regime (zero detuning). The positions of the excited Rydberg atoms are simulated using the Monte Carlo – rate equations model described in section 4.4. About 100 Rydberg atoms are excited, separated by $(9 \pm 3) \mu\text{m}$. At this separation, the van der Waals interaction between the atoms is negligible.

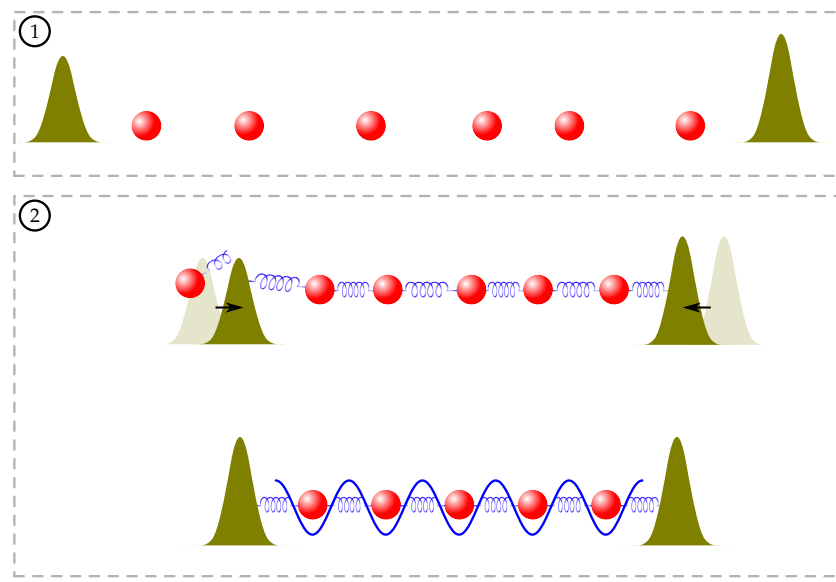


Figure 5.17 Deterministic chain preparation. It consists in two main step: 1) Irregular circular chain preparation and 2) Tailoring the chain using evaporative cooling and transferring into optical lattice. Circular atoms are represented by the red spheres. The two barriers (green) compress the chain, removing atoms one by one until reaching the desired number of atoms. Then the chain is transferred into the optical lattice (blue).

Circularization of the Rydberg atoms

Now, we apply a voltage across the capacitor, creating a homogeneous electric F , along Oz . This electric field, as discussed previously, defines a quantization axis and lifts the degeneracy of the manifold n . The levels, shifted by the linear Stark effect, make up an open “umbrella”, whose tip is at the circular state as depicted in Figure 5.18a. The lowest Stark levels of each m , i.e., the $|n, k, n - 1 - k\rangle$ levels, forms a staircase (blue lines). Neighboring steps are separated by

$$\hbar\nu_S \approx \frac{3}{2}nF, \quad (5.43)$$

which is about 100 MHz/(V/cm) for $n = 50$. A σ^+ -polarized radio-frequency couples all the levels of the staircase. An appropriate adjustment of the RF power and the electric field will adiabatically transfer the atoms from the 50S state ($m = 0$), climbing the staircase into the 50C circular state.

An intuitive way to explain the adiabatic passage is to use the dressed atom model to describe the atom-light interaction. Starting from the 50S state with N -RF photons, by successively absorbing a photon, the atom gets excited to the circular state. We denote an intermediate atom-light state in the process by $|50, m = p, N - p\rangle$, where p is the number of photons absorbed. The 50S and 50C states correspond to $|50, m = 0, N\rangle$ and $|50, m = 49, N - 49\rangle$ respectively. In a very weak RF field, the states are not coupled. Each atom-light state is shifted from the circular state by $(49 - p) \times \hbar(\nu_S - \nu_{RF})$, where ν_{RF} is the RF frequency. The levels are represented in Figure 5.18b by the dashed blue lines as a function of the electric field F . At $\nu_S = \nu_{RF}$, the system is degenerate. With

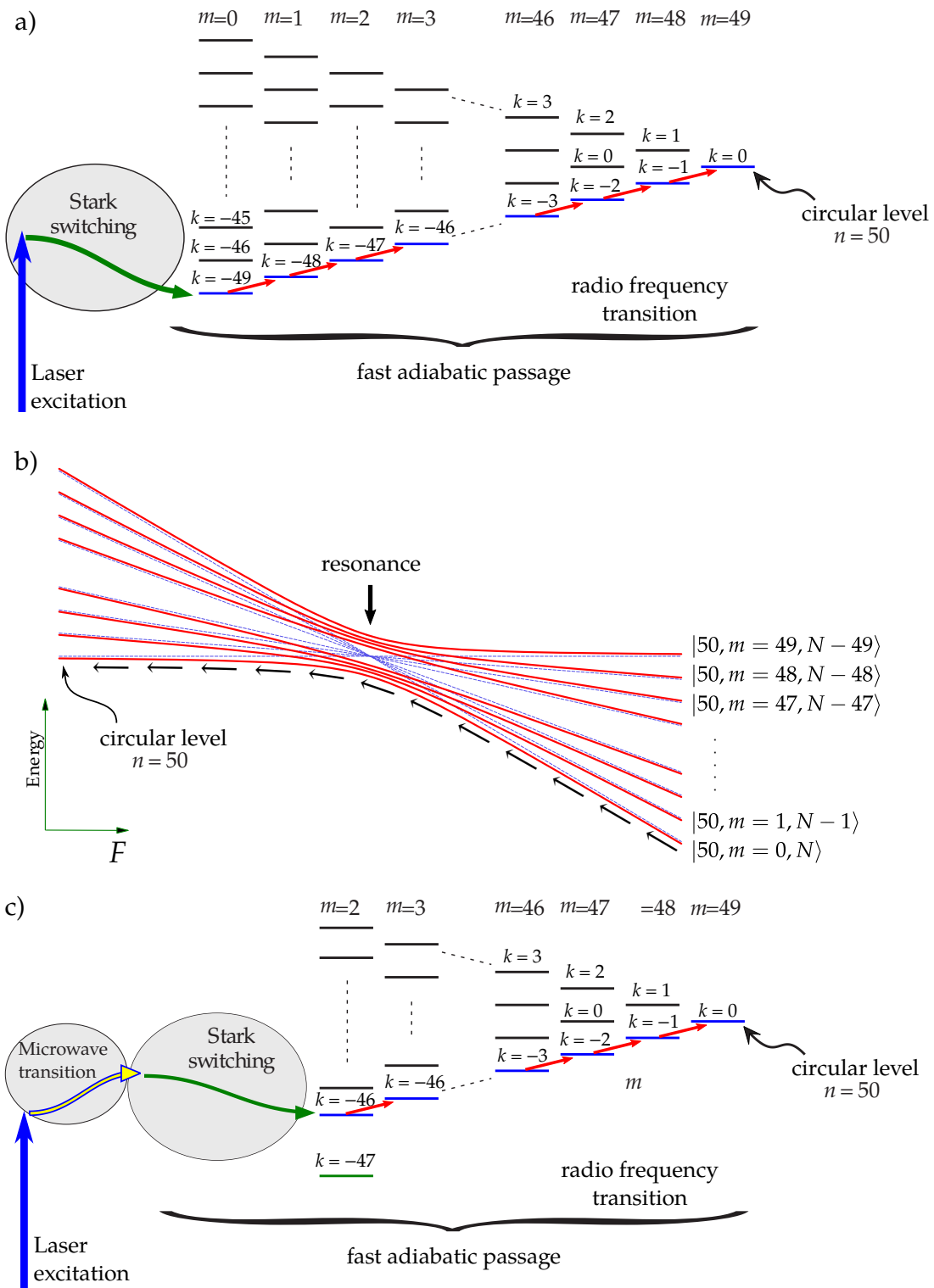


Figure 5.18 a) Level scheme of the circularization process for Hydrogen atom. b) Principle of the adiabatic passage. c) Level scheme of the circularization process for ^{87}Rb atom.

a higher power, the RF couples the levels, leading to an anti-crossing between them, resulting in the red lines in [Figure 5.18b](#). Starting from the $50S$ state in a high electric field, by adiabatically ramping down the electric field while keeping ν_{RF} constant, one ends up in the circular state.

Due to the quantum defect of Rubidium, the few first steps of the staircase are much lower in energy (few tens to hundreds GHz), and thus are not coupled by the RF. The $50F, m = 2$ is the lowest l state that can be involved in the adiabatic passage as depicted in [Figure 5.18c](#) (*c.f.* [Figure 1.7](#)). A two-photon microwave π -pulse transferring the atoms into the $50D$ state, followed by another one-photon microwave pulse transferring the atoms into the $50F, m = 2$ ($|k = -46, m = 2\rangle$) state at the beginning of the adiabatic passage is necessary. Alternatively, one can adjust the laser to directly excite the $50D$ instead of the $50S$ state, and then transfer them into the $50F, m = 2$ state ([Figure 5.18c](#)).

Technically, the σ^+ -polarized RF field is generated by applying voltages with synchronized phases and amplitudes on the four electrodes near the edges of the capacitor plates (green patches on [Figure 5.16](#)). The whole circularization process lasts a few μs and reaches a very high efficiency [94, 95]. Even if we cannot transfer all the atoms into the circular state, atoms in the elliptical states quickly decay and become untrapped in the next step of the experiment.

This step ends by applying a short pulse of a strong 780 nm wavelength laser to push out the ground state atoms. We are left with about 100 circular atoms aligned along Ox . Due to the weak interaction between the atoms (~ 250 kHz), we assume that, so far, the atoms have not moved.

5.5.2

Spin chain tailoring

In this step, we trap the circular atoms on a 1D chain using the Laguerre-Gaussian beam in combination with the two “plug” beams. We, first, compress and evaporatively cool the chain of circular atoms until obtaining the number of atoms of interest. Here, we aim at a chain with 40 circular atoms. We then adjust the distance between the atoms and transfer them into the standing-wave optical lattice. This step requires an appropriate control of the laser beams (position, power and waist) with a good timing.

Taking as the input the positions of the Rydberg atoms, obtained from the excitation model in the previous step, we simulate the classical motion of the atoms, looking for the optimal laser beam parameters. The simulation takes into account the van der Waals interaction between the atoms[†]. To keep things simple, we neglect the transverse motion and concentrate on the axial motion of the atoms only.

A remark on the simulation is that the problem involves many nonlinearly interacting bodies. As a result, the system is chaotic, i.e., a small deviation in the initial state leads to an appreciable difference in the final result, especially when the system evolves over a long time. We thus need a high precision numerical integrator. In addition, numerical methods for solving the equations of motion usually slightly modify the total energy, resulting in artificial excitation or damping of the system after a large

[†]We calculate the interaction between all the atoms, not just the nearest neighbors.

number of iterations. A symplectic integrator helps to suppress this numerical effect. We thus, use a recently developed sixth-order Runge-Kutta-Nyström method, following the scheme described in [176].

Optimizing the laser parameters using the simulation, we successfully load 40 circular atoms into the optical lattice with unit filling factor. The main criterion for the optimization throughout the process is to keep the atoms close to the motional ground state, and thus to try to suppress any heating effect as much as possible. Figure 5.19 shows a typical trajectory of the atoms over the process, while Figure 5.20 represents the time variation of each laser beam. The time evolution of the average kinetic and potential energies per trapped atom is plotted in Figure 5.21. In the following, we discuss in details the result. For clarity, we divide this step into four sub-steps:

- (a) Turning on the trap,
- (b) Atom evaporation,
- (c) Matching the distance,
- (d) Transfer into the optical lattice.

a) 1D trap of circular atoms: 0–100 ms

After the circularization of the atoms (the time origin is set to 0 ms), we turn on the Laguerre-Gauss beam. The repulsive van der Waals forces between the atoms, even weak, will give to the atoms a velocity. If one slowly switches on the beam, the atoms have enough time to drift out of the trap (Figure 5.22a). Abruptly switching on a tight trap, on the contrary, will directly give high potential energies to the atoms that are away from the trap center (Figure 5.22b). As a result, the atoms oscillate, rising the temperature. Optimally, we abruptly turn on the trap that is just high enough to capture all the atoms, then adiabatically ramp up the laser power, thus the trap depth and trap frequency, to the final value (2 W, corresponding to a 24 kHz transverse trapping frequency, Figure 5.20a) as depicted in Figure 5.22c.

In the meantime, we turn on in a similar manner the “plugs”, made of two 1 μm -wavelength Gaussian beams of 30 μm waist, propagating along Oy , crossing the Laguerre-Gaussian beam (Figure 5.16). These two plug beams form two barriers confining the atoms along Ox . One of the barriers is of 4 MHz height, slightly higher than the other, of 3 MHz. We quickly compress the chain by reducing the distance L between the two “plugs” from its initial value of 1 mm down to 0.5 mm as shown in Figure 5.20a. This fast compression helps to save time without significantly modifying the loading efficiency into the optical lattice later.

As can be seen in Figure 5.21, when abruptly turning on the trap, the kinetic energy of the atoms slightly increases. However, some of the atoms can easily escape out of the trap at this initial times, taking away with them a part of the van der Waals interaction energy. As the result, the remaining atoms are cooled down. The kinetic energy is decreased. As soon as the trap is tight and deep enough, there is no more atom escape. The chain is compressed, building up the interaction energy, and thus also the kinetic energy of the atoms.

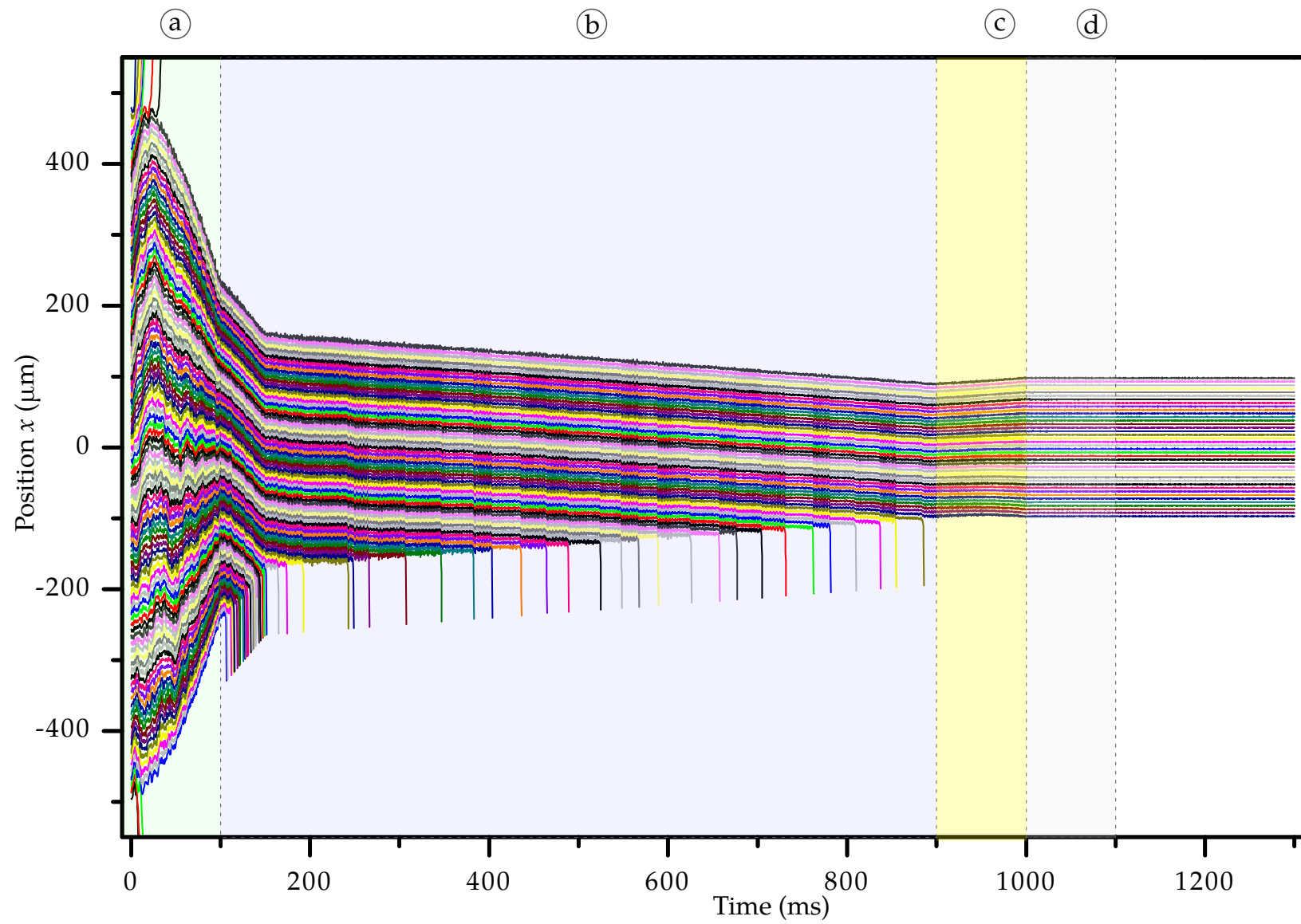


Figure 5.19 A typical trajectory of the atoms during the chain preparation. The process is divided into four steps: a) Turning on of the 1D trap, b) atom evaporation, c) matching the distance and d) loading of the optical lattice.

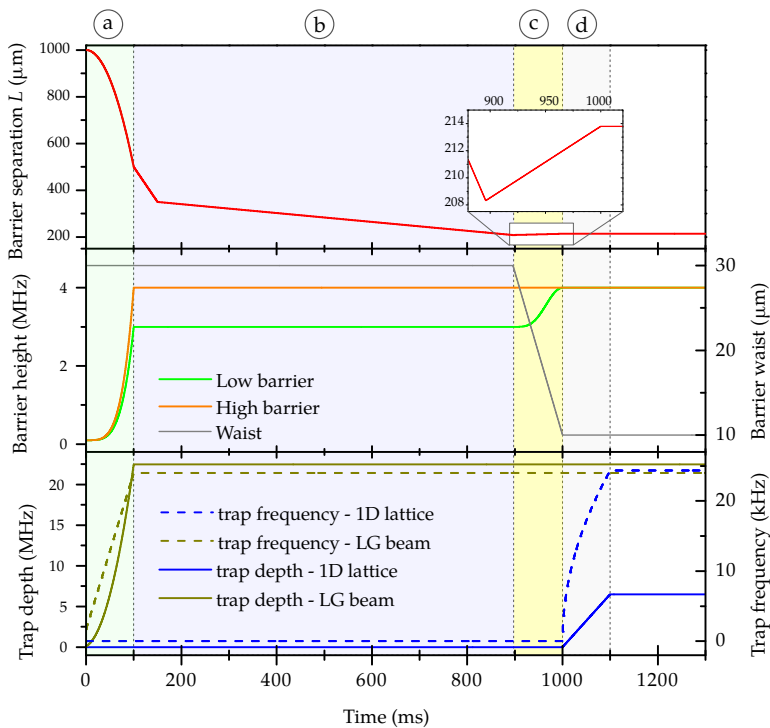


Figure 5.20 Time variation of the laser parameters during a chain preparation. Top: the distance between the two “plug” beams. Middle: the heights of the two “plug” beams are shown on the left axis and their waists are on the right axis. Bottom: the trap depth (left axis) and trap frequencies (right axis) of the Laguerre-Gaussian (LG) and the optical lattice beams.

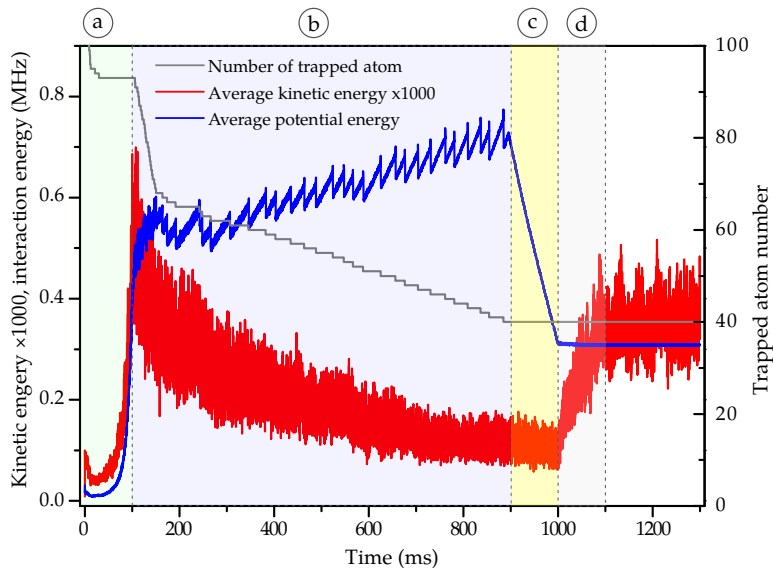


Figure 5.21 Evolution of the average kinetic (red) and van der Waals potential (blue) energies (per trapped atom) during a sequence preparing a chain of 40 circular atoms. The number of trapped atom is also shown on the right axis.

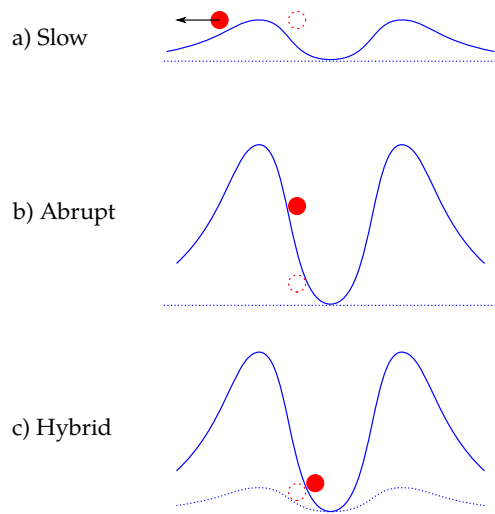


Figure 5.22 Turning on of the Laguerre-Gaussian trapping potential (blue lines). a) Slow switching on of the trap potential leads to a loss of atom. b) Abruptly switching on the trap potential gives the atom a high energy, resulting in significant heating effect. c) An optimized hybrid method to switching on the trap. The trap is turned on to capture the atom, and then adiabatically ramped up to its final value. The dotted open circles and the red filled circles respectively represent the positions of the atoms initially and when the trap reaches its final potential (blue lines).

b) Atom “evaporation”: 100–896 ms

This is the main step to prepare a deterministic number of atoms. We now slowly reduce the distance L between the two “plug” beams. As mentioned previously, the atoms keep being compressed, building up the repulsive van der Waals forces between them. The last atom at the weak “plug” beam is expelled out of the trap as soon as its energy exceeds the height of the barrier. As observed in [Figure 5.23a](#), which is a zoom in of [Figure 5.19](#), the atoms are successively removed one after another in a more or less regular rate.

Assuming that the atoms quickly attain their equilibrium during the atom evaporation, for a distance L of the two “plug” beams, there is a maximum number of atoms $N_{Max}(L)$ that can be trapped in between. As a result, by slowly reducing L , an atom is removed as soon as the number of trapped atoms exceeds $N_{Max}(L)$. In another word, the number of atoms left is $N_{Max}(L)$, which is determined by the final distance L of the two “plug” beams. [Figure 5.23b](#) plots the number of trapped atoms, averaged over 100 trajectories, as a function of L . It takes the shape of a staircase.

However, the atoms have a finite velocity. The escape of the atoms can thus, occur earlier or later than the moment when $N_{Max}(L)$ decreases by one unit. This effect blurs out the staircase. When more atoms are evaporated, the remaining atom chain is significantly cooled down. The staircase becomes sharper. The cooling effect is clearly observed on [Figure 5.21b](#) as a drop of the average potential energy (blue line) at every atom ejection, as well as a global diminution of the average kinetic energy (red line). Here, the thermalization of the chain is possible thanks to the many-body collisions under the van der Waals interaction. Note that, although the van der Waals potential

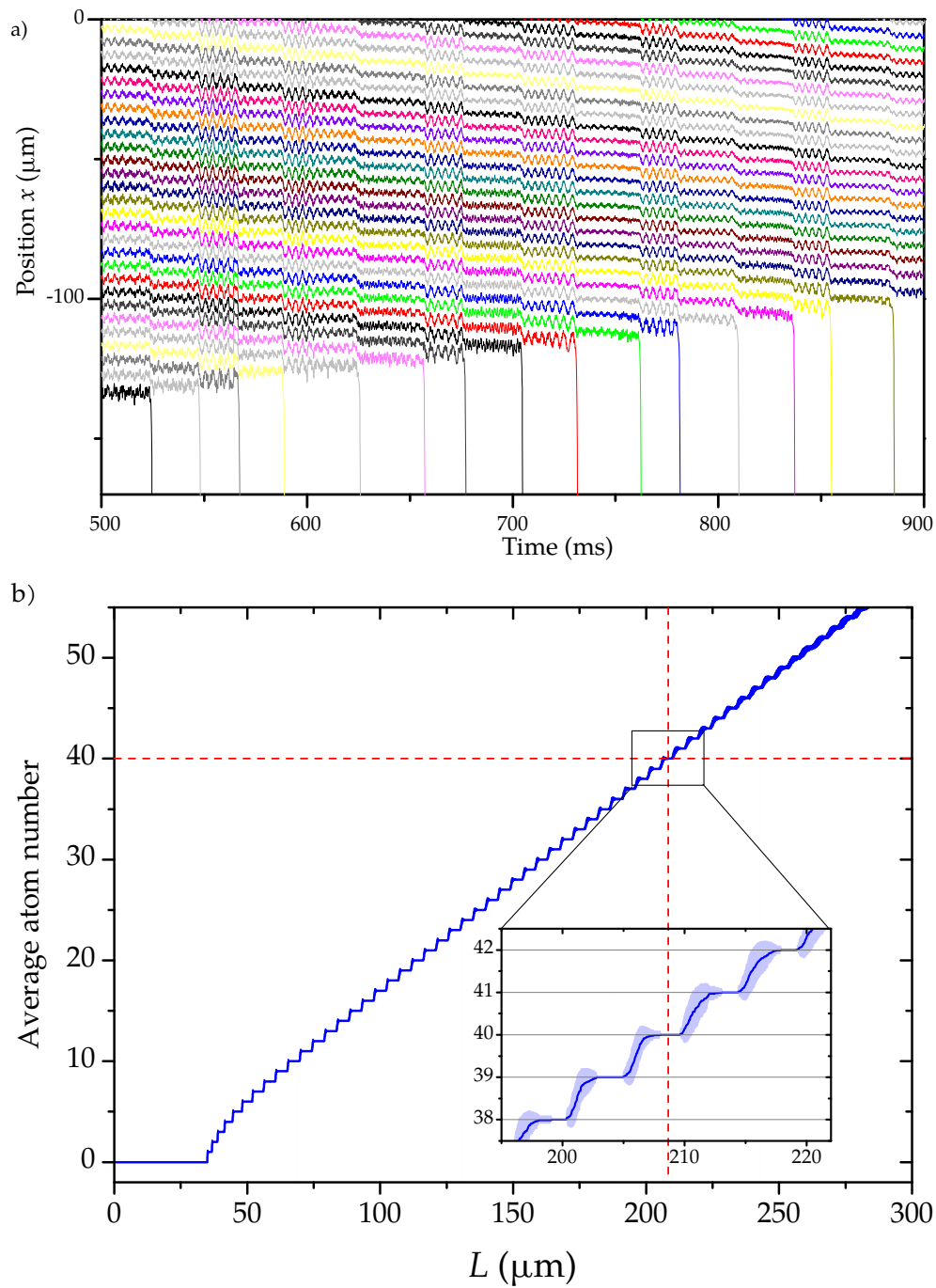


Figure 5.23 a) A zoom in of Figure 5.19 during the atom evaporation. b) Number of atoms left as a function of the distance between two barriers. A chain with up to 43 atoms can be obtained with 100% rate of success.

drops as $1/R^6$, the interaction with the next nearest neighbor is still a few kHz, of the same order of magnitude as the kinetic energy of the atoms.

Figure 5.23b also shows that one can control the number of trapped atoms from 1 to 43 with 100% of success rate. Aiming at a chain of 40 circular atoms, we stop the compression as soon as L reaches 208 μm . The mean inter-site distance is $(4.8 \pm 0.4) \mu\text{m}$.

c) Site matching: 896–1000 ms

This step prepares the transfer of the atomic chain into the optical lattice described previously. The power of the weak barrier is increased up to the same as that of the high barrier (4 MHz), to prevent further atom loss.

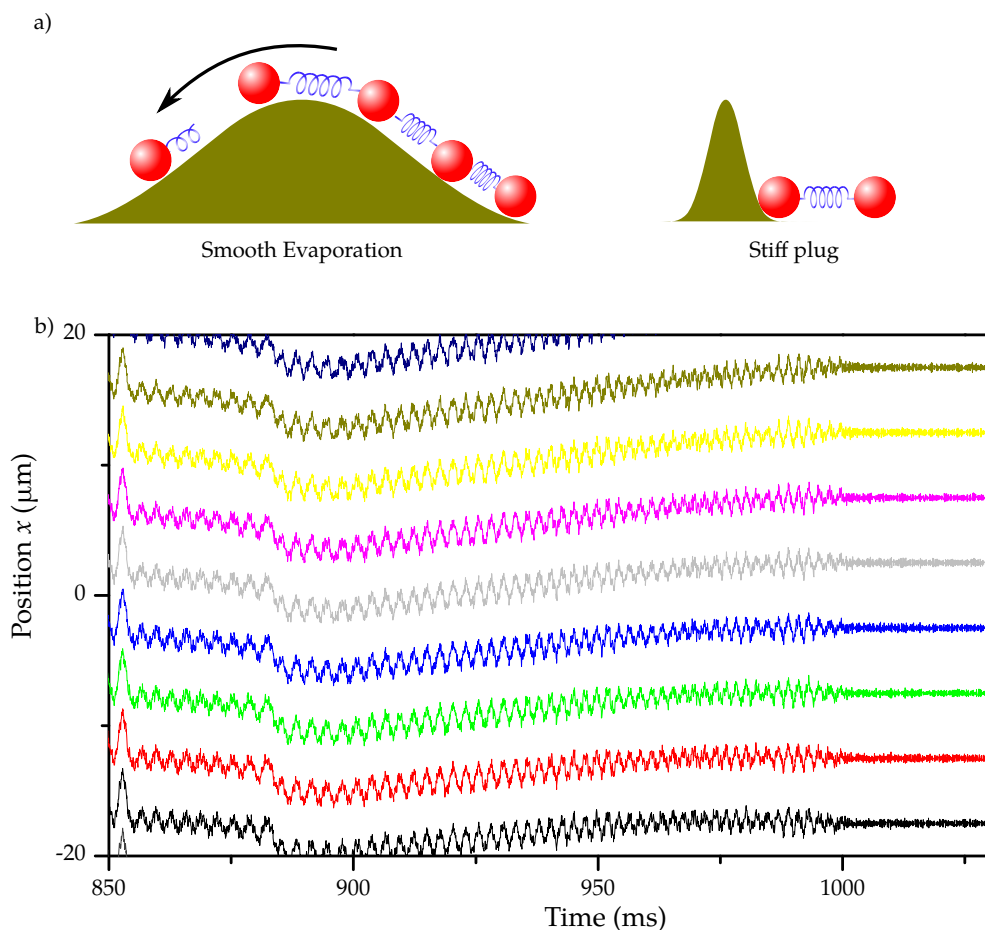


Figure 5.24 a) A large waist helps to smoothen the ejection of atoms during the evaporation while a small waist is more appropriate to fine adjust the position of the atoms. b) The positions of the atoms during the site-matching adjustment.

It is now, important to reduce the waist of the barriers. A large waist during the “evaporation” helps to smoothen the escape of atoms, thus maintaining some adiabaticity as depicted in **Figure 5.24a**. However, we want to push only the atoms at the two ends without disturbing the positions of the neighboring ones. A smaller waist is better. We thus, linearly reduce the waists of the “plug” beams from 30 μm to 10 μm

within $\sim 100 \mu\text{s}$.

In the meantime, we slightly increase L (to $\sim 214 \mu\text{m}$) so that the inter-atomic distance matches the inter-site spacing of the lattice, i.e., $5 \mu\text{m}$. Figure 5.24b plots the x positions of some atoms during this step. As the atoms get apart, from $4.8 \mu\text{m}$ to $5.0 \mu\text{m}$, the van der Waals interaction energy is reduced as represented in Figure 5.21c.

d) Loading of the optical lattice

At this moment, the power of the CO₂ laser is ramped up slowly in 100 ms, putting each circular atom in an individual harmonic well. The final state of a deterministic chain of 40 atoms is reached when the optical lattice has the desired trap frequency (24 kHz). Despite an increase of the temperature during the compression of the lattice, the final temperature is smaller than $1.5 \mu\text{K}$, corresponding to 15 kHz of average kinetic energy as observed in Figure 5.21. The residual oscillation amplitude is 100 nm. This corresponds to about 4 oscillation quanta per mode, knowing that the spatial extension of the ground state wavefunction is $\Delta x_0 = 50 \text{ nm}$. We reach the quantum limit for describing the atomic motion.

Even once the chain is prepared, one should keep the two barriers during the rest of the experiment. They help to compensate for the lack of van der Waals forces acting on one side of the last atoms of the chain, putting their equilibrium positions back to the bottom of the harmonic well.

5.6

Arbitrary chain initialization

As discussed previously, the phase diagram in Figure III.1 can be explored preparing the simulator in the region P_X and let it adiabatically evolve into the exotic phase of interest. In the region P_X , all the spin are polarized along the X direction. This state is obtained by applying a microwave pulse on the chain prepared above to globally rotate all the spins from the Z direction (50C) to the X direction. Thus a local state preparation is not necessary.

However, an arbitrary chain initialization would allow us to study quantum transport in different situations. With trapped circular atoms, individual atom addressing is possible by locally changing the atomic spacing. Two transverse focused laser beams along Oy are used as optical tweezers, slightly displacing the two neighbors of the atom of interest. Its van der Waals energy is accordingly shifted by a few MHz. The microwave transition to the 48C state is thus shifted by the same amount. A few μs microwave pulse will flip the spin of this atom without disturbing the others. The process is repeated where necessary to obtain an arbitrary initialization of the chain. The atoms at the two ends can be selectively addressed without the optical tweezers, since their van der Waals energy is different from that of the “bulk” atoms.

During the initialization process, it might be necessary to stop the exchange interaction. Instead of 48C state, we prepare the corresponding atoms in the 46C state. The exchange interaction between the 50C and 46C is below 5 mHz at a distance of $5 \mu\text{m}$. At the end, a hard microwave pulse brings the 46C atoms to the 48C state.

5.7

Site-resolved state-selective detection

The simulation result is read out by detecting the final state of the individual atoms. We need to first freeze the evolution of the spin chain at a chosen time by halting the exchange interaction. This is done by applying fast, strong microwave pulses, transferring the $48C$ state towards the $46C$ state, with which the exchange interaction of the $50C$ is negligible[§]. The two barriers are again set to uneven heights. One resumes the compression of the chain. The atoms are evaporated one after the other. They are guided to the region D shown in [Figure III.2](#) where the atoms can be state selectively detected by field ionization. Note that, during the simulation, the electric field F applied on the spontaneous-emission inhibition capacitor is varied between 2 and 7 V/cm. If one transfers the $48C$ atoms to the $46C$ state at an electric field of about 4 V/cm, the strong mixing of the $|46C; 50C\rangle$ state with nearby elliptical pair states will strongly reduce the lifetimes of the $46C$ and $50C$ states ([Figure 5.14](#)). To avoid this detrimental mixing, one has to lower the electric field F to ~ 2 V/cm before sending atoms to the $46C$ state. The repulsive interactions between the $46C - 46C$, $46C - 50C$ and $50C - 50C$ atoms are of the same order of magnitude, thus preventing the atoms from getting too close during the compression, which can lead to the ionization of the atoms.

The above scheme directly measures σ_Z of each atoms. Additional spin-spin correlation functions can be constructed by applying a hard pulse on the $48C - 50C$ transition before stopping the exchange interaction.

5.8

Effects of decoherence

For a quantum simulator, the longer coherence time, the better. We discuss here three main sources of decoherence: the Stark effect, the average of the trapping potential due to a finite site of the atoms and the spin-motion entanglement.

Stark effect

As discussed in [section 3.3](#), stray fields due to contact potential between Rubidium and the metallic surfaces of the the capacitor could be a problem. A study of the electric field in the vicinity of the atom chip, represented in Carla Hermann's thesis, estimates a residual electric field smaller than 0.05 V/cm, with a gradient of about 0.4 V/cm² at ~ 1 mm away from the metallic surfaces. The differential Stark shift of the $48C - 50C$ levels is of 560 kHz/(V/cm²). Taking into account the $\sim 200\ \mu\text{m}$ extension of the chain with 40 atoms, we estimate a maximum difference in the $48C - 50C$ transition frequency between the last atoms at the two ends to be about 50 Hz. At a distance of 5 μm , the exchange frequency ($4J$) is about 70 kHz. The Stark broadening is thus negligible at the scale of the exchange frequency.

[§]Alternatively, one can send the $50C$ atoms to the $52C$ state. The $48C - 52C$ exchange interaction is also negligible (<15 mHz).

Average of trapping potential

The ponderomotive energy acts on the electron as a nearly free charge. It does not depend on the principal quantum number n , at least for a uniform intensity. However, the trapping potential (created by the transverse Laguerre-Gaussian beam and the standing-wave optical lattice) is averaged over the electronic orbital. The radius of the circular orbital is $n^2 a_0 \approx 130$ nm for the 50C and ≈ 120 nm for the 48C states. The 50C and 48C atoms, due to their different sizes, experience different potentials. This leads to a shift in the 48C – 50C transition frequency, which depends on the position of the atoms. The spatial extension of the atoms thus gives rise to a broadening of the transition line. We numerically calculate and plot this shift as a function of the atom position (note that the trap is isotropic) in [Figure 5.25](#). The simulation of the chain preparation estimates the residual oscillation of the atoms in the optical lattice to be about 100 nm (see above). This corresponds to a line broadening of about 8 Hz, which is negligible at the scale of the exchange frequency. Note also that, the decoherence

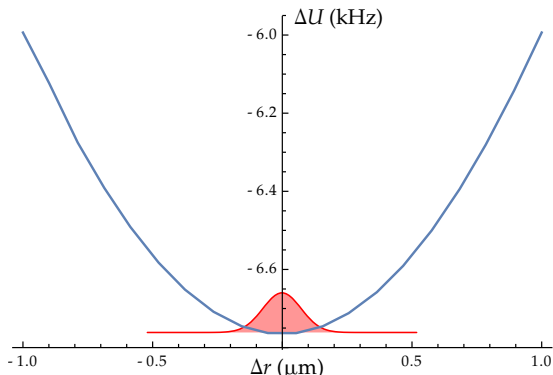


Figure 5.25 The frequency shift of the 48C – 50C transition as a function of the atom position. The extension of the atom is represented by a red shaded Gaussian profile.

due to the Stark effect and the averaging of the trapping potential can be suppressed using the Hahn spin-echo technique (see [section 3.3](#)).

Spin-motion entanglement

The entanglement between the motional and spin (atomic) states, induced by the exchange interaction, can lead to a collapse of the exchange oscillation. Let us consider two atoms in two adjacent sites. Initially they are in the 50C state and at the bottom of the trap. Suddenly flipping an atom to the 48C state makes the excitation (48C state) transfer back and forth between the two atoms. Using the formula (E.25) derived in [Appendix E](#), [Figure 5.26](#) plots the probability of detecting the first atom in the 48C state, as a function of time. The modulation of the exchange oscillation is thus small. The effect can be further reduced by tighten the trap. The spin-motion entanglement with more than two atoms would be an interesting problem to study.

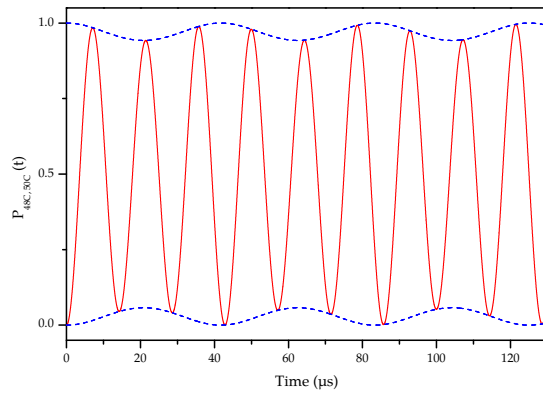


Figure 5.26 Probability of being in the 50C state for a pair of atoms initially in the $|50C; 48C\rangle$ state, calculated using (E.25). The dashed line show the envelop of the oscillation.

Summary

We have presented a full experimental scheme to realize a quantum simulator of the XXZ model for a 1D spin chain. It is based on the groundbreaking concept of trapping circular Rydberg atoms. Extremely long-lived spin chains are provided using spontaneous emission inhibition in a cryogenic environment. We also proposed an innovative method to prepare deterministically a chain with up to 40 atoms, pushing the capacity of the simulator out of the grasp of classical computation. Arbitrary chain initialization and site-resolved state-selective detection are also proven to be realistic, allowing the proposed system to address much larger range of 1D physics.

Conclusion and perspectives

“Ce qui embellit le désert, dit le petit prince, c'est qu'il cache un puits quelque part...”

— Antoine de Saint-Exupéry, *Le petit prince*

Towards quantum simulation with low angular momentum Rydberg atoms

During this PhD work, we were interested in building quantum simulators based on Rydberg atoms. Our first direction was to study the physics of Rydberg excitation in a ultra-cold atomic cloud. With the available experimental setup, we trapped and cooled ^{87}Rb atoms down to sub μK temperature using a superconducting atom chip. The excited Rydberg atoms are protected from blackbody radiation. Coating the chip with a layer of rubidium provided us with a good control of the electric field at the chip vicinity. We observed unprecedented long coherence times for Rydberg atoms near a metallic surface.

The study of the Rydberg excitation under strong blockade regime led us to several important results. First we developed a novel tool to precisely measure the distribution energy of an interacting Rydberg ensemble. This technique is based on probing the shift of the microwave transition frequency towards a nearby Rydberg level. We successfully observed the hydrodynamic expansion of a Rydberg cloud under the repulsive van der Waals forces between the atoms, and thus measured the limit of the frozen Rydberg gas approximation.

With the obtained experimental data, we used numerical approaches to have an insight into the Rydberg excitation process. The first simple Monte Carlo model was not powerful enough. We developed another more rigorous model that allowed us to reproduce most of the observed experimental data, both the optical excitation profiles and the microwave spectra. Note that the excitation was limited to the incoherent flipping of the atoms. An improvement in the power of the blue excitation laser would allow us to exploit the coherent collective behavior of the atomic cloud. This is one interesting direction to follow.

Being fascinated by quantum simulations, we investigated quantum transport in a 1D chain of low angular momentum number Rydberg atoms. A careful consideration pointed out that a regular chain, even as short as of a few atoms, is difficult to prepare based on the facilitated excitation effect. However, these studies led us to the new concept of building quantum simulators based on circular Rydberg atoms.

Towards quantum simulation with a 1D chain of trapped circular atoms

Elaborating on the unique properties of circular Rydberg atoms, we proposed a new platform for quantum simulation. It is based on a groundbreaking concept: the use of laser-trapped circular Rydberg atoms. We have performed numerical simulations and examined many technical details to make the proposal realistic. Its main features can be summarized as follows

1. Extremely long-lived circular atoms, with lifetimes in the minutes range, by the inhibition of spontaneous emission in combination with protection from black-body radiations.
2. Strong interaction between the circular atoms and tuneability of the interactions. The corresponding XXZ spin Hamiltonian is fully tunable over a wide range by microwave dressing and electric field variation.
3. Innovative deterministic preparation of a chain based on the repulsive interaction between the atoms. A long chain up to 40 atoms is reachable.
4. Laser-trapping by ponderomotive force acting on the Rydberg electron. Atom positions are thus well controlled at sub- μm precision.
5. Detection of any spin observable. The chain evaporation together with field ionization allows site-resolved state-selective detection of all spins.

In addition, the ability of arbitrary initialization of the spin chain enlarges the addressable range of quantum simulations with a trapped circular atoms. It opens a new avenue for quantum simulations. An experimental realization of the proposed system would lay a landmark in the evolution of quantum simulators.

In the following we discuss our short-term targets towards quantum simulations as well as some extensions and several physical domains that can be simulated using trapped circular atoms.

Beyond the grasp of the classical computation methods

Upgrades of the 1D system

Active cooling of a spin chain

From an experimental point of view, heating of the atoms is technically inevitable. In our proposed system, it may come from the fluctuations of the trapping-laser powers, which are translated into the fast variations of trap frequencies. It may also come from the micro-vibrations of lenses and mirrors which finally shake the trapped atoms. In addition, if the adiabaticity throughout the deterministic chain preparation is somehow violated, we will end up with a “hot” atom chain. Thermal motion of the atoms could wash out coherence between them. Thus, an active cooling mechanism would help to suppress these bothersome effects.

One way to include cooling into our system is to maintain a source of cold atoms in low angular momentum Rydberg state at the two ends of the final chain. These atoms can be excited from two clouds of ultra cold ground state atoms trapped in two optical

tweezers. The dipole-dipole interaction between the 50C chain atoms and the short-lived low l Rydberg atoms will transfer kinetic energy out of the chain. After a few cycles of Rydberg excitation, the whole chain can be cooled down close to its ground state of motion. A further study is necessary to determine which low- l Rydberg level is relevant.

2D network of spins

The use of laser-trapped atoms makes it rather easy to extend the system to 2D geometries. A straightforward method is to prepare several 1D chains and bring them together into a 2D configuration. The 1D standing-wave along Ox is shared between the chains. At the end, one obtains a 2D square lattice, either parallel or perpendicular to the quantization axis Oz . The latter leads to an isotropic Rydberg interaction while the former is an anisotropic interacting lattice.

A hexagonal lattice can also be achieved. Circular atoms are first confined in between two laser light sheets. Four plug beams are added up, forming a 2D square trap. One of the barrier is weaker than the others. Reducing the distances between the four beams will induce the atom evaporation. The final number of trapped atoms should be determined by the final relative positions of the beams. The atoms self-order into a 2D Wigner crystal similar to that in 2D Penning ion trap [64]. The crystal is then transferred into a hexagonal optical lattice [177].

Quantum simulation with trapped circular atoms

We sketch here several specific problems that are addressable with trapped circular atoms. They can range from few-particle physics, which are numerically solvable to benchmark the system, to many-body dynamics beyond the grasp of classical computation power.

Quantum transport along a spin chain

As soon as a regular chain of atoms can be realized, site-resolved state-selective detection of the spins would make the study of quantum transport possible. Due to the border effect, one or both ends of the chain is microwave promoted into the 48C state. Exchange interaction with the neighboring 50C atoms will propagate the excitation along the chain.

Local addressing of the initial spin states allows one to excite an atom in the middle of the chain into the 48C state. The probability amplitudes of being excited symmetrically propagates to the two ends, bounce and return to the initial position, where they interfere and make the excitation revive. [Figure 3a](#) represents a transport of an 48C excitation over a perfectly regular chain with 41 atoms as an example. Initially all the atoms are in the 50C state. One flips the 21th atom to the 48C state and calculates the excitation probability for each atom (color scale).

Furthermore, one can prepare a chain with several excited atoms. Quantum transport with multiple excitations in a long chain is not easy to predict with classical computation. The strong 48C – 48C interaction between the excitations would lead to non-trivial quantum transport.

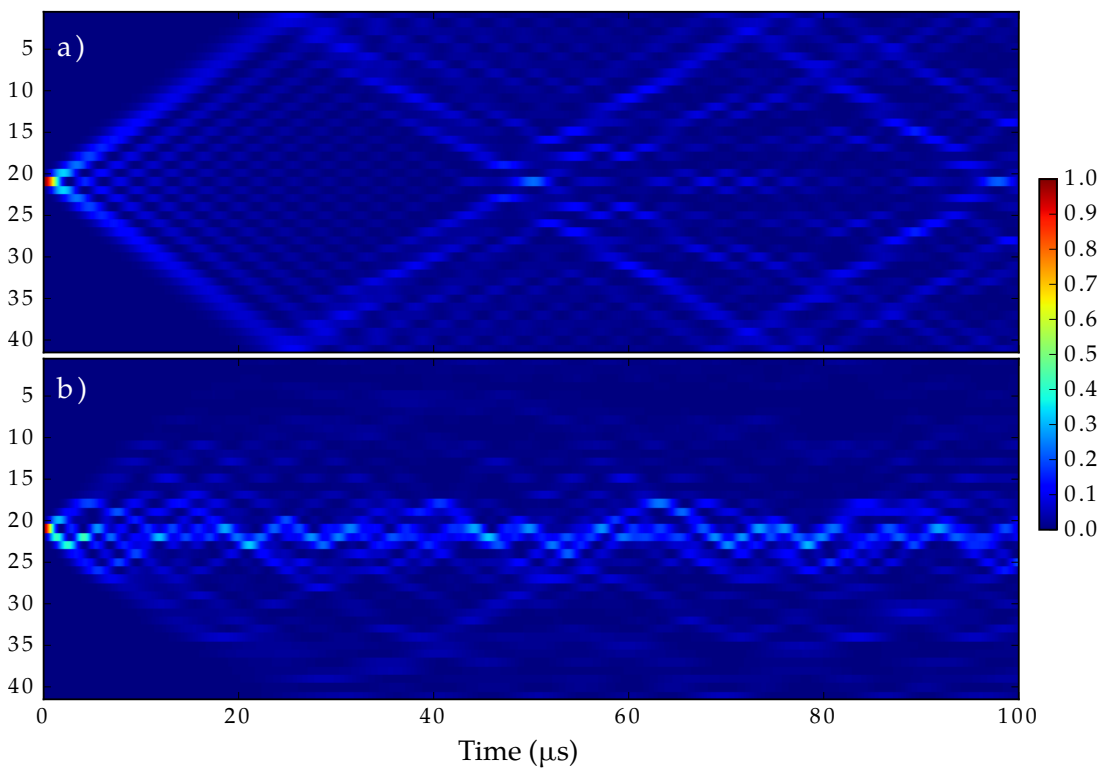


Figure 3 Excitation transport on a 1D chain with 41 atoms. a) The atoms are regularly separated by 5 μm . b) The deviation of the atom from the trap center is a Gaussian profile of 0.5 μm width. Initially all the atoms are prepared in the 50C state, but the 21th one in the 48C state.

Disorder and localisation

Imprinting a laser speckle pattern, one can introduce disorder into the chain. Tuning the relative strength of the disorder and the interaction will allow us to realize the phase transition from conducting state (non-localized state) to isolating state (localized state) as the disorder increases. Figure 3b represents as an example the time evolution of a chain with 41 atoms, whose positions deviate from the trap center by an amount randomly sorted from a Gaussian profile of 0.5 μm width. The excitation is “trapped” in the middle of the chain. Our model would provide a tool to study the many-body localization from the point of view of level statistics, which can be measured using our microwave tool (see chapter 4). Signatures of chaoticity of the Hamiltonian can also be looked for.

Slow dynamics and quenches

The phase diagram of the XXZ spin Hamiltonian is of great interest. Its structure has been theoretically predicted as shown in Figure III.1. With trapped circular atoms, by adiabatically varying Ω and/or J_Z , we will systematically reconstruct the phase diagram. A comparison between experimental results and theoretical prediction would give us an insight into the nearest neighbor spin chain.

Moreover, taking advantage of the long-lived chain and the fully controlled Hamiltonian, for instance, by slowly modifying the spin chain state, in a time scale much

longer than $1/(4J)$, one could investigate adiabatic processes in the quantum mechanical regime. It would provide insights into the limitations of adiabatic quantum computing [178].

For sudden changes of the Hamiltonian parameters, the evolution of the system after the quench is rather complex since it involves highly excited states of the final Hamiltonian [179]. Predictions using classical computation methods are difficult tasks since they involve a large portion of the Hilbert space. Studying this non-trivial dynamics requires a flexible quantum simulator such as trapped circular atoms.

Spin dynamics and atomic motion

In the described system, atomic motion has negligible influence on the spin states. However strong spin-motion entanglement can be created by either loosening the trap or using resonant exchange interaction between nC and $(n + 1)C$ states. By coupling the spin chain with a phonon bath, interesting behavior of the spin chain dynamics in the presence of dissipation can be studied with controlled parameters. The transport of entanglement, beyond that of electronic excitation, would be possible in a similar context to that in [180, 181].

2D physics

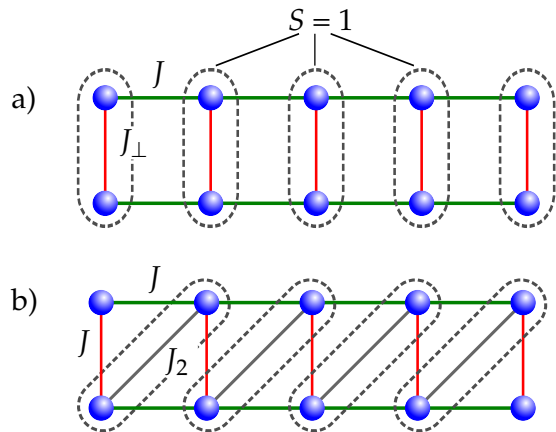


Figure 4 Two different mappings to realize an effective $S = 1$ chain from two coupled $S = 1/2$ Heisenberg chains. Figure extracted from [182].

The realization of 2D-spin networks would open more possibilities to simulate problems where modelization and numerical approaches are challenging. As an example, a square lattice with properly tuned anisotropic interactions would lead to a situation in which anti-ferromagnetic chains are ferromagnetically coupled (Figure 4). Such a 2D lattice is mapped onto an equivalent spin-one chain in the Haldane phase [182]. Its non-trivial topological order has not yet been probed from many-body measurements. The discovery of this topological phase was awarded the Nobel prize in 2016.

Realization of first building blocks for quantum simulation with trapped circular atoms

With these ideas in mind, we will step by step conduct proof-of-principle experiments to demonstrate the main features of quantum simulation with trapped circular atoms. Installing atom-circularization electrodes inside the present setup, we would be able to prepare an ensemble of $50C$ atoms. Successfully trapping them with a Laguerre-Gaussian $1\text{ }\mu\text{m}$ -wavelength laser beam will encourage us with the proposed scheme.

The demonstration of extremely long-lived circular Rydberg atoms would be then possible by placing the trapped ensemble of $50C$ atoms in between capacitor plates. An extra modification of the current cryostat in order to operate with liquid ^3He is necessary. At this point, a long coherence time for the $48C - 50C$ transition will be probed. If successful, these long-lived strong interacting qubits by themselves will find their applications in quantum information processing such as quantum gates based on the dipole blockade mechanism extended to circular atoms.

Adding two plug beams will allow us to prepare a deterministic chain of circular atoms. If the protocol works, even with a short chain, it provide us a tool to benchmark our quantum simulator. Microwave spectroscopy probing of the van der Waals interaction energy of the chain under different static electric fields will prove the tuneability of the spin Hamiltonian.

A site-resolved detection of the spin states if successfully implemented, will be the final validation of our proposal. We would be able to simulate the quantum transport with one or multiple excitations as well as explore the phase transition of the XXZ spin Hamiltonian. Furthermore, we would be able to push quantum simulations with trapped circular atoms beyond the grasp of classical computation methods.

Appendices

Electric dipole matrix element estimation



The electric dipole matrix element can be written as in (1.23) and (1.22), as a product of a radial part $\langle n' l' m' | r | n l m \rangle$ and an angular part $\langle l' (j') m'_{l(j)} | Y_1^q | l (j) m_{l(j)} \rangle$. Here we show how to calculate each of them using numerical methods.

A.1

Radial matrix element

We rewrite the Schrödinger equation (1.26) for the radial wavefunction R of an electron in the Coulomb potential

$$\frac{\partial^2 R}{\partial r^2} + \frac{2}{r} \frac{\partial R}{\partial r} + \left[2E_{n^*} + \frac{2}{r} - \frac{l(l+1)}{r^2} \right] R = 0 \quad (\text{A.1})$$

We follow the procedure of Zimmerman *et al.* [183] by making the substitutions

$$x = \ln(r) , \quad (\text{A.2})$$

and

$$Y(x) = R\sqrt{(r)} \quad (\text{A.3})$$

into (A.1). We obtain

$$\frac{d^2 Y}{dx^2} = g(x)Y(x) , \quad (\text{A.4})$$

where

$$g(x) = 2e^{2x}(-e^{-x} - E_{n^*}) + \left(l + \frac{1}{2} \right)^2 . \quad (\text{A.5})$$

Equation (A.4) can be numerically solved by the Numerov algorithm [184]. We need to provide E_{n^*} , l and two initial guesses of R explicitly. Knowing the radial wavefunctions, one can obtain the radial matrix element with no difficulty.

A.2

Angular matrix element

The angular matrix element is developed into an analytical form using a Clebsch Gordan coefficient and the Wigner-Eckart theorem [185]:

$$\begin{aligned} \langle l' m'_l | Y_1^q | l m_l \rangle &= \langle l' \| Y_1 \| l \rangle \langle l' m'_l | l 1 m_l q \rangle \\ &= \langle l' \| Y_1 \| l \rangle (-1)^{l'-m'_l} \sqrt{2l'+1} \begin{pmatrix} l' & 1 & l \\ -m'_l & q & m_l \end{pmatrix}, \end{aligned} \quad (\text{A.6})$$

where $\langle l' \| Y_1 \| l \rangle$ is the reduced matrix element and the Clebsch Gordan coefficient is written in terms of Wigner 3-j symbol. For low l states, one has to include the fine structure. The angular matrix element is written as

$$\langle l' j' m'_j | Y_1^q | l j m_j \rangle = \langle j' \| Y_1 \| j \rangle (-1)^{j'-m'_j} \sqrt{2j'+1} \begin{pmatrix} j' & 1 & j \\ -m'_j & q & m_j \end{pmatrix}. \quad (\text{A.7})$$

Factoring out the j and j' dependence of the reduced matrix element into a Wigner 6-j symbol, and a reduced matrix element that depends only on l and l' , we get

$$\begin{aligned} \langle j' \| Y_1^q \| j \rangle &= \langle l' s' j' \| Y_1^q \| l s j \rangle \\ &= \delta_{ss'} \sqrt{2j+1} \sqrt{2l'+1} (-1)^{1+s'+j+l'} \begin{Bmatrix} j' & 1 & j \\ l & s' & l' \end{Bmatrix} \langle l' \| Y_1^q \| l \rangle, \end{aligned} \quad (\text{A.8})$$

where $s = s' = 1/2$. Knowing that

$$\langle l' \| Y_1^q \| l \rangle = (-1)^{1-l} \sqrt{\frac{3}{4\pi}} \sqrt{2l+1} \begin{pmatrix} l & 1 & l' \\ 0 & 0 & 0 \end{pmatrix}, \quad (\text{A.9})$$

The angular matrix elements (A.6) and (A.7) can be expressed using (A.8) and (A.9) as

$$\begin{aligned} \langle l' m'_l | Y_1^q | l m_l \rangle &= (-1)^{1-l+l'-m'_l} \sqrt{\frac{3}{4\pi}} \sqrt{(2l+1)(2l'+1)} \times \\ &\quad \times \begin{pmatrix} l' & 1 & l \\ -m'_l & q & m_l \end{pmatrix} \begin{pmatrix} l & 1 & l' \\ 0 & 0 & 0 \end{pmatrix} \end{aligned} \quad (\text{A.10})$$

and

$$\begin{aligned} \langle l' j' m'_j | Y_1^q | l j m_j \rangle &= (-1)^{1+s'+j'+j-m'_j} \sqrt{\frac{3}{4\pi}} \sqrt{(2j+1)(2j'+1)(2l+1)(2l'+1)} \times \\ &\quad \times \begin{Bmatrix} j & 1 & j' \\ l' & 1/2 & l \end{Bmatrix} \begin{pmatrix} j' & 1 & j \\ -m'_j & q & m_j \end{pmatrix} \begin{pmatrix} l & 1 & l' \\ 0 & 0 & 0 \end{pmatrix}. \end{aligned} \quad (\text{A.11})$$

The Wigner 3-j symbol is estimated using Racah formula [186, 187]

$$\begin{pmatrix} a & b & c \\ \alpha & \beta & \gamma \end{pmatrix} = (-1)^{a-b-\gamma} \sqrt{\Delta(abc)} \times \times \sqrt{(a+\alpha)!(a-\alpha)!(b+\beta)!(b-\beta)!(c+\gamma)!(c-\gamma)!} \times \times \sum_t \frac{(-1)^t}{f(t)}, \quad (\text{A.12})$$

where

$$f(t) = t! (c-b+t+\alpha)! (c-a+t-\beta)! (a+b-c-t)! (a-t-\alpha)! (b-t+\beta)! . \quad (\text{A.13})$$

The sum runs over all integers t for which the factorial in $f(t)$ all have non-negative arguments. Similarly for the Wigner 6-j symbols

$$\left\{ \begin{matrix} a & b & c \\ \alpha & \beta & \gamma \end{matrix} \right\} = \sqrt{\Delta(abc)\Delta(a\beta\gamma)\Delta(\alpha bc)\Delta(\alpha\beta c)} \times \sum_t \frac{(-1)^t(t+1)!}{g(t)}, \quad (\text{A.14})$$

where

$$\begin{aligned} g(t) = & (t-a-b-c)! (t-a-\beta-\gamma)! (t-\alpha-b-\gamma)! (t-\alpha-\beta-c)! \times \\ & \times (a+b+\alpha+\beta-t)! (b+c+\beta+\gamma-t)! (c+a+\gamma+\alpha-t)! . \end{aligned} \quad (\text{A.15})$$

The sum also runs over all integers t for which the factorial in $g(t)$ all have non negative arguments.

In both formulae, $\Delta(abc)$ is a triangle coefficient given by

$$\Delta(abc) = \frac{(a+b-c)!(a-b+c)!(-a+b+c)!}{(a+b+c+1)!} . \quad (\text{A.16})$$

To speed up the numerical estimation of the factorials, one can use Stirling's approximation of the factorial for large arguments N

$$\ln N! \approx N \ln N - N + \ln(\sqrt{2\pi N}) . \quad (\text{A.17})$$

Laser frequency stabilization and laser distribution

B

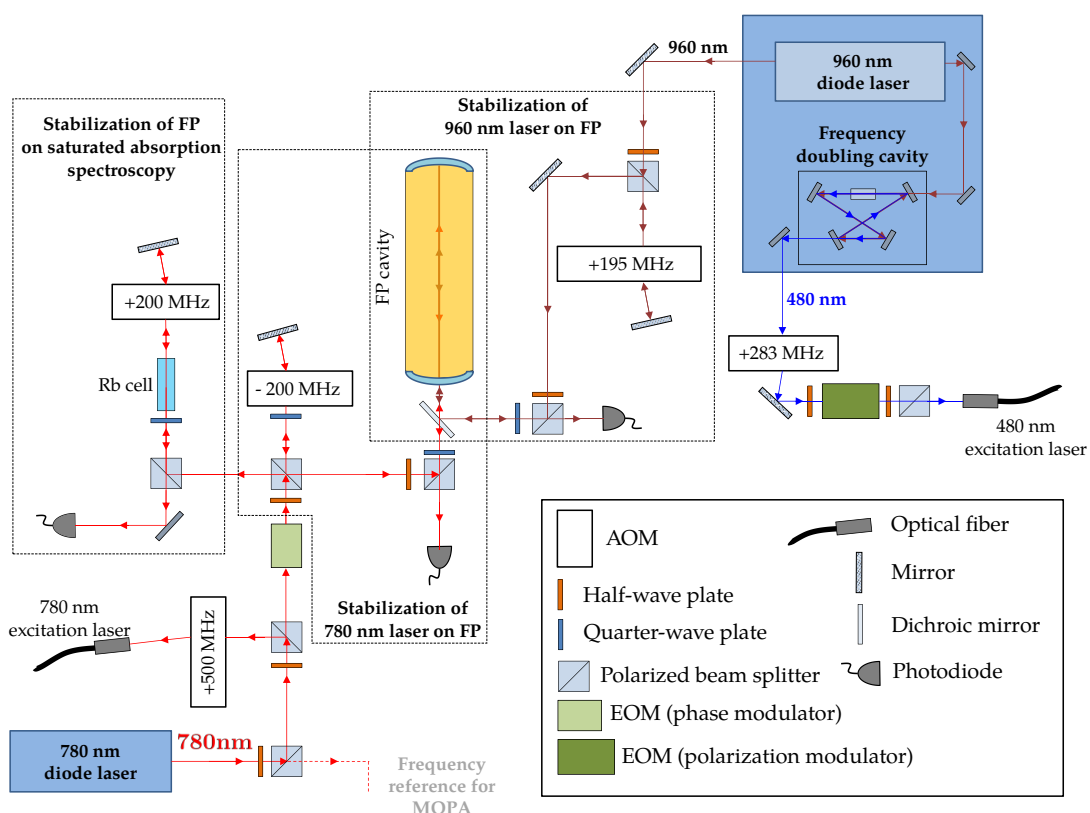


Figure B.1 Scheme of laser frequency stabilization for the 780 nm and 480 nm wavelength excitation lasers.

Figure B.1 depicts the scheme used to stabilize the lasers. The 780 nm-wavelength excitation laser is a Toptica DL Pro laser. The 480 nm-wavelength laser is provided by a Toptica TA-SHG 110, which consists in a Master oscillator power amplifier (MOPA) at 960 nm wavelength, followed by a frequency doubling cavity. Both the 780 nm and the 960 nm laser are frequency stabilized to a reflection peak of a Fabry-Perrot cavity,

whose length is stabilized to the crossover of the $F = 2 - F' = 2$ and $F = 2 - F' = 3$ transitions. In order to lock the laser frequencies, modulations at 20 MHz are applied on the phase of the 780 nm laser using an EOM, and on the current through the 960 nm laser diode (frequency modulation). Note that the resulting sidebands of the 960 nm laser is filtered out by the phase matching condition of the frequency doubling cavity.

As depicted in Figure B.2, the lasers necessary for the trapping and cooling of ^{87}Rb atoms are extracted from a Toptica TA-110 780 nm-wavelength MOPA. The 780 nm MOPA is ~ 160 MHz frequency-offset from the 780 nm excitation laser. Another laser whose frequency is stabilized to the $F = 1 - F' = 2$ transition, is used to repump the atoms that are scattered out of the cooling cycle into the $F = 1$ state.

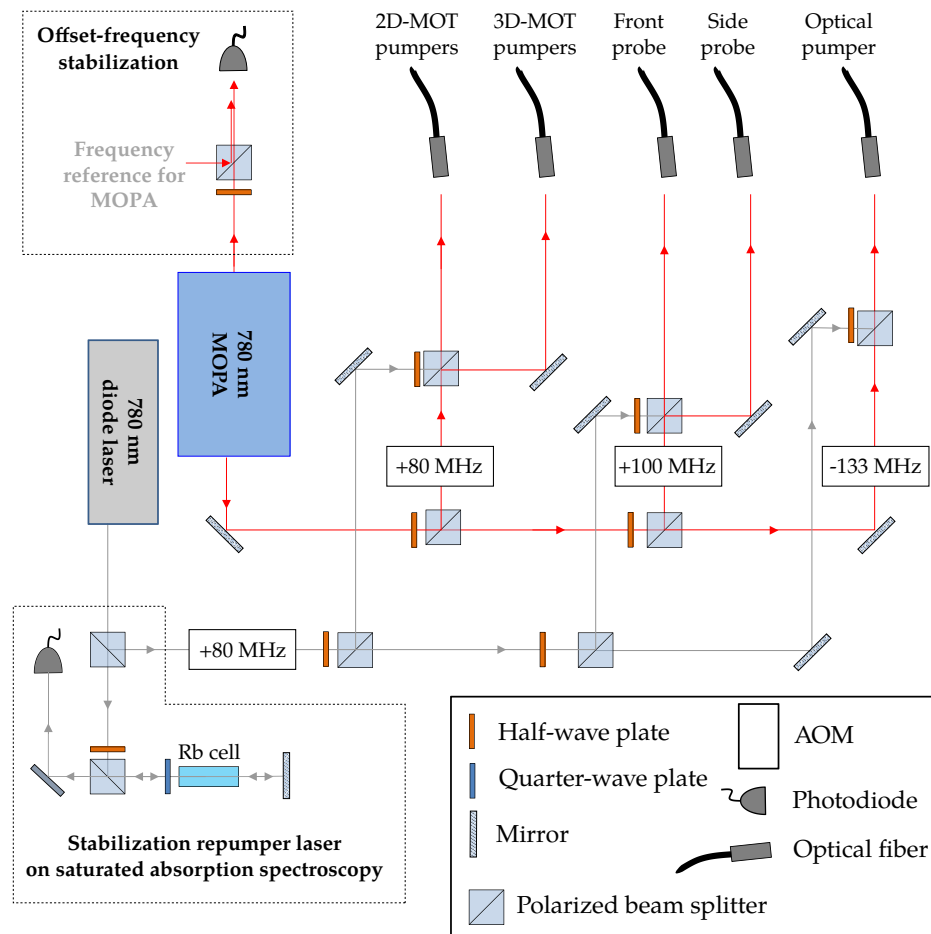


Figure B.2 Distribution of lasers for cold atom experiment. The superposition with repumping lasers (gray) is also shown.

Measurement of the trap dimension



Our imaging systems have a limited spatial resolution of about $\sim 10 \mu\text{m}$. The dimensions of a dense atomic cloud is, in general, below this limit. A direct *in situ* imaging cannot give a good enough estimation. Another approach is making use of the relation

$$M\omega_i^2\sigma_i^2 = k_B T, \quad (\text{C.1})$$

where ω_i and σ_i are the trap frequency and the trap width ($e^{-1/2}$ position) along the i direction. We need thus to measure the cloud temperature T and the trap frequencies.

C.1

Temperature measurement

The temperature is measured using the time-of-flight technique, which maps the momentum distribution into a spatial distribution according to

$$\sigma_i^2(t) = \sigma_i^2(0) + \Delta v_i^2 t = \sigma_i^2(0) + \frac{k_B T}{M} t^2, \quad (\text{C.2})$$

where t is the free fall duration from rest. Measuring the trap size at different times t allows us to extract the temperature T . For the trap described in chapter 4, the measurement gives $T = 500 \pm 150 \text{ nK}$.

C.2

Trap frequencies

Giving a small kick to the atomic cloud (for example instantaneously moving the trap center and then going back), makes the cloud oscillate around the trap bottom. The oscillation frequencies are the trap frequencies along the three main axes, given that the oscillation amplitudes are small. Experimentally, the position of the cloud after the kick is sampled as a function of time. Its Fourier transform reveals the main trap

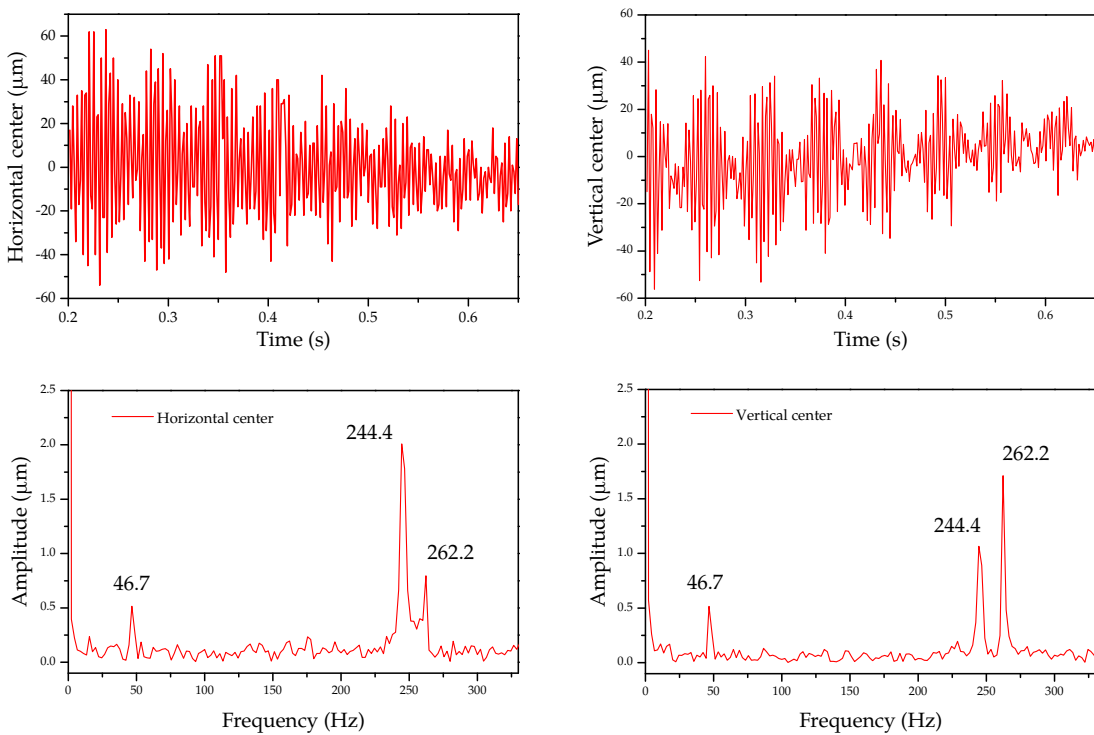


Figure C.1 Trap frequency measurement. Top: the position of the atomic cloud as a function of time after the kick along the horizontal and the vertical direction (relative to the camera). Lower: The corresponding Fourier transform of the cloud position. The probe beam is sent along the x direction.

frequencies as shown in Figure C.1. They are

$$\begin{aligned}\omega_x &= 2\pi \times 46.7 \text{ Hz} \\ \omega_y &= 2\pi \times 244.4 \text{ Hz} \\ \omega_z &= 2\pi \times 262.2 \text{ Hz}.\end{aligned}\tag{C.3}$$

Plugging into equation (C.1) we obtain the trap dimension of

$$\begin{aligned}\sigma_x &= 2\pi \times 23.6 \mu\text{m} \\ \sigma_y &= 2\pi \times 4.5 \mu\text{m} \\ \sigma_z &= 2\pi \times 4.2 \mu\text{m}.\end{aligned}\tag{C.4}$$

Fourier limited line width

D

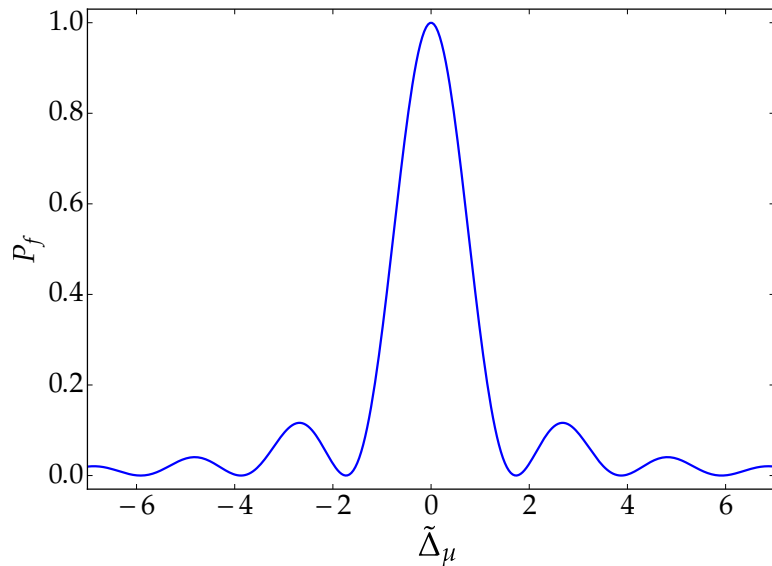


Figure D.1 Probability of being excited into state $|f\rangle$ of an atom initially in state $|i\rangle$ as a function of reduced detuning $\tilde{\Delta}_\mu$.

Let's consider an atom initially in a state $|i\rangle$ undergoes a transition by microwave to a state $|f\rangle$. The microwave frequency is detuned by Δ_μ away the resonance. The population in the final level oscillates as a function of time t

$$P_f(t) = \frac{\Omega_\mu^2}{\Omega_\mu^2 + \Delta_\mu^2} \sin^2\left(\frac{1}{2}\sqrt{\Omega_\mu^2 + \Delta_\mu^2}t\right) \quad (\text{D.1})$$

and is known as Rabi flopping. The coupling strength is represented by the Rabi frequency Ω_μ .

The excitation duration Δt_μ is chosen so that it makes a π pulse for the resonant excitation

$$\Delta t_\mu = \frac{\pi}{\Omega_\mu}. \quad (\text{D.2})$$

Substituting Ω_μ from (D.2) into (D.1), we obtain

$$P_f = \frac{1}{1 + \tilde{\Delta}_\mu^2} \sin^2\left(\frac{\pi}{2} \sqrt{1 + \tilde{\Delta}_\mu^2}\right), \quad (\text{D.3})$$

where $\tilde{\Delta}_\mu = \Delta_\mu \Delta t_\mu / \pi$. Equation (D.3) is similar to (but not identical to) a cardinal sine function squared and is plotted in Figure D.1. Accordingly, the excited state $|f\rangle$ can be populated with a nonzero probability for near-resonant excitations. Therefore, a finite excitation duration leads to a finite spectral line width. It is of about $2\pi/\Delta t_\mu$.

For an ensemble of Rydberg atoms initially in the $|i\rangle$ state, the van der Waals interaction shifts the transition frequency of each atom correspondingly. Let $n(\nu_i)$ be the energy distribution, i.e., the number of atoms whose transition frequency is ν_i . The average number of atoms being excited to the $|f\rangle$ state coupled by a microwave pulse of frequency ν is then given by

$$n_f(\nu) = \sum_{\nu_i} n(\nu_i) P_f(\nu - \nu_i). \quad (\text{D.4})$$

If the energy distribution is a continuous function, the number of Rydberg atoms whose transition frequency is between ν_i and $\nu_i + d\nu_i$ is written as $n(\nu_i)d\nu_i$. The average number of atoms being excited is expressed by an integral

$$n_f(\nu) = \int_{\nu_i} n(\nu_i) P_f(\nu - \nu_i) d\nu_i. \quad (\text{D.5})$$

Equations (D.4) and (D.5) are the convolution of the energy distribution $n(\nu_i)$ and the spectral broadening function P_f of the microwave pulse.

Two atoms: motion and spin exchange

E

Let us discuss the simplest case of two atoms in two lattice sites $R_0 = 5 \mu\text{m}$ apart. They are in two different states $|g\rangle$ and $|e\rangle$. We consider only a one-dimensional motion in the trap, along the two atom axis Ox . The trap frequency in this direction is ω_x . As discussed in [section 2.3](#), the effective interaction Hamiltonian of the system is

$$V_{\text{eff}} = \begin{pmatrix} |ge\rangle & |eg\rangle \\ |ge\rangle & |eg\rangle \end{pmatrix} \begin{pmatrix} C_{ge} & A_{ge} \\ A_{ge} & C_{ge} \end{pmatrix} = C_{ge}\Sigma_Z + A_{ge}\Sigma_X , \quad (\text{E.1})$$

where $\Sigma_Z = |ge\rangle\langle ge| + |eg\rangle\langle eg| = \mathbb{I}$ and $\Sigma_X = |ge\rangle\langle eg| + |eg\rangle\langle ge|$ are respectively the Z- and the X-Pauli matrices in the space of pair states. The direct and the exchange interactions are C_{ge} and A_{ge} respectively. The exchange interaction symmetrically and anti-symmetrically combines the two bare states into $|\pm\rangle = (|ge\rangle \pm |eg\rangle)/\sqrt{2}$. Their energies are

$$E_{\pm} = C_{ge} \mp A_{ge} . \quad (\text{E.2})$$

The direct interaction globally shifts these two levels and thus plays no role in the dynamics of the system. Since C_{ge} and A_{ge} depend on the distance R between the two atoms, when the two atoms are in the $|\pm\rangle$ state, they are symmetrically displaced from the trap center by an amount $0 < x_1 = -x_2 = x_d \mp x_e$, where x_d and x_e are respectively the displacement due to the direct and the exchange forces. One can see that x_d only slightly modifies the trap center of each atom. By redefining the energy origin and R_0 , we can neglect the direct interaction.

The motion of the atoms is described by two harmonic oscillators

$$H_{\text{osc}} = \hbar\omega_x(a_1^\dagger a_1 + a_2^\dagger a_2) , \quad (\text{E.3})$$

where a_i and a_i^\dagger are the annihilation and creation operators acting on the atom i respectively. The total Hamiltonian is thus

$$H = \hbar\omega_x(a_1^\dagger a_1 + a_2^\dagger a_2) + A_{ge}\Sigma_X . \quad (\text{E.4})$$

We assume that the exchange interaction varies C_α/R^α , where C_α is a proportionality

coefficient. For small displacements $x_i \ll R_0$, one can write

$$\begin{aligned} A_{ge} &\approx \frac{C_\alpha}{R_0^\alpha} \left[1 - \frac{\alpha}{R_0} (x_2 - x_1) \right] \\ &= \hbar \frac{\Omega_0}{2} \left[1 - \frac{\alpha}{R_0} (x_2 - x_1) \right], \end{aligned} \quad (\text{E.5})$$

where we introduce the exchange frequency $\Omega_0 = 2C_\alpha/(\hbar R_0^\alpha)$. Let M be the mass of one atom. Using $x_i = x_0(a_i + a_i^\dagger)$, where $x_0 = \sqrt{\hbar/(2M\omega_x)}$ is the oscillation ground state extension, we finally get

$$H = \hbar\omega_x(a_1^\dagger a_1 + a_2^\dagger a_2) + \hbar \frac{\Omega_0}{2} [1 - \eta(a_2 - a_1 + h.c.)] \Sigma_X, \quad (\text{E.6})$$

where we define the analog of a Lamb-Dicke parameter for ion traps

$$\eta = \alpha \frac{x_0}{L}. \quad (\text{E.7})$$

If the two atoms are in the $|\pm\rangle$ state, the displacement of the atoms can be approximated as $|\pm\beta\rangle |\mp\beta\rangle$ describing products of coherent states with opposite real amplitudes. In this notation, the first ket refers to the motion of the first atom. One can estimate β using the variational method, minimizing the average value of H in the state $|+\rangle|\beta\rangle|-\beta\rangle$. One gets

$$\beta = \frac{\Omega_0 \eta}{2\omega_x}. \quad (\text{E.8})$$

We now perform a unitary transformation defined by

$$U = D_1(\gamma_1 \Sigma_X) D_2(\Sigma_X), \quad (\text{E.9})$$

where the modified displacement operators D_i are

$$D_i(\gamma_i \Sigma_X) = e^{(\gamma_i a_i^\dagger - \gamma_i^* a_i) \Sigma_X}. \quad (\text{E.10})$$

Since the X-Pauli matrix commutes with all motional operators, $D_i^\dagger(\gamma_i \Sigma_X) = D_i(-\gamma_i \Sigma_X)$. The new Hamiltonian reads

$$\tilde{H} = D_1(-\gamma_1 \Sigma_X) D_2(-\gamma_2 \Sigma_X) H D_1(\gamma_1 \Sigma_X) D_2(\gamma_2 \Sigma_X). \quad (\text{E.11})$$

According to the Baker-Hausdorff lemma, we have

$$D_i(-\gamma_i \Sigma_X) a_i D_i(\gamma_i \Sigma_X) = a_i + \gamma_i \Sigma_X, \quad (\text{E.12})$$

$$D_i(-\gamma_i \Sigma_X) a_i^\dagger D_i(\gamma_i \Sigma_X) = a_i^\dagger + \gamma_i^* \Sigma_X, \quad (\text{E.13})$$

$$(\text{E.14})$$

and

$$D_i(-\gamma_i \Sigma_X) a_i^\dagger a_i D_i(\gamma_i \Sigma_X) = a_i^\dagger a_i + \gamma_i \Sigma_X a_i^\dagger + \gamma_i^* \Sigma_X a_i + |\gamma_i|^2, \quad (\text{E.15})$$

where we have used $\Sigma_X^2 = \mathbb{I}$. We get

$$\tilde{H} = \hbar\omega_x(a_1^\dagger a_1 + a_2^\dagger a_2) + \hbar\frac{\Omega_0}{2}\Sigma_X + \hbar\omega_x(|\gamma_1|^2 + |\gamma_2|^2) + \hbar\omega_x\left[\left(\gamma_1 + \frac{\Omega_0\eta}{2\omega_x}\right)\Sigma_X a_1^\dagger + \left(\gamma_2 + \frac{\Omega_0\eta}{2\omega_x}\right)\Sigma_X a_2^\dagger + \frac{\Omega_0\eta}{2\omega_x}(\gamma_1 + \gamma_2) + h.c.\right]. \quad (\text{E.16})$$

When choosing

$$\gamma_1 = \gamma_2 = -\beta = -\frac{\Omega_0\eta}{2\omega_x}, \quad (\text{E.17})$$

within irrelevant constants, the Hamiltonian simplifies to

$$\tilde{H} = \hbar\omega_x(a_1^\dagger a_1 + a_2^\dagger a_2) + \hbar\frac{\Omega_0}{2}\Sigma_X. \quad (\text{E.18})$$

This Hamiltonian describes two atoms undergoing an exchange, together with two uncoupled harmonic oscillators.

We now consider the time evolution of the system from a simple initial condition $|\Psi\rangle(0) = |ge\rangle|0\rangle|0\rangle$, i.e., the two atoms in $|e\rangle$ and $|g\rangle$ at the trap centers. We can decompose $|\Psi\rangle(0)$ as

$$|\Psi\rangle(0) = \frac{1}{\sqrt{2}}(|+\rangle|0\rangle|0\rangle + |-\rangle|0\rangle|0\rangle). \quad (\text{E.19})$$

The corresponding initial unitary transformed state is

$$|\tilde{\Psi}\rangle(0) = \frac{1}{\sqrt{2}}(|+\rangle|\beta\rangle|-\beta\rangle + |-\rangle|-\beta\rangle|\beta\rangle), \quad (\text{E.20})$$

which is a two oscillators Schrödinger cat. The time evolution of the system under \tilde{H} is trivial and is

$$|\tilde{\Psi}\rangle(t) = \frac{1}{\sqrt{2}}\left(e^{i\frac{\Omega_0 t}{2}}|+\rangle\left|\beta e^{-i\frac{\omega_x t}{2}}\right\rangle\left|-\beta e^{-i\frac{\omega_x t}{2}}\right\rangle + e^{-i\frac{\Omega_0 t}{2}}|-\rangle\left|-\beta e^{-i\frac{\omega_x t}{2}}\right\rangle\left|\beta e^{-i\frac{\omega_x t}{2}}\right\rangle\right). \quad (\text{E.21})$$

We now perform the inverse unitary transformation and finally obtain

$$|\Psi\rangle(t) = \frac{1}{\sqrt{2}}\left(e^{i\frac{\Omega_0 t}{2}}|+\rangle|-\xi\rangle|\xi\rangle + e^{-i\frac{\Omega_0 t}{2}}|-\rangle|\xi\rangle|-\xi\rangle\right), \quad (\text{E.22})$$

with

$$\xi = \beta\left(1 - e^{-i\frac{\omega_x t}{2}}\right). \quad (\text{E.23})$$

The motional and the atomic states are thus generally entangled. The entanglement disappears periodically at the trap frequency, when the cat amplitude ξ cancels. One

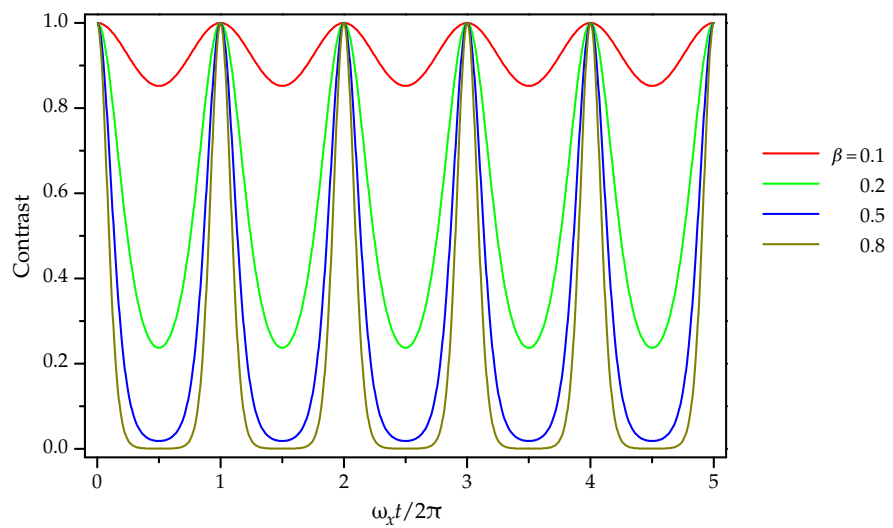


Figure E.1 Contrast of the exchange oscillation as a function of time for different value of β

can rewrite $|\Psi\rangle(t)$ as

$$|\Psi\rangle(t) = \frac{1}{2} |eg\rangle \left(e^{i\frac{\Omega_0 t}{2}} |-\xi\rangle |\xi\rangle - e^{-i\frac{\Omega_0 t}{2}} |\xi\rangle |-\xi\rangle \right) + \frac{1}{2} |ge\rangle \left(e^{i\frac{\Omega_0 t}{2}} |-\xi\rangle |\xi\rangle + e^{-i\frac{\Omega_0 t}{2}} |\xi\rangle |-\xi\rangle \right). \quad (\text{E.24})$$

The probability of finding the first atom being excited is

$$P_{eg}(t) = \frac{1}{2} \left(1 - |\langle \xi | -\xi \rangle|^2 \cos \Omega_0 t \right) = \frac{1}{2} \left(1 - e^{-4|\xi|^2} \cos \Omega_0 t \right). \quad (\text{E.25})$$

The contrast of the exchange oscillation is thus

$$C = e^{-8\beta^2(1-\cos \omega_x t)}. \quad (\text{E.26})$$

Figure E.1 plots the contrast of the exchange oscillation as a function of time. In the limit of a small β amplitude ($\Omega_0 \ll \omega_x/\eta$ weak exchange and tight trap), the contrast is slightly modulated

$$C \approx 1 - 8\beta^2(1 - \cos \omega_x t). \quad (\text{E.27})$$

For large β , the contrast exponentially decays in a short time scale. Equation (E.26) can be approximated by

$$C \approx e^{-4\beta^2 \omega_x^2 t^2}. \quad (\text{E.28})$$

Résumé en français

Simulation quantique et état de l'art

Les transitions de phase des systèmes magnétiques quantiques ont toujours suscité un grand intérêt à la fois du point de vue expérimental et théorique. Plusieurs modèles de réseaux de spins en interaction ont été développés pour décrire ces systèmes à une échelle microscopique. Cependant, les méthodes de calcul classiques, malgré leurs récents développements, ont des difficultés à traiter ce type de problèmes à N -corps fortement corrélés. La simulation de la dynamique d'un réseau de N spins en interaction demande de calculer l'exponentielle de matrices à 2^N éléments. Quand $N \geq 40$, le problème est hors de portée de nos super-ordinateurs actuels [14–17].

Richard Feynman, pendant ses cours des années 1980, a proposé de transcrire le système de spins d'intérêt sur un autre qui conserve les propriétés du système d'intérêt mais est plus facile à contrôler et étudier expérimentalement [11]. De façon générale, l'on prépare le système dans un état initial et le laisse évoluer vers l'état quantique final. On mesure ensuite quelque quantité d'intérêt.

La simulation quantique devient un domaine très actif. Elle est étudiée théoriquement et expérimentalement dans le monde entier. Plusieurs plateformes ont été développées : des ions piégés [27, 28], des qubits supraconducteurs [29], des atomes neutres en cavité ou dans des réseaux optiques [23–26], des boîtes quantiques [34–36], des molécules polaires [33] et beaucoup d'autres.

Les qubits supraconducteurs peuvent être manipulés avec une très haute fidélité [41, 42]. Ce sont des systèmes très prometteurs pour la simulation quantique numérique [43, 44] ou analogique [45, 46]. Néanmoins, ces systèmes souffrent d'une forte décohérence [49].

Les ions piégés ont permis la mise en œuvre la plus avancée de simulations quantiques numériques [55, 56], notamment la simulation de la création d'une paire de particules en l'électrodynamique quantique [57]. Des simulations quantiques analogiques avec des ions piégés ont aussi été menées, avec la réalisation de systèmes de spins frustrés, la propagation de l'intrication [58, 59] ou la localisation à N -corps [60], par exemple. Toutefois, la plupart de ces réalisations ont été effectuées avec une chaîne 1D et une interaction de longue ou moyenne portée [61, 62]. Pour passer à la géométrie 2D, il a été proposé d'utiliser une matrice de micro-pièges [67, 68] ou un piège Paul à 2D [65, 66], mais la cohérence de ces systèmes n'a pas encore caractérisée.

Les atomes froids en réseaux optiques sont des outils remarquables pour la simula-

tion quantique analogique [24–26]. Les atomes sont placés dans des trous de potentiel optiques à 1D, 2D ou 3D. La dynamique du système vient de la compétition entre l'effet tunnel d'un site à son voisin et l'interaction de deux atomes dans le même site. Ce sont des systèmes très flexibles qui permettent de réaliser différentes géométries et de contrôler de nombreux paramètres expérimentaux. Cependant, le taux tunnel est faible (quelques centaines de Hz) par rapport au temps de vie des atomes piégés (quelques secondes). L'évolution du système est donc limitée à quelques centaines de périodes tunnel. C'est un gros désavantage lorsque l'on cherche à simuler la dynamique lente de verres de spins ou la localisation à N corps. Passer à des molécules polaires [79, 80] ou des atomes avec un grand moment dipolaire magnétique [81, 82] n'est pas aisé.

Atomes de Rydberg et simulation quantique

Les atomes dans des états de Rydberg sont des atomes très excités (nombre quantique principal élevé), très proches du seuil d'ionisation [3, 83]. Ils ont des propriétés remarquables, et même très exagérées par rapport à celles des atomes dans des états "ordinaires". Parmi ces propriétés, on peut citer notamment leurs très grands éléments de matrice dipolaire, leurs très long temps de vie et malgré tout une structure interne relativement simple. Les éléments de matrice dipolaire des atomes de Rydberg sont typiquement mille fois ceux des atomes fondamentaux. L'état de Rydberg peut vivre plus qu'une centaine de microsecondes. En particulier, l'état de Rydberg circulaire, c'est à dire l'état de Rydberg de nombres quantique orbital et magnétique maximaux, a un temps de vie de l'ordre de la dizaine de millisecondes. Ses propriétés ont été exploitées par une série d'expériences d'électrodynamique quantique en cavité réalisées dans notre équipe du Laboratoire Kastler Brossel [84–95].

Avec leurs grands éléments de matrice dipolaire, les atomes de Rydberg interagissent fortement entre eux. L'interaction prend la forme d'un potentiel de van der Waals C_6/R^6 , où R est la distance entre deux atomes. Si R est de quelques microns, l'énergie d'interaction peut entrer dans la gamme des MHz, et même plus encore pour l'interaction d'échange résonant de Föster (qui varie comme $1/R^3$). On peut changer cette énergie d'interaction par des ordres de grandeur en modifiant le nombre quantique principal.

Un protocole pour la simulation quantique numérique avec atomes de Rydberg a été proposé [97, 98]. Il est basé sur le mécanisme de blocage dipolaire qui est la conséquence directe de l'interaction forte entre les atomes de Rydberg [99]. Dans un petit échantillon froids d'atomes fondamentaux, l'interaction de van der Waals est plus importante que la largeur de l'excitation (~ 100 kHz). Dès qu'un atome est excité, tous les autres sont mis hors résonance. Par conséquent, nous avons un et seulement un atome de Rydberg à la fois. C'est au cœur du principe de la réalisation d'une porte quantique CNOT. Selon l'état du qubit de contrôle, l'état de tous les autres qubits est inchangé ou est inversé [96, 99, 102–104].

Grâce à cette forte interaction, les atomes de Rydberg sont aussi des outils très prometteurs pour la simulation quantique analogique de réseaux de spins. L'intérêt pour ces atomes a récemment explosé, menant à de nombreuses propositions pour la simulation quantique avec des atomes de Rydberg [105–108]. Parmi plusieurs réalisations,

tions récentes, l'observation du transport cohérent d'une excitation sur une chaîne de trois atomes de Rydberg est très remarquable [109]. La dynamique d'une excitation sur une matrice avec plus de 20 atomes a été observée [110]. Pour résoudre le problème du faible taux tunnel dans les systèmes d'atomes froids dans réseaux optiques, il est possible de mélanger les atomes fondamentaux avec des atomes de Rydberg, c.-à-d. de les habiller avec des états de Rydberg [111–115]. Toutefois, ces expériences sont opérées à 300 K et souffrent du rayonnement du corps noir qui modifie l'interaction entre les atomes de Rydberg de façon imprévue [116–118]. Passer dans un environnement cryogénique est une tâche ardue.

Jusqu'à maintenant, les atomes de Rydberg utilisés dans les expériences ci-dessus ont toujours des moments angulaires faibles. La simulation quantique avec des atomes de Rydberg de faible l sont limitées. D'abord, les atomes de Rydberg ressentent des forces mécaniques fortes, répulsives ou attractives, à cause de leurs interactions fortes. Sans piégeage, n'importe quel cristal de Rydberg fond en quelques dizaines de microsecondes. Des techniques de piégeage des atomes de Rydberg dans des réseaux optiques ont été étudiées [119]. Néanmoins, le temps de vie des états de Rydberg est fortement raccourci à cause de la photoionisation par le laser de piégeage [120]. Par ailleurs, si le temps de vie des atomes de Rydberg est long par rapport à celui des états excités ordinaires, il n'est que de quelques centaines de microsecondes, ce qui correspond à une centaine de périodes d'échange. Donc la simulation de la dynamique lente d'un réseau de spins est hors de portée.

Dans ce contexte, cette thèse étudie l'interaction entre des atomes de Rydberg et explore de nouveaux plans pour réaliser des simulations quantiques avec des atomes de Rydberg. Expérimentalement, nous excitons les atomes vers des états de Rydberg par laser, de façon résonante ou désaccordée. Les atomes fondamentaux de rubidium sont piégés et refroidis dans un nuage dense, préparé en utilisant une puce à atome supraconductrice. Parce que les atomes de Rydberg sont très sensibles au rayonnement thermique, l'expérience est effectuée dans un environnement cryogénique auquel la puce supraconductrice est parfaitement adaptée. Les travaux de cette thèse ont contribué aux quatre réussites principales résumées ci-dessous.

Contrôle du champ électrique parasite et manipulation cohérente de niveaux de Rydberg au voisinage de la puce. L'inconvénient des grands éléments de matrice dipolaire est que les atomes de Rydberg sont extrêmement sensibles aux champs électriques parasites. Le dépôt lent d'atomes de rubidium sur la surface d'or de la puce est inévitable pendant une séquence expérimentale. Cela crée des taches de dipôles, créant un champ électrique inhomogène et instable au voisinage de la puce. Par effet Stark, le profil de l'excitation s'en trouve élargi (~ 40 MHz). L'effet de blocage dipolaire est donc détruit complètement. Résoudre ce problème était un défi majeur pour nous ainsi que pour d'autres groupes. Une solution, plutôt simple, consiste à couvrir la puce d'une couche épaisse de rubidium sur une large zone, saturant ainsi l'effet du dépôt lent de rubidium. L'inhomogénéité du champ électrique est alors bien supprimée. Nous disposons donc d'un bon environnement pour étudier l'interaction entre atomes de Rydberg. Ces travaux sont détaillés dans la thèse de Carla Hermann et ont fait l'objet d'un *highlight* dans Physical Review A [123].

Sondage micro-onde de l'énergie d'interaction van der Waals dans un nuage froid de Rydberg. Étant excités par laser à partir d'un nuage dense, les atomes de

Rydberg interagissent fortement entre eux. Le spectre micro-onde de la transition vers un niveau de Rydberg voisin nous permet de sonder précisément la distribution d'énergie d'interaction. Le changement de la fréquence micro-onde de la transition de chaque atome est proportionnel à son énergie d'interaction initiale. Nous avons utilisé cette technique afin d'observer l'expansion mécanique d'un ensemble d'atomes de Rydberg sous l'effet de la forte interaction répulsive. Cette observation révèle la limite de l'approximation du gaz gelé de Rydberg. Un modèle simple Monte Carlo a été développé et nous a permis d'expliquer les spectres micro-ondes mesurés. Cette méthode fait l'objet de la thèse de Raul Teixeira et est résumée dans un article paru dans Physical Review Letters [124].

Développement d'une simulation plus rigoureuse du processus de l'excitation des atomes de Rydberg. Bien que le modèle simple Monte Carlo réussisse à reconstruire les spectres micro-ondes mesurés, il échoue lorsqu'il s'agit des transitions optiques. Le problème est que cette simulation manque n'inclut aucun échelle de temps. Il nous faut lui fournir le nombre final d'atomes de Rydberg obtenu lors des expériences. Cette approche phénoménologique nous empêche d'explorer de nouvelles techniques d'excitation. En revisitant les équations de Bloch optiques, nous obtenons le taux d'excitation (et de désexcitation) pour chaque atome. Ces taux ne dépendent que du taux de déphasage, de la fréquence de Rabi d'excitation et de la présence éventuelle d'autres atomes de Rydberg à proximité. Le problème de l'excitation atomique est donc réduit à un processus stochastique classique, qui peut être calculé par une simulation Monte Carlo. Une échelle de temps apparaît naturellement dans la simulation. Nous n'avons plus besoin de savoir le nombre d'atomes de Rydberg à l'avance. Cette nouvelle méthode plus rigoureuse nous éclaire sur le processus d'excitation. Elle prend en compte les paramètres de l'excitation, de la distribution spatiale du nuage, du temps de vie fini et du mouvement des atomes de Rydberg pendant l'excitation à cause de l'interaction forte entre eux. Elle nous permet de reconstruire les spectres optiques ainsi que les spectres micro-ondes. Elle nous permet aussi de tester de nouvelles techniques d'excitation, en particulier l'excitation de Rydberg dans un nuage 1D pour produire une chaîne d'atomes pour la simulation quantique.

Simulation quantique avec atomes de Rydberg circulaires piégés par laser. Les atomes de Rydberg circulaires, malgré leurs propriétés uniques et leur exploitation fructueuse dans les expériences d'électrodynamique quantique en cavité, n'ont pas encore été exploités pour réaliser des simulations quantiques. Nous étudions l'interaction entre atomes circulaires et proposons une méthode pour réaliser des simulations quantiques d'une chaîne 1D de spins avec ce type d'atomes.

Le schéma du simulateur quantique proposé est représenté sur la figure ci-dessous. L'ingrédient principal de la proposition est un ensemble d'atomes de Rydberg circulaire piégés entre les deux plaques d'un condensateur. Quand la distance entre les deux plaques est plus petite que la demi-longueur d'onde émise, l'émission spontanée est inhibée. A une température au dessous de 1 K, les temps de vie des états circulaires entrent dans la gamme des minutes. Le temps de piégeage d'une chaîne d'une dizaine d'atomes est alors de quelques secondes.

Les atomes circulaires sont piégés par la force pondéromotrice agissant sur l'électron de valence , presque libre. Pour les états de Rydberg de moment angulaire faible, l'effet de photoionisation réduit fortement le temps de vie. Néanmoins, cet effet diminue

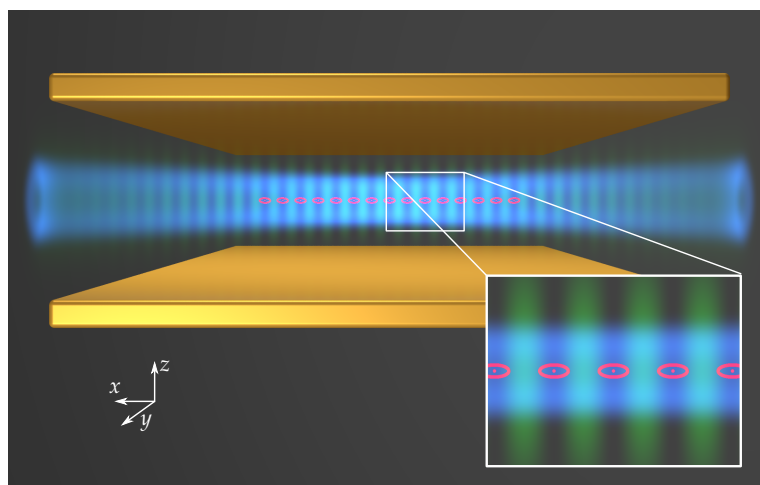


Schéma du simulateur quantique avec atomes de Rydberg circulaire. Les atomes circulaires (rouge) sont piégés par laser entre deux plaques d'un condensateur inhibant l'émission spontanée. Un réseau optique créé par un laser CO₂ (vert) est superposé avec un faisceau creux de Laguerre-Gauss (bleu).

exponentiellement avec l et devient négligeable pour les états circulaires. Un laser Laguerre-Gauss de longueur d'onde 1 μm, en combinaison avec un onde stationnaire créée par un laser CO₂ de longueur d'onde 10 μm, forme un réseau 1D. Les atomes sont piégés aux minima d'intensité et régulièrement espacés de 5 μm.

L'interaction de van der Waals entre les atomes permet de réaliser le Hamiltonien de spin XXZ où les couplages spin-spin correspondent à l'interaction directe (termes Z) et à l'interaction d'échange (termes X) entre les atomes. Nous encodons l'état du spin sur deux niveaux circulaires 50C et 48C, pour lesquels l'interaction directe et l'interaction d'échange sont du même ordre de grandeur. La transition entre ces deux niveaux est habillée par un champ micro-onde qui joue le rôle d'un champ magnétique dans ce modèle. Cet Hamiltonien XXZ est largement accordable via un champ électrique appliquée et l'habillage micro-onde, d'un Hamiltonien anti-ferromagnétique à un Hamiltonien ferromagnétique en passant par un Hamiltonien purement XX. C'est une caractéristique unique de cette proposition.

De plus, nous proposons une méthode novatrice pour préparer de façon déterministe une chaîne de plus de 40 atomes. C'est une variante du refroidissement par évaporation. Nous enlevons les atomes un par un de la chaîne d'une manière bien contrôlée. Cette technique est basée sur l'interaction répulsive entre les atomes, qui appuie fortement sur les atomes aux bouts de la chaîne comprimée. Elle peut être aussi appliquée aux géométries 2D ou même 3D. Des méthodes d'initialisation de la chaîne et de la détection de l'état de chaque atome sont aussi développées.

La proposition vise à surmonter les difficultés des autres systèmes de simulation quantique, incluant ceux avec des atomes de Rydberg de moment angulaire faible. Elle combine la flexibilité des atomes neutres dans les réseaux optiques, l'interaction forte typique des atomes de Rydberg et le contrôle exquis des ions piégés. La réalisation d'un tel système permettrait de simuler de façon quantique des systèmes hors de portée des méthodes classiques de calcul.

References

- [1] J. J. N. J. J. Sakurai, *Modern Quantum Mechanics* (ADDISON WESLEY PUB CO INC, 2010), 550 Seiten.
- [2] C. Cohen-Tannoudji, *Quantum Mechanics* (John Wiley and Sons Ltd, 2006), 1524 Seiten.
- [3] S. Haroche and J. Raimond, *Exploring the Quantum: Atoms, Cavities, and Photons*, Oxford Graduate Texts (OUP Oxford, 2006).
- [4] J. P. Dowling and G. J. Milburn, "Quantum technology: the second quantum revolution", *Philosophical Transactions of the Royal Society A: Mathematical, Physical and Engineering Sciences* **361**, 1655 (2003).
- [5] J. Koomey, S. Berard, M. Sanchez, and H. Wong, "Implications of Historical Trends in the Electrical Efficiency of Computing", *IEEE Annals of the History of Computing* **33**, 46 (2011).
- [6] Sadik C. Esener, Mark H. Kryder, William D. Doyle, Marvin Keshner, Mansud Mansuripur, and David A. Thompson, *WTEC Panel report on The Future of Data Storage Technologies*, tech. rep. (International Technology Research Institute, 1999).
- [7] G.-R. HOFFMANN, "Weather forecasting and parallel processing: a view from ECMWF", *International Journal of High Speed Computing* **05**, 63 (1993).
- [8] R. R. Joshi, "A new heuristic algorithm for probabilistic optimization", *Computers & Operations Research* **24**, 687 (1997).
- [9] Y. Chen, T. Luo, S. Liu, S. Zhang, L. He, J. Wang, L. Li, T. Chen, Z. Xu, N. Sun, and O. Temam, "DaDianNao: A Machine-Learning Supercomputer", in *2014 47th Annual IEEE/ACM International Symposium on Microarchitecture* (Dec. 2014).
- [10] E. Sykes and A. Mirkovic, "A Fully Parallel and Scalable Implementation of a Hopfield Neural Network on the SHARC-NET Supercomputer", in *19th International Symposium on High Performance Computing Systems and Applications (HPCS'05)* ().
- [11] R. P. Feynman, "Simulating physics with computers", *International Journal of Theoretical Physics* **21**, 467 (1982).
- [12] M. Suzuki, *Quantum Monte Carlo Methods in Condensed Matter Physics* (WORLD SCIENTIFIC PUB CO INC, 1993), 368 Seiten.

- [13] M. Troyer and U.-J. Wiese, "Computational Complexity and Fundamental Limitations to Fermionic Quantum Monte Carlo Simulations", *Phys. Rev. Lett.* **94**, 170201 (2005).
- [14] J. I. Cirac and P. Zoller, "How to Manipulate Cold Atoms", *Science* **301**, 176 (2003).
- [15] A. Friedenauer, H. Schmitz, J. T. Glueckert, D. Porras, and T. Schaetz, "Simulating a quantum magnet with trapped ions", *Nat Phys* **4**, 757 (2008).
- [16] Lloyd, "Universal Quantum Simulators", eng, *Science* **273**, 1073 (1996).
- [17] K. D. Raedt, K. Michelsen, H. D. Raedt, B. Trieu, G. Arnold, M. Richter, T. Lippert, H. Watanabe, and N. Ito, "Massively parallel quantum computer simulator", *Computer Physics Communications* **176**, 121 (2007).
- [18] I. Buluta and F. Nori, "Quantum simulators.", eng, *Science* **326**, 108 (2009).
- [19] I. M. Georgescu, S. Ashhab, and F. Nori, "Quantum Simulation", *Rev. Mod. Phys.* **86**, 153 (2014).
- [20] M. Nielsen and I. Chuang, *Quantum Computation and Quantum Information*, Cambridge Series on Information and the Natural Sciences (Cambridge University Press, 2000).
- [21] S. J. Devitt, W. J. Munro, and K. Nemoto, "Quantum error correction for beginners", *Reports on Progress in Physics* **76**, 076001 (2013).
- [22] Nobelprize.org, Nobel Media AB 2014., *The 2012 Nobel Prize in Physics - Press Release*, http://www.nobelprize.org/nobel_prizes/physics/laureates/2012/press.htm, Web. 25 Sep 2016.
- [23] D. Jaksch and P. Zoller, "The cold atom Hubbard toolbox", *Annals of Physics* **315**, 52 (2005).
- [24] M. Lewenstein, A. Sanpera, V. Ahufinger, B. Damski, A. Sen(De), and U. Sen, "Ultracold atomic gases in optical lattices: mimicking condensed matter physics and beyond", *Advances in Physics* **56**, 243 (2007).
- [25] I. Bloch, J. Dalibard, and S. Nascimbène, "Quantum simulations with ultracold quantum gases", *Nature Physics* **8**, 267 (2012).
- [26] I. Bloch, J. Dalibard, and W. Zwerger, "Many-body physics with ultracold gases", *Reviews of Modern Physics* **80**, 885 (2008).
- [27] R. Blatt and C. F. Roos, "Quantum simulations with trapped ions", *Nature Physics* **8**, 277 (2012).
- [28] C. Schneider, D. Porras, and T. Schaetz, "Experimental quantum simulations of many-body physics with trapped ions", *Reports on Progress in Physics* **75**, 024401 (2012).
- [29] A. A. Houck, H. E. Türeci, and J. Koch, "On-chip quantum simulation with superconducting circuits", *Nature Physics* **8**, 292 (2012).
- [30] D. Tanese, E. Gurevich, F. Baboux, T. Jacqmin, A. Lemaître, E. Galopin, I. Sagnes, A. Amo, J. Bloch, and E. Akkermans, "Fractal energy spectrum of a polariton gas in a Fibonacci quasiperiodic potential.", eng, *Phys Rev Lett* **112**, 146404 (2014).

- [31] A. Aspuru-Guzik and P. Walther, "Photonic quantum simulators", *Nature Physics* **8**, 285 (2012).
- [32] I. Carusotto and C. Ciuti, "Quantum fluids of light", *Rev. Mod. Phys.* **85**, 299 (2013).
- [33] H.-P. Büchler, G. Pupillo, A. Micheli, and P. Zoller, "Condensed Matter Physics with Cold Polar Molecules", in *Cold Molecules* (Informa UK Limited, June 2009).
- [34] J. Cai, A. Retzker, F. Jelezko, and M. B. Plenio, "A large-scale quantum simulator on a diamond surface at room temperature", *Nature Physics* **9**, 168 (2013).
- [35] E. Manousakis, "A Quantum-Dot Array as Model for Copper-Oxide Superconductors: A Dedicated Quantum Simulator for the Many-Fermion Problem", *Journal of Low Temperature Physics* **126**, 1501 (2002).
- [36] T. Byrnes, P. Recher, N. Y. Kim, S. Utsunomiya, and Y. Yamamoto, "Quantum Simulator for the Hubbard Model with Long-Range Coulomb Interactions Using Surface Acoustic Waves", *Phys. Rev. Lett.* **99**, 016405 (2007).
- [37] M. Greiner, O. Mandel, T. Esslinger, T. W. Hänsch, and I. Bloch, "Quantum phase transition from a superfluid to a Mott insulator in a gas of ultracold atoms", *Nature* **415**, 39 (2002).
- [38] D. Leibfried, B. DeMarco, V. Meyer, M. Rowe, A. Ben-Kish, J. Britton, W. M. Itano, B. Jelenković, C. Langer, T. Rosenband, and D. J. Wineland, "Trapped-Ion Quantum Simulator: Experimental Application to Nonlinear Interferometers", *Phys. Rev. Lett.* **89**, 247901 (2002).
- [39] R. Gerritsma, G. Kirchmair, F. Zähringer, E. Solano, R. Blatt, and C. F. Roos, "Quantum simulation of the Dirac equation", *Nature* **463**, 68 (2010).
- [40] K. Kim, M.-S. Chang, S. Korenblit, R. Islam, E. E. Edwards, J. K. Freericks, G.-D. Lin, L.-M. Duan, and C. Monroe, "Quantum simulation of frustrated Ising spins with trapped ions", *Nature* **465**, 590 (2010).
- [41] J. Clarke and F. K. Wilhelm, "Superconducting quantum bits.", eng, *Nature* **453**, 1031 (2008).
- [42] J. Q. You and F. Nori, "Superconducting circuits and quantum information", *Phys. Today* **58**, 42 (2005).
- [43] R. Barends, L. Lamata, J. Kelly, L. García-Álvarez, A. Fowler, A. Megrant, E. Jeffrey, T. White, D. Sank, J. Mutus, B. Campbell, Y. Chen, Z. Chen, B. Chiaro, A. Dunsworth, I.-C. Hoi, C. Neill, P. J. J. O'Malley, C. Quintana, P. Roushan, A. Vainsencher, J. Wenner, E. Solano, and J. M. Martinis, "Digital quantum simulation of fermionic models with a superconducting circuit.", eng, *Nat Commun* **6**, 7654 (2015).
- [44] R. Barends, A. Shabani, L. Lamata, J. Kelly, A. Mezzacapo, U. Las Heras, R. Babbush, A. Fowler, B. Campbell, Y. Chen, Z. Chen, B. Chiaro, A. Dunsworth, E. Jeffrey, E. Lucero, A. Megrant, J. Mutus, M. Neeley, C. Neill, P. J. J. O'Malley, C. Quintana, P. Roushan, D. Sank, A. Vainsencher, J. Wenner, T. White, E. Solano, H. Neven, and J. M. Martinis, "Digitized adiabatic quantum computing with a superconducting circuit.", eng, *Nature* **534**, 222 (2016).

- [45] C. Eichler, J. Mlynek, J. Butscher, P. Kurpiers, K. Hammerer, T. J. Osborne, and A. Wallraff, "Exploring Interacting Quantum Many-Body Systems by Experimentally Creating Continuous Matrix Product States in Superconducting Circuits", *Phys. Rev. X* **5**, 041044 (2015).
- [46] C. Neill, P. Roushan, M. Fang, Y. Chen, M. Kolodrubetz, Z. Chen, A. Megrant, R. Barends, B. Campbell, B. Chiaro, A. Dunsworth, E. Jeffrey, J. Kelly, J. Mutus, P. J. J. O'Malley, C. Quintana, D. Sank, A. Vainsencher, J. Wenner, T. C. White, A. Polkovnikov, and J. M. Martinis, "Ergodic dynamics and thermalization in an isolated quantum system", *Nature Physics advance online publication* (2016) [10.1038/nphys3830](https://doi.org/10.1038/nphys3830).
- [47] S. Boixo, T. F. Rønnow, S. V. Isakov, Z. Wang, D. Wecker, D. A. Lidar, J. M. Martinis, and M. Troyer, "Evidence for quantum annealing with more than one hundred qubits", *Nat Phys* **10**, 218 (2014).
- [48] B. Heim, T. F. Rønnow, S. V. Isakov, and M. Troyer, "Quantum versus classical annealing of Ising spin glasses.", eng, *Science* **348**, 215 (2015).
- [49] G. Ithier, E. Collin, P. Joyez, P. J. Meeson, D. Vion, D. Esteve, F. Chiarello, A. Shnirman, Y. Makhlin, J. Schriefl, and G. Schön, "Decoherence in a superconducting quantum bit circuit", *Phys. Rev. B* **72**, 134519 (2005).
- [50] D. J. Wineland, "Superposition, entanglement, and raising Schrödinger's cat (Nobel Lecture).", eng, *Angew Chem Int Ed Engl* **52**, 10179 (2013).
- [51] D. Wineland, C. Monroe, W. Itano, D. Leibfried, B. King, and D. Meekhof, "Experimental issues in coherent quantum-state manipulation of trapped atomic ions", *J. Res. Natl. Inst. Stand. Technol.* **103**, 259 (1998).
- [52] D. Leibfried, R. Blatt, C. Monroe, and D. Wineland, "Quantum dynamics of single trapped ions", *Rev. Mod. Phys.* **75**, 281 (2003).
- [53] C. Senko, P. Richerme, J. Smith, A. Lee, I. Cohen, A. Retzker, and C. Monroe, "Realization of a Quantum Integer-Spin Chain with Controllable Interactions", *Phys. Rev. X* **5**, 021026 (2015).
- [54] P. Jurcevic, P. Hauke, C. Maier, C. Hempel, B. Lanyon, R. Blatt, and C. Roos, "Spectroscopy of Interacting Quasiparticles in Trapped Ions.", eng, *Phys Rev Lett* **115**, 100501 (2015).
- [55] P. Schindler, M. Müller, D. Nigg, J. T. Barreiro, E. A. Martinez, M. Hennrich, T. Monz, S. Diehl, P. Zoller, and R. Blatt, "Quantum simulation of dynamical maps with trapped ions", *Nat Phys* **9**, 361 (2013).
- [56] B. Lanyon, C. Hempel, D. Nigg, M. Müller, R. Gerritsma, F. Zähringer, P. Schindler, J. Barreiro, M. Rambach, G. Kirchmair, M. Hennrich, P. Zoller, R. Blatt, and C. Roos, "Universal digital quantum simulation with trapped ions.", eng, *Science* **334**, 57 (2011).
- [57] E. A. Martinez, C. A. Muschik, P. Schindler, D. Nigg, A. Erhard, M. Heyl, P. Hauke, M. Dalmonte, T. Monz, P. Zoller, and R. Blatt, "Real-time dynamics of lattice gauge theories with a few-qubit quantum computer.", eng, *Nature* **534**, 516 (2016).

- [58] P. Jurcevic, B. P. Lanyon, P. Hauke, C. Hempel, P. Zoller, R. Blatt, and C. F. Roos, "Quasiparticle engineering and entanglement propagation in a quantum many-body system", *Nature* **511**, 202 (2014).
- [59] P. Richerme, Z.-X. Gong, A. Lee, C. Senko, J. Smith, M. Foss-Feig, S. Michalakis, A. V. Gorshkov, and C. Monroe, "Non-local propagation of correlations in quantum systems with long-range interactions.", eng, *Nature* **511**, 198 (2014).
- [60] J. Smith, A. Lee, P. Richerme, B. Neyenhuis, P. W. Hess, P. Hauke, M. Heyl, D. A. Huse, and C. Monroe, "Many-body localization in a quantum simulator with programmable random disorder", *Nature Physics advance online publication* (2016) [10.1038/nphys3783](https://doi.org/10.1038/nphys3783).
- [61] K. Kim, M.-S. Chang, R. Islam, S. Korenblit, L.-M. Duan, and C. Monroe, "Entanglement and tunable spin-spin couplings between trapped ions using multiple transverse modes.", eng, *Phys Rev Lett* **103**, 120502 (2009).
- [62] R. Islam, C. Senko, W. Campbell, S. Korenblit, J. Smith, A. Lee, E. Edwards, C.-C. J. Wang, J. Freericks, and C. Monroe, "Emergence and frustration of magnetism with variable-range interactions in a quantum simulator.", eng, *Science* **340**, 583 (2013).
- [63] J. W. Britton, B. C. Sawyer, A. C. Keith, C.-C. J. Wang, J. K. Freericks, H. Uys, M. J. Biercuk, and J. J. Bollinger, "Engineered two-dimensional Ising interactions in a trapped-ion quantum simulator with hundreds of spins.", eng, *Nature* **484**, 489 (2012).
- [64] J. G. Bohnet, B. C. Sawyer, J. W. Britton, M. L. Wall, A. M. Rey, M. Foss-Feig, and J. J. Bollinger, "Quantum spin dynamics and entanglement generation with hundreds of trapped ions.", eng, *Science* **352**, 1297 (2016).
- [65] P. Richerme, "2D ion crystals in radiofrequency traps for quantum simulation", ArXiv e-prints (2016).
- [66] M. Kumph, M. Brownnutt, and R. Blatt, "Two-dimensional arrays of radio-frequency ion traps with addressable interactions", *New Journal of Physics* **13**, 073043 (2011).
- [67] R. Schmied, J. H. Wesenberg, and D. Leibfried, "Optimal surface-electrode trap lattices for quantum simulation with trapped ions.", eng, *Phys Rev Lett* **102**, 233002 (2009).
- [68] M. Mielenz, H. Kalis, M. Wittemer, F. Hakelberg, U. Warring, R. Schmied, M. Blain, P. Maunz, D. L. Moehring, D. Leibfried, and T. Schaetz, "Arrays of individually controlled ions suitable for two-dimensional quantum simulations.", eng, *Nat Commun* **7**, ncomms11839 (2016).
- [69] J. F. Sherson, C. Weitenberg, M. Endres, M. Cheneau, I. Bloch, and S. Kuhr, "Single-atom-resolved fluorescence imaging of an atomic Mott insulator.", eng, *Nature* **467**, 68 (2010).

- [70] S. Kuhr, W. Alt, D. Schrader, I. Dotsenko, Y. Miroshnychenko, W. Rosenfeld, M. Khudaverdyan, V. Gomer, A. Rauschenbeutel, and D. Meschede, "Erratum: Coherence Properties and Quantum State Transportation in an Optical Conveyor Belt [Phys. Rev. Lett. 91 , 213002 (2003)]", *Phys. Rev. Lett.* **95**, 099901 (2005).
- [71] M. Friesdorf, A. Werner, W. Brown, V. Scholz, and J. Eisert, "Many-Body Localization Implies that Eigenvectors are Matrix-Product States.", eng, *Phys Rev Lett* **114**, 170505 (2015).
- [72] D. J. Luitz, N. Laflorencie, and F. Alet, "Many-body localization edge in the random-field Heisenberg chain", *Phys. Rev. B* **91**, 081103 (2015).
- [73] J. Dalibard, F. Gerbier, G. Juzeliūnas, and P. Öhberg, "Colloquium : Artificial gauge potentials for neutral atoms", *Rev. Mod. Phys.* **83**, 1523 (2011).
- [74] Y.-J. Lin, K. Jiménez-García, and I. Spielman, "Spin-orbit-coupled Bose-Einstein condensates.", eng, *Nature* **471**, 83 (2011).
- [75] B. Stuhl, H.-I. Lu, L. Aycock, D. Genkina, and I. Spielman, "Visualizing edge states with an atomic Bose gas in the quantum Hall regime.", eng, *Science* **349**, 1514 (2015).
- [76] M. Mancini, G. Pagano, G. Cappellini, L. Livi, M. Rider, J. Catani, C. Sias, P. Zoller, M. Inguscio, M. Dalmonte, and L. Fallani, "Observation of chiral edge states with neutral fermions in synthetic Hall ribbons.", eng, *Science* **349**, 1510 (2015).
- [77] O. Romero-Isart, C. Navau, A. Sanchez, P. Zoller, and J. Cirac, "Superconducting vortex lattices for ultracold atoms.", eng, *Phys Rev Lett* **111**, 145304 (2013).
- [78] A. González-Tudela, C.-L. Hung, D. E. Chang, J. I. Cirac, and H. J. Kimble, "Sub-wavelength vacuum lattices and atom–atom interactions in two-dimensional photonic crystals", *Nature Photonics* **9**, 320 (2015).
- [79] B. Yan, S. A. Moses, B. Gadway, J. P. Covey, K. R. A. Hazzard, A. M. Rey, D. S. Jin, and J. Ye, "Observation of dipolar spin-exchange interactions with lattice-confined polar molecules.", eng, *Nature* **501**, 521 (2013).
- [80] D. DeMille, "Quantum computation with trapped polar molecules.", eng, *Phys Rev Lett* **88**, 067901 (2002).
- [81] S. Baier, M. Mark, D. Petter, K. Aikawa, L. Chomaz, Z. Cai, M. Baranov, P. Zoller, and F. Ferlaino, "Extended Bose-Hubbard models with ultracold magnetic atoms.", eng, *Science* **352**, 201 (2016).
- [82] T. Lahaye, C. Menotti, L. Santos, M. Lewenstein, and T. Pfau, "The physics of dipolar bosonic quantum gases", *Reports on Progress in Physics* **72**, 126401 (2009).
- [83] T. F. Gallagher, *Rydberg atoms*, Vol. 3 (Cambridge University Press, 2005).
- [84] M. Brune, F. Schmidt-Kaler, A. Maali, J. Dreyer, E. Hagley, J. M. Raimond, and S. Haroche, "Quantum Rabi Oscillation: A Direct Test of Field Quantization in a Cavity", *Phys. Rev. Lett.* **76**, 1800 (1996).

- [85] M. Brune, E. Hagley, J. Dreyer, X. Maître, A. Maali, C. Wunderlich, J. M. Raimond, and S. Haroche, "Observing the Progressive Decoherence of the "Meter" in a Quantum Measurement", *Phys. Rev. Lett.* **77**, 4887 (1996).
- [86] J. M. Raimond, M. Brune, and S. Haroche, "Manipulating quantum entanglement with atoms and photons in a cavity", *Reviews of Modern Physics* **73**, 565 (2001).
- [87] S. Haroche, G. Nogues, A. Rauschenbeutel, S. Osnaghi, M. Brune, and J. M. Raimond, "Seeing a single photon without destroying it", *Nature* **400**, 239 (1999).
- [88] P. Maioli, T. Meunier, S. Gleyzes, A. Auffeves, G. Nogues, M. Brune, J. M. Raimond, and S. Haroche, "Nondestructive Rydberg Atom Counting with Mesoscopic Fields in a Cavity", *Phys. Rev. Lett.* **94**, 113601 (2005).
- [89] S. Gleyzes, S. Kuhr, C. Guerlin, J. Bernu, S. Deléglise, U. B. Hoff, M. Brune, J.-M. Raimond, and S. Haroche, "Quantum jumps of light recording the birth and death of a photon in a cavity", *Nature* **446**, 297 (2007).
- [90] C. Guerlin, J. Bernu, S. Deléglise, C. Sayrin, S. Gleyzes, S. Kuhr, M. Brune, J.-M. Raimond, and S. Haroche, "Progressive field-state collapse and quantum non-demolition photon counting", *Nature* **448**, 889 (2007).
- [91] S. Deléglise, I. Dotsenko, C. Sayrin, J. Bernu, M. Brune, J.-M. Raimond, and S. Haroche, "Reconstruction of non-classical cavity field states with snapshots of their decoherence.", eng, *Nature* **455**, 510 (2008).
- [92] C. Sayrin, I. Dotsenko, X. Zhou, B. Peaudecerf, T. Rybarczyk, S. Gleyzes, P. Rouchon, M. Mirrahimi, H. Amini, M. Brune, J.-M. Raimond, and S. Haroche, "Real-time quantum feedback prepares and stabilizes photon number states.", eng, *Nature* **477**, 73 (2011).
- [93] X. Zhou, I. Dotsenko, B. Peaudecerf, T. Rybarczyk, C. Sayrin, S. Gleyzes, J. M. Raimond, M. Brune, and S. Haroche, "Field Locked to a Fock State by Quantum Feedback with Single Photon Corrections", *Phys. Rev. Lett.* **108**, 243602 (2012).
- [94] A. Signoles, A. Facon, D. Gross, I. Dotsenko, S. Haroche, J.-M. Raimond, M. Brune, and S. Gleyzes, "Confined quantum Zeno dynamics of a watched atomic arrow", *Nature Physics*, 715 (2014).
- [95] A. Facon, E.-K. Dietsche, D. Gross, S. Haroche, J.-M. Raimond, M. Brune, and S. Gleyzes, "A sensitive electrometer based on a Rydberg atom in a Schrödinger-cat state", *Nature* **535**, 262 (2016).
- [96] M. Saffman, T. G. Walker, and K. Mølmer, "Quantum information with Rydberg atoms", *Rev. Mod. Phys.* **82**, 2313 (2010).
- [97] H. Weimer, M. Müller, H. P. Büchler, and I. Lesanovsky, "Digital quantum simulation with Rydberg atoms", *Quantum Inf Process* **10**, 885 (2011).
- [98] H. Weimer, M. Müller, I. Lesanovsky, P. Zoller, and H. P. Büchler, "A Rydberg quantum simulator", *Nat Phys* **6**, 382 (2010).
- [99] M. D. Lukin, M. Fleischhauer, R. Cote, L. M. Duan, D. Jaksch, J. I. Cirac, and P. Zoller, "Dipole Blockade and Quantum Information Processing in Mesoscopic Atomic Ensembles", *Phys. Rev. Lett.* **87**, 037901 (2001).

- [100] Y. Dudin and A. Kuzmich, "Strongly interacting Rydberg excitations of a cold atomic gas.", eng, *Science* **336**, 887 (2012).
- [101] D. Barredo, S. Ravets, H. Labuhn, L. Béguin, A. Vernier, F. Nogrette, T. Lahaye, and A. Browaeys, "Demonstration of a strong Rydberg blockade in three-atom systems with anisotropic interactions.", eng, *Phys Rev Lett* **112**, 183002 (2014).
- [102] T. Wilk, A. Gaëtan, C. Evellin, J. Wolters, Y. Miroshnychenko, P. Grangier, and A. Browaeys, "Entanglement of two individual neutral atoms using Rydberg blockade.", eng, *Phys Rev Lett* **104**, 010502 (2010).
- [103] L. Isenhower, E. Urban, X. Zhang, A. Gill, T. Henage, T. Johnson, T. Walker, and M. Saffman, "Demonstration of a neutral atom controlled-NOT quantum gate.", eng, *Phys Rev Lett* **104**, 010503 (2010).
- [104] S. Ravets, H. Labuhn, D. Barredo, L. Béguin, T. Lahaye, and A. Browaeys, "Coherent dipole-dipole coupling between two single Rydberg atoms at an electrically-tuned Förster resonance", *Nat Phys* **10**, 914 (2014).
- [105] D. W. Schönleber, A. Eisfeld, M. Genkin, S. Whitlock, and S. Wüster, "Quantum simulation of energy transport with embedded Rydberg aggregates.", eng, *Phys Rev Lett* **114**, 123005 (2015).
- [106] I. Lesanovsky, "Liquid ground state, gap, and excited states of a strongly correlated spin chain.", eng, *Phys Rev Lett* **108**, 105301 (2012).
- [107] A. Dauphin, M. Müller, and M. A. Martin-Delgado, "Rydberg-atom quantum simulation and Chern-number characterization of a topological Mott insulator", *Phys. Rev. A* **86**, 053618 (2012).
- [108] J. P. Hague, S. Downes, C. MacCormick, and P. E. Kornilovitch, "Cold Rydberg Atoms for Quantum Simulation of Exotic Condensed Matter Interactions", *J Supercond Nov Magn* **27**, 937 (2013).
- [109] D. Barredo, H. Labuhn, S. Ravets, T. Lahaye, A. Browaeys, and C. S. Adams, "Coherent Excitation Transfer in a Spin Chain of Three Rydberg Atoms", *Phys. Rev. Lett.* **114**, 113002 (2015).
- [110] H. Labuhn, D. Barredo, S. Ravets, S. de Léséleuc, T. Macrì, T. Lahaye, and A. Browaeys, "Tunable two-dimensional arrays of single Rydberg atoms for realizing quantum Ising models", *Nature* **534**, 667 (2016).
- [111] J. E. Johnson and S. L. Rolston, "Interactions between Rydberg-dressed atoms", *Phys. Rev. A* **82**, 033412 (2010).
- [112] J. Zeiher, R. van Bijnen, P. Schauß, S. Hild, J.-y. Choi, T. Pohl, I. Bloch, and C. Gross, "Many-body interferometry of a Rydberg-dressed spin lattice", *Nature Physics advance online publication* (2016) **10**.1038/nphys3835.
- [113] R. M. W. van Bijnen and T. Pohl, "Quantum Magnetism and Topological Ordering via Rydberg Dressing near Förster Resonances", *Phys. Rev. Lett.* **114**, 243002 (2015).
- [114] A. W. Glaetzle, M. Dalmonte, R. Nath, C. Gross, I. Bloch, and P. Zoller, "Designing Frustrated Quantum Magnets with Laser-Dressed Rydberg Atoms", *Phys. Rev. Lett.* **114**, 173002 (2015).

- [115] T. Macrì and T. Pohl, "Rydberg dressing of atoms in optical lattices", *Phys. Rev. A* **89**, 011402 (2014).
- [116] E. A. Goldschmidt, T. Boulier, R. C. Brown, S. B. Koller, J. T. Young, A. V. Gorshkov, S. L. Rolston, and J. V. Porto, "Anomalous Broadening in Driven Dissipative Rydberg Systems", *Phys. Rev. Lett.* **116**, 113001 (2016).
- [117] J. Zeiher, P. Schauß, S. Hild, T. Macrì, I. Bloch, and C. Gross, "Microscopic Characterization of Scalable Coherent Rydberg Superatoms", *Phys. Rev. X* **5**, 031015 (2015).
- [118] J. A. Aman, B. J. DeSalvo, F. B. Dunning, T. C. Killian, S. Yoshida, and J. Burgdörfer, "Trap losses induced by near-resonant Rydberg dressing of cold atomic gases", *Phys. Rev. A* **93**, 043425 (2016).
- [119] S. E. Anderson, K. C. Younge, and G. Raithel, "Trapping Rydberg Atoms in an Optical Lattice", *Phys. Rev. Lett.* **107**, 263001 (2011).
- [120] S. E. Anderson and G. Raithel, "Ionization of Rydberg atoms by standing-wave light fields", *Nature Communications* **4**, 2967 (2013).
- [121] J. M. McGuirk, D. M. Harber, J. M. Obrecht, and E. A. Cornell, "Alkali-metal adsorbate polarization on conducting and insulating surfaces probed with Bose-Einstein condensates", *Phys. Rev. A* **69**, 062905 (2004).
- [122] K. S. Chan, M. Siercke, C. Hufnagel, and R. Dumke, "Adsorbate Electric Fields on a Cryogenic Atom Chip", *Phys. Rev. Lett.* **112**, 026101 (2014).
- [123] C. Hermann-Avigliano, R. C. Teixeira, T. L. Nguyen, T. Cantat-Moltrecht, G. Nogues, I. Dotenko, S. Gleyzes, J. M. Raimond, S. Haroche, and M. Brune, "Long coherence times for Rydberg qubits on a superconducting atom chip", *Phys. Rev. A* **90**, 040502 (2014).
- [124] R. C. Teixeira, C. Hermann-Avigliano, T. L. Nguyen, T. Cantat-Moltrecht, J. M. Raimond, S. Haroche, S. Gleyzes, and M. Brune, "Microwaves Probe Dipole Blockade and van der Waals Forces in a Cold Rydberg Gas", *Phys. Rev. Lett.* **115**, 013001 (2015).
- [125] H. A. Bethe and E. E. Salpeter, *Quantum mechanics of one-and two-electron atoms* (Springer Science & Business Media, 2012).
- [126] P. J. Mohr, D. B. Newell, and B. N. Taylor, "CODATA Recommended Values of the Fundamental Physical Constants: 2014", ArXiv e-prints (2015).
- [127] L. P. P. V. B. Berestetskii, E. M. Lifshitz, *Quantum Electrodynamics* (Elsevier Science & Technology, 1996), 670 Seiten.
- [128] A. Tauschinsky, R. Newell, H. B. van Linden van den Heuvell, and R. J. C. Spreeuw, "Measurement of ^{87}Rb Rydberg-state hyperfine splitting in a room-temperature vapor cell", *Phys. Rev. A* **87**, 042522 (2013).
- [129] W. Li, I. Mourachko, M. W. Noel, and T. F. Gallagher, "Millimeter-wave spectroscopy of cold Rb Rydberg atoms in a magneto-optical trap: Quantum defects of the ns , np , and nd series", *Phys. Rev. A* **67**, 052502 (2003).
- [130] J. Han, Y. Jamil, D. V. L. Norum, P. J. Tanner, and T. F. Gallagher, "Rb nf quantum defects from millimeter-wave spectroscopy of cold ^{85}Rb Rydberg atoms", *Phys. Rev. A* **74**, 054502 (2006).

- [131] M. Mack, F. Karlewski, H. Hattermann, S. Höckh, F. Jessen, D. Cano, and J. Fortágh, "Measurement of absolute transition frequencies of ^{87}Rb to nS and nD Rydberg states by means of electromagnetically induced transparency", *Phys. Rev. A* **83**, 052515 (2011).
- [132] J. D. Jackson, *Classical Electrodynamics* (JOHN WILEY & SONS INC, 1998), 832 pages.
- [133] S. Svanberg, *Atomic and molecular spectroscopy: basic aspects and practical applications*, Vol. 6 (Springer Science & Business Media, 2012).
- [134] C. Cohen-Tannoudji, J. Dupont-Roc, and G. Grynberg, *Atom-Photon Interactions: Basic Processes and Applications*, A Wiley-Interscience publication (Wiley, 1998).
- [135] R. Celistrino Teixeira, "Effets mécaniques de l'interaction dipolaire des atomes de Rydberg sondés par spectroscopie microonde", PhD thesis (Université Pierre et Marie Curie - Paris VI, Sept. 2014).
- [136] C. H. Hermann Avigliano, "Towards deterministic preparation of single Rydberg atoms and applications to quantum information processing", PhD thesis (Université Pierre et Marie Curie - Paris VI, Nov. 2014).
- [137] M. Diederich, H. Häffner, N. Hermanspahn, M. Immel, H. Kluge, R. Ley, R. Mann, W. Quint, S. Stahl, and G. Werth, "Observing a single hydrogen-like ion in a Penning trap at $T = 4\text{ K}$ ", *Hyperfine Interactions* **115**, 185 (1998).
- [138] Nogues, G., Roux, C., Nirrengarten, T., Lupaşcu, A., Emmert, A., Brune, M., Raimond, J.-M., Haroche, S., Plaçais, B., and Greffet, J.-J., "Effect of vortices on the spin-flip lifetime of atoms in superconducting atom-chips", *EPL* **87**, 13002 (2009).
- [139] A. Emmert, A. Lupaşcu, G. Nogues, M. Brune, J.-M. Raimond, and S. Haroche, "Measurement of the trapping lifetime close to a cold metallic surface on a cryogenic atom-chip", *The European Physical Journal D* **51**, 173 (2009).
- [140] G. Reinaudi, T. Lahaye, Z. Wang, and D. Guéry-Odelin, "Strong saturation absorption imaging of dense clouds of ultracold atoms", *Opt. Lett.* **32**, 3143 (2007).
- [141] M. Anwar, D. V. Magalhães, S. T. Müller, M. Faisal, M. Nawaz, and M. Ahmed, "Revisiting the capture velocity of a cesium magneto-optical trap: model, simulation and experiment", *Laser Physics* **24**, 125502 (2014).
- [142] E. Majorana, "Atomi orientati in campo magnetico variabile", *Il Nuovo Cimento (1924-1942)* **9**, 43 (1932).
- [143] D. M. Brink and C. V. Sukumar, "Majorana spin-flip transitions in a magnetic trap", *Phys. Rev. A* **74**, 035401 (2006).
- [144] T. Nirrengarten, "Piégeage magnétiques d'atomes de Rudibium au voisinage d'une surface supraconductrice", PhD thesis (Université Pierre et Marie Curie - Paris VI, 2007).
- [145] W. Ketterle and N. V. Druten, "Evaporative Cooling of Trapped Atoms", in *Advances In Atomic, Molecular, and Optical Physics*, Vol. 37, edited by B. Bederson and H. Walther, Advances In Atomic, Molecular, and Optical Physics (Academic Press, 1996), pp. 181–236.

- [146] F. Dalfovo, S. Giorgini, L. P. Pitaevskii, and S. Stringari, "Theory of Bose-Einstein condensation in trapped gases", *Rev. Mod. Phys.* **71**, 463 (1999).
- [147] C. Roux, A. Emmert, A. Lupascu, T. Nirrengarten, G. Nogues, M. Brune, J.-M. Raimond, and S. Haroche, "Bose-Einstein condensation on a superconducting atom chip", *EPL (Europhysics Letters)* **81**, 56004 (2008).
- [148] R. F. Gutterres, C. Amiot, A. Fioretti, C. Gabbanini, M. Mazzoni, and O. Dulieu, "Determination of the ^{87}Rb $5p$ state dipole matrix element and radiative lifetime from the photoassociation spectroscopy of the Rb_2 $0_g^- (P_{3/2})$ long-range state", *Phys. Rev. A* **66**, 024502 (2002).
- [149] T. W. Hall and C. H. B. Mee, "The work function of rubidium", *physica status solidi (a)* **21**, 109 (1974).
- [150] W. Sachtler, G. Dorgelo, and A. Holscher, "The work function of gold", *Surface Science* **5**, 221 (1966).
- [151] A. Gaetan, Y. Miroshnychenko, T. Wilk, A. Chotia, M. Viteau, D. Comparat, P. Pillet, A. Browaeys, and P. Grangier, "Observation of collective excitation of two individual atoms in the Rydberg blockade regime", *Nat Phys* **5**, 115 (2009).
- [152] T. M. Weber, M. Höning, T. Niederprüm, T. Manthey, O. Thomas, V. Guarnera, M. Fleischhauer, G. Barontini, and H. Ott, "Mesoscopic Rydberg-blockaded ensembles in the superatom regime and beyond", *Nat Phys* **11**, 157 (2015).
- [153] B. M. Axilrod and E. Teller, "Interaction of the van der Waals Type Between Three Atoms", *The Journal of Chemical Physics* **11**, 299 (1943).
- [154] J. B. Balewski, A. T. Krupp, A. Gaj, D. Peter, H. P. Büchler, R. Löw, S. Hofferberth, and T. Pfau, "Coupling a single electron to a Bose-Einstein condensate", *Nature* **502**, 664 (2013).
- [155] E. D. Black, "An introduction to Pound–Drever–Hall laser frequency stabilization", *American Journal of Physics* **69**, 79 (2001).
- [156] A. Urvoy, F. Ripka, I. Lesanovsky, D. Booth, J. P. Shaffer, T. Pfau, and R. Löw, "Strongly Correlated Growth of Rydberg Aggregates in a Vapor Cell", *Phys. Rev. Lett.* **114**, 203002 (2015).
- [157] M. Viteau, P. Huillery, M. G. Bason, N. Malossi, D. Ciampini, O. Morsch, E. Arimondo, D. Comparat, and P. Pillet, "Cooperative Excitation and Many-Body Interactions in a Cold Rydberg Gas", *Phys. Rev. Lett.* **109**, 053002 (2012).
- [158] H. Schempp, G. Günter, M. Robert-de-Saint-Vincent, C. S. Hofmann, D. Breyel, A. Komnik, D. W. Schönleber, M. Gärttner, J. Evers, S. Whitlock, and M. Weidmüller, "Full Counting Statistics of Laser Excited Rydberg Aggregates in a One-Dimensional Geometry", *Phys. Rev. Lett.* **112**, 013002 (2014).
- [159] F. M. Leupold, "Bang-bang Control of a Trapped-Ion Oscillator", PhD thesis (ETH-Zürich, 2015).
- [160] D. V. Dmitriev, V. Y. Krivnov, A. A. Ovchinnikov, and A. Langari, "One-dimensional anisotropic Heisenberg model in the transverse magnetic field", *Journal of Experimental and Theoretical Physics* **95**, 538 (2002).

- [161] C. N. Yang and C. P. Yang, "One-Dimensional Chain of Anisotropic Spin-Spin Interactions. I. Proof of Bethe's Hypothesis for Ground State in a Finite System", *Phys. Rev.* **150**, 321 (1966).
- [162] D. V. Dmitriev and V. Y. Krivnov, "Anisotropic Heisenberg chain in coexisting transverse and longitudinal magnetic fields", *Physical Review B* **70** (2004) 10.1103/physrevb.70.144414.
- [163] F. Capraro and C. Gros, "The spin-1/2 anisotropic Heisenberg-chain in longitudinal and transversal magnetic fields: a DMRG study", *The European Physical Journal B* **29**, 35 (2002).
- [164] A. A. Ovchinnikov, D. V. Dmitriev, V. Y. Krivnov, and V. O. Cheranovskii, "Antiferromagnetic Ising chain in a mixed transverse and longitudinal magnetic field", *Physical Review B* **68** (2003) 10.1103/physrevb.68.214406.
- [165] Y. Hieida, K. Okunishi, and Y. Akutsu, "Anisotropic antiferromagnetic spin chains in a transverse field: Reentrant behavior of the staggered magnetization", *Physical Review B* **64** (2001) 10.1103/physrevb.64.224422.
- [166] D. V. Dmitriev, V. Y. Krivnov, and A. A. Ovchinnikov, "Gap generation in the XXZ model in a transverse magnetic field", *Physical Review B* **65** (2002) 10.1103/physrevb.65.172409.
- [167] J.-S. Caux, F. H. L. Essler, and U. Löw, "Dynamical structure factor of the anisotropic Heisenberg chain in a transverse field", *Physical Review B* **68** (2003) 10.1103/physrevb.68.134431.
- [168] M. Gross and J. Liang, "Is a circular Rydberg atom stable in a vanishing electric field?", *Phys. Rev. Lett.* **57**, 3160 (1986).
- [169] J. Mozley, P. Hyafil, G. Nogues, M. Brune, J.-M. Raimond, and S. Haroche, "Trapping and coherent manipulation of a Rydberg atom on amicrofabricated device: a proposal", *The European Physical Journal D - Atomic, Molecular, Optical and Plasma Physics* **35**, 43 (2005).
- [170] R. G. Hulet, E. S. Hilfer, and D. Kleppner, "Inhibited Spontaneous Emission by a Rydberg Atom", *Phys. Rev. Lett.* **55**, 2137 (1985).
- [171] E. de Prunelé, "Orientation effects in thermal collisions between "circular" – Rydberg-state atoms and ground-state helium", *Phys. Rev. A* **31**, 3593 (1985).
- [172] G. Gabrielse, X. Fei, L. A. Orozco, R. L. Tjoelker, J. Haas, H. Kalinowsky, T. A. Trainor, and W. Kells, "Thousandfold improvement in the measured antiproton mass", *Phys. Rev. Lett.* **65**, 1317 (1990).
- [173] P. Hyafil, J. Mozley, A. Perrin, J. Tailleur, G. Nogues, M. Brune, J. M. Raimond, and S. Haroche, "Coherence-Preserving Trap Architecture for Long-Term Control of Giant Ryberg Atoms", *Physical Review Letters* **93** (2004) 10.1103/physrevlett.93.103001.
- [174] M. Saffman and T. G. Walker, "Analysis of a quantum logic device based on dipole-dipole interactions of optically trapped Rydberg atoms", *Phys. Rev. A* **72**, 022347 (2005).

- [175] I. I. Beterov, D. B. Tretyakov, I. I. Ryabtsev, A. Ekers, and N. N. Bezuglov, "Ionization of sodium and rubidium nS , nP , and nD Rydberg atoms by blackbody radiation", *Phys. Rev. A* **75**, 052720 (2007).
- [176] S. Blanes and P. Moan, "Practical symplectic partitioned Runge–Kutta and Runge–Kutta–Nyström methods", *Journal of Computational and Applied Mathematics* **142**, 313 (2002).
- [177] P. Soltan-Panahi, J. Struck, P. Hauke, A. Bick, W. Plenkers, G. Meineke, C. Becker, P. Windpassinger, M. Lewenstein, and K. Sengstock, "Multi-component quantum gases in spin-dependent hexagonal lattices", *Nat Phys* **7**, 434 (2011).
- [178] B. Tamir and E. Cohen, "Notes on Adiabatic Quantum Computers", ArXiv e-prints (2015).
- [179] P. Calabrese and J. Cardy, "Time Dependence of Correlation Functions Following a Quantum Quench", *Phys. Rev. Lett.* **96**, 136801 (2006).
- [180] S. Möbius, S. Wüster, C. Ates, A. Eisfeld, and J. M. Rost, "Adiabatic entanglement transport in Rydberg aggregates", *Journal of Physics B: Atomic, Molecular and Optical Physics* **44**, 184011 (2011).
- [181] S. Wüster, C. Ates, A. Eisfeld, and J. M. Rost, "Newton's Cradle and Entanglement Transport in a Flexible Rydberg Chain", *Phys. Rev. Lett.* **105**, 053004 (2010).
- [182] S. R. White, "Equivalence of the antiferromagnetic Heisenberg ladder to a single $S=1$ chain", *Phys. Rev. B* **53**, 52 (1996).
- [183] M. L. Zimmerman, M. G. Littman, M. M. Kash, and D. Kleppner, "Stark structure of the Rydberg states of alkali-metal atoms", *Phys. Rev. A* **20**, 2251 (1979).
- [184] S. Hovanessian, *Computational mathematics in engineering*, Practice Counts (Lexington Books, 1976).
- [185] D. Brink and G. Satchler, *Angular Momentum*, Oxford science publications (Clarendon Press, 1993).
- [186] G. Racah, "Theory of Complex Spectra. II", *Phys. Rev.* **62**, 438 (1942).
- [187] U. Albert Messiah, A. Messiah, *Quantum Mechanics* (ELSEVIER SCIENCE & TECHNOLOGY, Jan. 11, 1981), 1152 Seiten.

Study of dipole-dipole interaction between Rydberg atoms

Toward quantum simulation with Rydberg atoms

Abstract: Quantum simulation offers a highly promising way to understand large correlated quantum systems, and many experimental platforms are now being developed. Rydberg atoms are especially appealing thanks to their strong and short-range dipole-dipole interaction.

In our setup, we prepare and manipulate ensembles of Rydberg atoms excited from an ultracold atomic cloud magnetically trapped above a superconducting chip. The dynamics of the Rydberg excitation can be controlled through the laser excitation process. The many-body atomic interaction energy spectrum is then directly measured through microwave spectroscopy. This thesis develops a rigorous Monte Carlo model that provides an insight into the excitation process. Using this model, we discuss a possibility to explore quantum simulations of energy transport in a 1D chain of low angular momentum Rydberg atoms.

Furthermore, we propose an innovative platform for quantum simulations. It relies on a groundbreaking approach, based on laser-trapped ensemble of extremely long-lived, strongly interacting circular Rydberg atoms. We present intensive numerical results as well as discuss a wide range of problems that can be addressed with the proposed model.

Keywords: quantum simulation, Rydberg atoms, circular atoms, dipole-dipole interaction, atom chip, microwave spectroscopy

Étude de l'interaction dipolaire entre atomes de Rydberg

Vers la simulation quantique de chaînes de spin

Résumé : La simulation quantique offre un moyen très prometteur pour comprendre les systèmes quantiques corrélés macroscopiques. De nombreuses plateformes expérimentales sont en cours d'élaboration. Les atomes de Rydberg sont particulièrement intéressants grâce à leur forte interaction dipolaire de courte portée.

Dans notre manip, nous préparons et manipulons des ensembles d'atomes de Rydberg excités à partir d'un nuage atomique ultra-froid piégé magnétiquement sur une puce à atome supraconductrice. La dynamique de l'excitation est contrôlée par le processus d'excitation du laser. Le spectre d'énergie d'interaction atomique des N corps est mesuré directement par spectroscopie micro-onde. Dans cette thèse, nous développons un modèle Monte Carlo rigoureux qui nous éclaire sur le processus d'excitation. En utilisant ce modèle, nous discutons de la possibilité de réaliser des simulations quantiques du transport d'énergie sur une chaîne 1D d'atomes de Rydberg de faible moment angulaire.

De plus, nous proposons une plateforme innovante pour la réalisation de simulations quantiques. Elle repose sur une approche révolutionnaire basée sur un ensemble d'atomes de Rydberg dont le temps de vie est extrêmement long, qui interagissent fortement et qui sont piégés par laser. Nous présentons les résultats de simulations numériques et nous discutons du large éventail de problèmes qui peuvent être traités avec le modèle proposé.

Mots-clés : simulation quantique, atomes de Rydberg, atomes circulaires, interaction dipolaire, puce à atome, spectroscopie micro-onde